Probing the Magnetic Field Induced Nano-structures in Magnetic Fluids Using Light Scattering

By

SURAJIT BROJABASI

Enrolment No: PHYS02 2009 04002

Indira Gandhi Centre for Atomic Research, Kalpakkam

Tamil Nadu, India 603 102

A Thesis submitted to the Board of Studies in Physical Sciences

In partial fulfillment of requirements

For the degree of

DOCTOR OF PHILOSOPHY

of

HOMI BHABHA NATIONAL INSTITUTE

April, 2015

Homi Bhabha National Institute

Homi Bhabha National Institute

Recommendations of the Viva Voce Board

As members of the Viva Voce Board, we certify that we have read the dissertation prepared by **Surajit Brojabasi** entitled "**Probing the Magnetic Field Induced Nano-structures in Magnetic Fluids Using Light Scattering**" and recommend that it may be accepted as fulfilling the dissertation requirement for the Degree of Doctor of Philosophy.

for [illegible] (Dean - Academic) **Date:** 30/10/15

Chairman-**Dr. T. Jayakumar**

[signature] **Date:** 30/10/15

Convener-**Dr. John Philip**

[signature] **Date:** 30/10/2015

Member 1-Examiner

[signature] **Date:** 30.10.2015

Member 2-**Dr. T. R. Ravindran**

[signature] **Date:** 30/10/2015

Member 3- **Dr. V. P. Venugopalan**

Final approval and acceptance of this dissertation is contingent upon the candidate's submission of the final copies of the dissertation to HBNI.

CERTIFICATE

I hereby certify that I have read this dissertation prepared under my direction and recommend that it may be accepted as fulfilling the dissertation requirement.

Date: 30.10.15

Place: Kalpakkam

Dr. John Philip

(Guide)

STATEMENT BY AUTHOR

This dissertation has been submitted in partial fulfillment of requirements for an advanced degree at Homi Bhabha National Institute (HBNI) and is deposited in the Library to be made available to borrowers under rules of the HBNI.

Brief quotations from this dissertation are allowable without special permission, provided that accurate acknowledgement of source is made. Requests for permission for extended quotation from or reproduction of this manuscript in whole or in part may be granted by the Competent Authority of HBNI when in his or her judgment the proposed use of the material is in the interests of scholarship. In all other instances, however, permission must be obtained from the author.

Surajit Brojabasi

(Surajit Brojabasi)

Kalpakkam

April, 2015

DECLARATION

I, hereby declare that the investigation presented in the thesis entitled "***Probing the Magnetic Field Induced Nano-structures in Magnetic Fluids Using Light Scattering***" submitted to **Homi Bhabha National Institute (HBNI)**, Mumbai, India, for the award of **Doctor of Philosophy** in **Physical Sciences** is the record of work carried out by me during the period from September 2009 to September 2014 under the guidance of **Dr. John Philip**, Head, SMARTS, Metallurgy and Materials Group, Indira Gandhi Centre for Atomic Research, Kalpakkam. The work is original and has not been submitted earlier as a whole or in part for a degree/diploma at this or any other Institution/University.

Surajit Brojabasi

(Surajit Brojabasi)

Kalpakkam

April, 2015

Dedicated to

My respected Parents, my beloved Wife, my Family Members, respected Teachers & Friends

"It would be a poor thing to be an atom in a universe without physicists and physicists are made of atoms. A physicist is an atom's way of knowing about atoms."

George Wald (1906-1997)
Noble Laureate

ACKNOWLEDGEMENT

I express my sincere gratitude to **Dr. P. R. Vasudeva Rao,** Director, IGCAR for his inspiration and encouragement. I also thank **Dr. Baldev Raj** and **Shri S. C. Chetal,** the former Directors of IGCAR for permitting me to pursue research in this reputed centre. I am grateful to **Dr. T. Jayakumar**, Director, Metallurgy and Materials Group for his kind motivation and useful advices.

I owe my deep sense of gratitude to my research supervisor **Dr. John Philip** for all I have learnt. Without his untiring mentorship, creative ideas, valuable discussions and suggestions, strong support and encouragement, this thesis wouldn't have been possible. I consider myself fortunate to work with him.

My sincere thanks to my Doctoral Committee members **Dr. T. Jayakumar**, **Dr. John Philip**, **Dr. T. R. Ravindran** and **Dr. V. P. Venugopalan** for their valuable suggestions and encouragement during my research period. I am thankful to **Dr. Sai Baba** for his kind advice and making my stay at JRF enclave pleasant. I thank all the staffs of SMARTS and RTS (**Dr. T. Saravanan, Mr. K. Arun Muthu, Mr. S. Bagavathiappan, Mr. B. B. Lahiri, Mr. T. Muthukumaran, Mrs. J. Sangeetha and Mr. S. Kalyani**) for their kind help and support, and I always cherish the wonderful moments at SMARTS.

My special thanks to my friends (**Prof. A. K. Singh**, Banaras Hindu University, Varanasi, **Prof. B. K. Singh,** Banaras Hindu University, Varanasi, **Prof. A. K. Mukherjee,** The University of Burdwan, West Bengal, **Dr. R. B. D. Kathiyababa, Dr. B. B. D. Kathiyababa, Dr. Manas Sardar, Dr. Rahul Pal, Dr. Vijutha and Dr. L.**

Herojit, Mr. Shuaib) for their kind support and encouragement during my research period. I am also thankful to my seniors (**Dr. Gnanaprakash, Dr. Ayyappan, Dr. P. D. Shima, Dr. Junaid M. Laskar, Dr. J. S. Nambam and Dr. S. S. Pati**), as well as my juniors (**Mr. Mahendran, Ms. Leona, Ms. Anbumozhi, Mr. A. W. Zaibudeen, Ms. Sithara Vinod, Mr. Amit Kumar Mishra and Mr. Surojit Ranoo**) for their valuable help, discussions and understanding throughout my research period.

I thank Late **Mr. Swapan Brojabasi (Father)**, **Smt. Maya Brojabasi (Mother)**, **Smt. Priyanka Brojabasi (Wife)**, **Mr. S. Brojabasi (Brother)**, **Ms. R. Brojabasi (Sister)**, **Mr. M. M. Mukherjee (Father-in-law)**, **Smt. Alo Mukherjee (Mother-in-law)**, **Ms. Jyoti Mukherjee (Sister-in-law) and Ms. Mayuri Mukherjee (Sister-in-law)** for all their support and encouragement. I am especially thankful to **Prof. Patrick Fournier,** Université de Sherbrooke, Canada for his valuable suggestions and support. I am thankful to my teachers & friends during my school and college days for their constant support and care throughout my career. Lastly, I thank each and everyone in the JRF enclave for their help and making my stay comfortable.

Surajit Brojabasi

(Surajit Brojabasi)

Kalpakkam

April, 2015

CONTENTS

Chapter III

Probing the Magnetic Field Induced Nano-structures in Magnetic Fluids by Light Transmission

Chapter IV

Probing the Field Induced Structural Transitions by Transmitted Light Speckle Dynamics in Magnetic Fluids

Chapter V

Magnetic Field Dependent Backscattering of Light in Water Based PAA Covered Fe_3O_4 Nanofluid

Chapter VI

Probing the Magnetic Field Dependent Structural Transitions

in Nanoemulsion by Near Infrared Light Absorption

Chapter VII

Probing the Effect of Suspended Nano-particle Size on Magnetic Field Induced Structural Transitions in Ferrofluids

Chapter VIII

Probing the Effect of Temperature on Magnetic Field Induced Structural Transitions in Ferrofluids

Chapter IX

Conclusions and Future Perspectives

SYNOPSIS

Magnetic fluids (Ferrofluids and Ferrofluid emulsions) are stimulus responsive soft materials whose physical properties can be strongly modified by an external magnetic field. Such magnetic fluids have several important technological applications. Magnetic fluids undergo interesting structural changes under an external magnetic field. Various techniques such as small angle neutron scattering (SANS), small angle X-ray scattering (SAXS), visible wavelength light transmission, Monte Carlo simulation, molecular dynamics, stochastic and Brownian dynamics simulation have been employed to get insight into the aggregation dynamics in magnetic fluids. Magnetic fluids exhibit field-induced optical anisotropy in the presence of an external magnetic field, which leads to many extraordinary magneto-optical properties such as static magnetic birefringence and dichroism, magnetically tunable refractive index, photonic hall-effect, vanishing of forward and backward scattered light and negative refractivity.

Optical studies show that magnetic fluids are ideal materials to study the scattering phenomena in different optical regimes, as the scatterer size can be tuned from Rayleigh regime (scatterer size $<< \lambda$) to geometrical regime (scatterer size $>> \lambda$) via Mie regime (scatterer size $\sim \lambda$) by varying the external magnetic field. The scatterer size increases with increasing external magnetic field due to aggregation of suspended nano-sized magnetic particles. The field induced aggregation in these systems is mainly due to the dipolar interaction between the dispersed nano-sized magnetic particles, which depends on the applied magnetic field strength and particle size.

Irrespective of several studies in the past, a complete understanding of field induced aggregation dynamics and associated magneto-optical properties in magnetic fluids is still lacking, which is important for practical applications. The main objective of this thesis work was to obtain better insights into the complex aggregation, disorder-order transitions, and the intriguing magneto-optical phenomena in magnetic fluids using the forward light scattering, backscattering, and absorption and speckle dynamics studies. The role of aggregation parameters such as suspended nanoparticle size, volume fraction and temperature on structural transitions and associated magneto-optical properties in magnetic fluids are investigated. The thesis consists of nine chapters. **Chapter 1** gives a brief description of soft matter, stimulus responsive materials, magnetic fluids and its extraordinary physical properties and literature survey on the study of field induced structural transitions, motivation and objectives of the present work. **Chapter 2** describes the details of the samples, characterization techniques, experimental setup and the procedure adopted for (i) capturing the scattered speckle patterns, (ii) measuring the transmitted, (iii) backscattered light intensity, (iv) absorption and (iv) speckle intensities as a function of magnetic field and time. **Chapter 3** presents the study of magnetic field dependent behavior of transmitted light intensity and scattered pattern in ferrofluid and nanoemulsion. The resonances in the total extinction efficiency and the forward anisotropy factor due to the changes in the dimension of scatterers due to dipolar interactions and the changes in the surface roughness of the field induced aggregates contribute to the observed variations in the transmitted light intensity and the scattered patterns. **Chapter 4** presents the study of transmitted light speckle pattern through ferrofluid and nanoemulsion in presence of an

external magnetic field. The linear increase in speckle contrast of transmitted light spot from ferrofluids in the presence of external magnetic field indicates a transformation from ‘dynamic’ to ‘fully developed’ speckle pattern due to the formation of chain-like structures by nano sized particles. The surface roughness of field induced aggregates is found to hamper the speckle pattern from being ‘fully developed’. The transmitted speckle correlation coefficient showed power law decay with external magnetic field. In nanoemulsion, the angular speckle correlation coefficient decays exponentially with measurement angles in the observation plane and the angular speckle correlation is found to be symmetric on either side of the transmitted bright spot. **Chapter 5** presents the study of the effect of applied magnetic field on the backscattered light intensity from a ferrofluid consisting of poly-acrylic acid coated Fe_3O_4 nanoparticles dispersed in water. The effect of applied magnetic field on the backscattering of light showed a continuous evolution of backscattered speckle pattern as a function of magnetic field strength. The speckle contrast is found to increase linearly with external magnetic field because of the evolution from highly dynamic to static scatterers in the dispersion. The backscattered light intensity is found to diminish with external magnetic field due to a delay of light propagation of standing waves in the scattering medium. **Chapter 6** presents the study of magnetic field dependent near infrared photon absorption in nanoemulsion. The absorption of near infrared photons is found to be dependent on the volume fraction and applied magnetic field because of the variation in the Mie absorption efficiency during the field induced structural transitions of emulsion droplets. The absorption increases linearly with the incident near infrared photon energy up to a certain external magnetic field. The imaginary part of the refractive index of

nanoemulsion is found to vary with external magnetic field and sample volume fractions. After a critical magnetic field, the field induced absorption of near infrared photons decreases because of the increase in the aspect ratio of the chain like aggregates and inter-chain spacing. **Chapter 7** presents the study of the effect of hydrodynamic particle size on the magnetic field induced light transmission and transmitted speckle pattern in water based ferrofluids containing functionalized Fe_3O_4 nanoparticles. The transmitted light intensity starts decreasing above a certain magnetic field and becomes a minimum at another field and these two critical fields signify the onset of linear aggregation process and zippering transitions, respectively. Both these critical fields shift towards lower magnetic fields with increasing hydrodynamic diameter, due to stronger magnetic dipolar interaction. The onsets of chaining and zippering transitions were clearly evident from the time dependent transmitted light intensity. Above the first critical field, the lobe part of the transmitted intensity and the lobe speckle contrast values increase with increasing external magnetic field due to the reduced Brownian motion of field induced aggregates. The speckle contrast was the highest for the nanoparticle with the largest hydrodynamic diameter, due to reduced Brownian motion of particles. **Chapter 8** describes the temperature dependent light transmission study which shows that the rate of extinction of normalized transmitted light intensity linearly decreases with increasing specimen temperature, indicating a slower rate of field induced aggregation kinetics at higher specimen temperature due to enhanced Brownian motion of suspended particles. **Chapter 9** summarizes the results obtained, conclusions and future scopes.

LIST OF FIGURES

LIST OF TABLES

LIST OF ABBREVIATIONS

PAA	Poly-acrylic acid
TMAOH	Tetra-methyl ammonium hydroxide
PDI	Polydispersity index
SDS	Sodium Dodecyl Sulphate
SC	Sample cuvette
IF	Interference filter
M	Mirror
PMT	Photomultiplier tube

ADC	Analog to digital converter
IPS	Inter-particle spacing
P_1	Polarizer
DC	Direct current
He-Ne	Helium–neon
LED	Light-emitting diode
USB	Universal serial bus
CCD	Charge-coupled device
DLS	Dynamic light scattering
2D	2 Dimensional
3D	3 Dimensional
SSC	Spectral speckle correlation
ASC	Angular speckle correlation
NIR	Near infrared
eV	Electron volt
OSS	Optical spatial soliton
FMR	Ferromagnetic resonance
SANS	Small angle neutron scattering
SAXS	Small angle X-ray scattering
TEM	Transmission electron microscopy
PHE	Photonic hall effect
THz	Terahertz
FOM	Figure of merit

LIST OF SYMBOLS

d	Diameter of nanoparticle
a	Radius of nanoparticle
d_1	Diameter of emulsion droplet

a_1	Radius of emulsion droplet
B	Magnetic field
t	Time
L	Sample cuvette path length
λ	Incident laser wavelength
D_T	Translational diffusion coefficient
$G(\tau)$	Correlation function of the scattered intensity
τ	Correlator time delay
$I(t)$	Light intensity at time t
A_1	Baseline of the correlation function
β	Intercept of the correlation function
k	Wave-vector
Γ	Decay rate
θ	Scattering angle
n'	Refractive index of dispersant
$g_1(\tau)$	Sum of all the exponential decays contained in the correlation function
d_h	Hydrodynamic diameter
k_B	Boltzmann's constant
T	Temperature
η	Viscosity
ϕ	Volume fraction
I_{total}	Normalized transmitted total intensity
I_{spot}	Normalized transmitted spot intensity

B_C	Critical field
B_{C1}	First critical field
B_{C2}	Second critical field
y	Exponent in power law dependence behavior in critical magnetic fields
m	Induced dipole moment of an individual nanoparticle
χ	Magnetic susceptibility
H	Magnetic field strength
μ_0	Magnetic permeability of vacuum
U_{ij}	Interaction energy due to dipolar interaction between i^{th} and j^{th} particle
r_{ij}	Position vector between i^{th} and j^{th} particle
Λ_{coup}	Magnetic coupling constant between particles
θ_{ij}	Angle between the vector r_{ij} and the external field
$S(k)$	Structure factor
$I(k)$	Scattered intensity from the sample
$I(k_0)$	Scattered intensity from ideal sample
ρ^*	Reduced particle number density
N	Number of nanoparticles
V	Volume of nanoparticle
D_f	Fractal dimension of the scatterers
ℓ^*	Transport mean free path of light
ℓ	Mean free path of light
μ	Magnetic permeability of Fe_3O_4 nanoparticle

$<\cos\theta>$	Forward anisotropy factor
(a_n , b_n , c_n , d_n)	Mie scattering parameters
$j_n, h_n^{(1)}$	Spherical Bessel and spherical Hankel functions of first kind of order n , respectively (prime as derivative)
ε_{MF}	Dielectric constant of ferrofluid
m_{MF}	Refractive index of ferrofluid
Q_{ext}	Total extinction efficiency factor
V_C	Verdet Constant
$\ell_\perp$	Magneto-transverse mean free path
$J_\perp$	Magneto-transverse light current
n_s	Refractive index of the scatterer
a_w	Waveguide damping coefficient
r	Waveguide length
$\frac{dy}{dx}$	Ratio of the length and the width of a speckle on the observation plane
$r_{incident}$	Incident laser light spot diameter
σ_φ	Variance of the phase fluctuations
σ_h	Variance of the surface height fluctuations
$\gamma_{12}(\tau)$	Degree of coherence of any two scattered lights
ξ_φ	Normalized auto-correlation function of the phases
D_P	% depolarization
P	% polarization
C	Speckle contrast

σ	Standard deviation of the speckle intensity
I^s	Speckle intensity
$<I^s>$	Mean speckle intensity
T_{exposure}	Exposure time
τ_c	Correlation time
m'	Slope
s_1	Linear fit constant
σ_b	Bandwidth of incident light
C_S	Speckle correlation coefficient
$C_{Theo.}$	Theoretical speckle contrast
C_{12}^{SSC}	Far field correlation coefficient
C_{12}^{ASC}	Angular speckle correlation coefficient
α_1	Angle of incidence
C_L	Lobe speckle contrast
θ_b	Backscattered angle
Q_b	Backscattered efficiency
$F_{\max}$	Maximum magnetic force between two nanoparticles
t_c	Initial time for two nanoparticles to aggregate
$p(\theta)$	Phase function
r_1	Initial separation distance between the nanoparticles
τ_B	Brownian relaxation time
τ_N	Néel relaxation time

V_h	Hydrodynamic volume of nanoparticle
V_m	Magnetic volume of the nanoparticle
f_0	Attempt frequency of magnetization
K	Magnetic anisotropy constant of the nanoparticles
ζ_0	Electrical surface potential of emulsion droplet
κ	Inverse Debye length
C_e	Electrolyte concentration
L_B	Bjerrum length
ρ_n	Number density of nanoemulsion droplets
v	Emulsion droplet volume
α	Light absorption coefficient
A	Near infrared photon absorption
C_{abs}	Light absorption cross-section
E	Photon energy
m_1	Refractive index of nanoemulsion
n_1	Real part of refractive index of nanoemulsion
k_1	Imaginary part of refractive index of nanoemulsion
p	Exponent in power law dependence behavior in imaginary part of the refractive index of nanoemulsion
Q_{abs}	Mie absorption efficiency
E_1	Electric field component of incident near infrared photons
ε''	Imaginary part of relative dielectric constant of emulsion droplet
t_{min}	Minimum time

B_{LC}	Transmitted lobe critical field
Q_{sca}	Scattering efficiency
R_{trans}	Rate of field induced light extinction
ρ	Density of the nanoparticles
V_{RMS}	Root mean square velocity of dispersed nanoparticles
G	Gauss

LIST OF PUBLICATIONS IN PEER-REVIEWED JOURNALS

1. Surajit Brojabasi, V. Mahendran, B. B. Lahiri and John Philip, "Temperature dependent light transmission in ferrofluids", **Optics Communications**, 342, (2015) pp. 224-229.

2. Surajit Brojabasi, T. Muthukumaran, J. M. Laskar and John Philip, "The Effect of Suspended Fe_3O_4 Nanoparticle Size on Magneto-Optical Properties of Ferrofluids", **Optics Communications**, 336, (2015) pp. 278-285.

3. Surajit Brojabasi, B. B. Lahiri, John Philip, "External magnetic field dependent light transmission and scattered speckle pattern in magnetically polarizable oil-in-water nanoemulsion", **Physica B: Condensed Matter**, 454, (2014) pp. 272-278.

4. Surajit Brojabasi, V. Mahendran, B.B. Lahiri, John Philip, "Near infrared light absorption in magnetic nanoemulsion under external magnetic field", **Optics Communications**, 323, (2014) pp. 54-60.

5. Surajit Brojabasi and John Philip, "Magnetic field dependant backscattering of light in water based ferrofluid containing polymer covered Fe_3O_4 nano-particles", **Journal of Applied Physics**, 113, (2013) pp. 054902.

6. Surajit Brojabasi and John Philip, "Transmitted Light Intensity and the Speckle Pattern in a Poly-Acrylic Acid Stabilized Ferrofluid in the Presence of an External Magnetic Field", **Journal of Nanofluids**, 2, (2013) pp. 237-248.

7. Junaid M. Laskar, **S. Brojabasi**, Baldev Raj, John Philip, "Comparison of light scattering from self assembled array of nanoparticle chains with cylinders", **Optics Communications**, 285, (2012) pp. 1242–1247. †

(† Not included in the thesis)

CONFERENCES & SYMPOSIA

1. Surajit Brojabasi and John Philip, "Magnetic Nanofluid — A Tunable Photonic Material", Paper presented (Poster) in "**International Union of Materials Research Society - ICA 2013**", Indian Institute of Science, Bangalore, India, during December 16-20, (2013), pp. 28

2. J. M. Laskar , **S.Brojabasi**, J. Philip & B. Raj., "Magnetic-field-induced aggregation kinetics in ferrofluids", **DAE-BRNS National Laser Symposium (NLS 19)**, Raja Ramanna Centre for Advanced Technology, Indore, India, during December 1-4, (2010), pp. 62.

Chapter-I Introduction

1.1 Introduction

The world is full of hidden knowledge that cries out for explanations. The essence of science is the observation and exploration of the world around us. Proper scientific observations enabled us to understand the phenomena behind the colors of rainbows and soap bubbles, the vapor trails of high-flying aircraft, the transformation of liquid water into ice, lightning and thunder, the beautiful hexagonal symmetry of small snowflakes etc. Physics provides the knowledge of the fundamental and unifying principles of nature.

Condensed matter physics deals with the many-body interactions and collective phenomena in the "condensed" phases of material [1-5]. The physical properties of condensed matter systems cannot be understood by considering single particles in isolation. Solids and liquids are collectively referred as condensed phase matters which are characterized by strong inter-molecular forces. However, in liquid the intermolecular forces are not as strong as in solids, which provide liquid to flow and change its shape. The condensed phases have low compressibility, i.e. the volume change per unit pressure change, compared to gases. Research activities in condensed matter gave birth to many interesting breakthroughs and enabled the production of several novel materials with superior physical properties.

1.2 Soft Matter

'Soft matter' is easily deformable and covers a large variety of systems, from polymers to colloids, from liquid crystals to surfactants, and from soap bubbles to solutions of macromolecules, granular matter etc. Unlike solids, soft materials have no crystalline symmetry and their behavior is different from fluids which have a uniform disorder. Soft

matter can move in unprecedented ways and thereby confer unique flow properties that distinguish them qualitatively from simple fluids.

Therefore, soft materials occupy a position between the two extremes: liquid and ideal solid state. As the soft matter is situated at the interface between chemistry, biology, and condensed matter physics, it is studied by physicist, chemists, chemical engineers and biologists [6-9]. Soft materials are highly sensitive to temperature and external pressure and generally structured on many length scales, leading to relaxation processes with timescales spanning many decades [10]. Its main physical behaviors occur at an energy scale comparable to room temperature and therefore can easily be deformed by thermal stresses or thermal fluctuations [11-14]. So the interactions that govern the behavior of soft materials are often weak and comparable in strength to thermal fluctuations. A minute change in molecular interaction may sometimes lead to a massive change of the macroscopic properties of soft matter systems. Also, soft materials are characterized by the viscoelastic behavior i.e. a fluid-like response on long time scales but solid like on shorter time scales and their mechanical response is strongly dependent on loading rate and time [15-19]. Self-organization, an irreversible growth process in thermal equilibrium, is one of the important properties in soft matter systems [20-23]. Through self assembly, soft matter can mimic living matter and can serve as model systems for biological systems and bio-inspired materials. Soft matter is a "mesoscopic matter" since the size of the basic constituents' ranges from a few nano-meters to about one micro-meters [24-26]. In particular, the 'soft' name, to a large extent, is attributed to a delicate interplay between energy and entropy on the atomistic scale, giving rise to nontrivial mesoscopic structure, and the interactions between effective units on the mesoscopic scale are often entropic in origin [14, 24]. Understanding the mesoscale structure and the effective interactions is the key to improvement of properties of soft materials. One of the fundamental reasons for the intense

research activities in soft matter systems is that they are highly dynamic and responsive to a range of different stimuli, making them ideal for a wide range of applications [27-29]. The intriguing optical properties of polymers and liquid crystals are extensively used to develop modern devices [13, 30-32]. The negative Poisson's ratio (auxetic) soft materials have huge applications in materials science and technology [33-36].

Soft matter is one of the ideal model systems to study the fundamental physical phenomena such as symmetry breaking and low energy excitations [6, 37, 38], topological defects [39], phase transition behavior [40-42], glass transition [41, 43-45], interparticle forces [46], and crystallization process [47]. By utilizing the theoretical concepts such as scaling, renormalization group etc., several authors studied the fundamental aspects like phase transition and critical phenomena [6, 48, 49]. Nikkhou *et al.* [50] demonstrated the creation and manipulation of precisely light controlled topological charges in nematic liquid crystals. The low energy optical spatial solitons (OSS) have been observed in soft matters such as liquid crystals, and these OSS can measure the fractal dimensions of the aggregates in soft matter systems [51].

Soft materials have gathered increasing interest over the past few decades due to the broad range of possible applications in environmental, biological, biomedical, pharmaceutical and clinical research [52-56]. One of the major reasons for the growing interest in soft matter is because of its ability to deliver poorly water soluble drug molecules in drug targeting [57, 58].

1.3 Magnetic Fluids

Magnetic fluids also known as 'Ferrofluids', 'Magnetic nanofluids', 'Ferrofluid emulsion or Nanoemulsion' are special category of magnetic soft materials consisting of nano-sized magnetic particles or droplets with super-paramagnetic nanoparticles dispersed in a carrier liquid [59-65]. 'Ferrofluids' consist of colloidal suspension of single domain ferro- or ferri-

magnetic nanoparticles stabilized by surfactants and dispersed in a carrier liquid, whereas 'Nanoemulsion' is a dispersion of oil droplets in water where each oil droplet contains magnetite nanoparticles and the nano-sized oil droplets are often electrostatically stabilized by an ionic surfactant like sodium dodecyle sulphate (SDS). These magnetic fluids offer the unique possibility of remotely tuning the particle interaction by external magnetic field [66, 67].

The first reported work, in this domain, was in 1779 by Gowan Knight [61, 68], who made suspension of iron filling in water, where the suspension was unstable. In 1930, Bitter [69] prepared a ferrofluid which was a colloidal solution of micron sized γ-Fe_2O_3 particles in ethyl ethanoate, but it was only stable under gravity but not under external magnetic field. In 1938 Elmore [70] prepared a ferrofluid with 20 nm size Fe_3O_4 particles, and this approach was later adopted by many researchers. The first modern day magnetic fluids was developed by NASA's Lewis Research Centre in the mid of 1960's, where Papell [59] prepared a dispersion of iron oxide nanoparticles suitable for dispersing in liquid propellant fuel, with an idea of filling the weightless fuel by an external magnetic field in the gravity free environment .

Later, magnetic fluids were produced with long term stability [59, 61]. To ensure the stability of magnetic fluids, the thermal motion of nano-sized magnetic particles has to overcome gravitational force and magnetic field gradients. To avoid this irreversible agglomeration, the nano-sized magnetic particles are coated with surfactant molecules.

1.3.1 Tunable Interparticle Interactions

Stimulus responsive materials undergo dynamic and reversible conformational changes under the action of external stimuli such as magnetic field, electric field, temperature, pH, and ionic strength [71-73]. Such materials have a wide range of applications in environmental, biomedical sciences, drug delivery, self-healing and fabrication of modern devices [74-77].

Magnetic fluids are a new class of stimulus responsive soft material because they possess tunable physical properties [78-80]. The nature of interacting force and interparticle interaction under different conditions are very important for achieving the tunable physical properties. The magnetic properties of magnetic fluids depends on the interparticle interaction, which have been studied both experimentally and theoretically [81]. The two mechanisms that are responsible for magnetic relaxation in ferrofluids are 'Brownian relaxation' and 'Néel relaxation' [59, 82]. Interparticle interactions influence the relaxation mechanisms which in turn can affect the magnetic dynamics in magnetic fluid. The relaxation mechanisms have been studied experimentally by static magnetic birefringence [83]. Room temperature ferromagnetic resonance was used to investigate particle-particle interaction in magnetic fluids [84]. The external magnetic field dependent magnetization of ferrofluid was evaluated theoretically by considering the Born-Mayer technique and expansion of dipolar coupling strength [85].

The interparticle correlations and its effect on magnetic properties of dense magnetic fluids was elucidated through a statistical model [86]. Experimental techniques were also developed to directly measure the forces between tiny colloidal particles [87, 88]. The dependence of interparticle interaction on frequency of applied ac magnetic field was studied, by floating the two microspheres on glycerin [89]. The unique tunable interparticle interaction has a dominent impact on the physical properties of magnetic fluids and hence such fluids were used to reduce the strength of magnetic field required to orient the nematic liquid crystals [90]. A glassy behavior was observed in frozen ferrofluids due to dipolar interactions [91]. The spin glass dynamics was observed in concentrated frozen ferrofluid, whereas the dilute system showed isolated particle dynamics [92].

1.3.2 Interesting Properties of Magnetic Fluids

Magnetic fluid consists of super-paramagnetic nanoparticles, which have become increasingly important in various technological applications [59, 93, 94]. The super-paramagnetic nanoparticles are distinguished from ferromagnetic nanoparticles by their material properties, small size and single magnetic domain. Their extreme magnetic susceptibility is due to the relatively miniscule size of the particles. Magnetic anisotropy of superparamagnetic nanoparticles has been analyzed by others techniques such as Mossbauer spectroscopy and ferromagnetic resonance (FMR) [95, 96]. Magnetic fluids possess structural anisotropy in the presence of an external magnetic field [60, 91]. The 'Neel relaxation' is caused by the reorientation of the magnetization vector inside the magnetic core against anisotropy energy barrier. 'Brownian relaxation' is due to rotational diffusion of particle as a whole in the carrier liquid. The time constant of Neel relaxation depends much stronger on the particle diameter than the Brownian relaxation time. The effective relaxation time is dominated by the faster relaxation process [59-61].

The measurement of dynamic magnetic behavior of magnetic fluid at low temperatures showed a hysteresis loop in the magnetization curve due to Neel relaxation processes, unlike the super-paramagnetic behavior at room temperature [97]. The magnetic properties of ferrofluid consisting of a mixture of micro and nano-magnetite particles has shown that the increase of nano-magnetite in suspensions induces a substantial increase in both the weak field susceptibility and coercivity of suspensions [98]. It has also been found that the saturation magnetization increases with the volume fraction of nanomagnetite. Using forced Rayleigh scattering technique, the periodic spatial modulation of an absorbing grating was studied [99, 100]. Here, the characteristic relaxation time of the pattern is found to be directly related to the cooperative diffusion coefficient of particles.

The measurement of complex susceptibility and permittivity of magnetic fluids by different techniques revealed the presence of a resonance in susceptibility profile over some frequency range, which was indicated by a transition of susceptibility from positive to negative value, where the permittivity was approximately constant over the measured frequency range [101, 102]. A new experimental method for the determination of the Landau–Lifshitz damping parameter in magnetic fluids was developed, which was based on the measurements of the frequency and field dependence of the complex magnetic susceptibility [103]. Jonsson *et al.* [104] experimentally verified the divergent behavior of the nonlinear field dependent AC susceptibility of interacting magnetic nanoparticles in a concentrated frozen ferrofluid using static scaling analysis of the nonlinear susceptibility data. Fannin *et al*. [105] observed an apparent super-diamagnetic effect in ferrofluid containing non-magnetic polystyrene beads due to the formation of holes with an apparent induced diamagnetic moment. Study of spin dynamics in a ferrofluid using a 'Selective Excitation Double Mössbauer (SEDM)' experimental technique has led to the understanding of static disorder, collective excitations and super-paramagnetic spin flips [106].

Magnetic fluids have an ability to change their rheological properties under the action of external magnetic field [107, 108]. They exhibit field-dependent viscosity, special adhesion properties, and a non-Newtonian behavior [109, 110]. Experimental studies in ferrofluids under shear flow have shown a magneto-viscous effect [60, 110]. The role of dipolar interactions on the viscosity of magnetic fluids under magnetic field was studied by molecular simulations and dynamical mean-field theory [111]. Measurement of magneto-rhelogical properties in inverse ferrofluid and various other magnetic fluid systems with and without additives were also studied [112-116].

Demouchy *et al.* measured the nanoparticle-diffusion coefficient and the Soret coefficient in ferrofluid by using two dimensional forced Rayleigh-scattering apparatus [117]. Bulk flow of a ferrofluid in a uniform rotating magnetic field was studied by using the ultrasonic velocity profile method [118].

Studies showed that dipolar chains of nonmagnetic particles in a suspension of ferrofluid fluctuate under the effect of Brownian noise at equilibrium, and these dipolar chains roughen dynamically on sudden decrease in external magnetic field [119]. On studying the time and size scaling of chain fluctuationsand the equilibrium and out of equilibrium behavior, it was shown that a non-Markovian anomalous diffusion process of particles contributes to such interesting effects.

Magnetic fluids exhibit several kinds of instabilities under magnetic field, gravity and temperature [59, 120-122]. The types of instabilities depend on the rheological parameters of magnetic fluids too. The Benard-Marangoni instability, a surface tension driven instability originates due to temperature variations inside magnetic fluids, depends on the rheological parameters of magnetic fluids [123]. Rayleigh-Taylor (RT) instability, a gravitational instability that occurs when a dense fluid lies above a less dense fluid causing fingering at the interface between the fluids when one of the fluids has magnetorheological property [124-126]. When a ferrofluid layer wass subjected to a uniform and vertically oriented magnetic field, an interfacial instability, called as the ‘normal field instability’, occured above a critical value of the magnetic field, giving rise to a hexagonal array (pattern) of peaks [127-129]. The instability mechanism was attributed to the presence of a vertical magnetic field, where the perturbations of the ferrofluid surface concentrate the magnetic flux. The resulting magnetic force tends to drive the perturbation further, while surface tension and gravitational forces have a stabilizing influence. When the magnetic force exceeds the stabilizing forces an instability develops [130].

The sedimentation instability, due to the Kelvin force is larger in areas with higher concentration of magnetic particles. Amplified concentration fluctuations can also lead to instability. When a ferrofluid droplet is confined in a Hell-Shaw cell (effectively 2D geometry) in the presence of a uniform magnetic field, a branched structure evolves which was called as labyrinthine instability [59, 121, 131, 132].

In presence of static normal and parallel external magnetic fields, wave turbulence was observed in magnetic fluid surfaces [133, 134]. Stable soliton-like structure was observed on the surface of magnetic fluid, generated by a local perturbation in the hysteretic regime of the Rosensweig instability [135].

In presence of DC axial magnetic field, a ferrofluid drop in Hele-Shaw cell forms the familiar labyrinth pattern [59]. With subsequent application of a rotating uniform magnetic field, smooth spirals form. If the rotating magnetic field is applied first, the drop holds together for low dc-axial magnetic fields and no labyrinth pattern develops. Motion of droplet on a planar surface is one of the vital studies in droplet based lab on a chip technology [136]. Nguyen *et al.* experimentally investigated the magneto-wetting effect of a ferrofluid droplet on a planar homogeneous surface [137]. In presence of a uniform magnetic field, ferrofluid droplet on a superhydrophobic surface deformed in nonlinear pattern and increasing the magnetic flux density increases the droplet width and decreases the droplet height [138].

Enhancement and tunability of thermal conductivity in ferrofluids along the external magnetic fieldwas observed recently [78, 139]. Also, magnetic fluids were shown to be a model system to investigate thermal ratcheting behavior [140]. Under horizontal sinusoidal vibrations, a transition from an ordered solid-like phase to a disordered liquid-like phase of spikes on a ferrofluid surface was reported [141]. The melting transition occurs for a critical spike displacement which was found to follow the Lindemann criterion, for two different lattice

topologies (hexagonal and square) and over a wide range of lattice wavelengths. This dissipative out-of-equilibrium system was shown to exhibit strong similarities with 2D melting in solid-state physics.The zero-field birefringence of magnetic fluids have been studied both experimentally and theoretically [142, 143]. The laser self-induced tunable birefringence and thermo-optical effects in a magnetic fluid were also studied recently [143, 144].

1.3.3 Applications of Magnetic Fluids

Applications of magnetically tunable soft matters are increasing day by day in various fields e.g. mechanical engineering, optical engineering, and biotechnology. [61, 145]. Magnetic fluids are being used in micro robot [146], hydrostatic bearing [147], liquid seal [148], defect detection [149, 150], optical grating [151], optical limiter [152], actuator [153], optical fiber modulator [154, 155], magneto optical waveguide [156], magneto optical wavelength filter [157], optical switches [158], tunable optical capacitors [159], optical sensors [160, 161], weak molecular force probes [162], miniature smart cooling [163] etc.

Magnetic fluids have several applications in biomedical research fields [164] e.g. biosensors [165], microfluidic devices [166], hyperthermia treatment [167, 168], tumor treatment[169], cell toxicity study[170], and magnetic resonance imaging based drug targeting [171] etc.

1.3.4 Probing of Internal Structures in Magnetic Fluids

In the presence of external magnetic field, the nano-sized particles in magnetic fluids experience attractive force along the field direction and a repulsive force normal to it [172]. The randomly oriented dispersed Brownian nano-sized particles undergo head to tail aggregation, thereby forming chain-like structures aligned along the magnetic field direction. Due to the lateral coalescence of the chains, they form thick columns by undergoing secondary aggregation [61, 63, 173].

Various experimental and theoretical studies have been employed to get insight into the magnetic field induced aggregation dynamics and structural transitions in magnetic fluids. The experimental techniques used are small angle neutron scattering (SANS) [174-178], time-resolved stroboscopic small angle aeutron scattering (SANS) [179], X-ray scattering [180, 181], small angle X-ray scattering (SAXS) [177, 182], visible wavelength light transmission [183, 184], infrared light transmission [185], THz time-domain spectroscopy [186], raman spectroscopy [187, 188], scattering dichroism [189], cryo transmission electron microscopy (Cryo-TEM) [190-192], confocal microscopy [193], optical microscopy [194, 195], ultrasound wave propagation [196-198], and holographic optical tweezer [199]. The computational techniques used are Monte carlo simulation [200-204], molecular dynamics simulation [205-207], Brownian dynamics simulation [208], stochastic dynamics simulation [209], and dipolar hard-sphere model [210].

1.3.5 Structural Transitions in Magnetic Fluids

Besides the field induced structural transitions in magnetic fluids, several interesting optical phenomena were also observed that have caught up the imagination of physicists [63, 184, 211-217]. The magnetic field induced optical anisotropy in magnetic fluids lead to many extraordinary magneto-optical properties such as static magnetic birefringence, linear dichroism, Faraday rotation, Faraday ellipticity, circular dichroism, etc. [218-222]. The refractive index in magnetic fluids increases with increase in external magnetic field [63, 223]. Yang *et. al.* [224] reported the magnetic field dependent behavior of refractive index of magnetic fluid films. With increasing sample temperature the value of the refractive index of magnetic fluid films was found to decrease in the presence of an external field. The refractive index increases with increasing film thickness or field strength, but was found to be independent of the sweep rate of the field.

Pinheiro *et al*. [225] studied the light scattering by magnetic spheres and vanishing of energy transport velocity in disordered magnetic particles. They have also studied the influence of magnetic scatterers on single and multiple scattering of light, and their implications in the coherent backscattering effect and localization parameter [226]. In the small-particle limit, single scattering exhibits not only a forward-backward spatial asymmetry, but also an unusual resonance effect. Recently, Hem Bhatt *et al.* [227] have studied the magnetic field dependent resonant behavior, forward-backward anisotropy factor, light diffusion constant, and energy transport velocity in bidispersed magnetic colloids consisting of micrometer size magnetic spheres dispersed in a nonmagnetic liquid carrier. Lacoste *et al.* [228] experimentally and theoretically studied the Photonic Hall Effect (PHE) in ferrofluids which originates due to orientation of the magnetic moments of the suspended nanoparticles. The PHE was found to depend on the concentration of the scatterers, external magnetic field, and the polarization of the incident light.

Laskar *et al.* [229] reported the tunable enhanced light transmission with a Fano-like profile in a magnetically polarizable nanoemulsion. Optical negative refraction was reported in ferrofluids containing isotropic Fe_3O_4 nanoparticles, each having an isotropic silver (Ag) shell, in the presence of an external DC magnetic field [215]. The all-angle broadband optical negative refraction, controllable by external magnetic field, was found to arise from the field induced chains or columns.

The dielectric and magneto-optical effects of ferrofluids were investigated using THz time-domain spectroscopy [186]. The refractive index and absorption coefficient of ferrofluid for THz waves were found to increase with the increase of nanoparticle concentration in ferrofluid, which makes the ferrofluid a promising magneto-optical material in the THz regime with potential applications in THz functional devices for THz sensing, modulation,

phase retardation, and polarization control. Shalaby *et al*. [230] demonstrated a high magneto-optical figure of merit (FOM) Faraday rotation in ferrofluids in THz optical frequency region. They observed that ferrofluids shows high transparency in the THz regime that in turn leads to a high FOM. Pinzón *et al.* [231] experimentally demonstrated a tunable polarized induced light transmission in ferrofluids loaded with carbon nanotubes in the presence of a uniform magnetic field.

The non-linear optical properties of coated magnetite nanoparticles were investigated due to their potential applications in nonlinear optical devices [232, 233]. Vivacqua *et al.* [234] experimentally investigated the occurrence of the optical Kerr effect and two-photon absorption when an oil-based magnetic Fe_3O_4 nanoparticles suspension subjected to a high intensity femto second laser pulse.

1.4 Motivation

The magnetic field induced optical properties of magnetic fluids make them ideal materials to study the scattering phenomena in different optical regimes as the scatterer size can be tuned from Rayleigh regime (scatterer size << λ) at low field to Mie regime (scatterer size ~ λ) in the intermediate field range and finally to the geometrical regime (scatterer size >> λ) at high magnetic field, where λ is the incident light wavelength [172]. Also, when the size of the magnetic particles is small (in nano range), the challenge in studying field induced structural transitions and aggregation dynamics increases manifold because of the limited available experimental tools. This is one of the reasons to utilize light scattering and speckle correlation in studying the field induced structural transitions and their kinetics in magnetic fluids. For very small particles with their size much less than the incident light wavelength, the turbidity of colloidal suspension increases substantially due to aggregation. Though this particular

aspect has been exploited to measure the colloidal aggregation rate and the stability in non magnetic systems, it is not used for the magnetic ones to the best of our knowledge.

The field induced aggregation process in magnetic fluids is mainly due to dipolar interaction between the dispersed nano-sized magnetic particles, which depends on the applied magnetic field strength and particle size [235]. Though many studies were carried out to probe the effects of dipolar interaction on field induced aggregation and de-aggregation and associated magneto-optical properties in these systems [111, 119, 205, 236-244], a complete understanding of field induced aggregation dynamics in magnetic fluids is lacking. A proper understanding of the field induced optical properties of magnetic fluids can results in the better utilization of these materials for various technological applications, especially in photonic and opto-fluidic devices. This was the motivation to undertake the present work.

1.5 Objectives

The main objective of this work is to obtain better insight into the complex field induced aggregation, disorder-order transitions, and the intriguing magneto-optical phenomena in magnetic fluids using the forward light scattering, backscattering, and absorption and the speckle pattern studies. Further, the role of suspended nanoparticle size and temperature on aggregation process are also investigated systematically.

1.6 Overview of the Thesis

The thesis contains nine chapters. The summary of each chapter is given below:

Chapter 1 gives a brief description of soft matter and its importance for fundamental research and industrial applications. A brief introduction on stimulus responsive materials and magnetic fluids is also provided. The variations of physical properties of magnetic fluids are presented. A detailed literature survey on the study of field induced structural transitions in magnetic

fluids by various techniques is provided in this chapter. The effect of field induced structural transition on light propagation and the optical properties are also discussed in detail.

Chapter 2 describes the details of the samples, characterization techniques, experimental setup and the procedure adopted for (i) capturing the scattered speckle patterns, (ii) measuring the transmitted, (iii) backscattered light intensity, (iv) absorption and (v) speckle intensities as a function of magnetic field and time. **Chapter 3** presents the study of magnetic field dependent behavior of transmitted light intensity and scattered pattern in ferrofluid and nanoemulsion.

Chapter 4 presents the study of transmitted light speckle pattern through ferrofluid and nanoemulsion in presence of an external magnetic field. **Chapter 5** presents the study of the effect of applied magnetic field on the backscattering light intensity from a ferrofluid consisting of poly-acrylic acid coated Fe_3O_4 nanoparticles dispersed in water. **Chapter 6** presents the study of magnetic field dependent near infrared photon absorption in nanoemulsion. **Chapter 7** presents the study of the effect of hydrodynamic particle size on the magnetic field induced light transmission and transmitted speckle pattern in water based ferrofluids containing functionalized Fe_3O_4 nanoparticles. Three water-based ferrofluids, containing Fe_3O_4 nanoparticles functionalized with poly-acrylic acid (PAA), tetra-methyl ammonium hydroxide (TMAOH) and phosphate are used in this study. **Chapter 8** presents the study of the influence of temperature on the magnetic field induced light transmission in a kerosene based ferrofluid where the direction of propagation of light is parallel to the direction of the external magnetic field. **Chapter 9** provides the summary of the results obtained, conclusions and future scopes.

2.1 Introduction

This chapter describes the details of ferrofluid and ferrofluid emulsion used, experimental setup and the procedure adopted for studying the field induced structural transitions, aggregation dynamics and speckle patterns. The bare iron oxide nanoparticles of average diameter ~10 nm dispersed in water or kerosene is used for ferrofluids The iron oxide nanoparticles are synthesized by co-precipitation method [245, 246]. For ferrofluid emulsion, the average oil droplet size was ~ 220nm. Ferrofluid emulsions are prepared using an emulsification protocol [64, 247]. The nanoparticle samples are characterized by X-ray diffraction, optical microscopy, transmission electron microscopy, thermo gravimetric analysis and dynamic light scattering techniques to get detailed information about the size, shape, coating thickness, hydrodynamic size etc. [246, 248, 249]. The details of the samples used are discussed in section 2.2. Measurement of forward and backscattered light intensity and recording of the scattered pattern as a function of external magnetic field (B) and time (t) are carried out using the experimental set up are discussed in section 2.3. Besides, the measurement of transmittance and absorption spectra as a function of incident light wavelength, temperature and external magnetic field are also carried out to understand the field induced structural transitions. The experimental setups designed to carry out these studies are discussed in section 2.3.

2.2 Magnetic Fluid Samples

2.2.1 Ferrofluid (or Magnetic Nanofluid)

Magnetic nanofluid, commonly known as ferrofluid used in the present work is a stable colloidal dispersion of magnetite (Fe_3O_4) nanoparticles [61, 248]. Two types of ferrofluids are

used water based and kerosene based ferrofluids. The coating materials used for water based ferrofluids are poly-acrylic acid (PAA), tetra-methyl ammonium hydroxide (TMAOH) and phosphate. The hydrodynamic size of the nanoparticles ranges from ~15 – 48 nm. For kerosene based ferrofluid, average crystallite diameter of nanoparticle (d) was ~6.5 nm, and was coated with oleic acid. The organic layer thickness of oleic acid around the particles is about 1.5 nm. The hydrodynamic size and polydispersity index is measured by dynamic light scattering using Zetasizer-Nano (Malvern Instrument). The PDI (polydispersity index) of the ferrofluids sample used in the present study is 0.092. A dispersion with a PDI value lower than 0.1 is considered as fairly monodisperse. The dispersions used in the experiments had excellent long term stability even after prolonged application of very strong magnetic fields. Figure 2.1 shows the schematic of a ferrofluid sample.

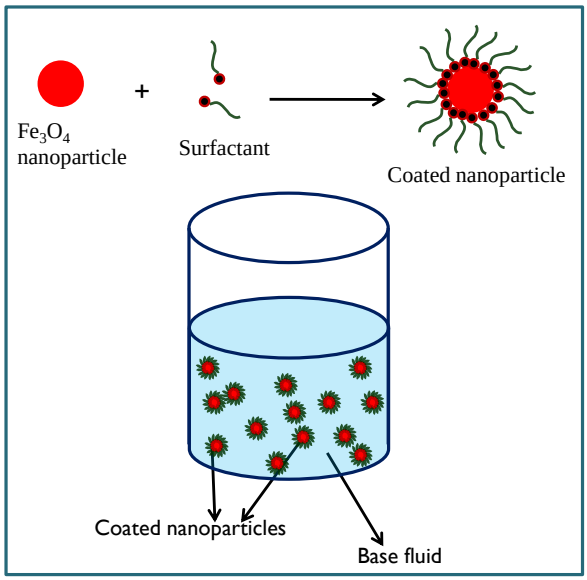

Fig. 2.1 Schematic of ferrofluid sample.

2.2.2 Ferrofluid Emulsion (or Nanoemulsion)

Ferrofluid emulsion or nanoemulsion (here after referred as nanoemulsion), used in the experiment, is a dispersion of octane oil droplets (average diameter d_1 ~ 220 nm, polydispersity < 5 %) in water. Each of these oil droplets contains oleic acid coated magnetic

(Fe_3O_4) nanoparticles. The oil droplets are electrostatically stabilized with an anionic surfactant of sodium dodecyl sulphate (SDS) which has a chemical formula of (CH_3 $(CH_2)_{10}CH_2SO_4^-$ Na^+). Figure 2.2 shows the schematic of the ferrofluid emulsion sample [64, 250].

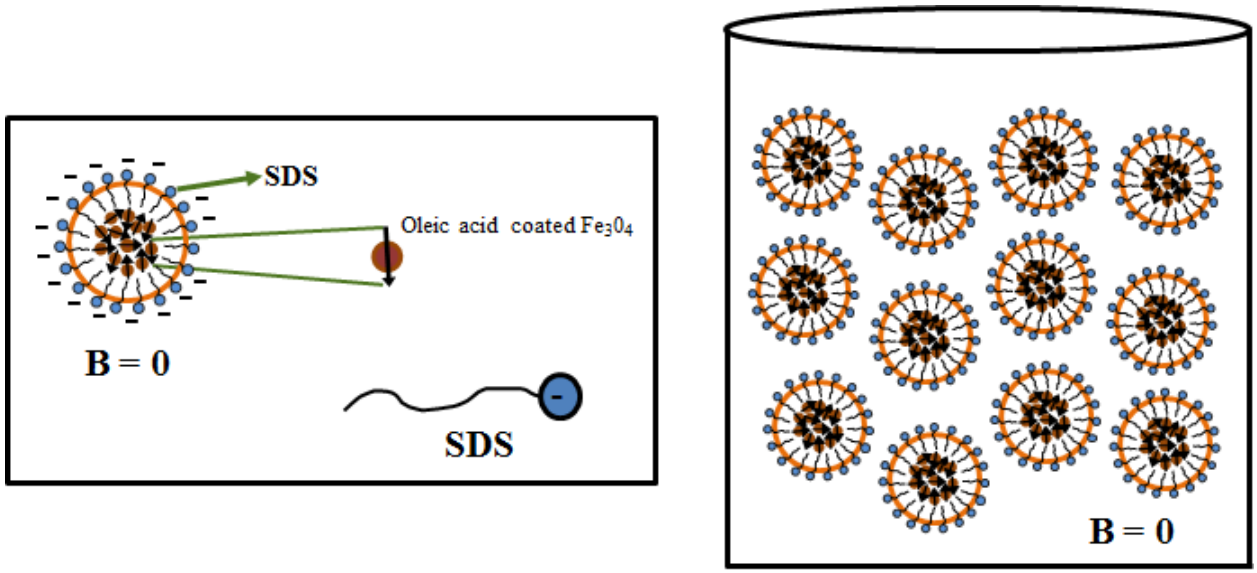

Fig. 2.2 Schematic of ferrofluid emulsion (or nanoemulsion) sample. *B* – External Magnetic field, SDS – Sodium dodecyl sulphate.

2.3 Measurement of Scattered Light Intensity and the Scattered Pattern

2.3.1 Experimental Setup

Figures 2.3 and 2.4 show the schematics of the experimental setup used to measure the transmitted and backscattered light intensity as a function of external magnetic field and time. Figure 2.5 shows the photograph of the experimental set-up.

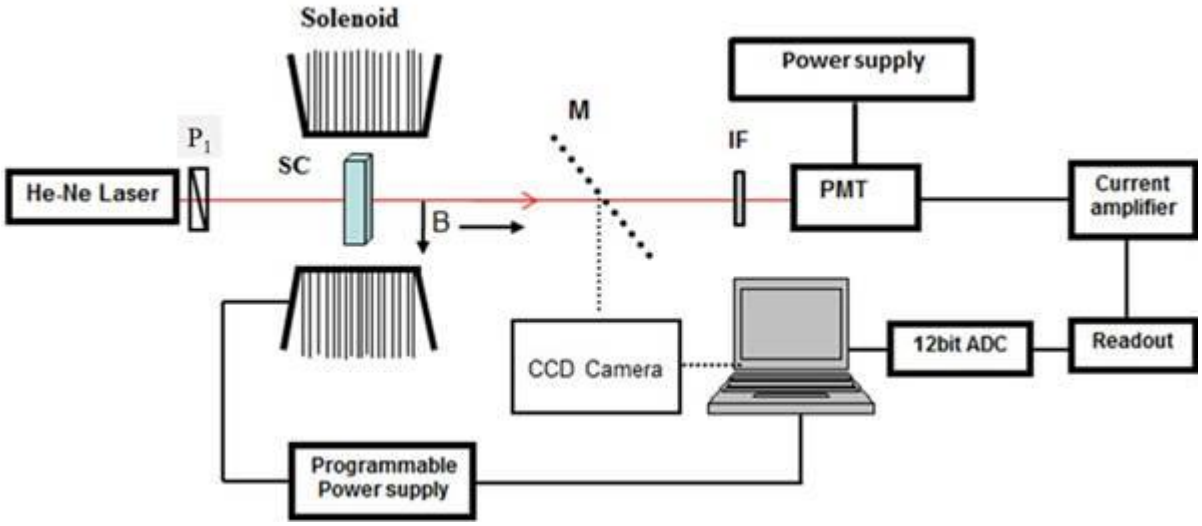

Fig. 2.3 The schematic of the experimental setup for measuring the transmitted light intensity and scattered pattern; P_1 – Polarizer, SC – Sample cuvette, IF – Interference filter, M – Mirror, PMT – Photomultiplier tube, ADC – Analog to digital converter.

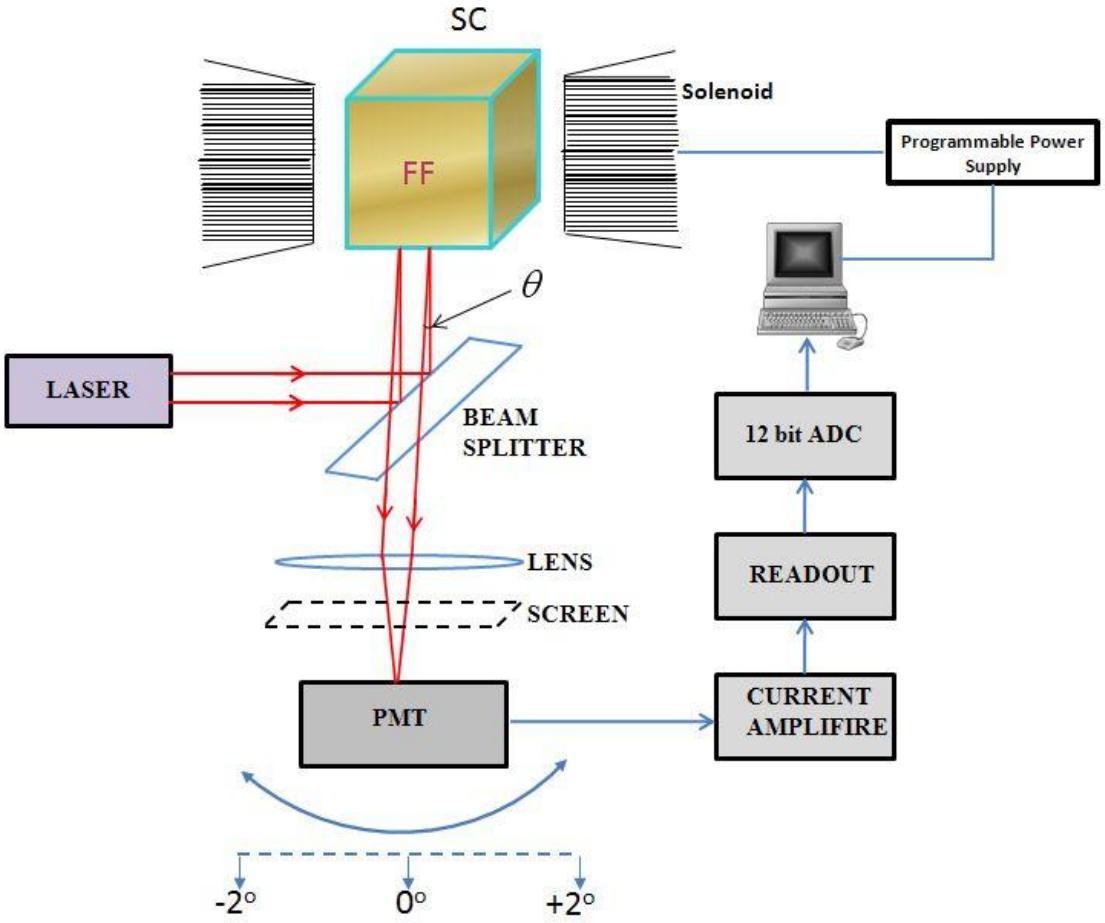

Fig. 2.4 Schematics of experimental setup to measure backscattered light intensity and the scattered pattern in the presence of an external magnetic field.

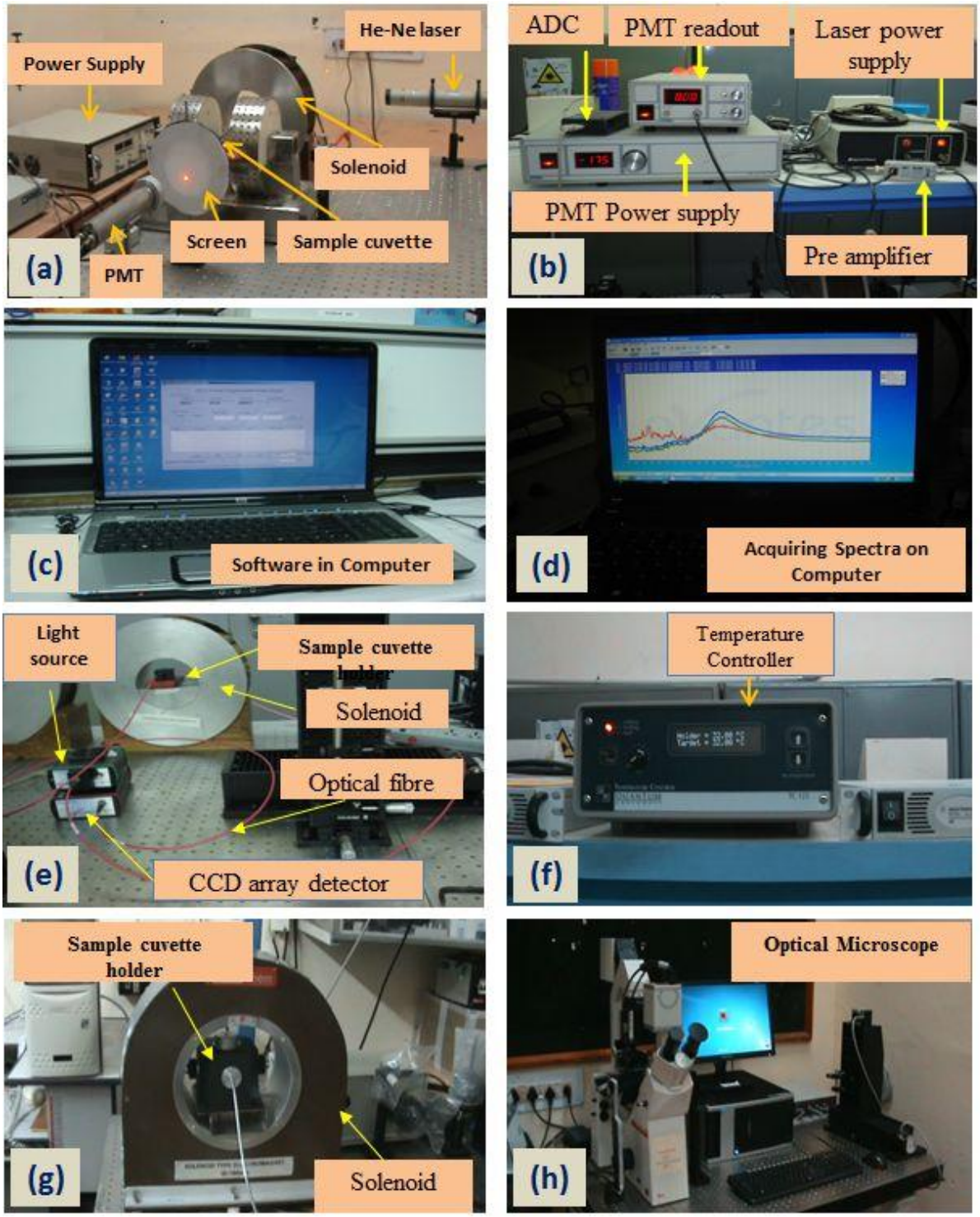

Fig. 2.5 Photographs of the experimental set up (a) for measuring the transmitted intensity and scattered pattern as a function of external magnetic field and time, (b) of the data acquisition system, (c) of the software for programmable control of the power supply and acquiring light

intensity data, (d) of the software for data acquisition of light transmission and absorption, (e) for measuring the transmittance and absorption spectra as a function of external magnetic field, (f) for measuring sample temperature, (g) of the sample cuvette holder for temperature dependent study in presence of external magnetic field, (h) for capturing field induced images by phase contrast optical microscope.

Here P_1, SC, PMT, ADC and IF are the polarizer, sample cuvette, photomultiplier tube, analog to digital converter and interference filter, respectively. The sample is taken in a cuvette of path length L=1 mm and then placed inside a solenoid. The magnetic field inside the solenoid is varied by changing the current passing through its coil using a programmable DC power supply, which is interfaced with a computer. The software has a provision to allow magnetic field ramping up or down at different rates with appropriate steps or delays. The direction of the external field is made perpendicular or along the direction of propagation of the incident light. An amplitude and frequency stabilized He-Ne laser (Spectra-physics, USA, model- 117 A) of wavelength, $\lambda \sim 632.8$ nm with an output power 4.5 mW is used as a light source. The variation in the magnetic field within the sample was ± 2%. However, the variation within the laser spot diameter was less than 1%.

2.3.2 Transmitted and backscattered Intensity Data Acquisition System

For the transmitted and backscattered light intensity measurement a 'Oriel-Newport, model-77265' photomultiplier tube (PMT) is used. A PMT is a vacuum tube consisting of an input window, a photocathode, focusing electrodes, an electron multiplier and an anode unusually sealed in an evacuated glass tube [251, 252].

A power supply (model: 70705, Oriel instruments) is used to provide highly regulated voltage to the PMT. This power supply has a voltage range of -200 to 2000 Volts. The output of the PMT is fed to a readout (model: 70701, Oriel instruments) through a current pre-amplifier

(model: 70710, Oriel instruments) with variable gain. The 70701 readout has a 3 ½ digit LED display for the calibrated output signal. The input voltage can be varied from ± 0.1 to 10 times, and has an offset range from 0 to 100 %. The 70710 Current Pre-amplifier is designed for use with current source as photomultiplier tube and is a low noise current-to-voltage amplifier. It converts the low current output from PMT to a voltage signal for the 70701 readout. It has six switchable amplification options: 10^4, 10^5, 10^6, 10^7, 10^8, and 10^9 volts per ampere. The analog output from the 70701 readout is connected to a 12 bit analog to digital converter (ADC, 200 kS/s, 12 bit, 16-ch Multifunction USB Module, model: 4716, Advantech) that is interfaced with a computer through a USB port. The transmitted intensity data is acquired and saved in a personal computer.

2.3.3 Recording of Scattered Pattern

For recording of the scattered light pattern, the scattered light from the sample is projected on a screen as shown in Figs. 2.3 and 2.4, and the pattern is recorded using a CCD camera (digital video camera recorder, DCR SR 45 E, Sony Corporation, Japan).

2.4 Measurement of Magnetic Field and Temperature dependent Transmittance and Absorption Spectra

Figure 2.6 shows the schematics of the experimental setup used to measure the transmittance and absorption of light as a function of external magnetic field and temperature.

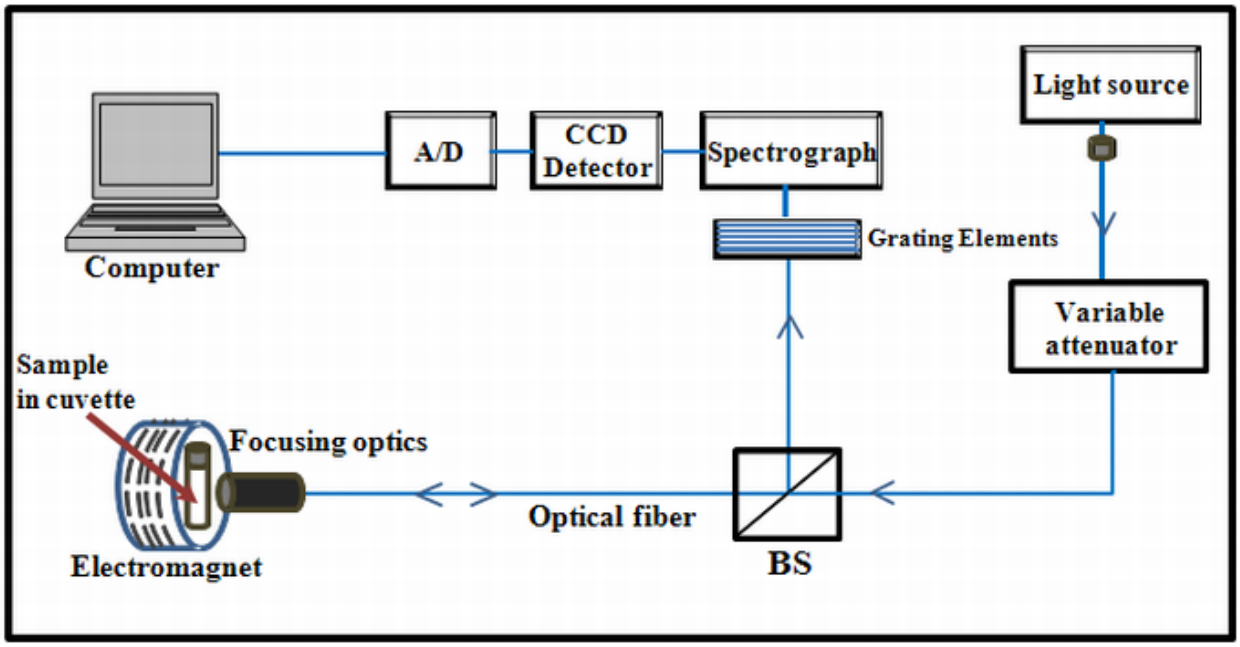

Fig. 2.6 Schematic of experimental set up to study the external magnetic field induced light transmission and absorption.

The sample is taken in a cuvette which is kept inside the cuvette holder. The cuvette holder is placed inside a solenoid in such a way that the direction of the light passing through the sample is along the direction of the external magnetic field. The magnetic field is varied by changing the current passing through the coil using a DC programmable power supply. A standard fiber optic spectrometer (AvaSpec-2048, Avantes, USA), with a tungsten halogen light source, is used to record the absorption spectra. The spectrometer has a usable wavelength (λ) range of 200-1100 nm. The detector is a CCD linear array with 2048 pixels, with a signal to noise ratio of 200:1. The resolution of the spectrometer is 0.04 nm. The integration time and ramp rate are optimized to record the exact spectrum for each external magnetic field. For temperature dependent study the cuvette is kept inside a peltier based temperature controlled cuvette holder. The sample temperature is varied using a programmable temperature controller.

2.5 Dynamic Light Scattering

Dynamic light scattering (DLS) is a well established technique for measuring the size of particles typically in the sub micron region. DLS measures Brownian motion and relates this to the size of the particles. Brownian motion is the random movement of particles dispersed in a liquid or gaseous medium. DLS is a noninvasive technique that measures a large population of particles in a very short time period. Because of the sensitivity to trace amounts of aggregates and the ability to resolve multiple particle sizes, DLS is ideally suited for dispersion and macromolecular applications at low sample concentration and volume[253].

Accurate and stable values of specimen temperature and medium viscosity are essential for DLS measurements. DLS technique measures the time dependent fluctuations in the intensity of scattered light that occurs because of the Brownian motion of particles. Analysis of this intensity fluctuation allows the determination of the translational diffusion coefficient of particles[253, 254].

The particles in the dispersion are in constant, random Brownian motion and hence, the intensity of scattered light fluctuates as a function of time. The correlator used in a DLS instrument provides the correlation function $G(\tau)$ of the scattered intensity:

$$G(\tau) = \langle I(t).I(t+\tau) \rangle \tag{2.1}$$

where, τ is the correlator time delay and *I(t)* is the light intensity.

For a large number of monodisperse particles in Brownian motion, the correlation function, $G(\tau)$ is an exponential decaying function of the correlator time delay τ:

$$G(\tau) = A_1 [1 + \beta \exp(-2\Gamma\tau)] \tag{2.2}$$

where, A_1 is the baseline of the correlation function, β is the intercept of the correlation function. The decay rate is given by the following expression.

$$\Gamma = D_T k^2 \tag{2.3}$$

where, D_T is the translational diffusion coefficient and *k* is the wave-vector and is given by

$$k = (4\pi n/\lambda)\sin(\theta/2) \tag{2.4}$$

where, *n* is the refractive index of dispersant, θ is the scattering angle.

For polydisperse samples, the equation (2.2) can be written as:

$$G(\tau) = A_1[1 + \beta g_1(\tau)^2] \tag{2.5}$$

where, $g_1(\tau)$ is the sum of all the exponential decays contained in the correlation function and is given by

$$g_1(\tau) = \exp(-2\Gamma\tau) = \exp(-2D_T k^2 \tau) \tag{2.6}$$

The hydrodynamic diameter is defined as the diameter of a hard sphere that diffuses at the same rate as the particle under examination. The size of a particle (hydrodynamic diameter) is calculated from the translational diffusion coefficient by using the Stokes-Einstein equation:

$$d_h = \frac{k_B T}{3\pi\eta D_T} \tag{2.7}$$

where, d_h is the hydrodynamic diameter, D_T is the translational diffusion coefficient, k_B is the Boltzmann's constant, *T* is the absolute temperature, η is the viscosity of the medium.

Size is obtained from the correlation function by using different algorithms. There are two commonly used approaches: (1) By fitting a single exponential to the correlation function to obtain the mean size (z-average diameter) and an estimate of the width of the distribution (polydispersity index) using Cumulants analysis or (2) By fitting a multiple exponential to the correlation function to obtain the distribution of particle sizes using Non-negative least squares. The size distribution obtained is a plot of the relative intensity of light scattered by particles in various size classes and is therefore known as an intensity size distribution.

A typical DLS system comprises of six main components. A laser is used as a light source to illuminate the sample within a cell. Most of the laser beam passes straight through the sample, but some are scattered by the particles in the sample. A detector is used to measure the intensity of the scattered light. As particles scatter light in all directions, it is possible to place the detector in any position and it will still detect the scattering. The intensity of the scattered light must be within a specific range for the detector to measure successfully. If too much light is detected, the detector will become saturated. To overcome this, an attenuator is used to reduce the intensity of the laser and hence the intensity of scattering. For samples that do not scatter much light, such as very small particles or samples of low concentration, the amount of scattered light must be increased. For samples that scatter more light, such as large particles or sample of higher concentration, the amount of scattered light must be decreased. The scattering light signal from the detector is then passed to a digital signal processing board called correlator. The correlator derives the rate at which intensity is varying. This correlator information is then passed to a computer, where the analysis of the data using suitable algorithms provides information of the particle size and distribution.

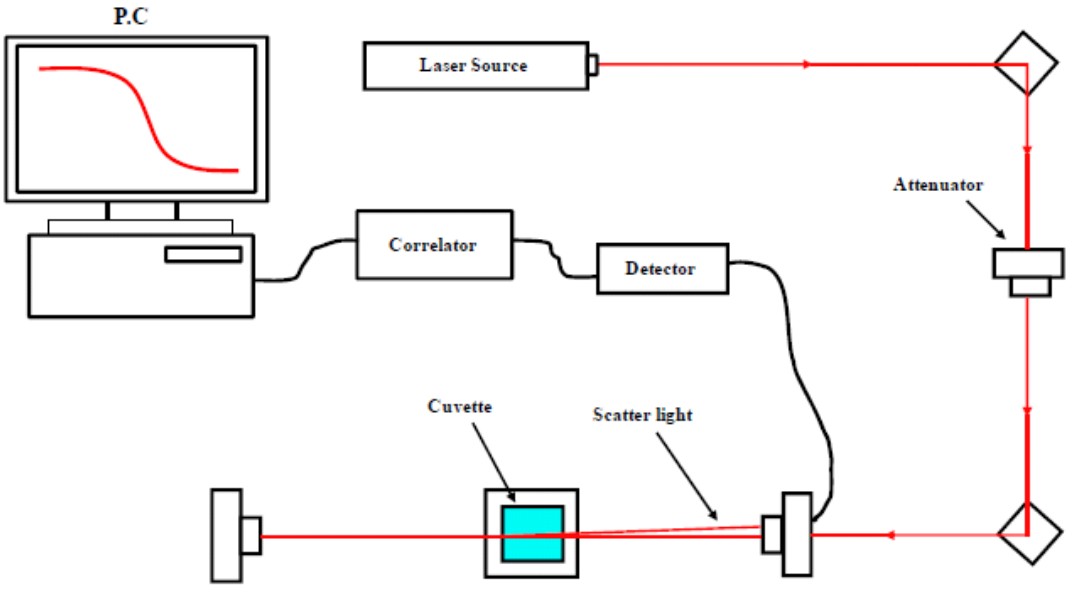

Fig. 2.7 Schematic diagram of dynamic light scattering (DLS) set up.

The major advantages of non-invasive backscattering geometry used in DLS are as follows: (i) as the backscattered intensity is measured, the incident beam does not have to travel through the entire sample. Therefore, higher concentrations of sample can be used; (ii) not prone to multiple scattering; (iii) contaminants such as dust particles within the dispersant are typically large compared to sample size and mainly scatter the light in forward direction. Therefore by measuring the backscatter, the effect of contaminants is greatly reduced.

2.6 Phase Contrast Optical Microscope

Phase contrast microscopy, has been utilized to produce high contrast images of transparent specimens such as living cells, microorganisms, colloidal particles, lithographic patterns and sub-cellular particles (such as nuclei and other organelles). Phase contrast microscopy is an optical microscopy technique that converts phase shifts in light passing through a transparent specimen to brightness changes in the image [255]. Phase shifts themselves are invisible, but become visible when shown as brightness variations. When light waves travel through a medium other than vacuum, interaction with the medium causes the wave amplitude and phase to change in a manner dependent on properties of the medium.

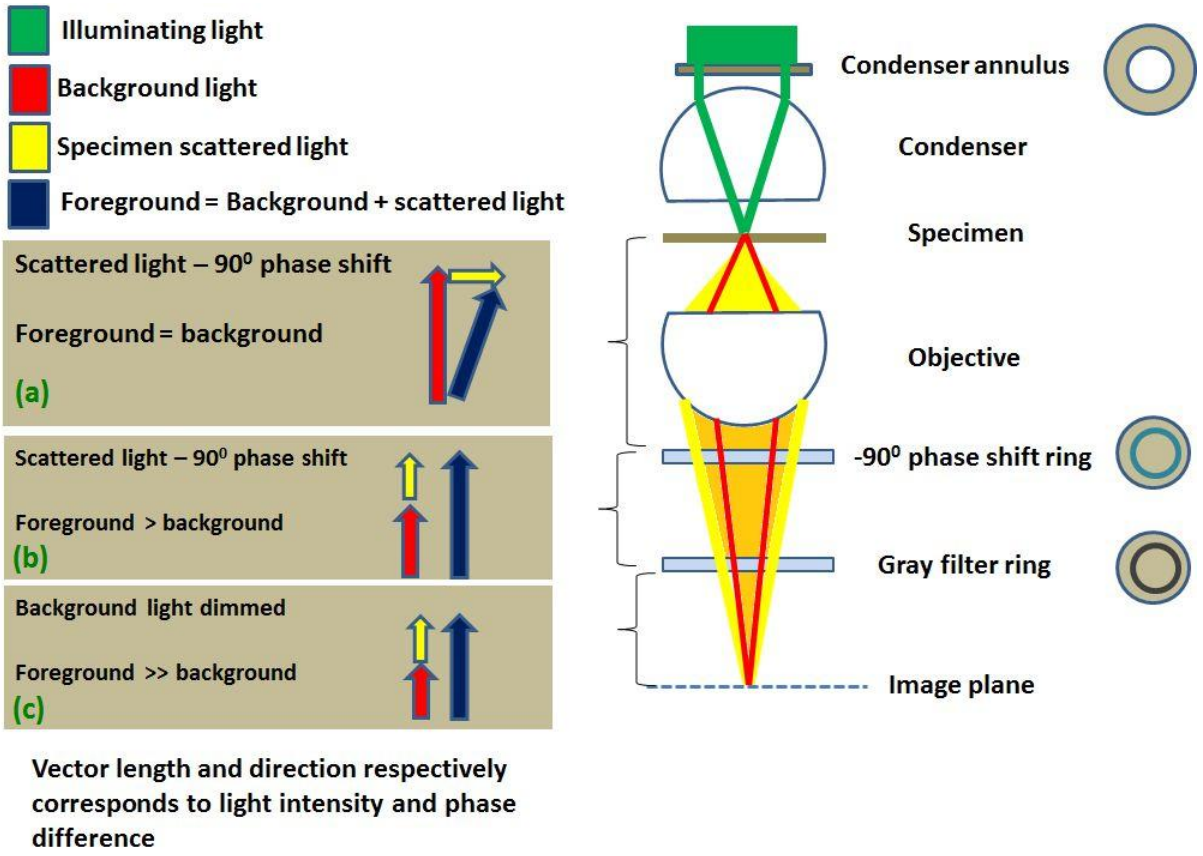

Fig. 2.8 Phase contrast optical microscopy and its working principle.

In a phase contrast microscope, partially coherent illumination produced by the tungsten-halogen lamp is directed through a collector lens and focused on a specialized annulus positioned in the sub stage condenser front focal plane. The basic principle to make phase changes visible in phase contrast microscopy is to separate the illuminating background light from the specimen scattered light, which make up the foreground details, and to manipulate these differently. The ring shaped illuminating light (green) that passes the condenser annulus is focused on the specimen by the condenser. Some of the illuminating light is scattered by the specimen (yellow). The remaining light is unaffected by the specimen and forms the background light (red). When observing unstained specimen, the scattered light is weak and typically phase shifted by -90° relative to the background light.

Thus the foreground (blue vector) and the backgrounds (red vector) nearly have the same intensity, resulting in a low image contrast (a).

In a phase contrast microscope, the image contrast is improved in two steps. The background light is phase shifted -90° by passing it through a phase shift ring. This eliminates the phase difference between the background and the scattered light, leading to an increased intensity difference between foreground and background (b). To further increase contrast, the background is dimmed by a gray filter ring (c). Some of the scattered light will be phase shifted and dimmed by the rings. However, the background light is affected to a much greater extent, which creates the phase contrast effect. The above describes negative phase contrast. In its positive form, the background light is instead phase shifted by +90°. The background light will thus be 180° out of phase relative to the scattered light. This results in that the scattered light will be subtracted from the background light in (b) to form an image where the foreground is darker than the background.

In the present study, the microstructure of magnetic fluids (ferrofluid & nanoemulsion) in presence of external magnetic field is studied using a Leica Inverted microscope equipped with a digital camera (JVC) and frame grabber card. The obtained images are processed using 'Leica Win' software.

Chapter III Probing the Magnetic Field Induced Nano-structures in Magnetic Fluids by Light Transmission

3.1 Introduction

Scattering and propagation of light through mesoscopic and low dimensional objects is a fundamental problem which dates back to Lord Rayleigh [256, 257]. It has been a subject of intense activity during the last few decades due to scientific curiosity and more importantly due to their practical applications [184, 185, 199, 258-260]. Aggregation of solid particles (sizes varying from nm to μm) in colloids alter the propagation pathways of light waves and generates many new phenomena [215, 228, 261, 262]. Opto-fluidics refers to manipulation and controlling of light in fluids on the micro to nanometer scale where fluids give adaptability, mobility and accessibility to nano-scale photonic devices [263-265].

Magnetic fluids are unique material as they offer the possibility of tuning the particle interaction by external magnetic field that makes them ideal candidates for fundamental research and potential technological applications [63, 266-269]. The field induced aggregation and de-aggregation process of magnetic nanoparticles in magnetic fluids can alter the propagation of light waves that gives rise to exciting optical phenomena which are of fundamental interests and have enormous applications [150, 215, 229]. These magnetic fluids are excellent model systems to study light scattering phenomena because the scatterers' sizes can be tuned from Rayleigh regime to Mie regime and finally to the geometrical regime by simply changing the external magnetic field [63, 270].

The aim of this chapter is to investigate the effect of external magnetic field on the transmitted light intensity and scattered pattern in ferrofluid and nanoemulsion during structural transition of nano-sized magnetic particles in dispersion. First, the behavior of light transmission in ferrofluid as a function of external magnetic field and volume fraction is analyzed. Subsequently, the variation of transmitted light intensity as a function of particle volume

fraction and external magnetic field during structural transitions of nanoemulsion droplets in water is explained.

3.2 Experimental Details

The ferrofluid and nanoemulsion samples used in this study are disordered magnetic media as explained in Chapter II (section 2.2). The transmitted light intensity is measured as a function of *B* using the experimental set up shown in Figure 2.3. In the case of nanoemulsion, the direction of incident light is parallel to the direction of *B*, whereas it is perpendicular to the direction of *B* in the case of ferrofluid. The detailed procedure for acquiring the transmitted light intensity through the samples and the scattered light as a function of *B* are explained in Chapter II (section 2.3).

3.3 Results and Discussions

3.3.1 Magnetic Field Induced Light Transmission in Ferrofluid

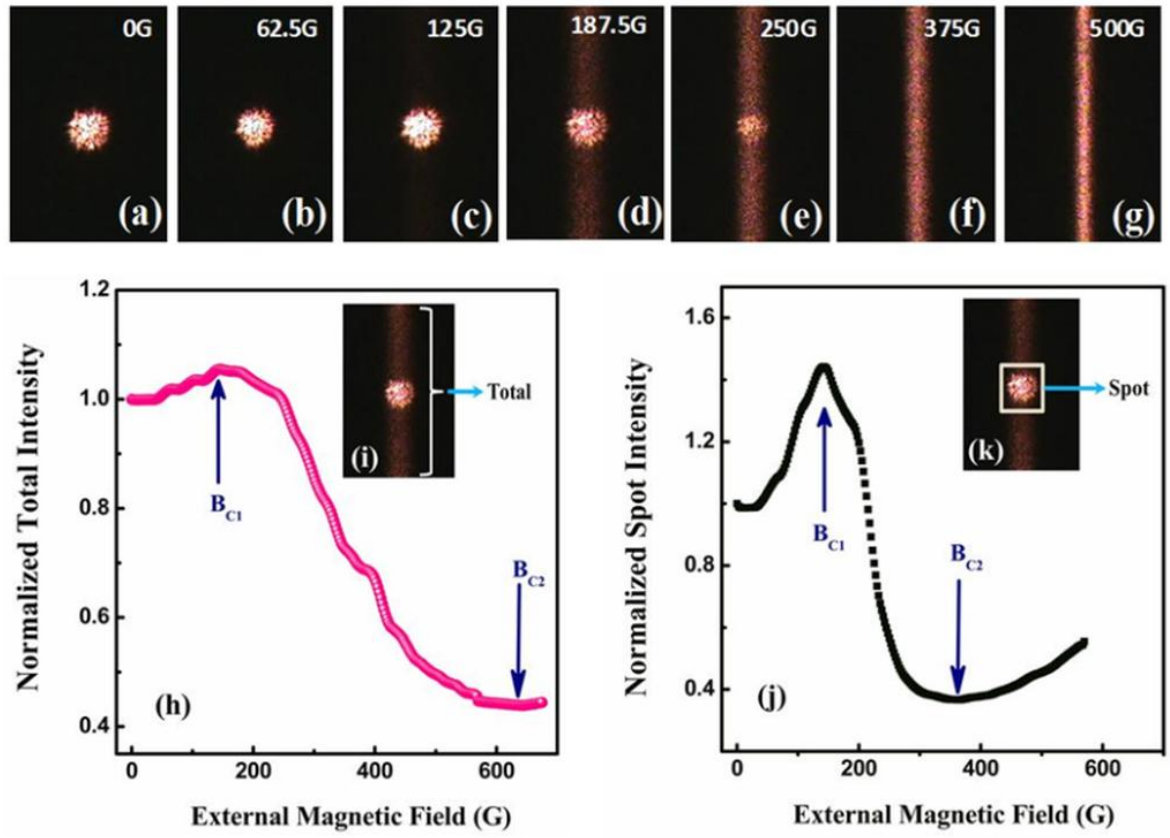

Fig.3.1. (a – g) Images of the transmitted light from ferrofluid (poly-acrylic acid coated Fe_3O_4 nanoparticles in water) at different external magnetic field (B = 0, 62.5, 125, 187.5, 250, 375, 500 G). (h) Total normalized transmitted light intensity as a function of external magnetic field at field ramp rate ~ 2.5 G/s and sample volume fraction (ϕ) ~ 0.00916. Inset image (i) shows the total portion of the transmitted light captured by PMT. (j) Normalized transmitted light spot intensity as a function of external magnetic field at field ramp rate ~ 2.5 G/s and ϕ ~ 0.00916. Inset image (k) the transmitted light spot portion captured by PMT.

Figure 3.1(a - g) show the images of the transmitted laser light from ferrofluid (poly-acrylic acid coated Fe_3O_4 nanoparticles in water) at different B (= 0, 62.5, 125, 187.5, 250, 375, 500 G). The particle volume fraction of the sample is $\phi \sim 0.00916$. Here, B is increased at a ramp rate of 2.5 G/s and the direction of B is kept perpendicular to the direction of the incident light. The transmitted circular light spot was transformed into a straight line at 187.5 G. The spot intensity above 250 G was fully redistributed within the straight line lobe. The observed transformation of the transmitted light spot into straight line [Fig.3.1 (d) – (g)] is attributed to the scattering of light from the field induced cylindrical structures whose axes are perpendicular to the incident light. Figures 3.1(h) and 3.1(j) shows the normalized transmitted total (I_{total}) and the spot intensities (I_{spot}), respectively from ferrofluid as a function of B. The inset images (i) and (k) of Figures 3.1(h) and 3.1(j) show the transmitted total and spot intensity, respectively. Both the I_{total} and I_{spot} intensities start decreasing after a certain external field [Figs. 3.1(h) and 3.1(j)], called the first critical magnetic field (B_{C1}), and become minimum at a second critical magnetic field (B_{C2}). The appearance of the B_{C1} and B_{C2} depends on the particle volume fraction (ϕ) [271]. Experimental measurement on four different ϕ shows that both B_{C1} and B_{C2} follow power law decay with ϕ ($B_C \sim \phi^{-y}$) where the exponents are 0.39 and 0.56, respectively. Scaling analysis predicts such power law dependence where the exponents can vary from 0.25 to 0.75, due to structural transitions of magnetic nanoparticles into chainlike structure in dispersion [183, 272]. The values of the B_{C1} and B_{C2} at different ϕ are shown in the table 3.1

	ϕ	B_{C1}	B_{C2}
1.	0.00298	162.5	665
2.	0.00398	145	567.5
3.	0.00603	122.5	437.5
4.	0.00913	105	360
		y = 0.39	y = 0.56

Table 3.1 B_{C1} & B_{C2} at different ϕ and the y values for B_{C1} & B_{C2}.

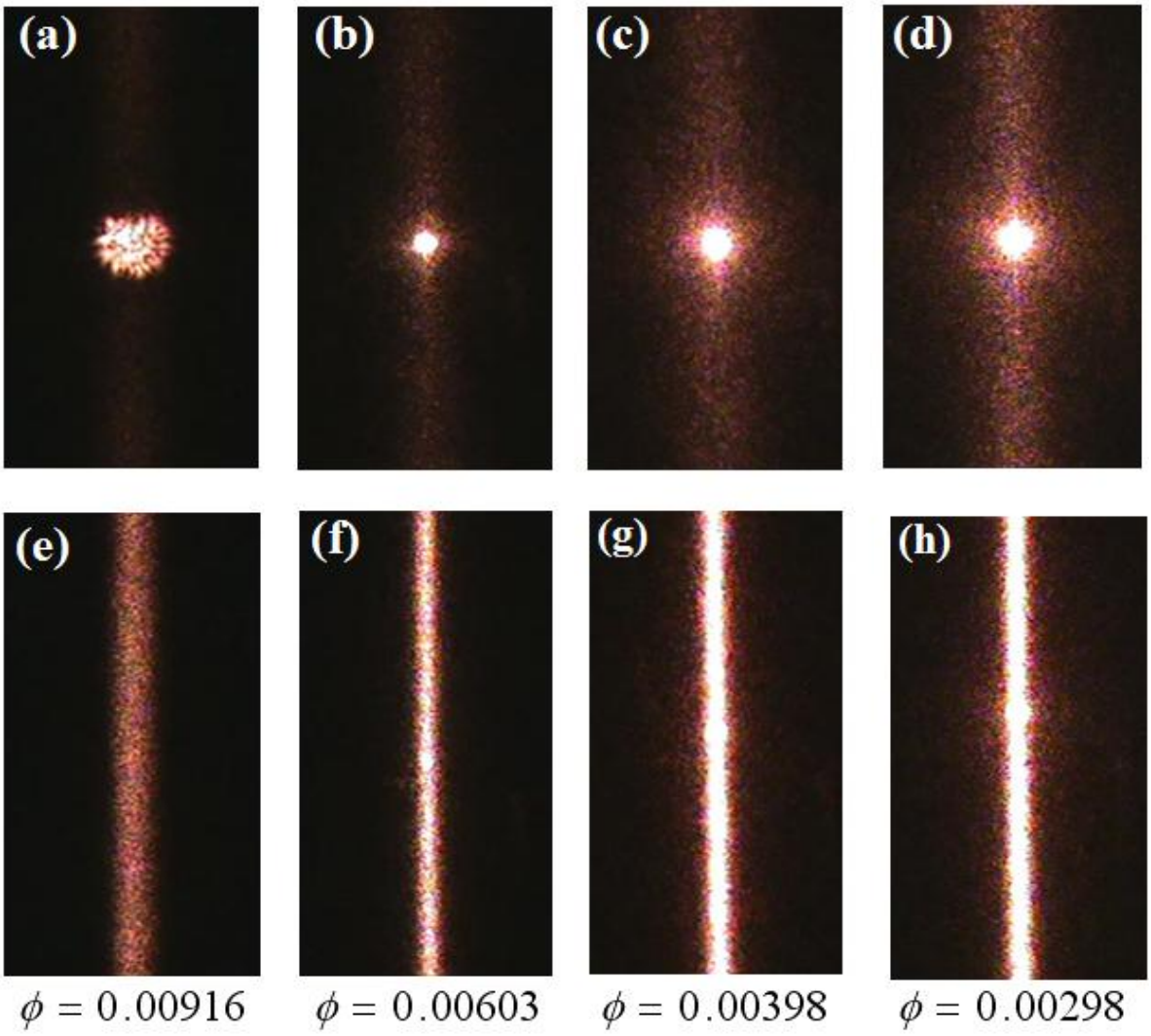

Fig. 3.2 Images of the total transmitted light pattern at critical fields (B_{C1} and B_{C2}) for different volume fraction (ϕ) of poly-acrylic acid coated Fe_3O_4 nanoparticles in dispersion. Images (a – d) for B_{C1} and (e – h) for B_{C2}. [(a),(e)- ϕ = 0.00916; (b),(f)- ϕ = 0.00603; (c),(g)- ϕ = 0.00398; (d),(h)- ϕ = 0.00298].

Figures 3.2 shows the images of the scattered pattern at the two critical magnetic fields i.e., Figures 3.2 (a – d) at B_{C1} and Figures 3.2 (e – h) at B_{C2} for ϕ = 0.00916, 0.00603, 0.00398, 0.00298, respectively. The spot and total intensities are distinct for different ϕ.

3.3.2 Possible Reasons for Enhancement and Extinction of Light in Ferrofluid

Figures 3.1(h) and 3.1(j) show that before B_{C1}, the normalized intensities I_{total} and I_{spot} increase with B and above B_{C1} they decrease with increasing B. In the absence of B, the magnetic nanoparticles are dispersed in base fluid with their moments oriented in random directions. In presence of B ($B = \mu_0 H$, where μ_0 is the magnetic permeability of free space and H is the magnitude of the field strength), the magnitude of the induced dipole moment of an individual nanoparticle is [183, 273]

$$m = \frac{\pi}{6} d^3 \chi H \tag{3.1}$$

where, d is the diameter of the nanoparticles and χ is the effective susceptibility of an individual nanoparticle. The anisotropic interaction energy U_{ij} between two identical, parallel, point dipoles with magnitude m is given by [59, 274]

$$U_{ij}(r_{ij}, \theta_{ij}) = \frac{m^2 \mu_0}{4\pi} \left(\frac{1 - 3\cos^2 \theta}{r_{ij}^3}\right) \tag{3.2}$$

where, μ_0 is the magnetic permeability of free space, r_{ij} is the magnitude of the vector describing the distance between the centers of i^{th} and j^{th} nanoparticles, and θ_{ij} is the angle between the vector $\vec{r}_{ij}$ and the external field vector. The magnetic coupling constant between two nanoparticles is defined as the ratio of the anisotropic interaction energy (U_{ij}) between them to the thermal energy of the system and is given by [235]

$$\Lambda_{coup} = \frac{\pi \mu_0 d^3 \chi^2 H^2}{72 k_B T} \tag{3.3}$$

When the coupling constant is much greater than one $(\Lambda_{coup} >> 1)$, the magnetic nanoparticles form chain-like structures along the field direction. As *B* is increased in steps, the moments of the nano-particles start to align themselves along the field direction which forms doublets, triplets and short chains like structures inside the base fluid. Such external field induced aggregations of magnetic nanoparticles in dispersion have been earlier confirmed experimentally and by using computer simulation techniques [190, 266, 275-277]. The enhancement of the normalized transmitted intensity up to B_{C1} can be explained by the evolution of the field dependent structure factor, $S(k) = I(k)/I_0(k)$, where $k(= 2\pi/\lambda)$ denotes the wave vector, $I(k)$ is the scattered intensity of the sample and $I_0(k)$ stands for the scattered intensity of the 'ideal' sample, i.e. the system without any inter-particle correlations [278]. Camp *et al*. has shown by Monte Carlo Simulation that in low k region, up to $kd \approx 3$, $S(k)$ increases rapidly and shows asymmetric peaks in the region $0.001 \le \rho^* \le 0.45$, where $\rho^* (= Nd^3/V)$ is the reduced particle number density, N is the number of particles and V is the volume [202, 279]. For $0.005 \le \rho^* \le 0.06$ and $N = 256$, $S(k)$ showed a power-law behavior in the range $1 \le kd \le \pi$ as $S(k) \sim k^{-Df}$ where D_f is the fractal dimension of scatterers. For

large values of the size parameter (*ka*), $S(k)$ is almost constant. In our case, for volume fraction, ϕ = 0.00916, nanoparticle diameter, $d \sim 15nm$, IPS [235] value is ~ 93 nm, therefore, at $B = 0$, *ka* = 0.074431, $N = 7.726136 \times 10^{20}$ and $\rho^* = 26.07571$ and *ka* value gradually increases with *B*. So, below B_{C1}, for small kd, $S(k)$ has a large value consisting of asymmetric peaks, which indicates the enhancement of the scattered intensity in ferrofluid.

After B_{C1}, Figure 3.1(h) & 3.1(j) show the decrease in normalized transmitted light intensities (I_{total} & I_{spot}) upon increasing the *B*. The extinction of light transmission in ferrofluid in presence of an external field can be due to absorption or scattering or both. Optical absorption studies shows no absorption peaks in the visible region in presence of weak external field, which ruled out the possibilities of absorption induced extinction of light transmission [183]. With increasing the *B*, the size of the scatterers increases due to dipolar attractions that can result in the enhancement of the transport mean free path (ℓ^*) [271]. It was reported that the localization parameter $(k\ell^*)$ has an oscillatory dependence on scatterers magnetic permeability (μ), where, $\ell^* = \dfrac{\ell}{1 - \langle \cos\theta \rangle}$, here ℓ is the photon mean free path and $\langle \cos\theta \rangle$ is the forward anisotropy factor which depends on the Mie scattering parameters (a_n, b_n) and for the lowest order terms in the size parameter (*ka*), the forward anisotropy factor, $\langle \cos\theta \rangle = \dfrac{\mathrm{Re}(a_1 b_1^*)}{(|a_1|^2 + |b_1|^2)}$ [226]. The Mie scattering parameters (a_n, b_n) depend on the refractive index of the scattering medium [227]. In ferrofluid, the dielectric constant (ε_{MF}) and refractive index ($m_{MF} \approx \sqrt{\varepsilon_{MF}}$) increase with *B*, which changes the Mie scattering parameters [224]. Recent studies on forward light scattering in ferrofluid show that the total extinction efficiency factor,

$Q_{ext} = \frac{2}{(ka)^2} \sum_{n=1}^{\infty} (2n+1)\,\mathrm{Re}(a_n + b_n)$ and $\langle \cos\theta \rangle$ changes with the field dependent size parameter (*ka*) [183, 227]. At some critical fields, the scatterer sizes are such that resonances occur in the $\langle \cos\theta \rangle$ and Q_{ext}. A theoretical analysis by Hem Bhatt *et al.* [227] on magnetic field dependent resonant behavior in bi-dispersed magnetic colloid composed of micrometer size magnetic spheres dispersed in a nonmagnetic liquid carrier shows that the magnetic Mie resonances and reduction in energy transport velocity can cause a delay in the field dependent resonant light transport. The field dependent resonant behavior causes the building up of standing waves inside the scatterer and results in an extra delay in light transmission in ferrofluid. These magnetic resonances should have caused the extinction of transmitted light intensity (I_{spot} or I_{total}) in ferrofluid.

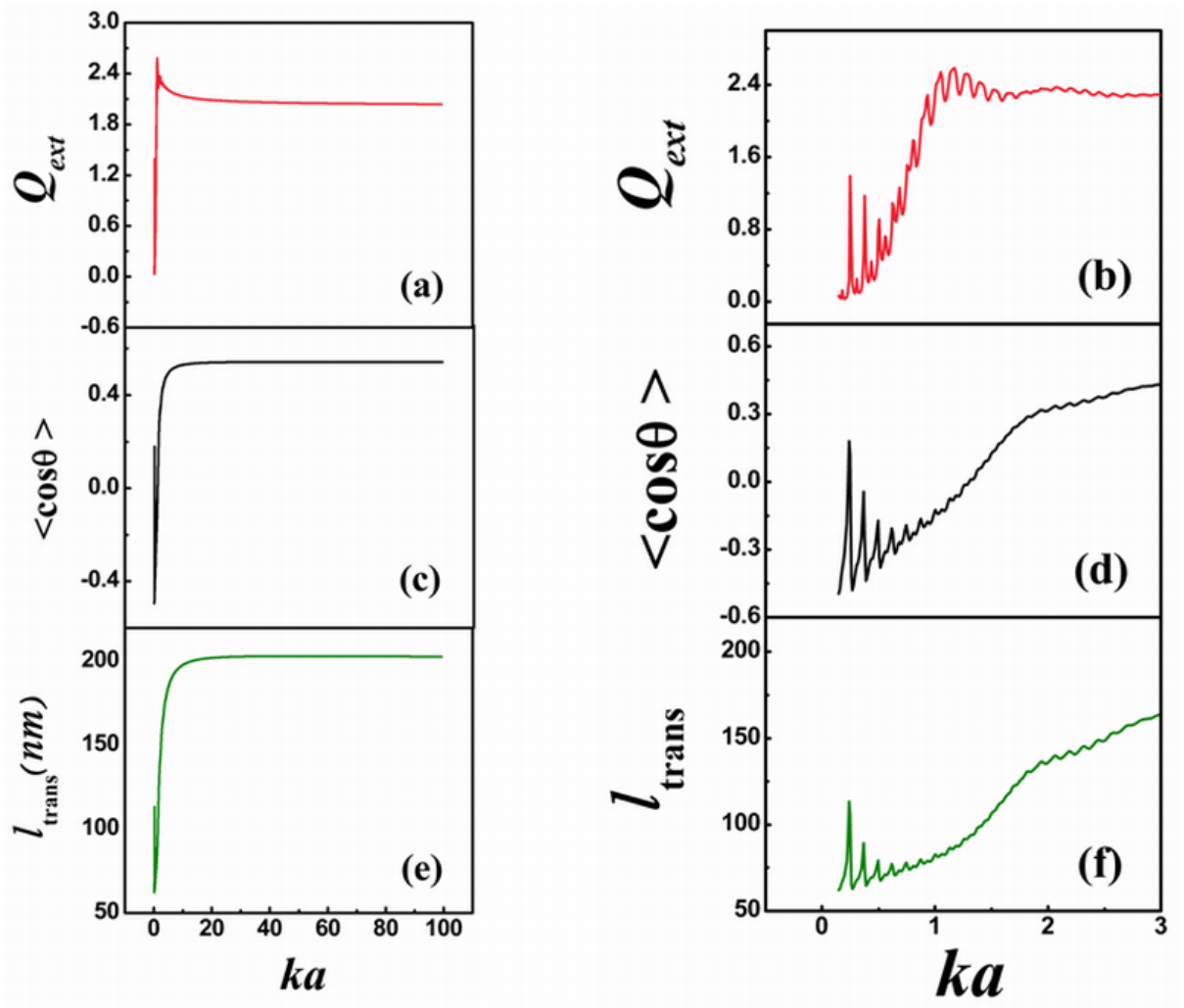

Fig. 3.3. (a) Total extinction efficiency factor (Q_{ext}) as a function of size parameter (*ka*). (c) Forward scattering anisotropy factor $(\langle \cos\theta \rangle)$ as a function of size parameter (*ka*). (e) Transport mean free path (ℓ^*) as a function of size parameter (*ka*). (b, d & f) Enlarge views of Q_{ext}, $\langle \cos\theta \rangle$, and ℓ^* within small values of size parameter (*ka*).

Figure 3.3(a) shows the variation of the total extinction efficiency (Q_{ext}) with the size parameter (*ka*) and Fig. 3.3(b) shows the zoomed view of the Q_{ext} at lower *ka* values. The Q_{ext} shows the resonant behavior with increasing the *ka*. Figures 3.3 (c & e) shows the variation of the forward anisotropy factor ($< \cos\theta >$) and the transport mean free path

($\ell^* = \ell/(1-<\cos\theta>)$) with size parameter (*ka*). Figures 3.3 (d) & (f) show the zoomed view at lower *ka*. Both $<\cos\theta>$ and ℓ^* show resonant behaviors with increasing the *ka*.

Rikken & Tiggelen [280] showed that the normalized magneto-transverse light current ($J_\perp$), perpendicular to both the light direction and external field direction, is proportional to the mean free path ($\ell_\perp$) along the direction of $J_\perp$. The magneto-transverse mean free path ($\ell_\perp$) is given by [280, 281]

$$\ell_\perp = \frac{3n_s n}{(n_s^2 - n^2)(n_s^2 + 2n^2)} \frac{V_C B \lambda^2}{\pi^2} \tag{3.4}$$

Here, V_C is the Verdet constant, *n* and n_s are the refractive indices of the matrix and the scatterer, respectively. The dielectric constant and refractive index of ferrofluid increase with the increase of *B* [224]. From Eq. (3.4) it is evident that the magneto-transverse mean free path as well as the normalized magneto-transverse light intensity increases with *B* in ferrofluid. Therefore, the light intensity (magneto-transverse light intensity) perpendicular to the directions of incident light and *B* should increase with external field and can lead to an extinction of light.

When an incident light gets scattered from a cylindrical surface, the scattered pattern forms the shape of a cone. The intersection of the cone of the scattered light on the observation screen gives the scattered pattern, the shape of which depends on the angle between the incident light and the cylinder axis [282]. When the angle with the cylinder axis is 90°, the scattered pattern takes the shape of a straight line with a spot at the centre, and when the angle with the cylinder axis is 0^0, the scattered pattern takes the shape of a ring with a spot on the circumference [282]. Therefore, the observed scattered pattern under an applied magnetic field consisting of a straight line with a laser spot at the centre (Figures 3.1c - g & 3.2), is due to the scattering of light from the linear chainlike aggregates of nanoparticles (cylinders). Interaction of light with

such chainlike structures in magnetic fluids, with their axis parallel to the direction of the incident light, gives rise to a ring like pattern in the transmitted light intensity with speckles [229]. When the incident light is normal to the cylinder axis, the scattered light forms a straight line pattern with a laser light spot at the center. If there is only one scattering cylinder, then the incident laser spot contains a diffraction pattern. However, under an applied field, large number of cylindrical aggregates of magnetic nanoparticles is formed in the ferrofluid, which results in multiple light scattering from the cylinders inside the nanofluid. The maxima and minima of the diffraction pattern from different cylinders overlap each other, resulting in a diffused pattern, which is a cumulative effect of light scattering from many cylindrical surfaces. Therefore, the observed scattered straight light pattern is a surface scattering phenomenon that depends only on the incident angle and does not contain information regarding the detailed internal structures of the ferrofluid.

3.3.3 Magnetic Field Induced Light Transmission in Nanoemulsion

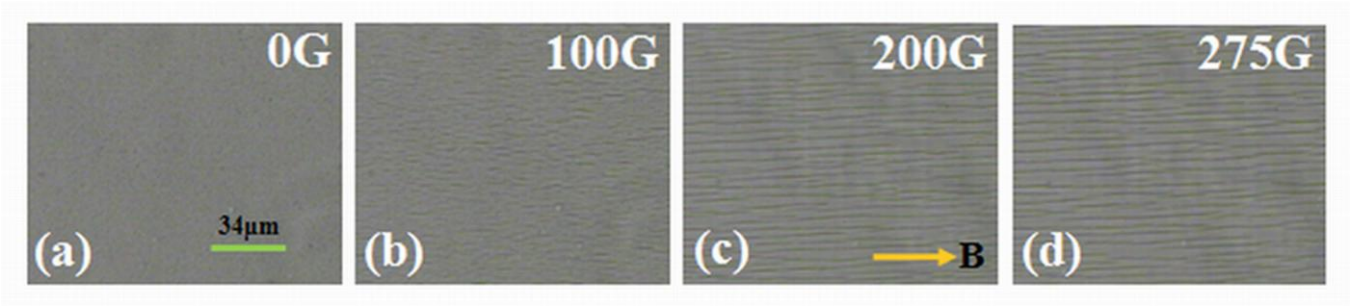

Fig.3.4. Phase contrast microscopic images of nanoemulsion in presence of external magnetic fields (B = 0, 100, 200, 275 G). The direction of B is shown by the arrow.

Figure 3.4 (a – d) shows the phase contrast microscopic images of the nanoemulsion at different B (= 0, 100, 200 and 275 G) where the direction of B is indicated by an arrow in Fig. 3.4c. The ϕ of the nanoemulsion used is ~ 0.0042. In the absence of B, the nanoemulsion

droplets are randomly dispersed in water (Fig. 3.4a). When magnetic field is applied, the magnetic moments of the individual magnetic grains inside the emulsion droplets are oriented along the external field direction. The dipolar interaction strength between the droplets is also expressed by Eq. (3.3) where $d = d_1$ is the diameter of the oil droplet. At $\Lambda_{coup} >> 1$, the dispersed nanoemulsion droplets undergo a disorder-order transition, leading to the formation of linear chain-like structures due to head-on aggregation along the direction of *B*. Figure 3.5a shows the schematic of the random orientation of the nanoemulsion droplets (inside the box) in absence of *B*. The formation of chainlike structures by nanoemulsion droplets at different *B* is shown in Figures 3.5(b – d). Such external field induced aggregation of magnetic nanoemulsion droplets have been earlier confirmed experimentally [172, 283, 284] and using computer simulation [275]. The interaction of light with such chainlike structures, with their axis parallel to the direction of the incident light, gives rise to a ring like pattern in the transmitted light intensity with speckles. The formation of the ring like pattern at different *B* is shown in Figures 3.5 (b – d). Figure 3.5(a) shows no ring like pattern at zero *B* (= B_0).

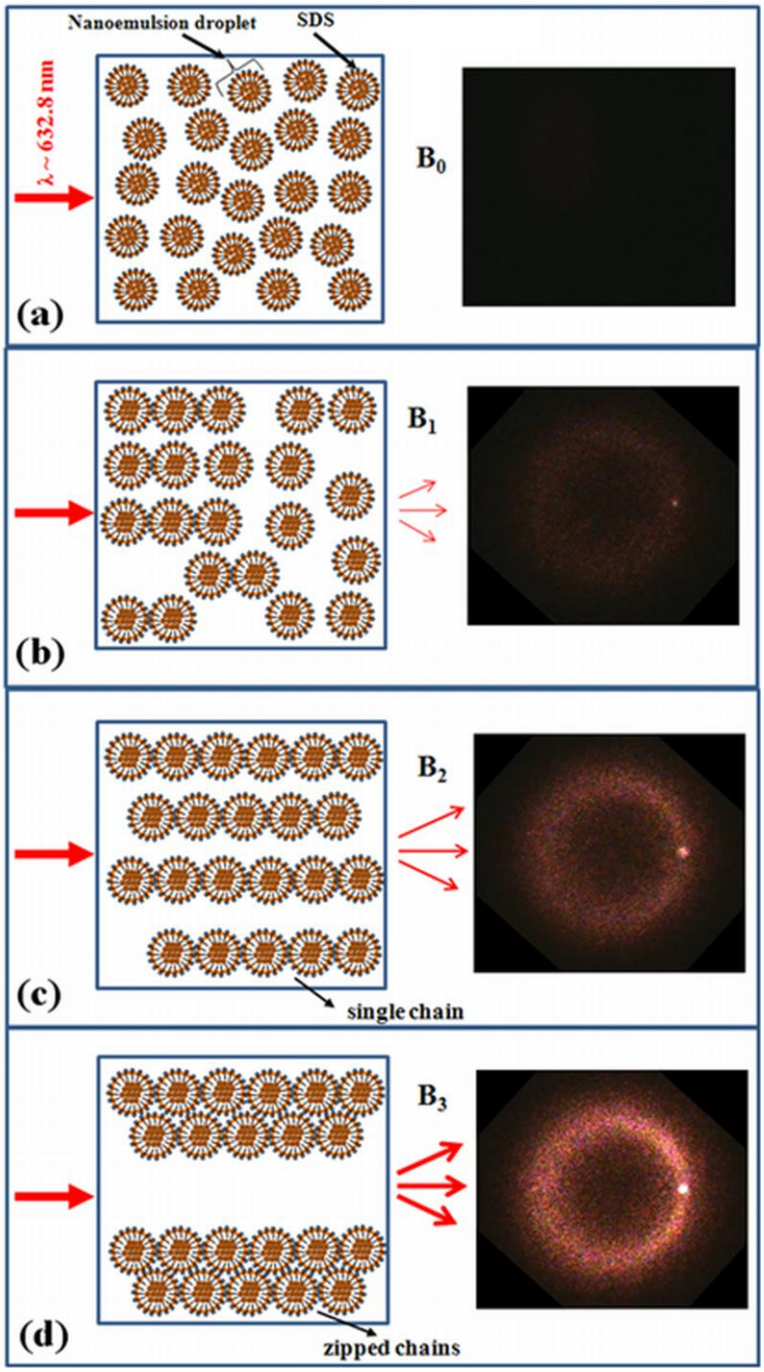

Fig.3.5. (left) Schematic of the nanoemulsion at different external magnetic field (B_0 is the zero external field and $B_1 < B_2 < B_3$) and (right) the corresponding transmitted light pattern projected on a screen.

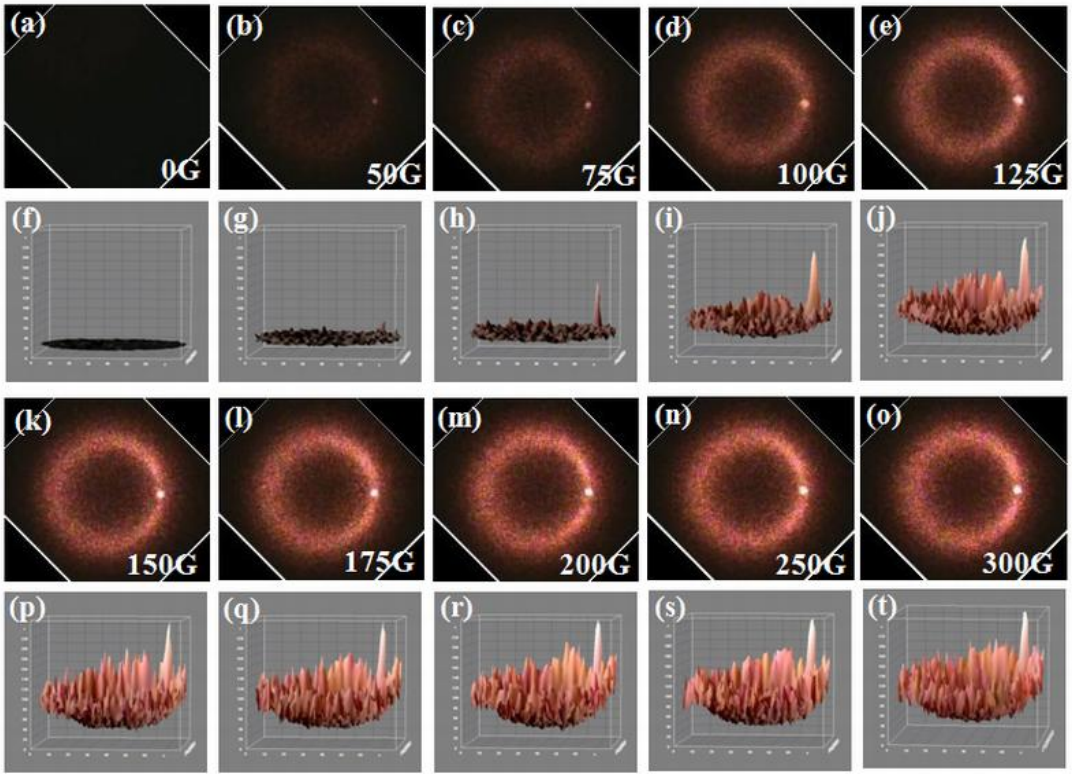

Fig.3.6. (a-e) & (k-o) Images of the transmitted light from nanoemulsion with volume fraction (ϕ) ~ 0.0042 in presence of external magnetic fields (B = 0, 50, 75, 100, 125, 150, 175, 200, 250 and 300 G). Images (f-j) & (p-t) are their corresponding 3D surface plots.

Figures 3.6(a - e) & 3.6 (k – o) show the images of transmitted light pattern from the nanoemulsion of ϕ ~ 0.0042 at various B = 0, 50, 75, 100, 125, 150, 175, 200, 250 and 300 G. Figures 3.6 (f – j) & 3.6 (p – t) show the corresponding speckle intensity distributions. In the absence of magentic field, no transmitted ring like pattern and speckles are observed (Figs. 3.6a and 3.6f, respectively). Below B ~ 50 G, the nanoemulsion remains opaque but above 50 G it becomes transparent. With increasing B, the intensity of the transmitted light also increases.

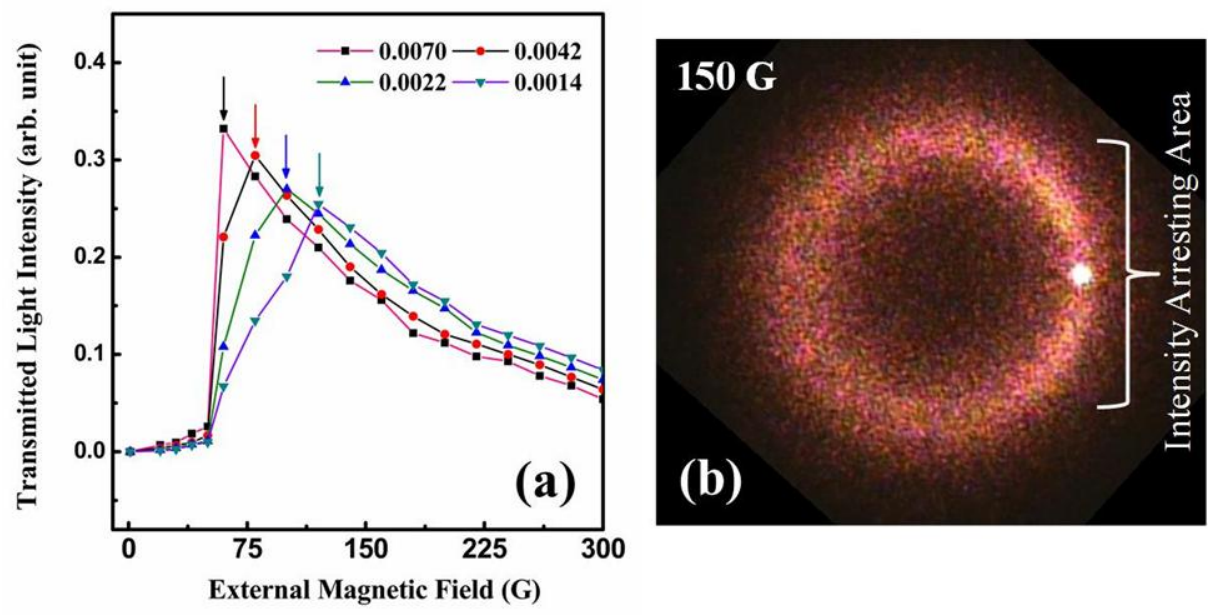

Fig.3.7. (a) Transmitted light intensity as a function of external magnetic field from nanoemulsion at volume fraction, $\phi \sim$ 0.0070, 0.0042, 0.0022 and 0.0014. (b) The ring like structure at external field, B = 150 G and the area over which transmitted light intensity is measured is indicated by the bracket.

Figure 3.7(a) shows the variation of transmitted light intensity as a function of B in nanoemulsions for four different ϕ values of 0.0070, 0.0042, 0.0022 and 0.0014. Figure 3.7(b) shows the transmitted light pattern (ring pattern) for $\phi \sim$ 0.0042 at 150 G, where the area over which intensity is measured is also shown. In case of ferrofluid, the highest value of normalized transmitted intensity is observed at zero field value and the normalized intensity decreases with increasing B whereas, it can be seen from Figure 3.7(a) that, the transmitted light intensity is almost zero up to 50 G in nanoemulsion. Beyond 50 G the transmitted intensity increases with increasing B and becomes a maximum at a critical field (B_C). Above B_C, the transmitted intensity again decreases with increasing B. It is further observed that the position of B_C shifts towards lower B at higher ϕ. For nanoemulsion with higher ϕ, the

transmitted light intensity increases more rapidly up to a critical field, beyond which the transmitted light intensity decreases at a faster rate compared to the lower ϕ. Figure 3.8 shows the variation of the critical magnetic field as a function of ϕ in nanoemulsion.

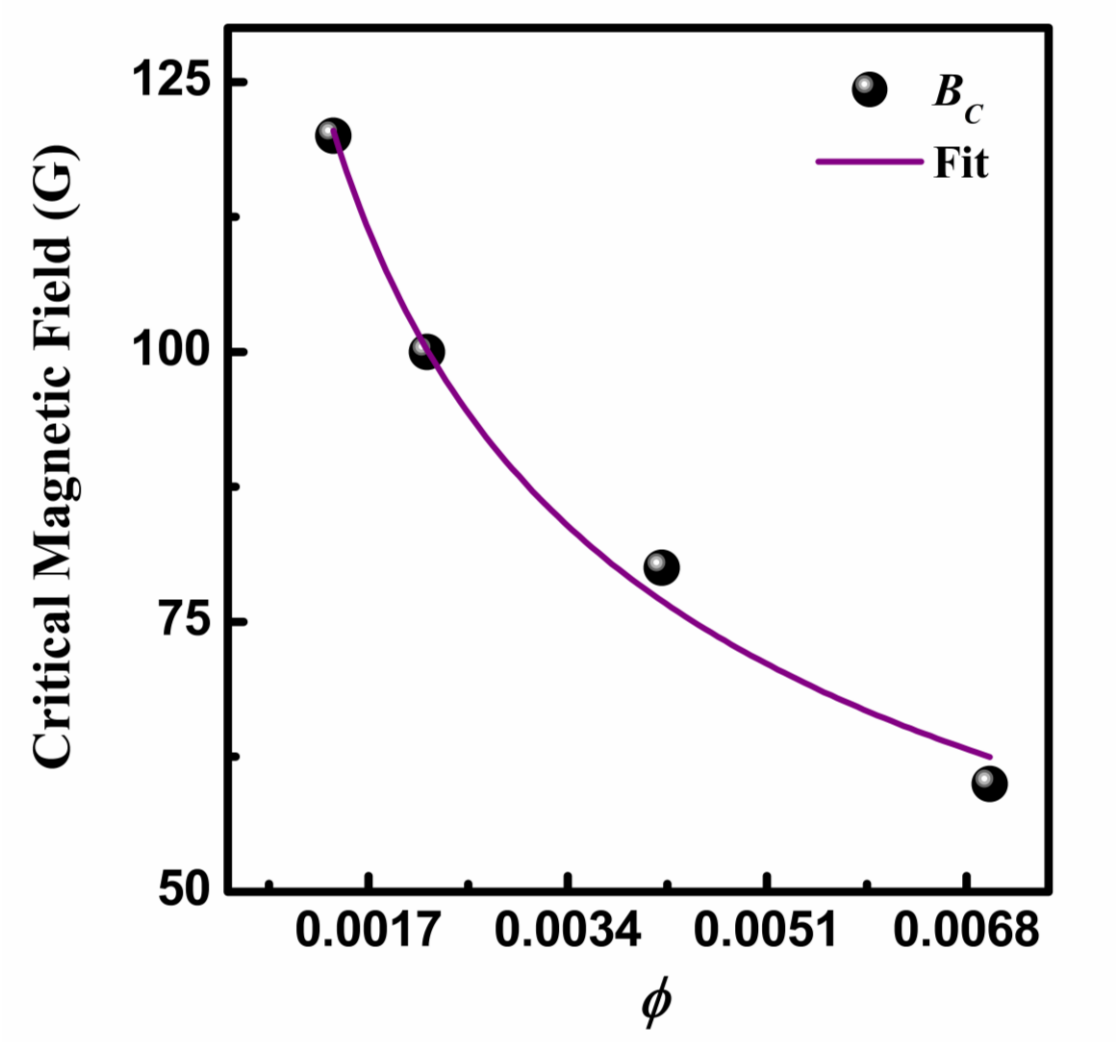

Fig.3.8. Critical magnetic field (B_C) as a function of volume fraction (ϕ) in nanoemulsion. B_C follows a power law decay with ϕ ($B_C \sim \phi^{-y}$) where the exponent value is 0.41.

Here, also the B_C shows a power law dependence with ϕ as: $B_C \sim \phi^{-y}$ where $y = 0.41$, and this is due to the external field induced disorder-order type structural transitions [271].

3.3.4 Possible Reasons for Variations of Field Induced Transmitted Intensity in Nanoemulsion

The variation of the transmitted light intensity as a function of B can be described using Mie scattering theory. At B = 0 G, the size of the nanoemulsion droplet (diameter ~ 220nm) is of the same order as λ (= 632.8 nm). With increasing B, the scatterer size increases due to field induced head-on aggregation [229]. When the scatterer size is comparable or higher than λ, the scattering falls in the Mie regime. In the present case, for droplet radius (a_1) ~ 110 nm, the size parameter (ka_1) at zero field is ~ 1.45 and for this ka_1 value, the Mie forward total extinction efficiency(Q_{ext}) [285, 286] is very high (~2.33). This indicates that at B = 0 G, due to intense scattering from the suspended particles, the forward light transmission becomes zero. This explains the reason for the observed opacity of nanoemulsion. With increasing B, the size parameter increases due to field induced aggregation of nanoemulsion droplets and Q_{ext} decreases from the initial higher value [229]. Moreover, the inter-chain spacing increases with external magnetic field due to the progressive aggregation and formation of chains of larger lengths. Therefore, the effective scattering cross section decreases with increasing B, which results in an increase in the transmitted light intensity beyond B ~ 50 G and up to B_C. As shown in Figure 3.7 (a), beyond B_C the transmitted light intensity again decreases with increasing B that can be explained as a result of the formation of tube like geometry by external field induced chain-like structures where the tube length and diameter increases with B [229]. These tube like structures behave like a waveguide due to the presence of π electrons on the surface of nanoemulsion droplets and when light propagates through such waveguides the transmitted light intensity decreases exponentially along the waveguide as $\exp(-a_w r)$, where a_w and r are the waveguide damping coefficient and waveguide length, respectively [229, 287]. The length of the tube like structures increases with B which leads to an increase in attenuation of light and a

decrease in the transmitted light intensity with external field beyond B_C. With increasing ϕ, the attenuation starts at a lower external field that causes the B_C to shift to a lower field at higher ϕ.

3.3.5 Variations of Transmitted Lobe Intensity as a Function of Magnetic Field in Nanoemulsion

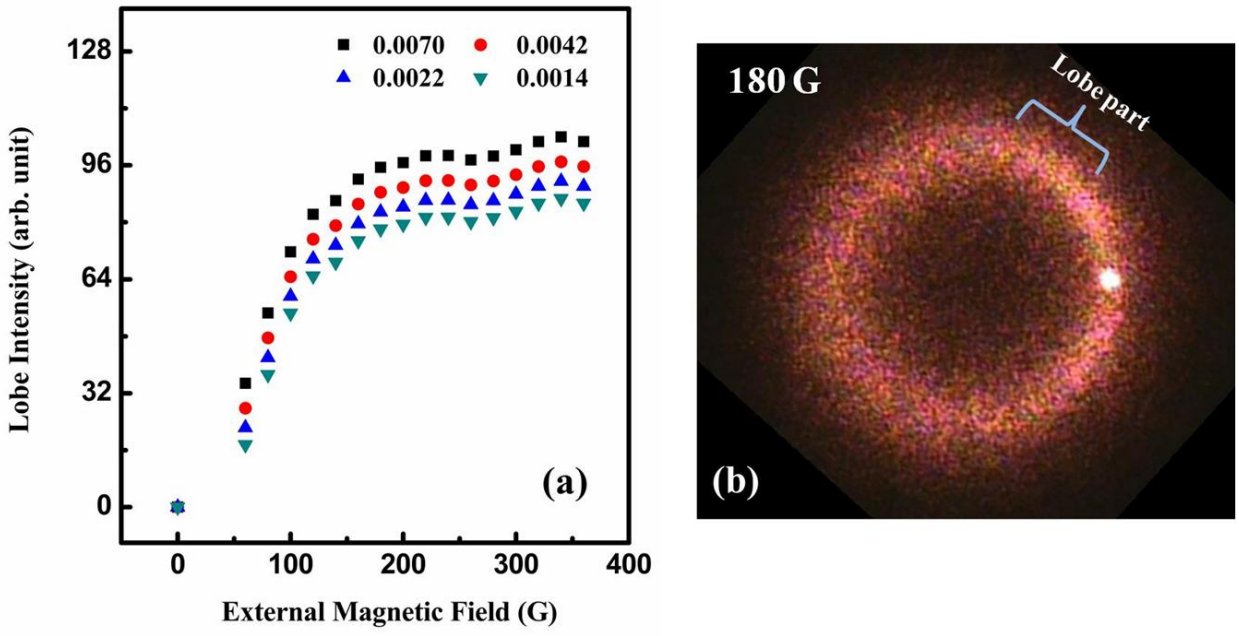

Fig. 3.9. (a) Intensity of a portion of the lobe as a function of external magnetic field for nanoemulsion at volume fraction, $\phi \sim 0.0070$, 0.0042, 0.0022 and 0.0014. (b) The transmitted light intensity pattern for nanoemulsion of $\phi \sim 0.0042$ at 180 G and the area over which intensity is measured is also indicated.

In nanoemulsion, a ring like pattern is observed as the external field direction is parallel to the incident light direction. Figure 3.9(a) shows the variation of the intensity of the lobe part (on the scattered ring) as a function of B for nanoemulsion at four different ϕ. Figure 3.9(b) shows the transmitted light pattern from nanoemulsion of $\phi \sim 0.0042$ at 180 G, where the area over

which intensity is measured is also shown. It can be seen that the lobe intensity increases with external magnetic field and remains almost constant beyond 200 G. Similar trends were observed in all the four volume fractions. Nevertheless, in nanoemulsions with higher ϕ, it was observed that the intensity of the lobe part increases more rapidly because of the enhanced scattering. At higher external fields (B >200 G), most of the nanoemulsion droplets form chains that are oriented along the direction of B and no more free droplets are available for chain formation. Hence, the intensity of the lobe part remains almost constant at higher B.

3.4 Conclusions

The behavior of light transmission through ferrofluid and nanoemulsion in presence of an external magnetic field is presented in this chapter. The transmitted light intensity in both the systems strongly depends on the external magnetic field and sample volume fraction. The resonances in the total extinction efficiency and forward anisotropy factor caused by the changes in the dimensions of scatterers due to dipolar interaction are considered to contribute to the variation in field induced transmitted light intensity in ferrofluid. Also in ferrofluid, the critical magnetic fields follow power law decay with particle volume fraction due to structural transitions of magnetic nanoparticles into chainlike structures. In nanoemulsion, up to 50 G, due to intense scattering the sample remains opaque. Beyond 50 G, the size parameter increases due to field induced aggregation where the Mie extinction efficiency decreases. The intensity of the transmitted light pattern is found to increase with external magnetic field up to a certain critical field beyond which it decreases because of the formation of waveguide like structures. The critical field is found to shift to a lower magnetic field at higher volume fraction and follows a power law behavior with volume fraction, indicating a disorder to order transition. The intensity of the lobe part of the transmitted light pattern increases with external magnetic field up to 200 G and beyond that it remains nearly constant.

Chapter IV Probing the Field Induced Structural Transitions by Transmitted Light Speckle Dynamics in Magnetic Fluids

4.1 Introduction

Wave propagation through disordered, random media has revealed many interesting phenomena [223, 288-294]. Optical speckle is an interference pattern of many scattered wavelets produced by the interaction of a coherent light beam with scatterers [295, 296]. The study of speckle parameters such as size, intensity, contrast, polarization, correlation coefficients etc. provides insight into scatterers because each speckle from a scattering centre is its fingerprint [296-301]. Analysis of speckle parameters has been used to measure the surface roughness [302, 303], assessment of biological tissue viability and burn diagnosis [304], viscoelastic properties of tissue [305], particle aggregation dynamics in dispersion [261], and heterodyne scattering [306]. Multi-dimensional entanglement has been studied by two photon speckles, which are used in bi-photon interferometer [306, 307]. Multi-speckle diffusing wave spectroscopy has been used to study the properties of colloidal particles suspended in a random packing of glass spheres [308, 309]. The light speckle has been used to generate photo-electromotive-force that has many practical applications [310, 311]. Speckle pattern by light transmission through colloids provides intensity fluctuations which is analogous to universal conductance fluctuation of mesoscopic conductors [312]. Astonishing memory effect is observed in speckle pattern when coherent light waves are transmitted through disordered media [313, 314]. The transverse spatial coherence of light changes when light wave propagates through dense, multiple scattering, random dielectric media [293, 315].

Magnetic colloidal dispersions are interesting materials both from fundamental and application point of view due to their unique optical [63, 238, 316-318], electrical [319], thermal [163] and rheological [114] properties. Several optical studies have been undertaken to investigate external field induced aggregation process in magnetic fluids [320]. Laskar *et al*. [172] showed

that the time dependent variations of the transmitted light intensity at several critical magnetic fields decreases drastically due to the coarsening of the field induced linear aggregates in ferrofluids. Also, optical speckle study is shown to be a finest technique to probe aggregation phenomena in colloids [261]. Though many light scattering studies have been reported to probe the structural transition in magnetic nanofluids, the effect of external magnetic field on the transmitted speckle properties in magnetic fluids has not been studied systematically.

The aim of this work is to investigate the effect of external magnetic field on the transmitted light speckle pattern in ferrofluid and nanoemulsion during structural transition of nano-sized magnetic particles in dispersion. First, the behavior of transmitted light speckle pattern and speckle parameters in ferrofluid in presence of external magnetic field are analyzed. Subsequently, the reasons for the external field induced variation of the speckle parameters in nanoemulsion are explained.

4.2 Experimental Details

The ferrofluid and nanoemulsion samples used in this study is a disordered magnetic medium as described in Chapter II (section 2.2). The experimental set up is shown in Figure 2.3. In the case of nanoemulsion the direction of incident light is parallel to the direction of *B*, whereas it is perpendicular to the direction of *B* in the case of ferrofluid. The detailed procedure of acquiring the scattered light and speckle patterns as a function of *B* are explained in Chapter II (section 2.3).

4.3 Results and Discussions

4.3.1 Field Induced Variations of Speckle Parameters in Ferrofluid

4.3.1.1 Speckle Size and Intensity

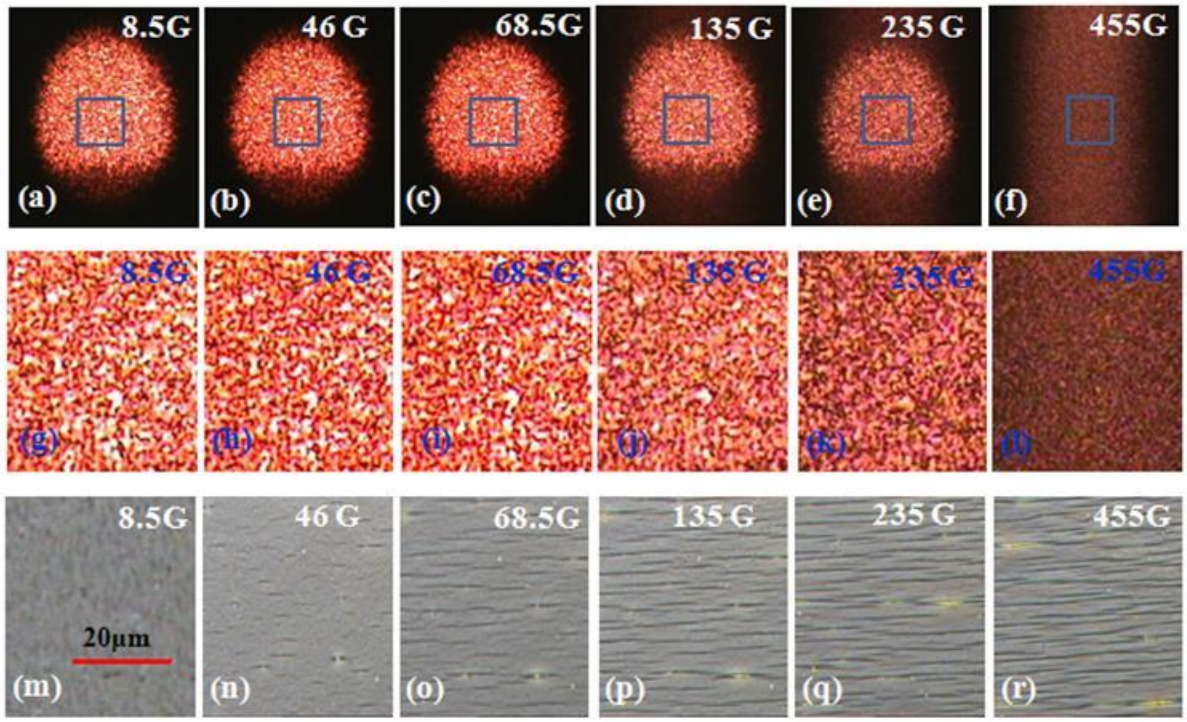

Fig. 4.1. Images (a - f): Transmitted laser light spots through ferrofluid at different external magnetic field (B = 8.5, 46, 68.5, 135, 235, 455 G). Images (g - l): Speckle pattern of the boxed area of the transmitted light spots (a – f). Images (m – r): Phase contrast microscopic images of ferrofluid in presence of different external magnetic fields (B = 8.5, 46, 68.5, 135, 235, 455 G).

Figures 4.1(a – f) shows the images of transmitted light spot from the ferrofluid at different B (= 8.5, 46, 68.5, 135, 235, 455 G). The enlarged square regions in Figures 4.1(a – f) shows the speckle pattern within the transmitted light spots. The scattering of light wave from magnetic nanoparticles in water produces scattered wavelets with phase differences [244]. Interference of

these de-phased wavelets results in the granular pattern known as speckle. The speckle pattern in the transmitted light spot consists of a multitude of bright points where the interference has been constructive, and dark points where the interference has been destructive, and irradiance levels in between these extremes which has the appearance of a chaotic muddle of speckles [296]. With increasing external field, the speckle pattern in the transmitted light spot from ferrofluid changes along with the field induced transition into a chain-like structure from individual magnetic nanoparticles in water. Figures 4.1 (m – r) shows the representative phase contrast microscopic images of ferrofluid at different external fields that demonstrates evolution of chain-like structure in presence of an external field from magnetic nanoparticles.

The propagation of light through disordered complex media like magnetic fluid provides information about the scattering media and the analysis of speckle parameters is one of the finest techniques for the remote measurement of the properties of scattering surfaces [295, 296, 321-323]. The speckle photographic technique is a useful to determine the displacement of the scattering object by measuring the dimensions of speckle emerging from scatterers. The dimension of speckles on the observation plane depends on the surface roughness and surface curvature of scatterers. When light is scattered from any cylindrical surface, the ratio of the length (dy , perpendicular to the cylinder axis) and the width (dx , parallel to the cylinder axis) of a speckle on the observation plane is [324]

$$\frac{dy}{dx} = \frac{(kr_{incident})}{(ka)(\sin\theta/4)} = \left(\frac{1}{\textbf{\textit{Size parameter}}}\right)\left(\frac{kr_{incident}}{\sin\theta/4}\right) \qquad (4.1)$$

here, $r_{incident}$ is the incident light spot diameter and θ is the scattering angle.

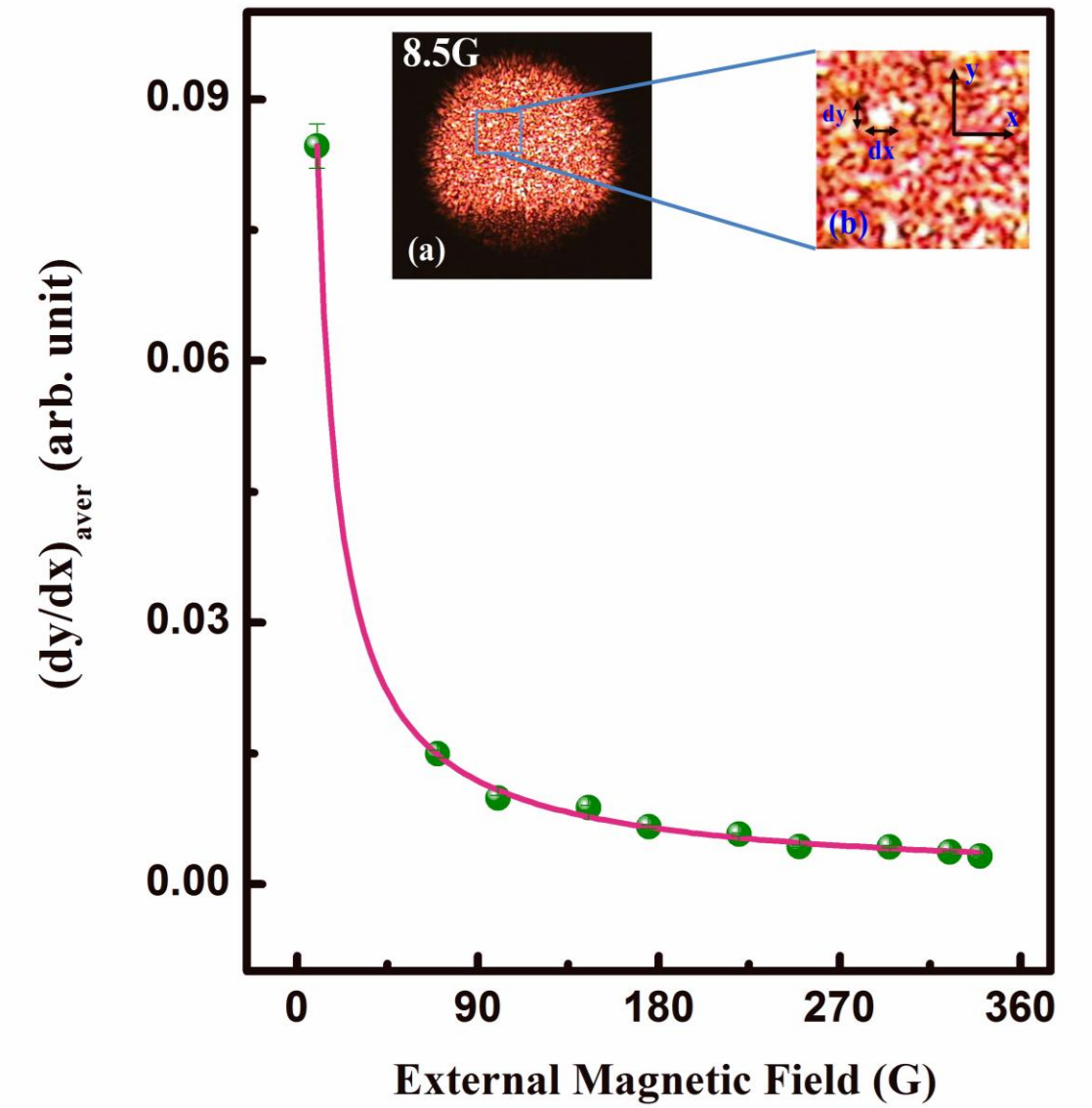

Fig.4.2. Plot of the average speckle size distribution as a function of external magnetic fields; *dx* and *dy* are the horizontal and vertical lengths of any speckle [Inset image (b)] on the transmitted light spot [Inset image (a)] at external field, B = 8.5 G and $(\frac{dy}{dx})_{aver}$ is the average ratio of the horizontal and vertical lengths of all speckles on the transmitted spot. $(\frac{dy}{dx})_{aver}$ follows a power law decay with external magnetic field $\left[(\frac{dy}{dx})_{aver} \sim B^{-0.89}\right]$.

Inset (a) and (b) of Figure 4.2 shows the images of the transmitted light spot and the speckle pattern of a particular area [box shown in (a)] from ferrofluid at B = 8.5 G. In inset (b) of Figure 4.2, dy and dx represents the length (perpendicular to the external field direction) and width (parallel to the external field direction) of any speckle on the observation plane, respectively. The plot of the average speckle size distribution vs external fields, (Figure 4.2) shows that the average speckle size distribution ($\frac{dy}{dx}$)follows a power law decay with the external magnetic field$\left((\frac{dy}{dx})_{aver} \sim B^{-0.892} \right)$. Under the field induced aggregation, the surface roughness, size parameter as well as scattering cross-section of the aggregate increases with *B*. Therefore, anisotropic speckle size on the transmitted light spot should decay with *B* because of the enhancement of size parameter (Eq. 4.1), which is found to be in good agreement with our experimental data.

Figures 4.3 (a – e) and 4.3 (f – j) shows the images of transmitted light spots and their corresponding 3D intensity surface plots for the speckle intensity distribution in the presence of *B*. Figures 4.3 (o – k) and 4.3 (t – p) show the recovery of transmitted spot intensity and the corresponding 3D surface plots for speckle intensities during the reduction in the *B* from maximum to zero. It can be seen that the speckle intensities on the transmitted light spot from ferrofluid recover their initial values during the decrease in *B*, which indicates the field induced reversibility of the aggregation process.

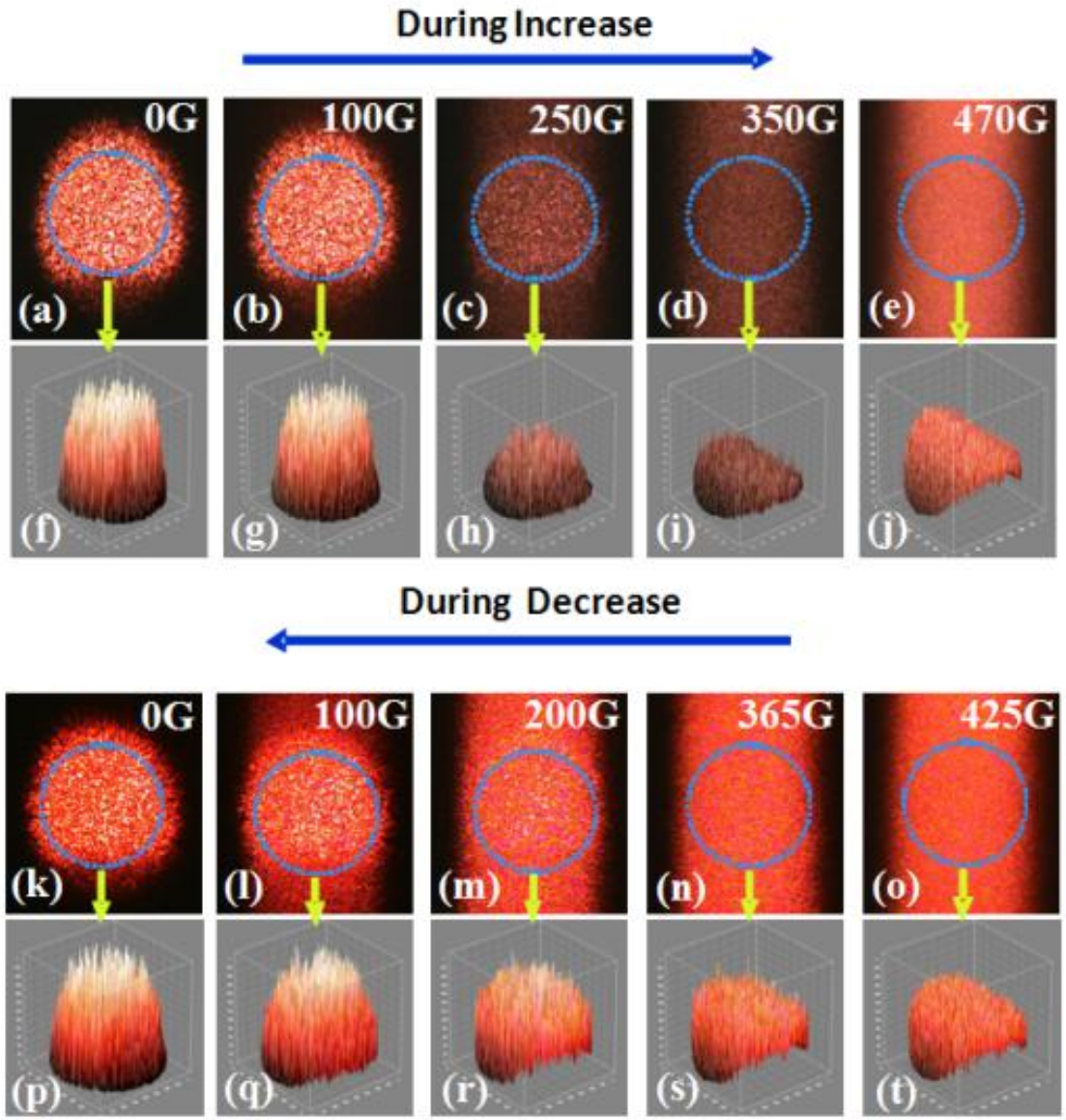

Fig. 4.3. Images of the transmitted light spots from ferrofluid (volume fraction, ϕ = 0.00916) and their corresponding 3-D surface plots for speckle intensities in presence of different external magnetic fields. Images (a – e) & (f – j) are the spot images and their corresponding 3D surface plots during the increase of external fields. Images (o – k) & (t – p) are the spot images and their corresponding 3-D surface plots during the decrease of external fields. Field ramp rate ~ 2.5 G/s.

4.3.1.2 Effect of Surface Roughness on Degree of Coherence and Percentage of Depolarization

The speckle pattern depends on light parameters such as angle, polarization and wavelengths of the incident light and surface profile (roughness) of the scattering objects [296, 325, 326]. The variance of the phase fluctuations (σ_φ) in the scattered wavelets is related to the variance of the surface height fluctuations (σ_h) by $-\sigma_\varphi = (\frac{4\pi}{\lambda})\sigma_h$ [296]. Figures 4.4(a) and 4.4(b) shows the speckle pattern of the transmitted light spot from ferrofluid of ϕ = 0.00916 at B = 135 and 455 G, respectively. At this field strength [B = 135 G], the scattering occurs mainly from the single chain-like structures with certain surface height fluctuation as shown in Figure 4.4(c).

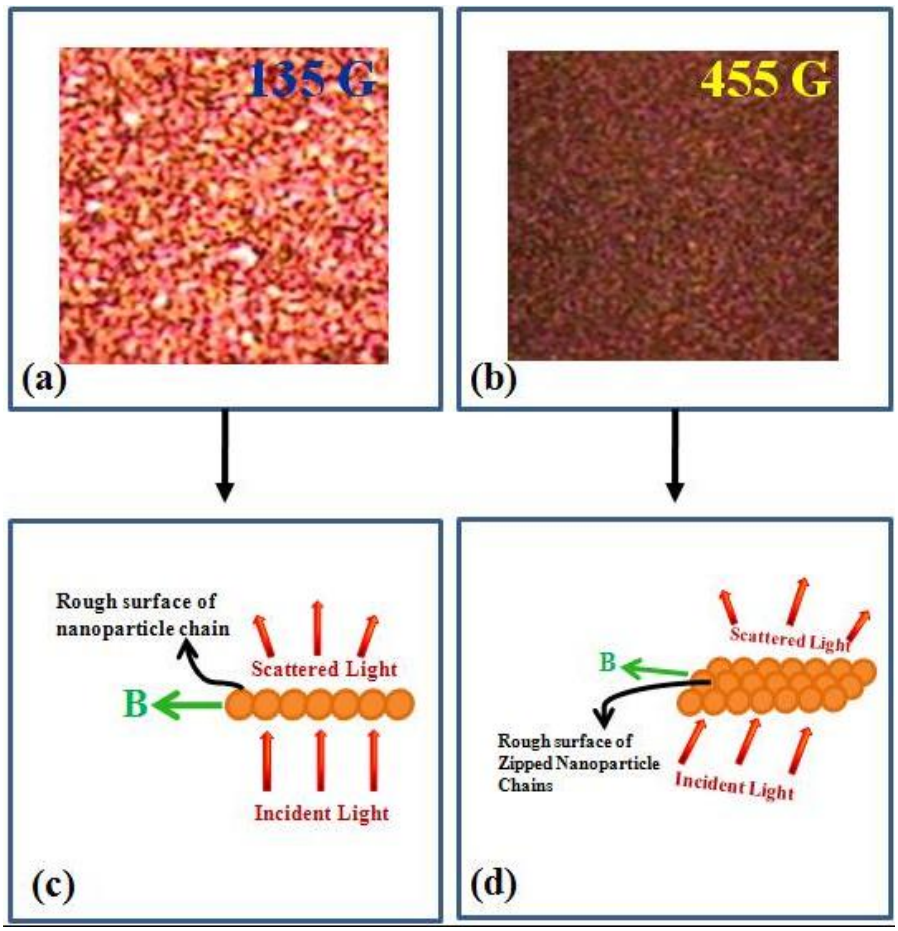

Fig. 4.4. (a) and (b)—Images of the speckle pattern on the transmitted light spot at B = 135 & 455G, respectively. (c) and (d)—Schematics of light scattering by the rough surfaces of a single and zipped nanoparticle chain, respectively.

After the second critical field [B = 360 G for ϕ = 0.00916], zippering transition occurs [172], which increases the scatterer surface roughness as shown schematically in Figure 4.4(d). Therefore, the surface roughness of the aggregates increases with external field that resulted in the variation of phase fluctuations in the scattered wavelets and the transmitted speckle pattern. In light scattering experiment, information about the disordered soft condensed matter system can be extracted by measuring the coherence property of the scattered wave-field [327-329]. It is known that the transverse spatial coherence of light changes when it propagates through a disordered, dense, multiple scattering dielectric medium [293, 328]. The degree of coherence of photons plays a key role in determining its energy flow [330]. The speckle patterns generated by the propagation of light through scattering media also depends on the coherence property of the scattered light [295, 296]. When light waves scatter from rough scattering surface, the degree of coherence of any two scattered light waves is given by [296]

$$\overline{\gamma_{12}}(\tau) = \exp[-(\frac{4\pi}{\lambda})^2 \sigma_h^2 \{1 - \xi_\varphi\}] \qquad (4.2)$$

where, τ is the relative time delay between the two light waves (1 & 2), σ_h is the variance of the surface height fluctuations of the scattering surface and ξ_φ is the normalized auto-correlation function of the phases. In ferrofluid, the field induced aggregation of magnetic nanoparticles in dispersion enhances the surface roughness (Fig. 4.4c-d). This means that the degree of coherence of the scattered wave-fields exponentially decreases with increasing external magnetic field [Eq. 4.2]. Therefore, the external field can affect the degree of

coherence and variation of phase fluctuations of the scattered light waves, which is in good agreement with our results.

Further, the propagation of polarized light wave through disordered media depolarizes the wavelets due to interaction with many depolarizing scattering surfaces [296, 331, 332]. Tong *et al.* [333] experimentally shown that the speckle contrast of a fully developed speckle pattern can be reduced from 1 to 0.5 due to polarization changes. The speckle patterns formed by scattering change polarization diversity between incoming and outgoing waves and the surface roughness of the scatterer surface favors polarization diversity [296]. The percentage of depolarization is defined as [331, 332]

$$D_P = \%\ \text{depolarization} = 100 - \%\ \text{polarization} \tag{4.3}$$

$$\text{where, \% polarization} = P = \left| \frac{I^s_{B=0} - I^s_{B\neq 0}}{I^s_{B=0} + I^s_{B\neq 0}} \right| \times 100 \tag{4.4}$$

where $I^s_{B=0}$ and $I^s_{B\neq 0}$ are the speckle intensities on the transmitted light beam spot without and with *B*, respectively.

Figure 4.5(a) represents the percentage of depolarization of the scattered wavelets from ferrofluid as a function of *B*. The images (b) and (c) of Figure 4.5 show the transmitted light spots at B = 0 G and B = 135 G and the images (d) and (e) of Figure 4.5 show the corresponding 3D intensity surface plots of the speckles on the transmitted light spots for the area shown by rectangle in (b) and (c) of Figure 4.5, respectively. Considering the speckle intensity values of the transmitted light spots at different *B* and by using Equations (4.3 & 4.4), we obtain Figure 4.5(a), where the percent of depolarization is found to decrease with the increase of *B*. Egan *et al.* [331] experimentally demonstrated that the depolarization decreases with the increase in the size of individual scattering particles. Our findings are found to be consistent with the above observations.

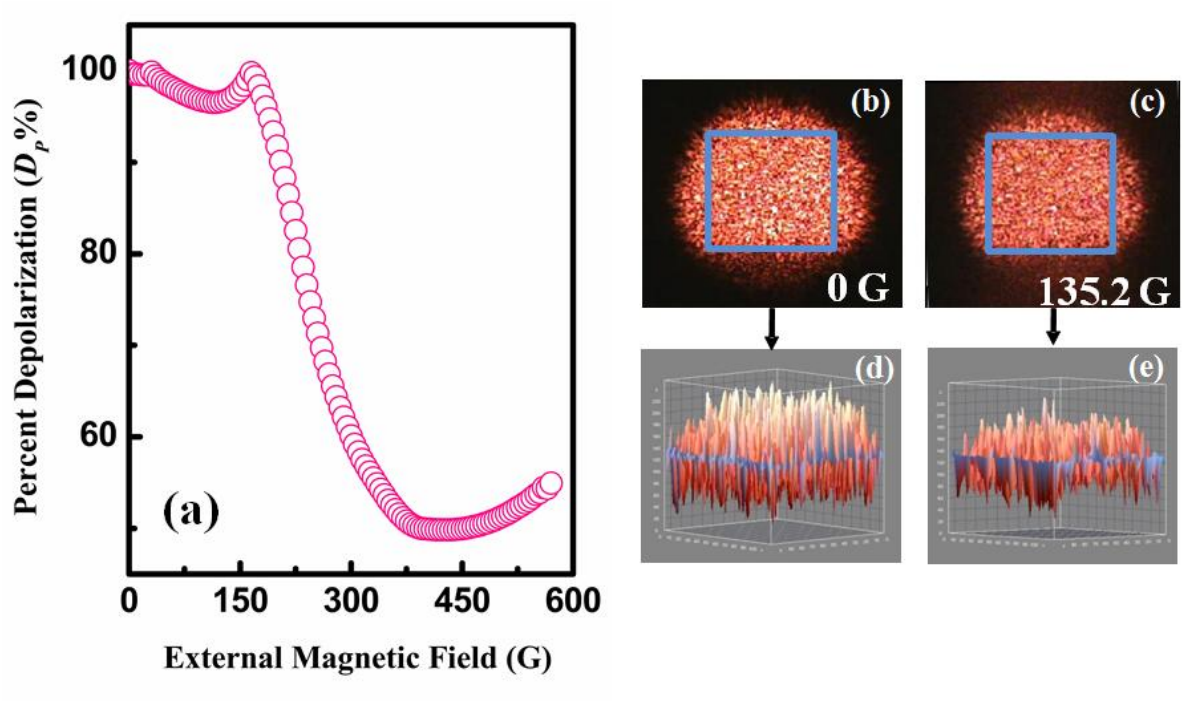

Fig.4.5. (a) Percentage of depolarization (D_P%) of transmitted light spot speckles from ferrofluid as a function of external magnetic field (B). Images (b) & (c) Transmitted light spots at B = 0 & 135G, respectivley and (d) & (e) 3D surface plots for speckle intensities from particular areas of transmitted light spots of (b) & (c), respectively.

4.3.1.3 Speckle Contrast

The intensity fluctuations of the speckle pattern of the transmitted light spot from a nanofluid changes with time ('dynamic' speckle pattern), because of the Doppler shifts of the scattered wavelets due to the Brownian motion of dispersed nanoparticles. The level of blurring of any speckle pattern is quantified by the Speckle Contrast (C). The speckle contrast is defined as the ratio of the standard deviation (σ) of the intensity to the mean intensity $< I^s >$ of the speckle pattern.[296, 321, 334]

$$C \equiv \frac{\sigma}{< I^s >} = \frac{\sqrt{< (I^s)^2 > - < I^s >^2}}{< I^s >} \tag{4.5}$$

Goodman and Parry[296, 335] showed that for static speckle pattern, the speckle contrast is equal to unity, which is the maximum value for a fully developed speckle pattern. When scattering objects are dynamic, the *C* value is less than unity and the pattern becomes blurred. Speckle contrast depends on the scattering particle velocity and for Lorentzian velocity distribution, which is applicable for Brownian particles, the speckle contrast is given by [296, 335]

$$C = \sqrt{\frac{\tau_c}{2T_{exposure}}\{1-\exp(-\frac{2T_{exposure}}{\tau_c})\}} \qquad (4.6)$$

where, $T_{exposure}$ is the exposure time and τ_c is the correlation time. Small value of C corresponds to a small τ_c (i.e. fast moving speckles) and C approaching unity corresponds to a large τ_c (i.e. for stationary speckles). By measuring the speckle intensities of the transmitted light spot at different external magnetic fields, the speckle contrast (C) is calculated by using Eq. (4.5).

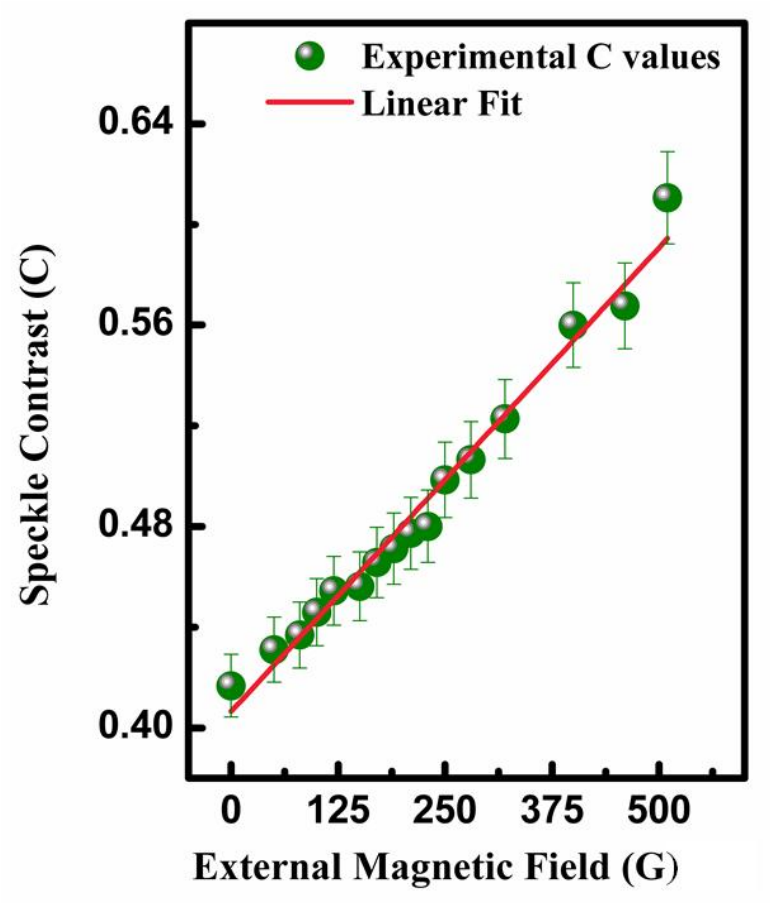

Fig. 4.6. Linear variation of speckle contrast (*C*) of transmitted light spot speckles with external magnetic field (*B*). The best fit on the experimental data points is given by- $C = m'B + s_1$, where m' (slope) = 3.685*10^{-4} and s_1=0.4065.

Figure 4.6 shows a linear increase in the contrast of speckles on the transmitted light spot with increase in *B*. The speckle intensity and the intensity fluctuations in the transmitted light spot is found to decrease with the external field [Fig. 4.3] whereas the speckle contrast increases, which signifies a transition from a dynamic to a near stationary speckle pattern by losing the free movement of scatterers in the dispersion under external field.

We observe that the percentage of polarization of the transmitted light waves from nanofluid increases with an increase of external magnetic field, which affects the transmitted light

speckle pattern. For partially polarized speckle, the relation between C and the degree of polarization (P) is given by[296]

$$C = \sqrt{\frac{1+P^2}{2}} \tag{4.7}$$

Figure 4.7 shows the plot of the variation of the speckle contrast with the change of the degree of polarization. The theoretical plot $C_{Theo.}$ vs. P is obtained by using Eq. (4.7), where the theoretical data is divided by 1.486 to superimpose it on the experimental curve.

Applying the speckle intensity values at different external fields as shown in Figure 4.3 (3D surface plots for speckle intensities during increase of B), the P (experimental) and C_{Expt} values for different B are obtained. The plot of C_{Expt} vs. P (Fig. 4.7) shows that the speckle contrast (C_{Expt}) increases with increase in the degree of polarization in presence of B, which is in good agreement with the theory. This shows that the field induced aggregation process in ferrofluid increases the degree of polarization of the scattered light waves as well as the speckle contrast.

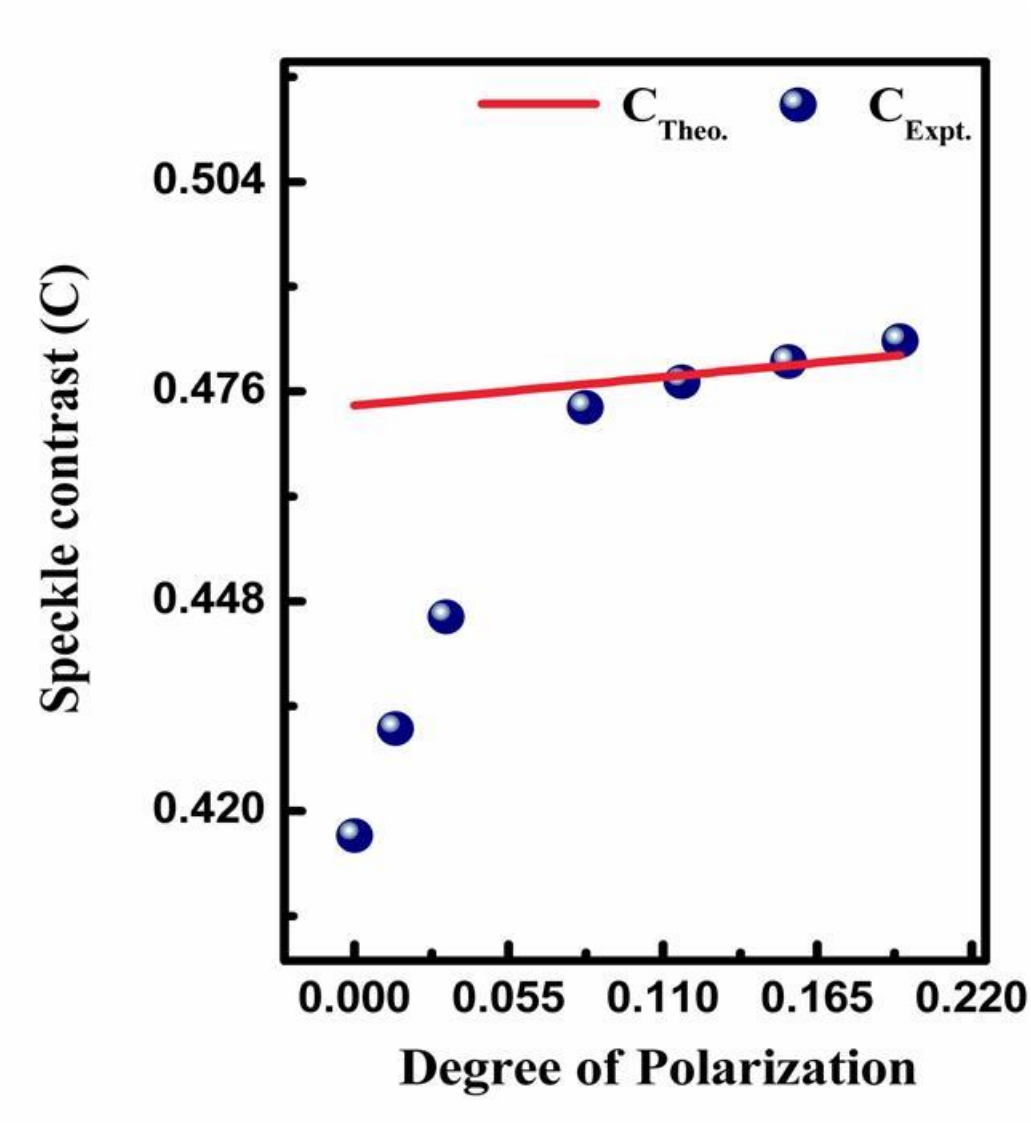

Fig.4.7. Variation of speckle contrast (*C*) with the degree of polarization (*P*) of the scattered waves. Closed circles: Experimental data from transmitted light spot speckles at different external magnetic fields (*B*). Theoretical fit: $C_{Theo} = m'P + s_1$ where m' =0.03456 and s_1 = 0.47414 , are obtained by using Eq. (4.7) where the theoretical data are divided by 1.486.

It has been shown that the speckle contrast reduces due to the Brownian motion of scattering particles in a colloidal media [336]. Figure 4.6 shows that the speckle contrast of the

transmitted light spot increases with the increase of *B* but the contrast (*C*) is much lower than unity at higher field *B* > 250 G, though the scatterers (chain-like structure) are almost stationary in the dispersion [Figs. 4.1 (m–r)]. Therefore, the increase in the speckle contrast value with *B* indicates that the role of surface roughness is less predominant compared to the scatterer size and other effects. The relationship between the *C* and the scatterer surface roughness (σ_h) for light with a finite bandwidth (σ_b) is given by [295]

$$C = \frac{1}{[1+(4\sigma_b\sigma_h)^2]^{1/4}} \tag{4.8}$$

Figure 4.8 shows the theoretical plot of *C* with surface roughness by using equation (4.8), where the scatterers σ_h is an increasing function of *B*. Figure 4.8 further shows that *C* drastically decreases with increasing σ_h. However, the field induced chainlike structure in ferrofluid increases the speckle contrast but the speckle contrast is less than unity due to increased surface roughness.

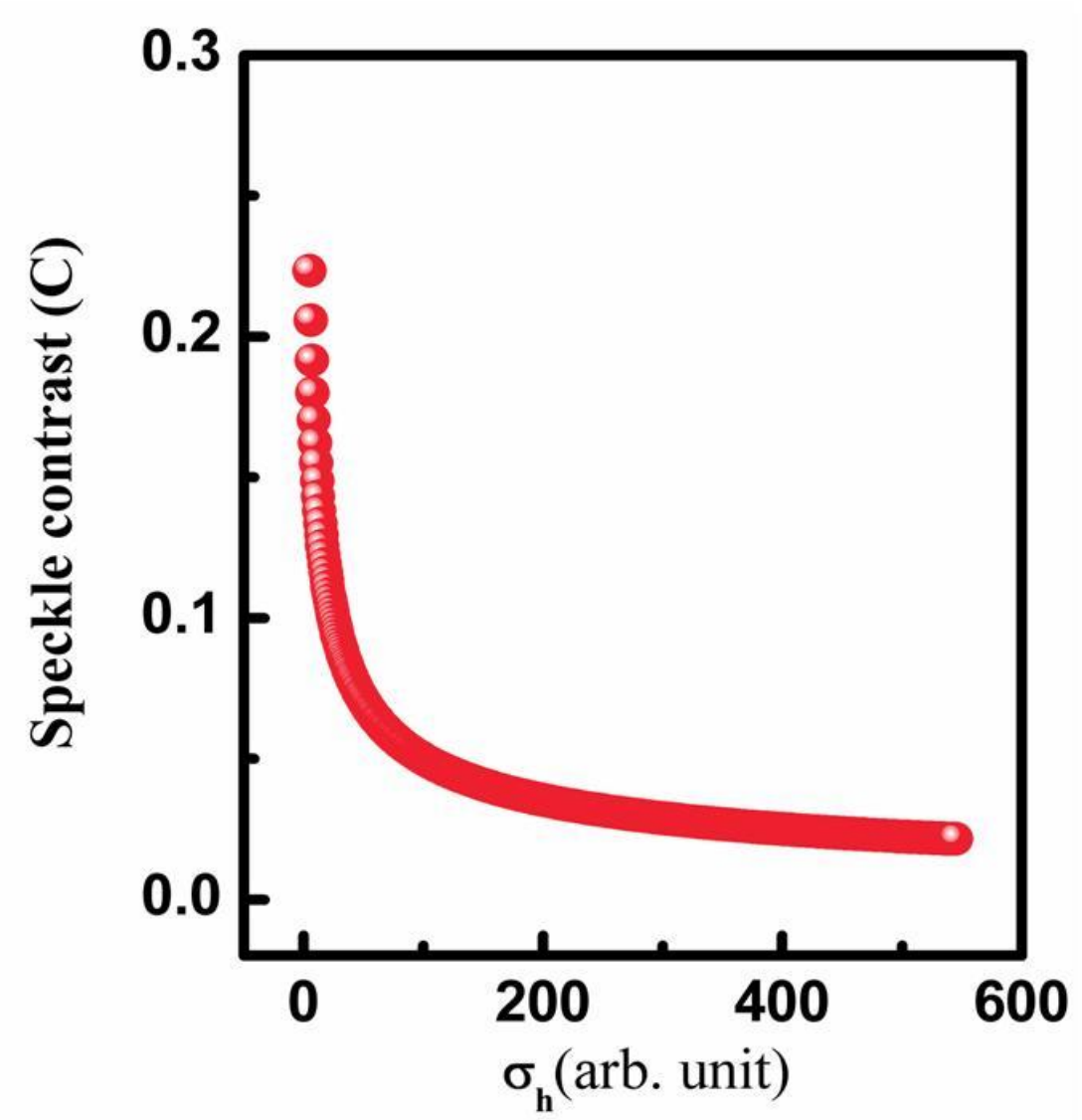

Fig.4.8. Variation of speckle contrast (C) with surface roughness (σ_h) of the scattering surface.

4.3.1.4 Speckle Correlation Coefficient

The speckle correlation coefficient (C_S) of the speckle intensities I_n with n =(1, 2) of the two different speckle pattern is defined as [337, 338]

$$C_S = \frac{< I_1^s I_2^s > - < I_1^s >< I_2^s >}{[(< (I_1^s)^2 > - < I_1^s >^2)(< (I_2^s)^2 > - < I_2^s >^2)]^{1/2}} \tag{4.9}$$

where, I_1^s and I_2^s are the intensities of two different speckle patterns and < > denotes the average.

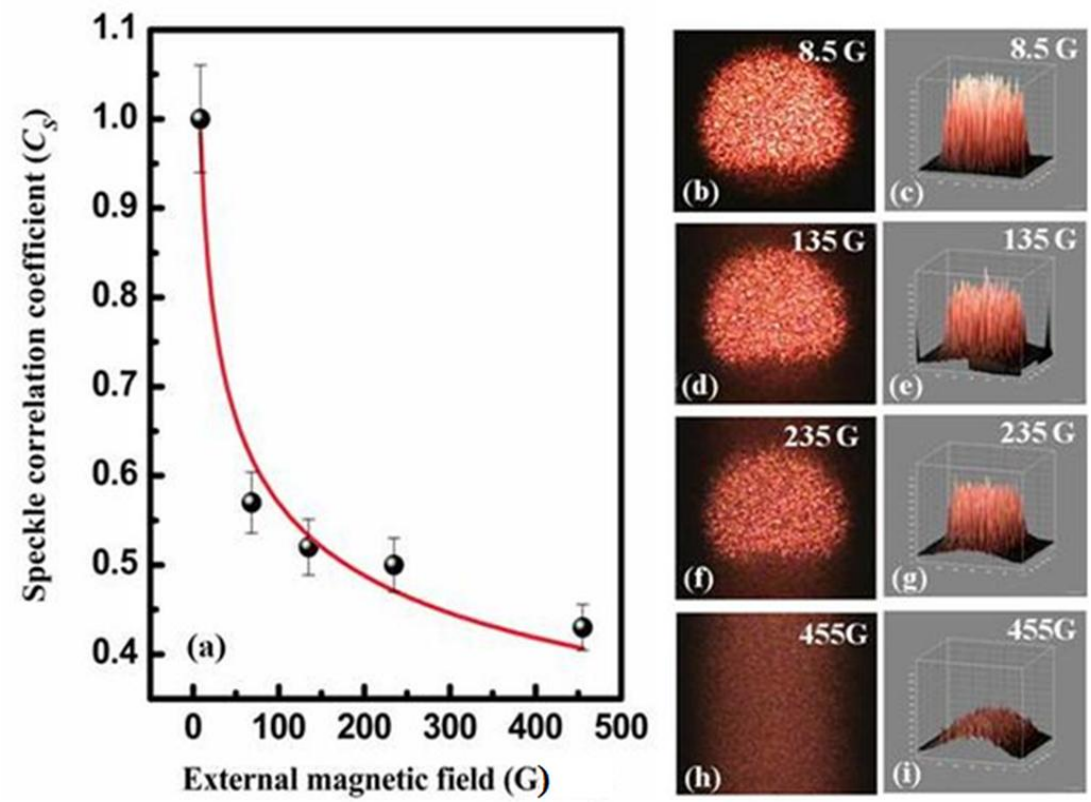

Fig.4.9. (a) Variation of the Speckle correlation coefficient (C_S) of the transmitted light spot speckles with external magnetic fields (B); $C_S \sim B^{-0.22}$. Images (b, d, f, h) : Transmitted light spots at different fields and Images (c, e, g, i): the corresponding 3D surface plots of speckles intensity.

Figure 4.9(a) shows the variation of the speckle correlation coefficient (C_S) with B. Here, C_S is obtained from the speckle intensities $I_1^s = I_{B=8.5}^s$ and $I_2^s = I_{B=8.5}^s, I_{B=68.5}^s, I_{B=135}^s, I_{B=235}^s, I_{B=455}^s$. The images (b, d, f, h) & images (c, e, g, i) of Figure 4.9 are the transmitted spot images and their corresponding 3D surface plots for speckle intensities at B = 8.5, 135, 235, 455 G,

respectively. The C_S value is maximum (i.e. equal to unity) when $I_1^s = I_{B=8.5}^s$ and $I_2^s = I_{B=8.5}^s$, but it decreases for other I_2^s. Here, the speckle correlation coefficient shows a power law decay with $B(C_S = 1.5858B^{-0.22})$. Again, the speckle correlation coefficient depends on the surface roughness of the scattering surface, the angle of incidence and the wave number differences of the incident wavelengths [337, 339]. For spectral speckle correlation (SSC), where the angle of incidence (α_1) is fixed but there is a difference between the incident wave numbers $(\Delta k = k' - k'')$, the far field correlation coefficient (C_{12}^{SSC}) decays exponentially with increasing surface roughness (σ_h) as $C_{12}^{SSC} = \exp[-4\sigma_h^2 (k' - k'')^2 \cos^2 \alpha_1]$ [339]. In angular speckle correlation (ASC) where the angle of incidence is changing, at fixed incident wave-number, the far field correlation coefficient is $C_{12}^{ASC} = \exp(-\sigma_h^2 k^2 \delta\alpha_1^2 \sin^2 \alpha_1)$ where $\delta\alpha_1 = \alpha_1^{/} - \alpha_1^{//}$ [339]. Both SSC and ASC strongly depend on the scatterer surface roughness and the correlation coefficients for both cases decrease with increasing surface roughness. The field induced aggregation process leads to chain-like structures and zipped chains at higher *B* with larger surface roughness, which causes a decrease in C_S with increasing *B*.

Studies on the propagation of light waves through optically dense colloidal suspensions by Scheffold and Maret [260] showed a buildup of anomalous long range correlation in the transmission speckle pattern. The speckle correlation coefficient depends on the phase shifts between the multiple scattered wavelets in the outfield area and the transport mean free path (ℓ^*) of the light waves inside the scattering medium. The increase in ℓ^* decreases the transmission speckle correlation. The formation of field induced aggregates in ferrofluid increases ℓ^* (Chapter III - Figs. 3.3 e & f) which results in the decay of C_S with increase in *B*.

4.3.2 Field Induced Variations of Lobe Speckle Parameters in Nanoemulsion

In the case of nanoemulsion, a ring like pattern was observed because, the field direction was along the incident light direction. In chapter III, section 3.2.5 showed the variation of the intensity in the transmitted lobe part (on the scattered ring) as a function of *B* in nanoemulsion. The lobe consists of speckles whose dynamics changes with *B*.

4.3.2.1 Lobe Speckle Contrast

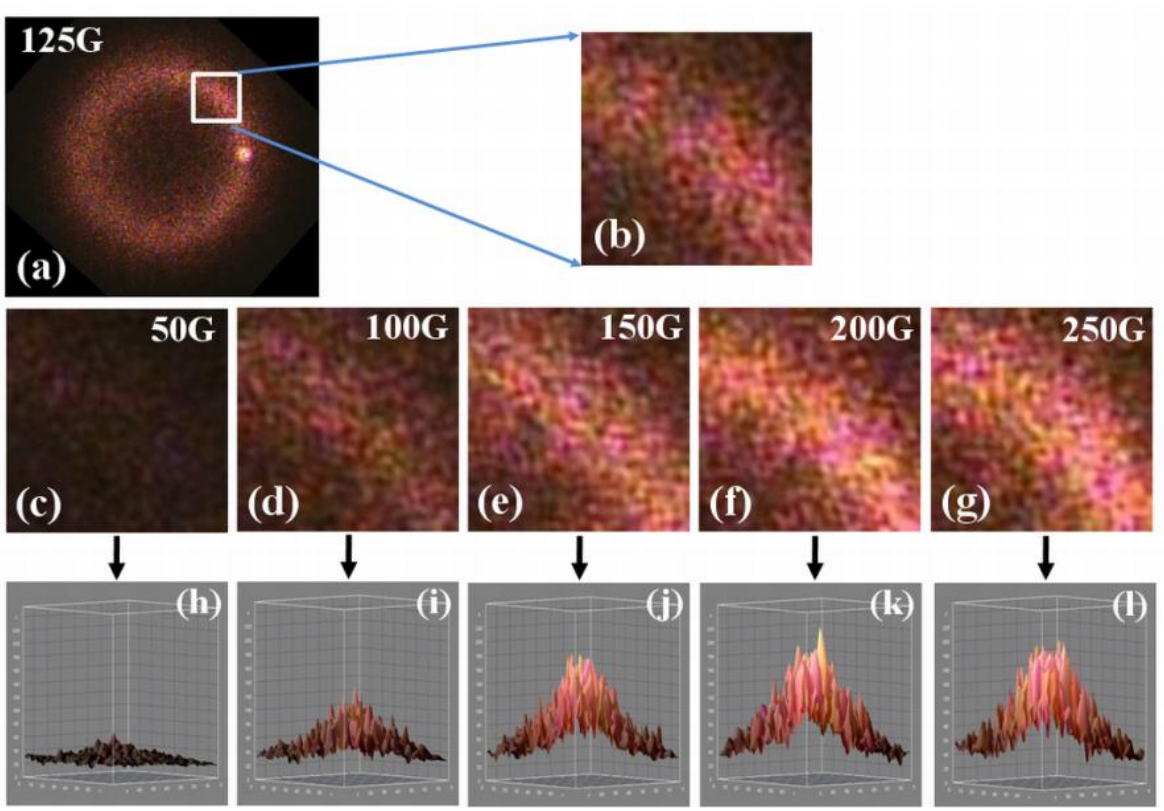

Fig.4.10. (a) Image of the transmitted light pattern from nanoemulsion at external magnetic field, *B* = 125G. (b) The speckle pattern of the boxed region is shown. (c-g) The speckle pattern for the same lobe part at different external magnetic fields (*B* = 50, 100, 150, 200, 250G) and (h-l) are their corresponding 3D surface plots.

Figure 4.10 shows the transmitted light intensity at *B* = 125 G for nanoemulsion of $\phi \sim 0.0042$ and Figure 4.10(b) shows the magnified view of the section of the lobe part of the transmitted

light pattern with speckles. Figures 4.10 (c-g) show the images of the lobe parts at different B = 50, 100, 150, 200 and 250 G. Figures 4.10 (h-l) shows the corresponding 3D surface plots of the speckle intensity distribution of the lobe parts under similar B values. The speckle patterns consist of a combination of bright and dark points that correspond to maximum and minimum intensities, respectively. It can be clearly seen that the lobe speckle intensity increases with increase in B. With increasing B, the aggregation and formation of chain like structures increases leading to an increase in the scattering and speckle contrast.

One of the most common ways to quantify the variation of speckle pattern is by measuring the speckle contrast (C) [295, 321, 340]. The measurement of the lobe speckle contrast (C_L) is performed for nanoemulsion of four different ϕ = 0.0070, 0.0042, 0.0022 and 0.0014 in the external magnetic field range of 50-360 G by using Eq. (4.5). The variation of lobe speckle contrast as a function of B is shown in Figure 4.11. For all four volume fractions, the lobe speckle contrast (C_L) increases with increasing B up to ~ 170 G and beyond that the C_L remains nearly constant. The value of C_L is higher for nanoemulsion with higher ϕ. The field induced increase in C_L indicates that the random Brownian movement of the magnetic nanoemulsion droplets decreases with increase of B. For higher B, most of the nanoemulsion droplets are oriented along the direction of B, leading to a reduced scatterer movement.

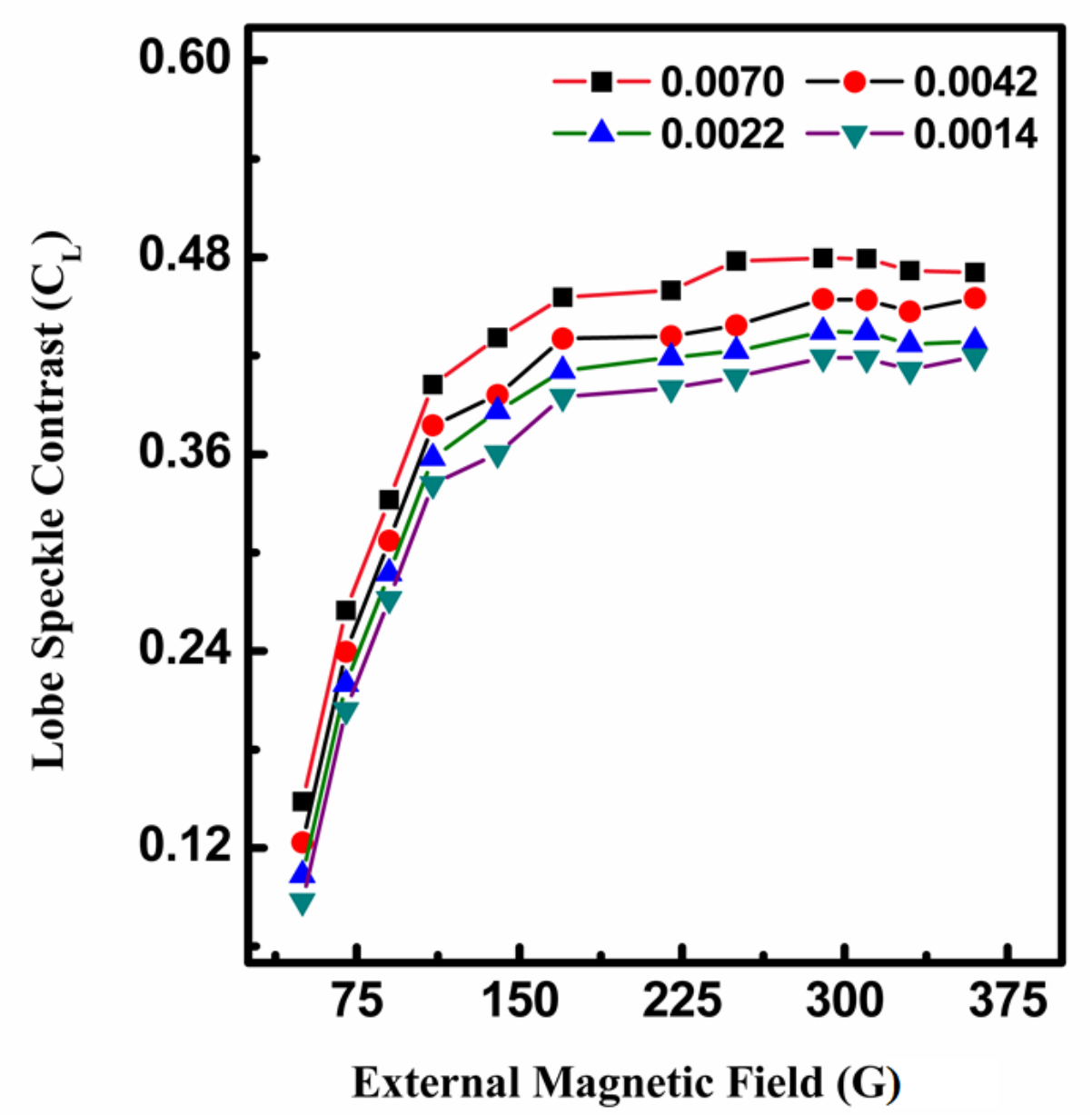

Fig.4.11. Lobe speckle contrast (C_L) as a function of external magnetic fields (B) from nanoemulsion at volume fraction, $\phi \sim$ 0.0070, 0.0042, 0.0022 and 0.0014.

This causes the phase of the scattered waves from the chain-like structures to constructively interfere with reduced fluctuations and ultimately results in an increased speckle contrast. Nevertheless, the C_L value is significantly lower than unity for higher fields (B >150 G) which is due to an increase in surface roughness of the chain like structures owing to zippering

transitions at higher field values. The surface roughness of aggregates increases with *B* that hampers the speckle pattern from being fully developed[296].

4.3.2.2 Angular Speckle Correlation Coefficient

The angular speckle correlation coefficient (C_{ASC}) between the speckle intensities at two different angles (θ_1 and θ_2) can be described by the Equation (4.9) where $I_1^s = I_{\theta_1}^s$ and $I_2^s = I_{\theta_2}^s$. C_{ASC} is calculated by fixing one observation angle (θ_1) and varying the other (θ_2). Figure 4.12 shows the variation of C_{ASC} as a function of observation angle.

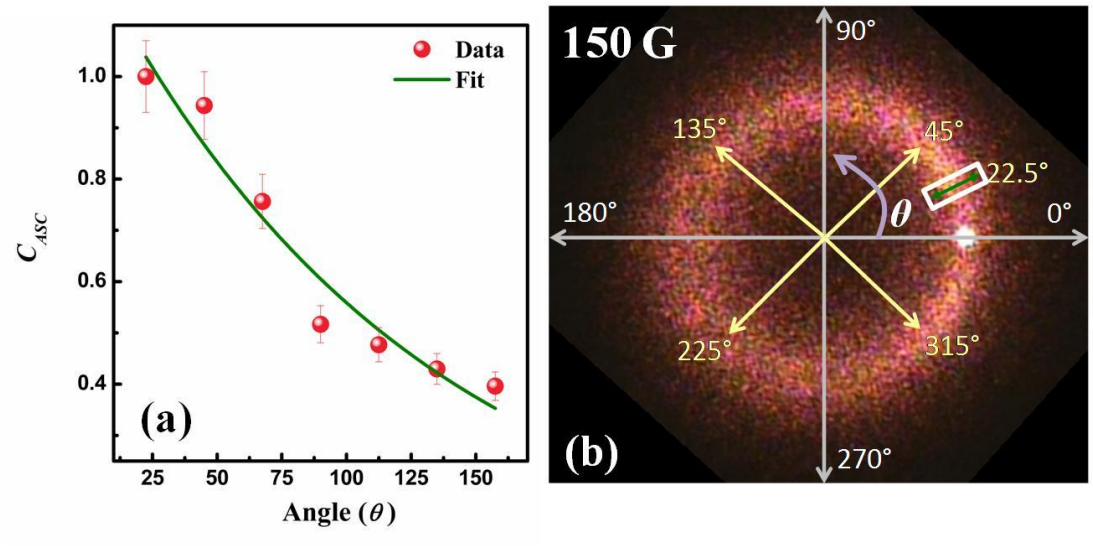

Fig.4.12. (a) Variation of the angular speckle correlation coefficient (C_{ASC}) as a function of observation angle (θ). The best fit is given by $C_{ASC} \sim \exp(-0.0079\theta)$ where θ is the observation angle. (b) Image shows the transmitted light pattern for nanoemulsion of volume fraction , $\phi \sim 0.0042$ at external field, B=150G and the angular position of the detector.

To avoid the bright transmitted spot, forward transmission direction (0^0 or 360^0) was not considered in the present study. In Figure 4.12, first observation angle (θ_1) is fixed at 22.5^0 and the second observation angle (θ_2) is varied from 22.5 to 157.5^0 in steps of 22.5^0. The image in

Figure 4.12(b) shows the ring like transmitted intensity pattern for nanoemulsion of $\phi \sim 0.0042$ at 150 G, where the angular position of the detector is also shown. The C_{ASC} decays exponentially with observation angle as $C_{ASC} \sim \exp(-0.0079\theta)$, where θ is the angle as shown in Figure 4.12(b). Similarly, considering the first observation angle at 337.5^0 (fixed) and varying the second observation angle from 337.5 to 202.5^0 in steps of 22.5^0, we obtained the C_{ASC} values as a function of θ in the opposite direction and it was observed that C_{ASC} decays with θ exactly in the same manner. Hence, our study shows that angular speckle correlation distribution is symmetric on either side of the transmitted bright spot. The degree of spectral speckle correlation coefficient depends on the surface roughness, wavelength difference, incident angle and number of independent scattering cells in the illuminated region [337]. Figure 4.12(a) shows the angular speckle correlation coefficients calculated at a fixed external magnetic field, where the increase in surface roughness of the scatterers is not significant.

4.4 Conclusions

The behavior of transmitted light speckle pattern from ferrofluid and nanoemulsion in presence of an external magnetic field is presented in this chapter. The variation of transmitted light speckle parameters with external magnetic field is attributed to the changes of dimension and surface roughness of the field induced aggregates. The external field induced decay of degree of coherence and variation of phase fluctuations of the scattered light waves due to the enhancement of surface roughness greatly affects speckle pattern on the transmitted light spot in ferrofluid. The speckle contrast of transmitted light spot (in ferrofluid) and lobe part (in nanoemulsion) increases with external magnetic field which indicates a transformation from dynamic to nearly static speckle pattern due to the formation of chain-like structures from nano sized particles undergoing Brownian motion in the dispersion medium. The surface roughness of the field induced aggregates in both the systems hampers the speckle pattern from being

'fully developed' (speckle contrast < 1 at higher external field). In ferrofluid, the percent of depolarization of the scattered wave-fields decreases with an increase in the number of field induced aggregates. Also, the transmitted speckle correlation coefficient shows a power law decay with external magnetic field in ferrofluids. For nanoemulsion, the angular speckle correlation coefficient decays exponentially with difference between the measurement angles in the observation plane and the angular speckle correlation is found to be symmetric on either side of the transmitted bright spot.

Chapter V Magnetic Field Dependent Backscattering of Light in Water Based PAA Covered Fe_3O_4 Nanofluid

5.1 Introduction

Wave propagation through ordered and weakly disordered scattering media have been explored in the paste [341-344]. Experimentally, the phenomenon of weak localization of light has been widely studied in coherent backscattering from colloidal suspension [345], cold atom gases [346], disordered liquid crystals [347], disordered micro cavities [348], etc. Also, the backscattering and vanishing of energy transport velocity have been studied by Pinheiro *et al* [225, 226]. The interaction of light with disordered particles provides new ways to probe nonlinear optical effects, optical bistability, etc. which are important for the future technologies such as bistable switching devices, neural optical computers, etc..

In this chapter, we probe the magnetically induced changes in backscattered light intensity and speckle profiles in ferrofluid during structural transitions. First, the external field induced variations of backscattered speckle pattern and speckle contrast are analyzed. Then the possible reasons for the field induced changes in the backscattered light intensity and its angular dependence are investigated. Subsequently, the tuning behavior of backscattered light intensity is also discussed.

5.2 Experimental Details

The details of the ferrofluid samples used in this study are explained in Chapter II (section 2.2). The backscattered light intensity is measured as a function of *B* using the experimental set up shown in Figure 2.4. The direction of *B* was perpendicular to the incident light direction in this case. The experimental details for acquiring the backscattered light intensity and speckle patterns from the samples as a function of *B* are explained in Chapter II (section 2.3).

5.3 Results and Discussions

5.3.1 Field Induced Backscattered Speckle Dynamics in Ferrofluid

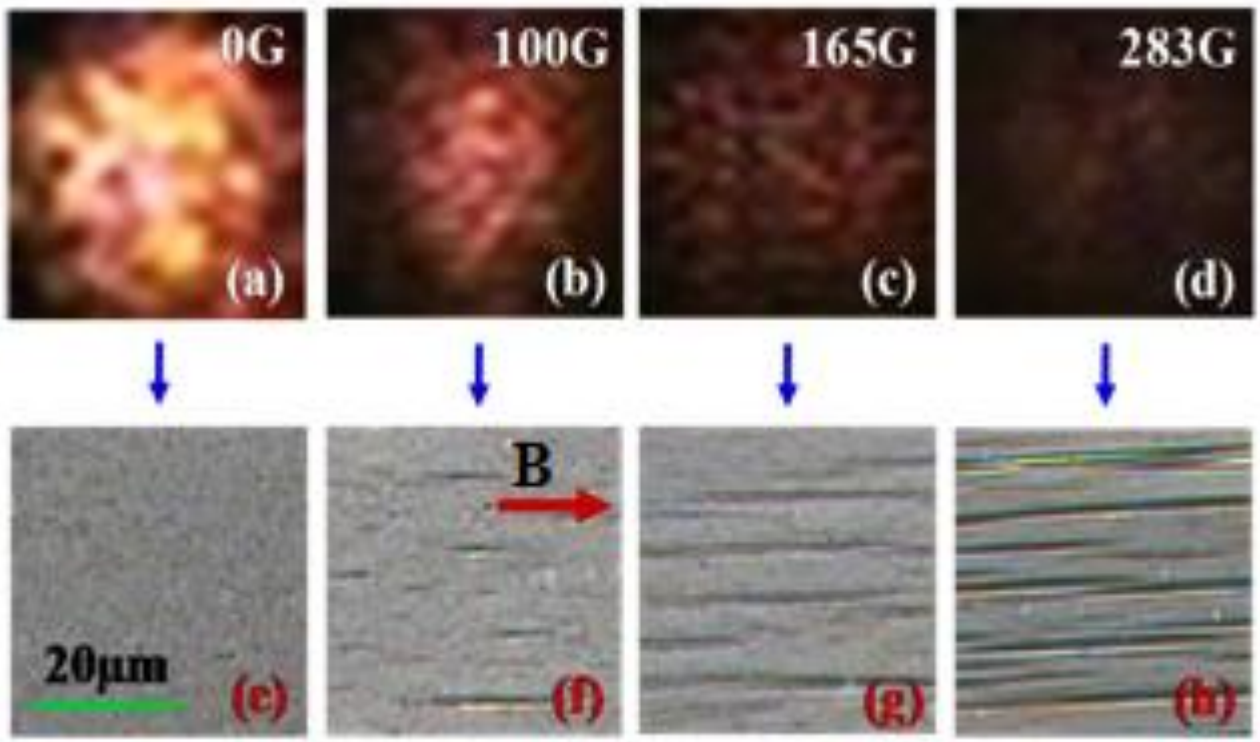

Fig. 5.1. (a - d) Images of backscattered light from ferrofluid at different external magnetic fields (B = 0, 100, 165, 283 G) and the corresponding (e - h) phase contrast microscopic images of ferrofluid at the same external fields.

Figure 5.1 (a – d) show the images of backscattered light from ferrofluid in presence of different magnetic field values of 0, 100, 165 and 283 G. It is observed that the light intensity diminishes with increasing B. Figure 5.1 (e - h) shows the phase contrast microscopic images of ferrofluid observed under similar B. In the presence of B, the magnetic nanoparticles in water form aligned structures when the magnetic coupling constant, Λ_{coup} (Eq. 3.3 in Chapter III) is much greater than one. The speckles observed in the backscattered light images are shown in Figures 5.1 (a – d). As λ (~ 632.8 nm) and beam width $(\sim 1mm)$ of the incident light are larger than the size of the nanoparticles (diameter, $d \sim 15nm$), constructive and destructive

interferences of the scattered light wavelets from all possible scattering trajectories produce intensity fluctuations, which are called speckles, as shown in Figures 5.1 (a-d). The speckle pattern resulting from a medium is its fingerprint and is being exploited in speckle imaging or diffuse wave spectroscopy [244, 308, 309]. Piederriere *et al.* [349] have shown that the backscattered speckle size (produced by strongly-scattering liquid media such as monodisperse polystyrene microspheres in solutions, mixtures of different sized microspheres, milk, blood and pig skin) depends on the scattering and anisotropy coefficients. The backscattered light images [Fig. 5.1 (a-d)] from ferrofluid show that the speckle intensities diminish with increasing *B* as the nanoparticles form long chains [Fig. 5.1 (e – h)].

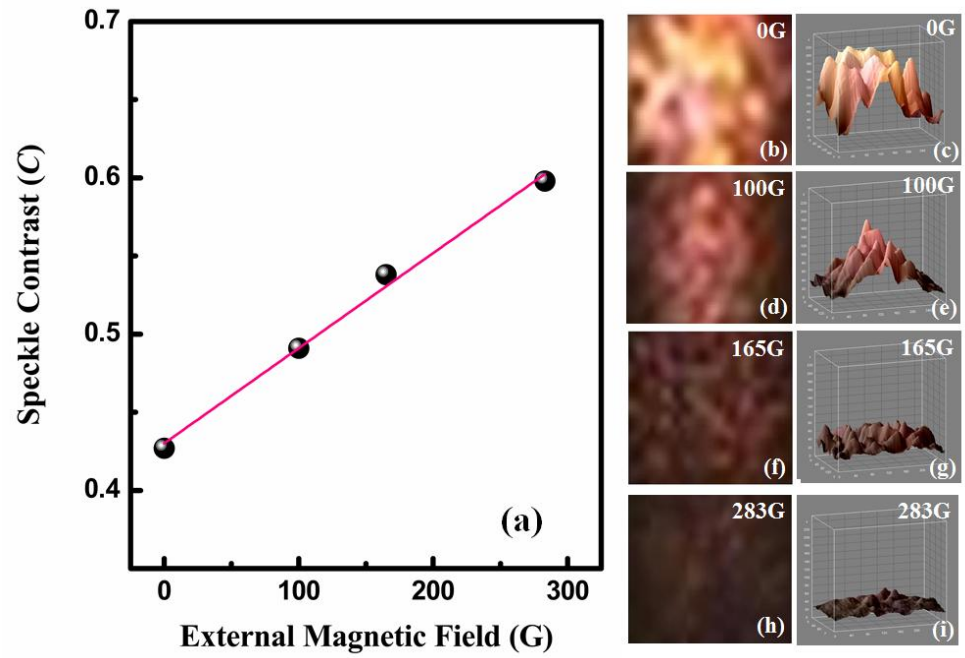

Fig. 5.2. (a) Variation of speckle contrast (*C*) of backscattered speckles with external magnetic fields (*B*). Images (b, d, f, h): backscattered light at different external magnetic fields from ferrofluid and images (c, e, g, i) are the corresponding 3D surface plots.

Figure 5.2(a) shows the variation of *C* of the backscattered light with *B* which is calculated by using the intensity values at different fields shown in the images (c, e, g, i) of Figure 5.2 and by using Equation 4.5 (Chapter IV). The linear increase in the backscattered *C* with *B* indicates a transformation of 'dynamic' to nearly static speckle pattern due to the formation of chainlike structures.

5.3.2 Field Induced Variations of Backscattered Light Intensity and Possible Reasons for Extinction of Backscattered Light

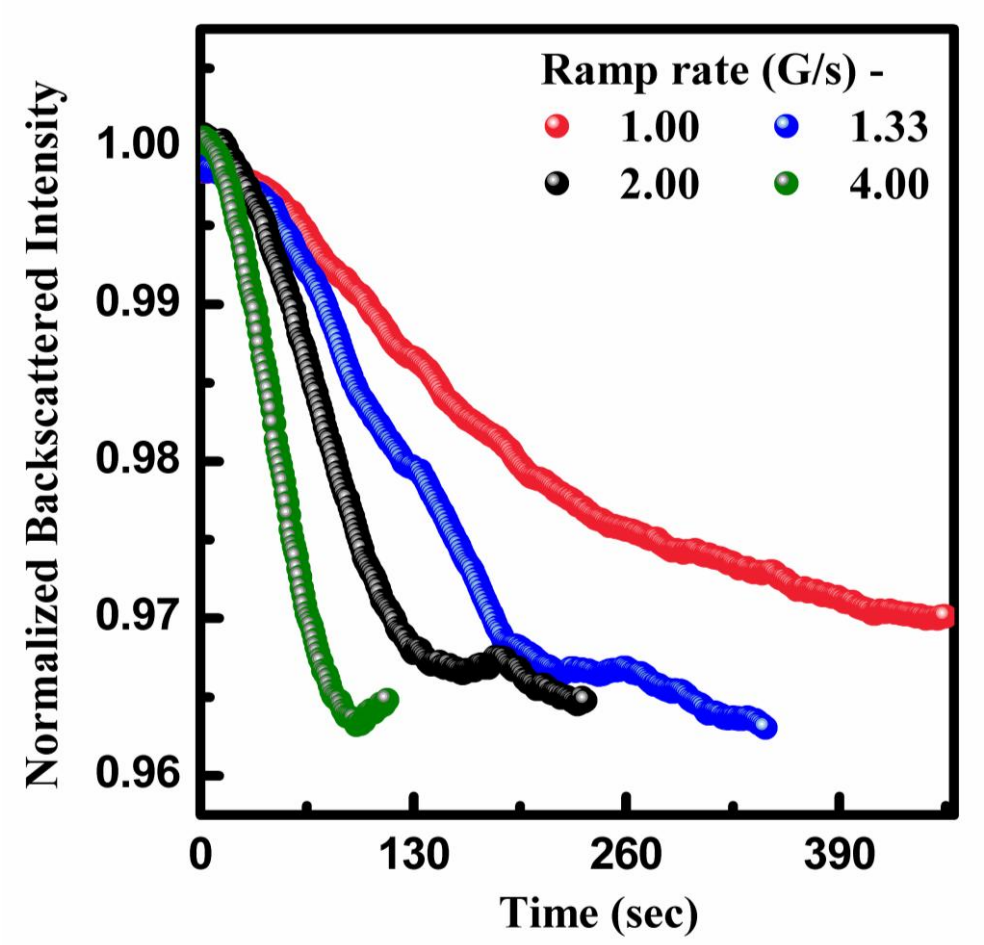

Fig. 5.3. Variation of backscattered light intensity as a function of time (*t*) at different magnetic field ramp rates. Backscattered angle, $\theta_b = 179.8^0$, $\phi \sim 0.00816$.

Figure 5.3 shows the backscattered light intensity from ferrofluid as a function of time for different field ramp rates, at a fixed backscattering angle ($\theta_b = 179.8^\circ$) and ϕ = 0.00816. The backscattered light intensity decreases in presence of *B* and the rate of decrease is found to be faster for higher field ramp rates. The possible reasons behind the lowering of backscattered light intensity with *B* are discussed below.

In absence of *B*, the ferrofluid behaves as a disordered soft matter with no birefringence or circular dichroism [61, 218]. The application of magnetic field induces magneto-optical anisotropy such as birefringence, transmittivity, Faraday rotation and Cotton-Mouton effect [350, 351]. Theoretical studies show that coherent backscattering is altered by Faraday rotation and natural optical activity in a medium of inhomogeneities smaller than the wavelength [352, 353]. Experimental observation shows that the maximum Faraday shift is ~2^0 at *B* = 150 Gauss [183]. Such shift can affect the backscattering but it does not cause such a dramatic change of backscattered light intensity. Also, optical absorption studies in ferrofluid show the absence of absorption peaks in the visible region and hence in the weak *B* (0 < *B* < 600 G) region, absorption does not have a role in the extinction of backscattered light [183].

With increasing *B*, the size of the scatterers increases due to dipolar attractions that can result in an increase in the length of ℓ^* [271]. At some critical fields, the scatterer sizes are such that resonances occur in the anisotropy factor $\langle \cos\theta \rangle$ and in the extinction efficiency factor (Q_{ext}) [183]. The field dependent resonant behaviors cause the building up of standing waves inside the scatterer and results in an extra delay in light transmission through ferrofluid. Such resonances might cause the extinction of backscattered light intensity in presence of a magnetic field.

According to Mie scattering theory, the backscattered efficiency (Q_b) is given by[286],

$$Q_b = \frac{1}{(ka)^2}\left|\sum_{n=1}^{\infty}(2n+1)(-1)^n(a_n - b_n)\right|^2 \tag{5.1}$$

where the scattering parameters (a_n and b_n) are given by,

$$a_n = \frac{m_{MF}^2 j_n(m_{MF}x)[xj_n(x)]' - \mu j_n(x)[m_{MF}xj_n(m_{MF}x)]'}{m_{MF}^2 j_n(m_{MF}x)[xh_n^{(1)}(x)]' - \mu h_n^{(1)}(x)[m_{MF}xj_n(m_{MF}x)]'} \tag{5.2}$$

$$b_n = \frac{\mu j_n(m_{MF}x)[xj_n(x)]' - j_n(x)[m_{MF}xj_n(m_{MF}x)]'}{\mu j_n(m_{MF}x)[xh_n^{(1)}(x)]' - h_n^{(1)}(x)[m_{MF}xj_n(m_{MF}x)]'} \tag{5.3}$$

where, m_{MF} is the external magnetic field dependent refractive index of the ferrofluid [224] and the functions $j_n(z)$ and $h_n^1(z) = j_n(z) + iy_n(z)$ are the spherical Bessel functions of order $n(n = 1,2,...)$ and of the given arguments, $z = x$ or $m_{MF}\,x$, respectively, and primes signify derivatives with respect to the arguments.

The size parameter ($x = ka$) increases with B due to aggregation of nanoparticles. Using Equations (5.1) to (5.3), the backscattering efficiency (Q_b) as a function of $x = ka$ is calculated and is shown in Figure (5.4). The resonant behavior of the backscattering efficiency with size parameter is evident from Figure (5.4). The inset of Figure (5.4) shows the zoomed view at lower *ka* values. Similar Mie resonances in forward-backward anisotropy factor with size parameter have been observed earlier [183]. The external field dependent resonant states in backscattered efficiency and forward-backward anisotropy factor that introduces a delay in light propagation inside the medium due to the formation of standing waves would have resulted in the observed extinction of backscattered light. As the evolution into chainlike structures from magnetic nanoparticles becomes more rapid with increasing magneticfield ramp rate, the rate of decrease in backscattered intensity is more [235].

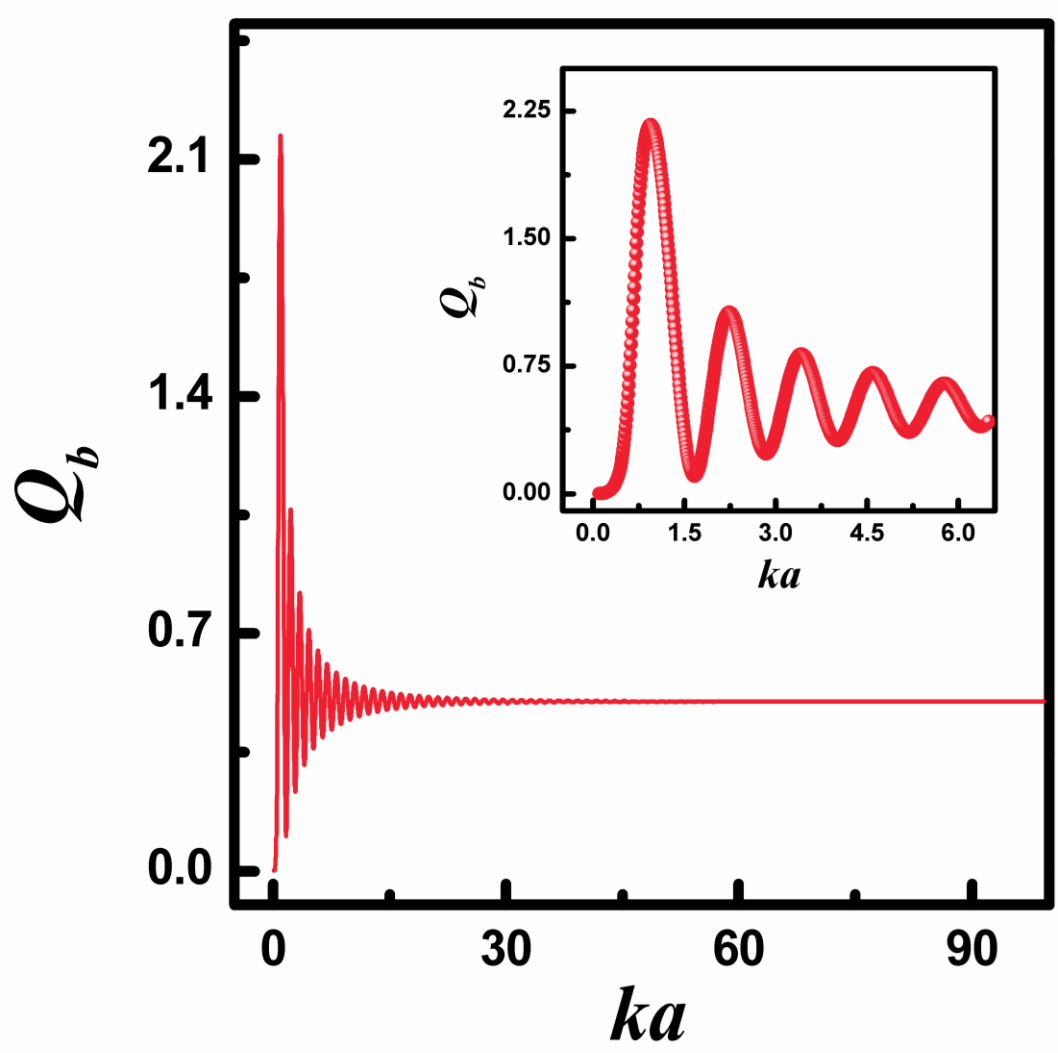

Fig. 5.4. Backscattered efficiency (Q_b) as a function of size parameter (ka). Inset figure shows the enlarged view of variation of Q_b within small values of ka.

5.3.3 Angular Variation of Backscattered Light in Presence of External Magnetic Field

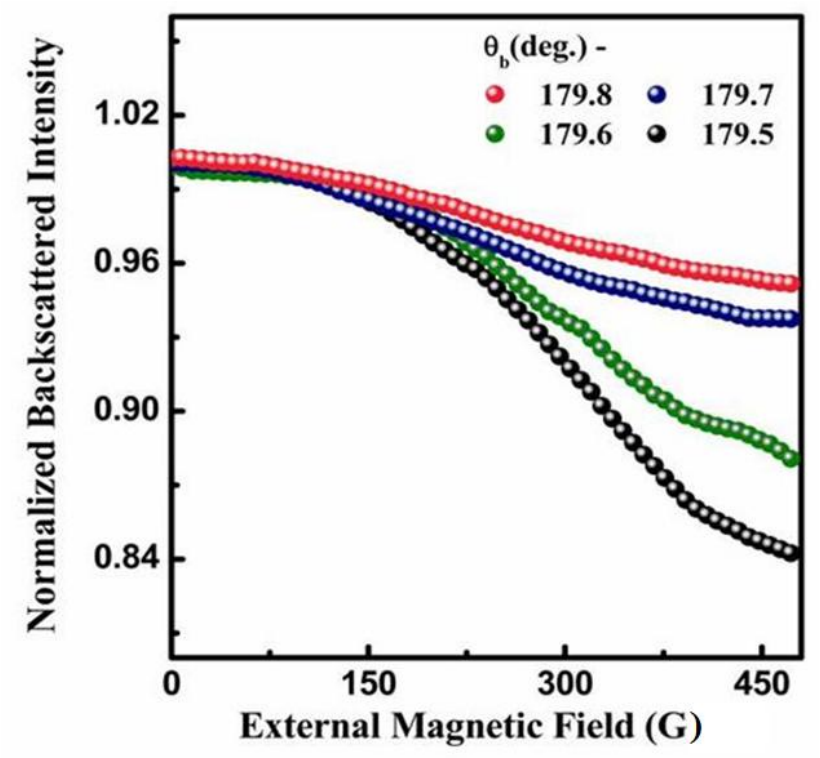

Fig. 5.5. Angular variation of backscattered light intensity from ferrofluid in presence of external magnetic field at a ramp rate of 1 G/s.

The field induced aggregation process in ferrofluid leads to a reduction in the backscattered light intensity within small backscattered angular range [i.e. within $(\theta_b - \Delta\theta_b) < \theta_b < (\theta_b + \Delta\theta_b)$ where $\Delta\theta_b$ is the small angular change from $\theta_b = 180^\circ$]. In Figure 5.5, it is observed that a small change in the backscattered angle leads to large changes in the backscattered intensity.

For an infinite cylinder, by using diffraction theory approximation, the phase function $p(\theta,\varphi)$ which is the function of the total light scattered into a unit solid angle in a given direction (θ,φ) is[286],

$$p(\theta) = \frac{\pi}{4x}\left[\frac{1+\cos\theta}{\pi}\frac{x\sin(x\sin\theta)}{x\sin\theta}\right]^2 \qquad (5.4)$$

For backscattered light from a cylindrical surface, the backscattered phase function $p(\theta_b)$ decreases with change in the backscattered angle.

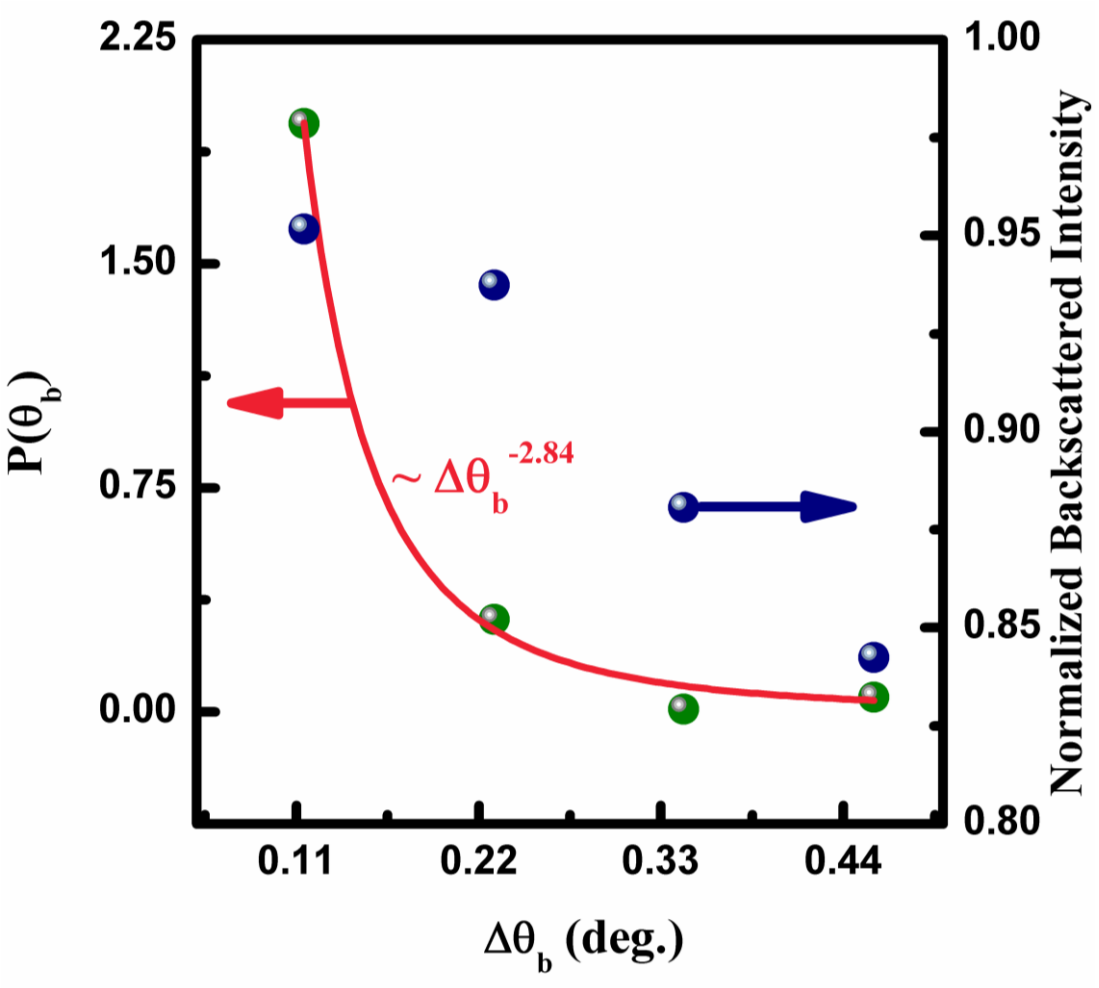

Fig. 5.6. Plot of backscattered phase function $p(\theta_b)$ and backscattered light intensity with $\Delta\theta_b$ from $\theta_b = 180^0$. $p(\theta_b)$ varies as $(\Delta\theta_b)^{-2.84}$ with size parameter, $ka = 1000$. The variation of normalized backscattered light intensity from ferrofluid with $\Delta\theta_b$ from $\theta_b = 180^0$ is measured at $B = 472$G.

Figure 5.6 shows the variation of backscattered phase function $p(\theta_b)$ with $\Delta\theta_b$ where $p(\theta_b)$ decays with $\Delta\theta_b$ as $\sim \Delta\theta_b^{-2.84}$ for fixed size parameter, $x = 1000$. The variation of backscattered light with change in backscattered angle ($\Delta\theta_b$) for an external field, *B* = 472 G (obtained from Figure 5.5) also shows decay behavior with $\Delta\theta_b$, though considerable deviation from the theoretical curve [$p(\theta_b) vs. \Delta\theta_b$] is observed. Therefore, the observed decrease in the backscattered phase function $p(\theta_b)$ with an increase in $\Delta\theta_b$ is in reasonable agreement with the theory. This explains the angular dependence of backscattered light intensity in presence of *B*.

5.3.4 Tunability of Backscattered Light

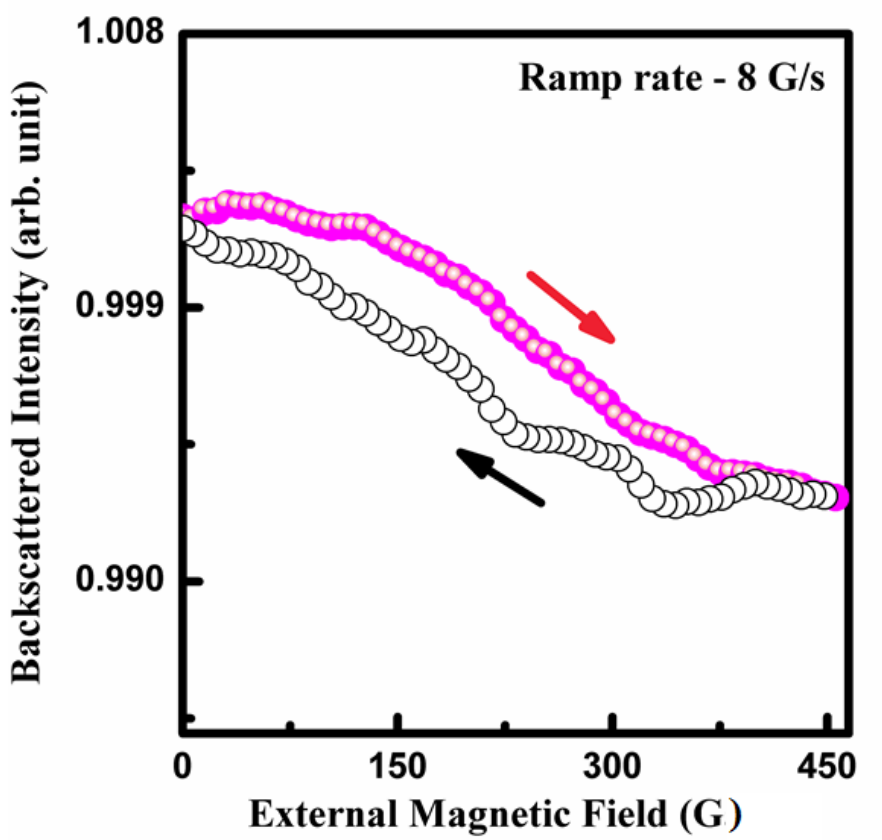

Fig.5.7 Tunable backscattering of light from ferrofluid in presence of external magnetic fields with θ_b = 179.8^0 and field ramp rate 8 G/s.

Figure 5.7 shows the field induced tunable behavior of backscattered light from ferrofluid. Here, the measurements are done in presence of *B* on ferrofluid of ϕ = 0.00816 at fixed θ_b = 179.8^0 and ramp rate (8 G/s). The backscattered light intensity recovers to the original level with a small hysteresis. This result shows that the aggregation process is reversible. The area between the intensity curves during the 'increase' and 'decrease' is defined as the hysteresis area. Physically, the variation of hysteresis area between the 'increase' and 'decrease' of external field is due to the difference in the aggregate size during these processes. During 'increase', nanoparticle aggregates are formed, which de-aggregate upon removal of the external field because of the dominance of thermal energy due to Brownian motion. The initial time (t_c) for two particles to aggregate is $t_c = \frac{a}{5}\frac{6\pi a\eta}{F_{\max}}((\frac{r_1}{2a})^5 - 1)$ where the magnetic force between the particles at contact is given by $F_{\max} = \frac{\mu_0}{4\pi}\frac{3m^2}{8a^4}$, r_1 is the initial separation distance between the particles and η is the viscosity of the carrier liquid[235, 282]. The time required for aggregation of the particles and linear aggregates in a carrier liquid for a given external field depends on two competing forces experienced by them: the magnetic force due to field induced magnetic moment and the viscous force. The magnetic force depends on the particle size, number of particles in the linear aggregates and external field strength, whereas the viscous force depends on the particle or aggregate size and viscosity of the carrier liquid. Therefore, for a given sample concentration, the aggregation time changes with the change of external field strength. The dispersed magnetic particles in a carrier liquid can relax either by particle rotation in the liquid by Brownian relaxation with a rotational diffusion time given by $\tau_B = 3V_h\eta/k_BT$, where V_h is the hydrodynamic particle volume and η is the viscosity of the carrier liquid. The rotation of the magnetic vector within the particle by Neel relaxation

mechanism occur with a characteristic time (τ_N) is $\cong \frac{1}{f_0}\exp(\frac{KV_m}{k_BT})$ for $\frac{KV_m}{k_BT} << 1$, where f_0 is the attempt frequency of magnetization, K is the anisotropy constant of the material, and V_m is the magnetic volume of the particle [59, 82, 354]. The typical Brownian and Neel relaxation times for the dispersed particles in the present ferrofluid are about 10^{-7} and 10^{-9} s, respectively. The value of τ_N increases sharply with the size of the particle due to the exponential dependence on V_m. This reversible behavior of backscattered light intensity with external magnetic field provides a new approach to fabricate tunable photonic devices using ferrofluid.

5.4 Conclusions

The evolution of backscattered speckle pattern during field induced structural arrangements of magnetic nanoparticle dispersion is investigated experimentally for the first time. The backscattered speckle contrast increases towards its saturation value with external field, which signifies a nearly static speckle pattern by losing the scatterers movement due to aggregation. The backscattered light intensity decreases with external magnetic field due to the delay in the light propagation inside ferrofluid owing to the formation of standing waves inside the scatterers. It is observed that a small change in backscattered angle gives rise to a large variation in the backscattered light intensity in the presence of an external magnetic field. The reversibility in the backscattered light intensity offers possibilities of exploiting such ferrofluids for photonic device applications.

Chapter VI Probing the Magnetic Field Dependent Structural Transitions in Nanoemulsion by Near Infrared Light Absorption

6.1 Introduction

Absorption is the study of interaction of waves with matter, which is probably the most widespread and precise analytical technique used to study isolated atoms, molecules, small clusters in gas, condensed phases, bio molecules, and the structures and dynamics of quantum systems from atomic domain to natural proteins[355-357]. Infrared absorption spectroscopy is a powerful technique for in-situ analysis of chemical, bio-medical and nano-fluidic systems [358-360]. Aggregation processes of dielectric and metal nanoparticles were also studied using infrared absorption spectroscopy [361, 362]. Saito *et al.* [185] measured the optical attenuation constants of magnetic nanofluid at infrared region during field induced aggregation of magnetic nanoparticles in dispersion.

Recently, optical properties of nanofluids have been a topic of intense research due to their fascinating properties and interesting applications [63, 199, 222, 320, 363]. Among nanofluids, magnetic nanocolloid possess the unique property of tunability of particle interaction by external magnetic field, which makes it an attractive candidate for fundamental research and has enormous applications in optical domain [150, 152, 160, 229, 271, 364, 365]. Extinction coefficient of magnetic fluids has been studied in detail using spectral transmittance approach and molecular dynamics simulation where it has been shown that the extinction coefficient increases with increasing particle volume fraction and particle diameter (for a fixed volume fraction) [366, 367]. Heterodyne interferometry technique has also been used for studying the low magnetic field induced tiny variations in the complex refractive index for anisotropic and opaque magnetic fluid thin film specimens [368].

In this chapter, the behavior of near infrared (NIR) photon absorption by a magnetically polarizable oil-in-water emulsion or nanoemulsion in presence of an external magnetic field is

studied. The near infrared absorption as a function of sample volume fraction and external magnetic field is probed. Also, using the near infrared absorption profile in the Rayleigh regime, the imaginary part of the refractive index (k_1) of magnetic nanoemulsion, that depends on the sample volume fraction and external magnetic field, is evaluated for the first time.

6.2 Experimental Details

The nanoemulsion samples used in this study is a disordered magnetic medium as explained in Chapter II (section 2.2). The detailed procedure of acquiring the absorption spectra through the samples as a function of *B* is explained in Chapter II (section 2.4). Here the direction of incident light is parallel to the direction of *B*.

6.3 Results and Discussions

6.3.1 Near Infrared (NIR) Light Absorption by Nanoemulsion

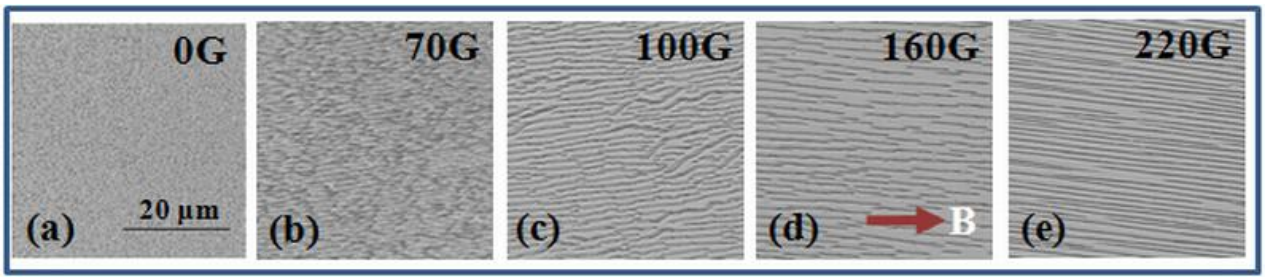

Fig. 6.1. Phase contrast microscopic images of nanoemulsion at different external magnetic fields (*B* = 0, 70, 100, 160, 220G).

Figure 6.1 shows the phase contrast microscopic images of the nanoemulsion observed at different *B* (0 to 220 G). The direction of *B* is shown by the arrow. It can be seen that at zero field the nanoemulsion droplets are randomly oriented and as *B* increases, the droplets orient themselves along the direction of *B* leading to a chain like structure. In magnetic nanoemulsion, oil droplets are electro-statically stabilized with sodium dodecyl sulphate (SDS). When the droplet double layer is very thin ($\kappa a_1 < 5$), the electrostatic force profile follows the equation

$$F_{\eta}(r_1) = 4\pi\varepsilon_1\zeta_0^2 a_1^2\left[\frac{\kappa}{r_1} + \frac{1}{r_1^2}\right]\exp[-\kappa(r_1 - 2a_1)] \tag{6.1}$$

where $a_1 (= \frac{d}{2})$ is the droplet radius, r_1 is the droplet separation distance, ε_1 is the dielectric permittivity of the suspending medium, ζ_0 is the electrical surface potential and κ is the inverse Debye length that depends on the electrolyte concentration (C_e) and can be represented as $\kappa^{-1} = \left(\frac{1}{4\pi}\right)\left[2L_B^2 C_e\right]^{-0.5}$, where '$L_B$' is the Bjerrum length [62, 64].

In presence of *B*, when the ratio of the dipolar interaction strength to thermal energy, is much greater than one $(\Lambda_{coup} >> 1)$ (as discussed in Chapter III, Section 3.2.1), the nanoemulsion droplets in dispersion undergo an disorder-order transition, i.e. Brownian to a linear chain-like structure- with head-on aggregation along the *B* direction which is shown in Figure 6.1.

Figure 6.2(a) shows the absorption of near infrared (NIR) photons by nanoemulsion as a function of photon energy (*E*) for $\phi = 0.0014, 0.0019, 0.0022, 0.0067$ in the absence of *B*. Here, the absorption linearly increases with *E* and ϕ, which indicate that absorption increases with the number density (ρ_n) of nanoemulsion droplets in the dispersion ($\phi = \rho_n \upsilon$, where υ is the droplet volume [369]).

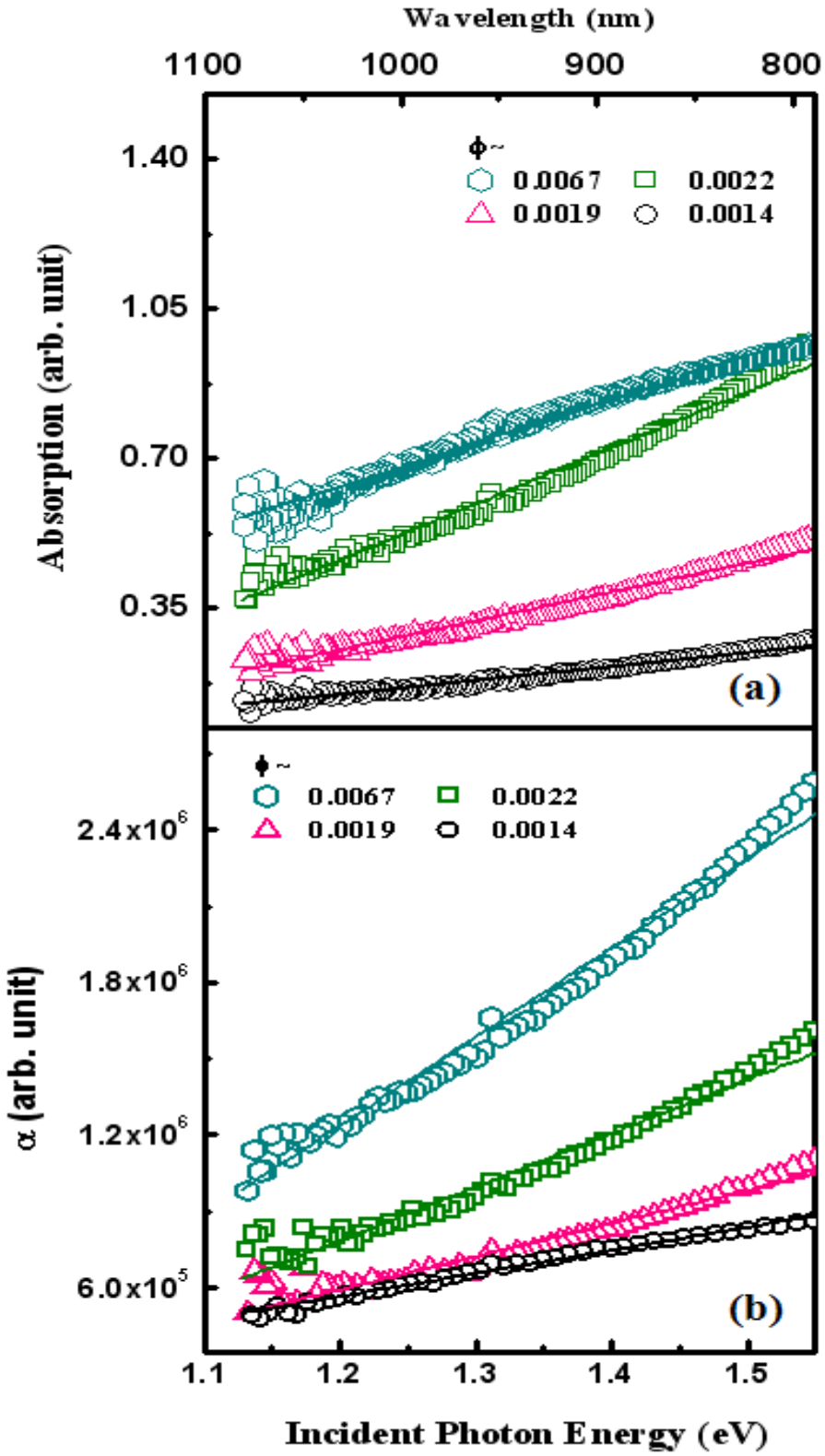

Fig. 6.2. (a) Near infrared (NIR) photon absorption (*A*) with photon energy (*E*, in eV) at zero external field by nanoemulsion with different volume fraction, ϕ = 0.0067, 0.0022, 0.0019,

0.0014. Solid lines correspond to linear regression analysis of the experimental data. (b) Absorption coefficient (α) as a function of photon energy at different ϕ = 0.0067, 0.0022, 0.0019, 0.0014 of nanoemulsion. Solid lines correspond to linear regression analysis of the calculated data from (a).

Here the emulsion droplet size $(d \sim 220\,\text{nm})$ is much smaller than the λ of the NIR photons ($\lambda = 800-1100\,\text{nm}$) and according to Rayleigh scattering theory $(d < \lambda)$, the absorption cross-section (C_{abs}) is given by the relation: $C_{abs} = \alpha\upsilon$, where, $\alpha = \frac{4\pi k_1}{\lambda}$ is the absorption coefficient, k_1 is the imaginary part of the refractive index ($m = n_1+ik_1$) of the nanoemulsion [286]. The real part of the refractive index (n_1) of the nanoemulsion indicates the speed and the imaginary part (k_1) signifies absorption losses during the propagation of an electromagnetic wave through the medium [286]. The absorption cross-section is related to the *E* as

$$C_{abs} = \frac{4\pi\upsilon k_1}{hc} \times E \tag{6.2}$$

where *h* is the Plank's constant. It is clear from Equation 6.2 that C_{abs} increases linearly with increasing *E* in the Rayleigh regime. It is evident from Figure 6.2a that the higher energy infrared photon causes more absorption for all ϕ (=0.0067, 0.0022, 0.0019, 0.0014) of the nanoemulsion samples. It must be noted that, Figure 6.2a actually shows that absorption (*A*) increases with ϕ and the relation between *A* and α is [370]

$$\alpha = \frac{2303A\rho_n}{\phi L} \tag{6.3}$$

where ρ_n is the density of the nanoemulsion droplet and *L* is the optical path length (~1mm). From Equations 6.2 - 6.3 it is evident that *A* is directly proportional to α and C_{abs}.

Figure 6.2b shows α as a function of E for the nanoemulsion specimens of four different ϕ. α values are obtained from the absorption values (Fig. 6.2a) using Equation 6.3. It can be seen from Figure 6.2b that α increases with ϕ due to the increase in number density of the nanoemulsion droplets. It is further observed from Figure 6.2b that α increases linearly with E which is expected from Equations 6.2 – 6.3. The solid lines in Figure 6.2b indicate the linear regression analyses of the experimental data and the slopes of these linear fits provide the average values of the imaginary part of the refractive index (k_1) of nanoemulsion samples.

6.3.2 Magnetic Field Dependent NIR Light Absorption by Nanoemulsion

Figures 6.3 a & b show absorption (A) as a function of incident photon energy (E) for a nanoemulsion of $\phi = 0.0019$ in the presence of B. As B increases from (0 to 60G), A is found to increase over the entire energy range. But from 70 to 250G, the A of NIR photons decreased. Figure 6.3c shows the linear increase of absorption (A) with E (eV) at different B (= 0, 45, 50, 60 G). This figure is similar to Figure 6.2a, where A linearly increases with E. But beyond 65 G, the variation of A with E is not linear (Fig. 5.3b). Hence, from Figure 6.2a and Figure 6.3c it can be inferred that the field induced increase in A up to 65 G follows Rayleigh scattering theory (scatterer size < λ).

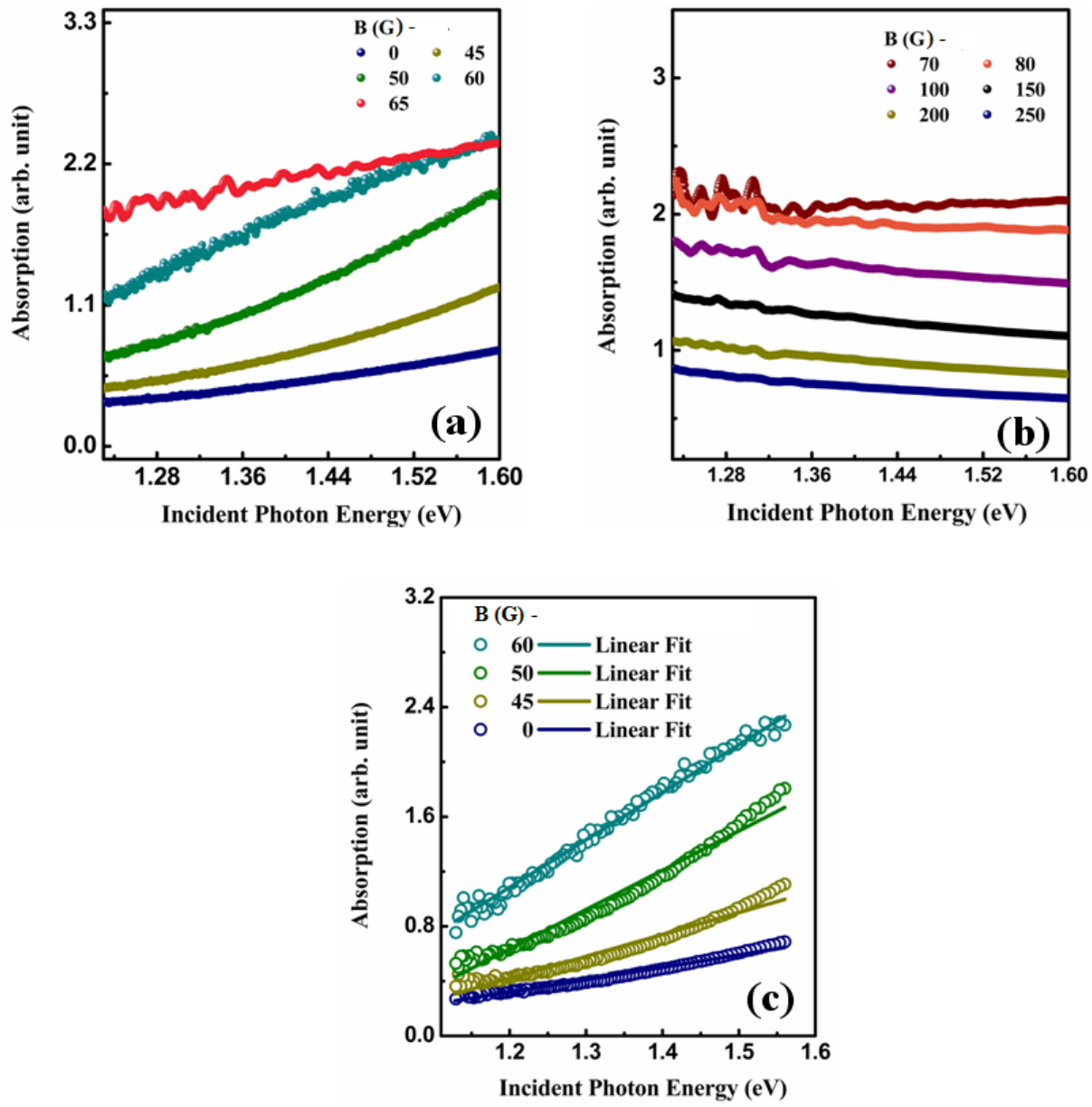

Fig. 6.3. Absorption (A) as a function of incident photon energy (E, in eV) at different external magnetic fields (B) by nanoemulsion ($\phi \sim 0.0019$). (a) B varies from 0 to 65G , (b) B varies from 70 to 250G , and (c) A vs. E plot for B = 0, 45, 50, 60G and best linear fit.

According to Rayleigh scattering theory, higher the energy of the incident photon more is the absorption (Eq. 6.2). This is evident from Figure 6.3c under the presence of B (up to 65 G).

The field induced increase in the absorption of NIR photons was also observed with increasing ϕ.

Figure 6.4a shows the absorption of NIR photons as a function of magnetic field for different E at $\phi = 0.0019$. From zero to ~30 G, the increase in absorption is found to be negligible, but beyond 30 G the absorption increases rapidly with B. It has been earlier shown that for very low B (B < 30 G), the nanoemulsion specimen remains opaque and field induced chain like structures do not form [229]. Hence, below 30 G absorption remains almost constant, whereas, for B > 30 G, absorption increases due to formation of external field induced chain like structures. Beyond B ~ 80 G, absorption decreases with B. It is observed that absorption is significantly higher for photons with higher energy up to 65 G. Figure 6.4b shows the continuous evolution of absorption of NIR photons of energies 1.55, 1.46 and 1.38 eV with B where it shows that up to ~ 80 G, absorption of NIR photons increases with B. From Figure 6.4b it can be seen that (i) peak value of absorption increases with increasing E and (ii) the absorption peak shifts to lower B with increasing E. With increasing E, the λ decreases and hence, absorption increases in the Rayleigh regime (Eq. 6.2), which leads to higher absorption peak values with increasing E.

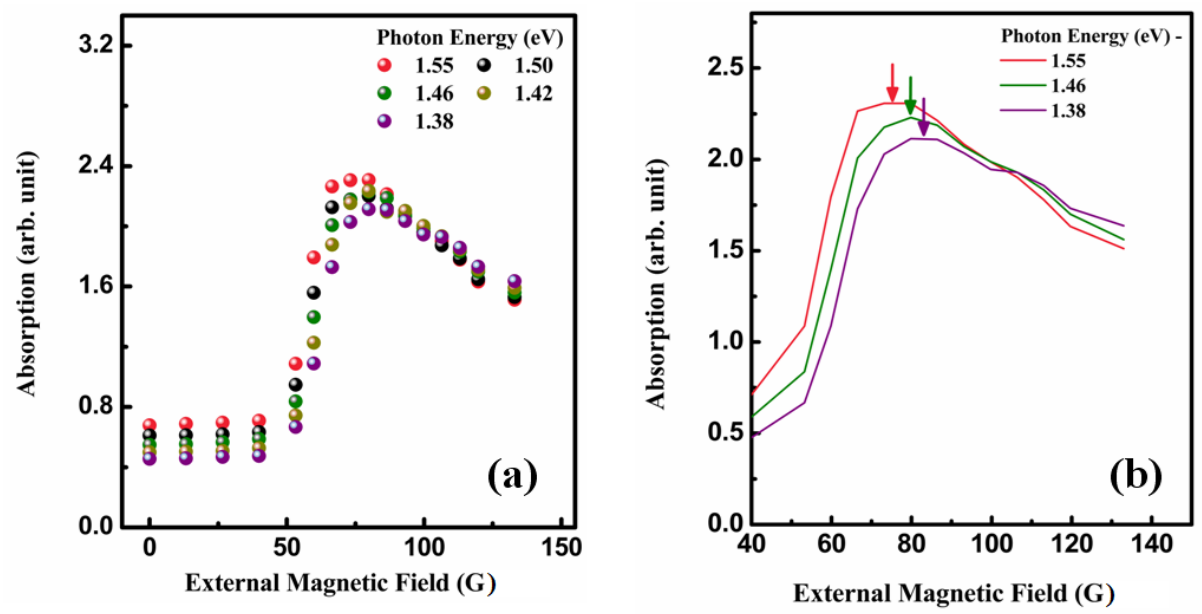

Fig. 6.4. (a) Absorption of different energy (E = 1.55, 1.50, 1.46, 1.42, and 1.38 eV) NIR photons as a function of external magnetic field (B) for nanoemulsion (ϕ = 0.0019). (b) The continuous change of external field induced absorption of NIR photons with energies E = 1.55, 1.46, and 1.38 eV.

The position of the absorption peak for particular E signifies transition from Rayleigh to Mie regime for the corresponding λ. For decreasing E, the field induced aggregate size comparable to the corresponding λ increases and the required B for the Rayleigh to Mie transition also increases. Hence, absorption peak shifts to lower B with increasing E.

6.3.3 Field Induced Variations of Imaginary Part of the Refractive Index (k_1) of Nanoemulsion

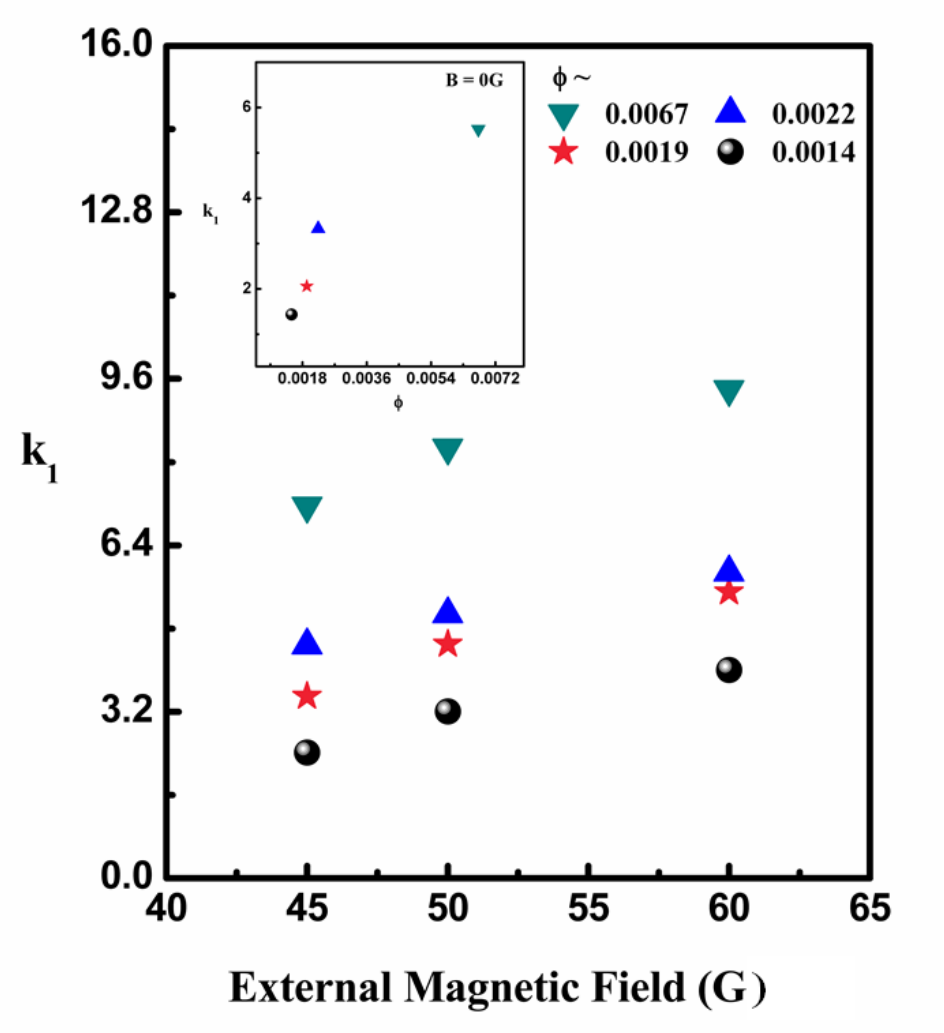

Fig. 6.5. Imaginary part of refractive index (k_1) of nanoemulsion as a function of external magnetic fields for different volume fraction, ϕ = 0.0014, 0.0019, 0.0022, 0.0067. Inset: k_1 as a function of ϕ at zero field.

The k_1 values at different B are obtained from the slopes of the best fit curves of α *vs.* E plots for different B and ϕ (From Fig. 6.3c for ϕ = 0.0019 at different B). In a magnetic nano-colloid

the refractive index depends on the concentration of magnetic nanoparticles in dispersion and *B* [224, 371]. Figure 6.5 shows the variation of k_1 values with *B* at different ϕ. It is observed that k_1 values increase with ϕ at fixed *B* (= 0, 45, 50, 60 G). The inset of Figure 6.5 shows the variation of k_1 as a function of ϕ at zero external field. It is also observed that for a particular volume fraction, k_1 increases with *B*. These observations can be explained by the fact that absorption increases due to two different reasons, viz. increase in number density (i.e. ϕ) of the nanoemulsion and external field induced chain like structure formation. Figure 6.6 shows the plot of the calculated k_1 values with theoretical k_1 values at four different ϕ at zero external field. The slope of the linear regression analysis is nearly unity which shows that the experimentally calculated values are in good agreement with the theoretical values. This shows that NIR absorption profiles can be used for the accurate estimation of k_1 of the nanoemulsion. It must be noted that the above mentioned methodology is valid only in the Rayleigh regime (i.e. for *B* up to 65 G). Beyond Rayleigh regime, the scattering follows Mie theory due to increased sizes of field induced aggregates.

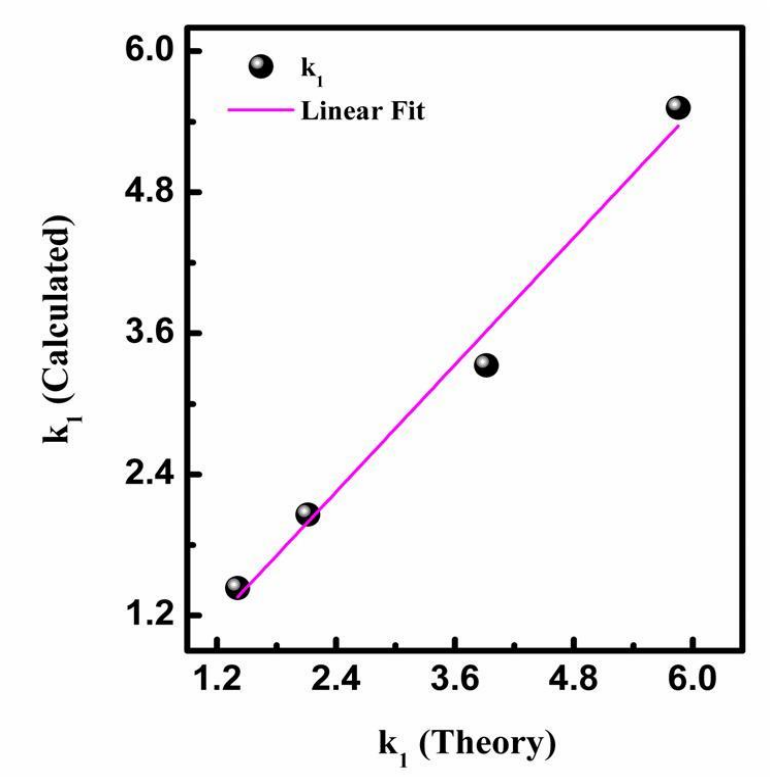

Fig. 6.6. Variation of the calculated values of $k_1$with theoretical values obtained using Eq. 6.2. Slope of the linear fit is $\sim 0.90 \pm 0.07$. Volume fractions, ϕ ~ 0.0014, 0.0019, 0.0022 and 0.0067.

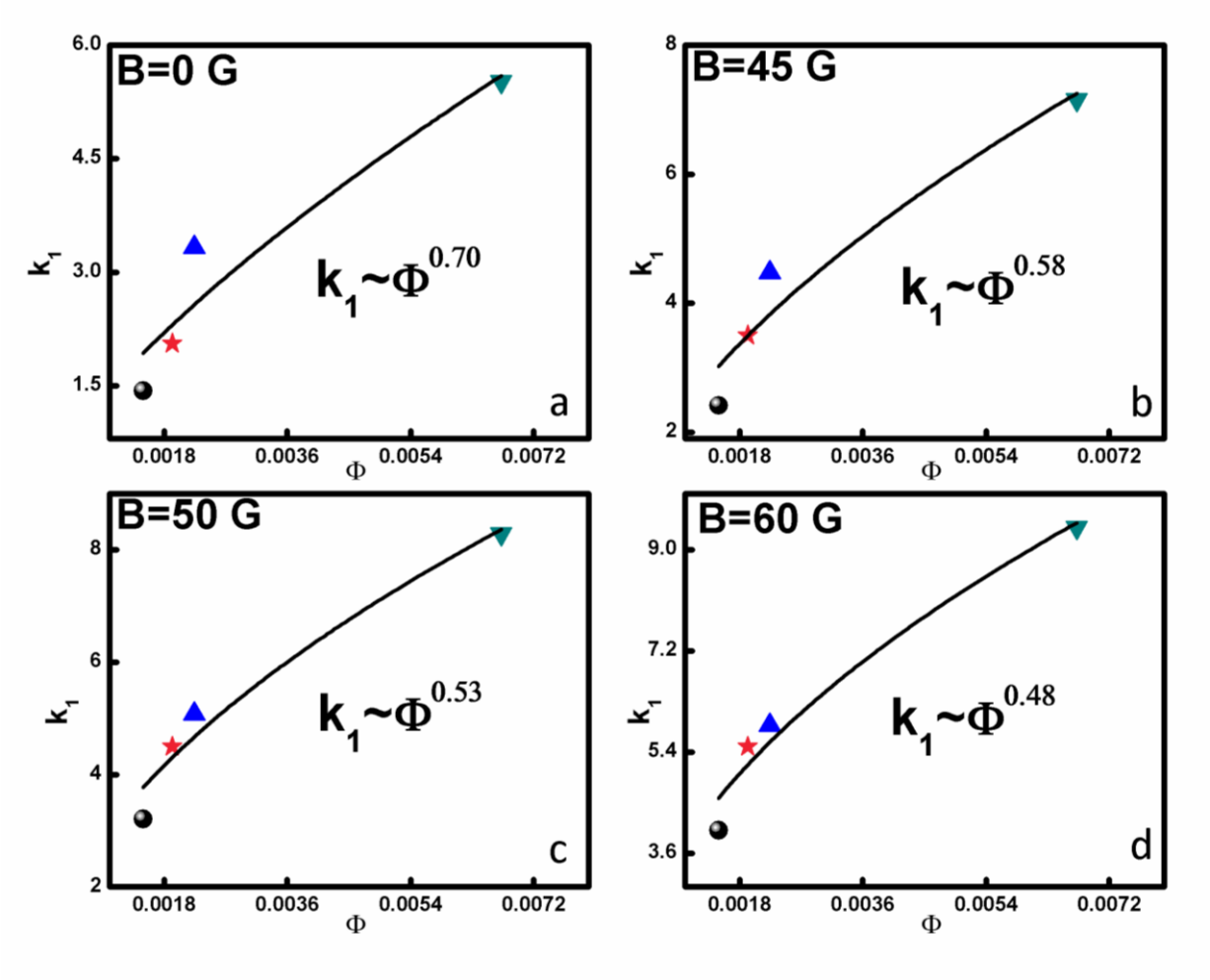

Fig. 6.7. k_1 as a function of ϕ at (a) zero *B*, (b) 45G, (c) 50G, (d) 60G. k_1 follows a power law ($k_1 \sim \phi^p$) dependence with ϕ for different *B*, where the exponent (p) values are 0.70, 0.58, 0.53, 0.48 at 0, 45, 50, 60G, respectively.

Figure 6.7 shows the variation of k_1 with ϕ for different *B*. It can be seen from the Figure that k_1 increases with ϕ for different *B*. It was further observed that the increase in k_1 with ϕ

follows a similar trend in all the cases and the data are fitted using a power law: $k_1 \sim \phi^p$, where the exponents (p) are 0.70, 0.58, 0.53, 0.48 at 0, 45, 50, 60 G, respectively. Figure 6.8 shows the variation of p with B where p decreases linearly with increasing B with a maximum at zero field. In presence of B, the nanoemulsion droplets undergoes a disorder to order transition and chain like structures along the direction of B start growing, which increases the absorption of NIR photons. The decreasing values of p with increasing B indicates the formation of chain like ordered structures and field induced increase in absorption of NIR photons.

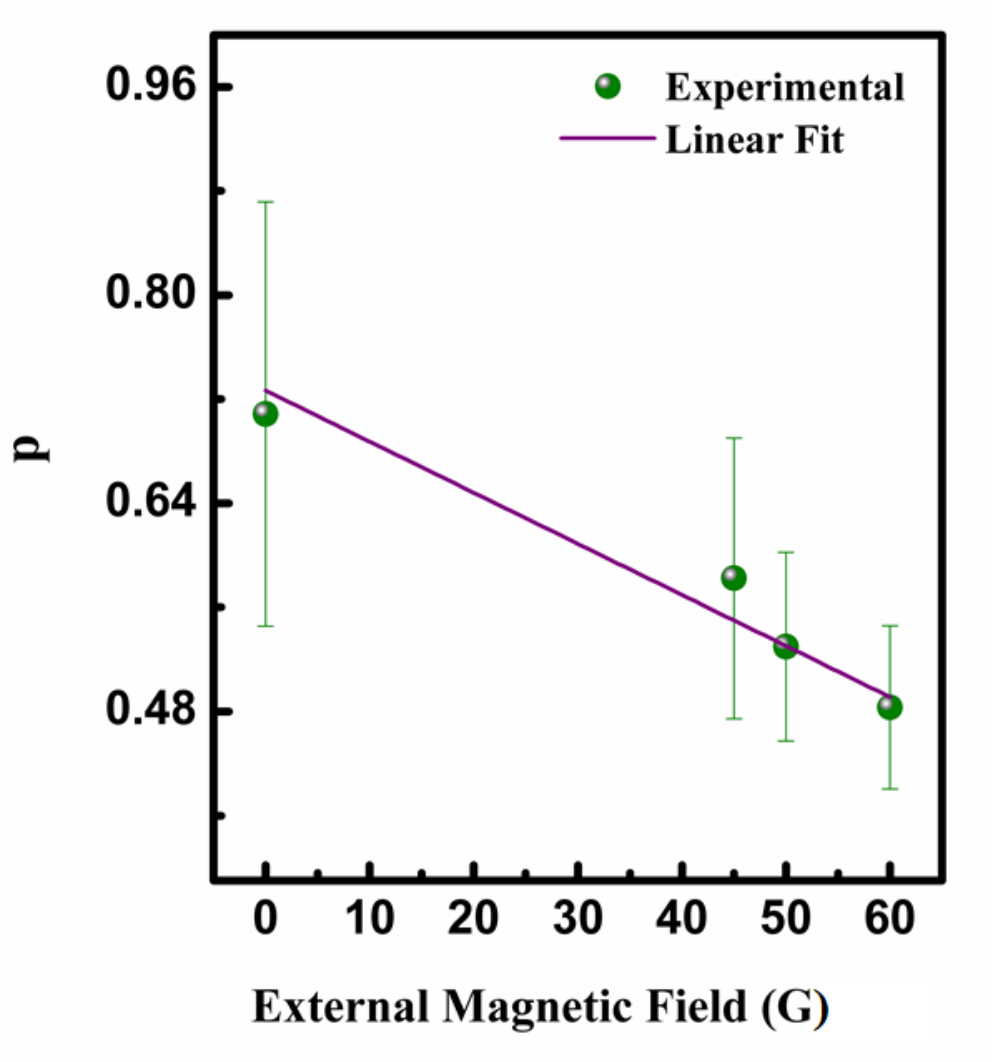

Fig. 6.8. Exponent (*p*) values as a function of external magnetic fields (*B*). Solid line corresponds to linear regression analysis.

6.3.4 Explanation of Magnetic Field Dependent Variations of NIR Light Absorption Based on Mie Theory

The field induced aggregation of nanoemulsion droplets due to dipolar attraction increases the scatterer sizes (Fig. 6.1 b–e) and when the scatterer sizes are comparable to or higher than the λ of NIR photons, the interactions of NIR photons with such scatterers are beyond the Rayleigh regime and fall in the Mie regime.

According to Mie scattering theory, the absorption efficiency (Q_{abs}) is given by [285, 286]

$$Q_{abs} = \frac{4\varepsilon''}{x^2}\int_0^x <|E_1|^2> x'^2 dx' \tag{6.4}$$

where, $x = ka_1$ is the size parameter, ε'' is the imaginary part of the relative dielectric constant of the scatterers, E_1 is the electric field component of the incident near infrared photons and

$$<|E_1|^2> = \frac{1}{4}\sum_{n=1}^{\infty}(m_n|c_n|^2 + n_n|d_n|^2) \tag{6.5}$$

where the Mie scattering parameters are given by

$$c_n = \frac{\mu_1 j_n(x)[xh_n^1(x)]' - \mu_1 h_n^1(x)[x j_n(x)]'}{\mu_1 j_n(m_1x)[xh_n^1(x)]' - h_n^1(x)[m_1x j_n(m_1x)]'} \tag{6.6}$$

$$d_n = \frac{\mu_1 m_1 j_n(x)[xh_n^1(x)]' - \mu_1 m_1 h_n^1(x)[x j_n(x)]'}{m_1^2 j_n(m_1x)[xh_n^1(x)]' - \mu_1 h_n^1(x)[m_1x j_n(m_1x)]'} \tag{6.7}$$

and

$$m_n = 2(2n+1)|j_n(z)|^2,\ n_n = 2n(2n+1)\left\{(n+1)\left|\frac{j_n(z)}{z}\right|^2 + \left|\frac{zj_n(z)}{z}\right|^2\right\}$$

where, m_1 is external magnetic field dependent refractive index of the nanoemulsion [224, 371], μ_1 is the ratio of the magnetic permeability of the nanoemulsion droplets to that of the dispersion medium. The function $j_n(z)$ and $h_n^1(z) = j_n(z) + iy_n(z)$ are the spherical Bessel functions of order n ($n = 1,2,...$) and primes signifies derivatives.

The size parameter ($x = ka_1$) increases with B due to the aggregation of nanoemulsion droplet in the dispersion. Using Equations 6.4 – 6.7, the Q_{abs} as a function of size parameter for three different E (=1.55, 1.46, 1.38 eV) is computed and shown in Figure 6.9.

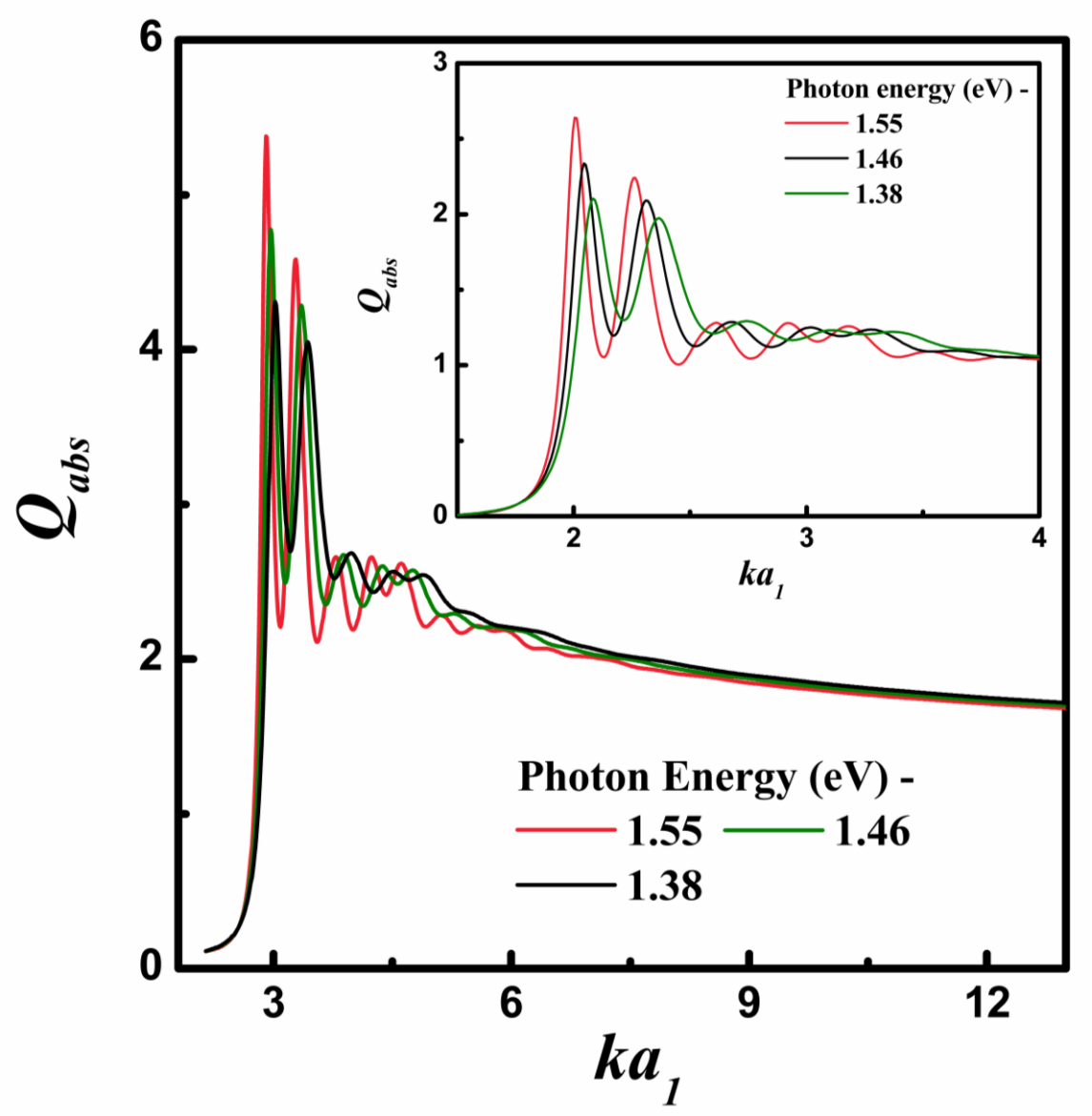

Fig. 6.9. Absorption efficiency (Q_{abs}) as a function of size parameter (ka_1) for different photon energy (E = 1.55, 1.46, and 1.38 eV). Inset: Magnified view of the continuous variation of Q_{abs} with ka_1 for E = 1.55, 1.46, and 1.38 eV.

The inset of Figure 6.9 shows the increasing nature of the Q_{abs} at lower ka_1. At lower values of ka_1, according to the Rayleigh scattering theory, Q_{abs} and C_{abs}, which is directly related to absorption, increase with B, which is in good agreement with the experimental observations (Figs. 6.3 – 6.4). It can be observed from Figure 6.4 that the absorption of NIR photons of different energy increases up to 65G, where the nanoemulsion droplets in the dispersion forms short chain like structures (Figs. 6.1b-c). Beyond B = 65 G, the short chains form longer chain-like structures (Figs. 6.1d-e) along the B direction and absorption starts decreasing (Fig. 6.4). The Q_{abs} for NIR also starts decreasing above $ka_1 \sim 3.79$ (inset of Fig. 6.9). With the increase in B, the chain length increases due to head to tail aggregation of emulsion droplets (Figs. 6.1c-e). Simultaneously, the space between the chains also increases which decreases the effective scattering cross section and Q_{abs}. The decreasing trend in Q_{abs} with size parameter (Fig. 6.9) explains the decay of absorption of NIR photons in nanoemulsion beyond B = 65 G (Fig. 6.3 and 6.4).

6.4 Conclusions

The effect of external magnetic field on the NIR photon absorption in nanoemulsion is investigated. The absorption depends on the sample volume fraction and in presence of an external magnetic field, the NIR photon absorption by nanoemulsion increases up to a critical external magnetic field and beyond that the absorption decreases which is attributed to the change in Mie absorption efficiency. Up to a critical external magnetic field, the dimensions of field induced aggregates are smaller than the wavelengths of the interacting NIR photons

(Rayleigh regime), where the imaginary part of the refractive index of nanoemulsion increases with sample volume fraction. The calculated k_1 follows a power law increment with sample volume fraction ($k_1 \sim \phi^p$, where p is the exponent) where p linearly decreases with external magnetic field, which clearly indicates that the field induced structural ordering of nanoemulsion droplets significantly contribute towards the absorption of NIR photons. Beyond the Rayleigh regime, the field induced increment in the aggregate length and inter chain distance between aggregates resulted in a reduction in the NIR absorption.

Chapter VII Probing the Effect of Suspended Nano-particle Size on Magnetic Field Induced Structural Transitions in Ferrofluids

7.1 Introduction

The effect of external magnetic field on aggregation of magnetic nanoparticles and its influence on propagation of light have been studied extensively [372]. Recently, the role of the applied field exposure time and viscous force on the particle aggregation and de-aggregation kinetics in magnetic nanofluids was studied experimentally using light scattering techniques [235]. Also, the kinetics of particle aggregation in magnetic nanofluid has been studied using various techniques [187, 208, 209, 373]. Studies show that the functional groups adhered to nanoparticles (stabilizers) can influence the kinetics of field induced chainlike formation in magnetic nanofluid [374]. Among other influencing parameters, the dipolar interaction among the magnetic nanoparticles is the main driving force for particle aggregation process and field induced structural transitions [59]. However, for a given condition (constant external magnetic field strength and particle volume fraction), the particle size has a strong influence on the dipolar interactions, that can affect the magneto-optical properties of nanofluids significantly. Studies show that the non-linear index of refraction and photon absorption in magnetic nanofluids are affected by nanoparticles size and the coating agents [375]. However, no systematic experimental study has been reported on the role of suspended particle size on the external field induced particle aggregation process, and the resulting optical properties of magnetic fluids.

In this chapter, the variation of normalized transmitted light intensity and transmitted speckle patterns as a function of external magnetic field in three different water based ferrofluids containing magnetic nanoparticles of three different hydrodynamic diameters is presented. The

primary objective of this study is to obtain insight into the effect of particle size on magnetic field induced aggregation and its kinetics.

7.2 Experimental Details

The details of the ferrofluid samples used in this study is explained in Chapter II (section 2.2). The transmitted light intensity is measured as a function of *B* using the experimental set up shown in Figure 2.3. The direction of the incident light is perpendicular to the direction of *B*. The detailed procedure of acquiring the transmitted light intensity through the samples and the scattered light as a function of *B* and size measurement by DLS are explained in Chapter II (sections 2.3 & 2.5).

7.3 Results and Discussion

7.3.1 Field Induced Light Transmission Through Three Ferrofluids having Different Sized Magnetic Nanoparticles in Dispersion

Figure 7.1 shows the transmitted light scattering pattern, projected on a screen, from three different ferrofluids at B = 0, 100, 200, 300 and 400 G. Figures 7.1(a–e) correspond to PAA coated Fe_3O_4 nanofluid, Figures 7.1(f–j) correspond to TMAOH coated Fe_3O_4 nanofluid and Figures 7.1(k–o) correspond to phosphate coated Fe_3O_4 nanofluid. For all the three cases, ϕ =0.00916. In the absence of B (= 0 G) only a bright circular spot is observed. But on increasing B, a straight line like pattern is observed. Similar trend was observed in all the three cases. Nevertheless, features of the straight line pattern are slightly different for the three samples. For the PAA coated Fe_3O_4 nanofluid, the straight line pattern is formed within a field of 100 G, whereas, in the other two samples they are discernible above 100 G only. The straight line like pattern is observed at a lower B for the TMAOH coated Fe_3O_4 nanofluid, compared to the phosphate coated Fe_3O_4 nanofluid.

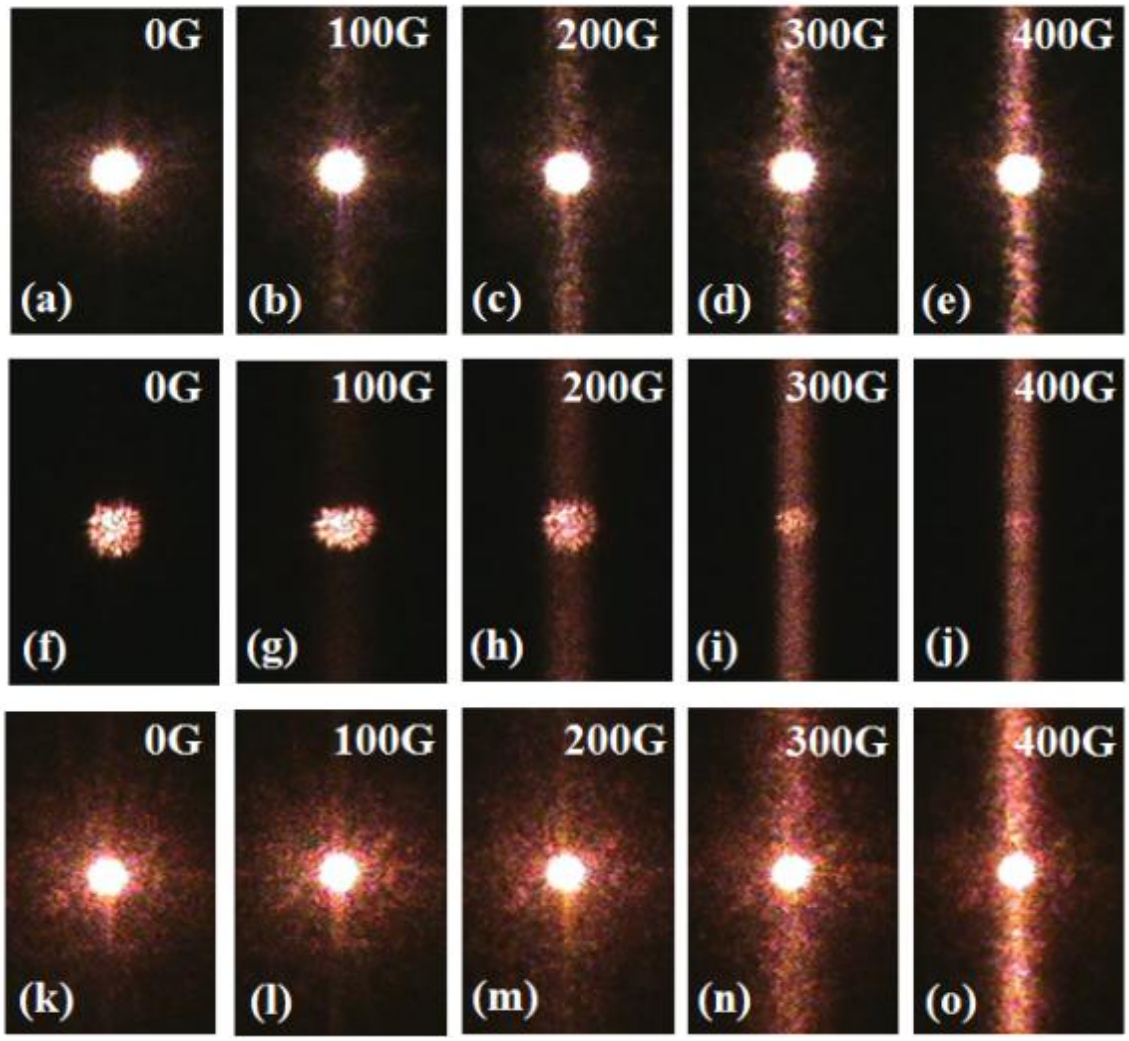

Fig. 7.1. Transmitted light intensity projected on a screen from three different ferrofluids at different external magnetic fields (B = 0, 100, 200, 300, 400G). (a-e) PAA coated Fe_3O_4 nanoparticles. (f-j) TMAOH coated Fe_3O_4 nanoparticles. (k-o) Phosphate coated Fe_3O_4 nanoparticles. In all cases volume fraction, ϕ = 0.00916.

In the presence of B, the coated Fe_3O_4 nanoparticles in dispersion form chainlike structures that are aligned along the direction of B [235, 273, 282, 376].

The optical properties of particle aggregates in dispersion are different from that of solid particles, because the optical cross-sectional area of the particle aggregates in the former

becomes larger than the bare solid particles of the same mass [262]. The field induced evolution of transmitted light pattern (straight-line like), in ferrofluids depends on the hydrodynamic diameter (d_h) of magnetic nanoparticles [282]. As the d_h of the PAA coated nanoparticles is the highest, the straight line like pattern is fully evolved within a field strength of 100 G. On the other hand, for the TMAOH and phosphate coated nanoparticles, straight line like pattern is observed at a higher *B*. Because the coating layer thickness in all the three cases are nearly same (~1–1.5 nm) and the primary Fe_3O_4 nanoparticle size is ~10 nm, the observed hydrodynamic diameters indicates that 2–4 primary particles form aggregates upon coating with different functional groups.

Figure 7.2 shows the normalized transmitted light intensity as a function of *B* for the three different ferrofluids. The inset of Figure 7.2 shows the transmitted light pattern from the phosphate coated magnetic (Fe_3O_4) fluid (d_h = 15 nm) at 430 G. In general, the normalized transmitted light intensity as a function of *B* shows a similar behavior for all the three samples. Initially, the normalized transmitted light intensity increases and attains a maximum at a certain *B*, called the first critical field (B_{C1}). Beyond B_{C1}, the normalized transmitted light intensity decreases continuously and becomes a minimum at a second critical field (B_{C2}). The values of B_{C1} (and B_{C2}) for the ferrofluids with phosphate, TMAOH, and PAA coated magnetic nanoparticles are 126 (632), 98 (478) and 78 (382) G, respectively. This shows that the critical fields shift towards higher values with decreasing d_h of the suspended nanoparticles.

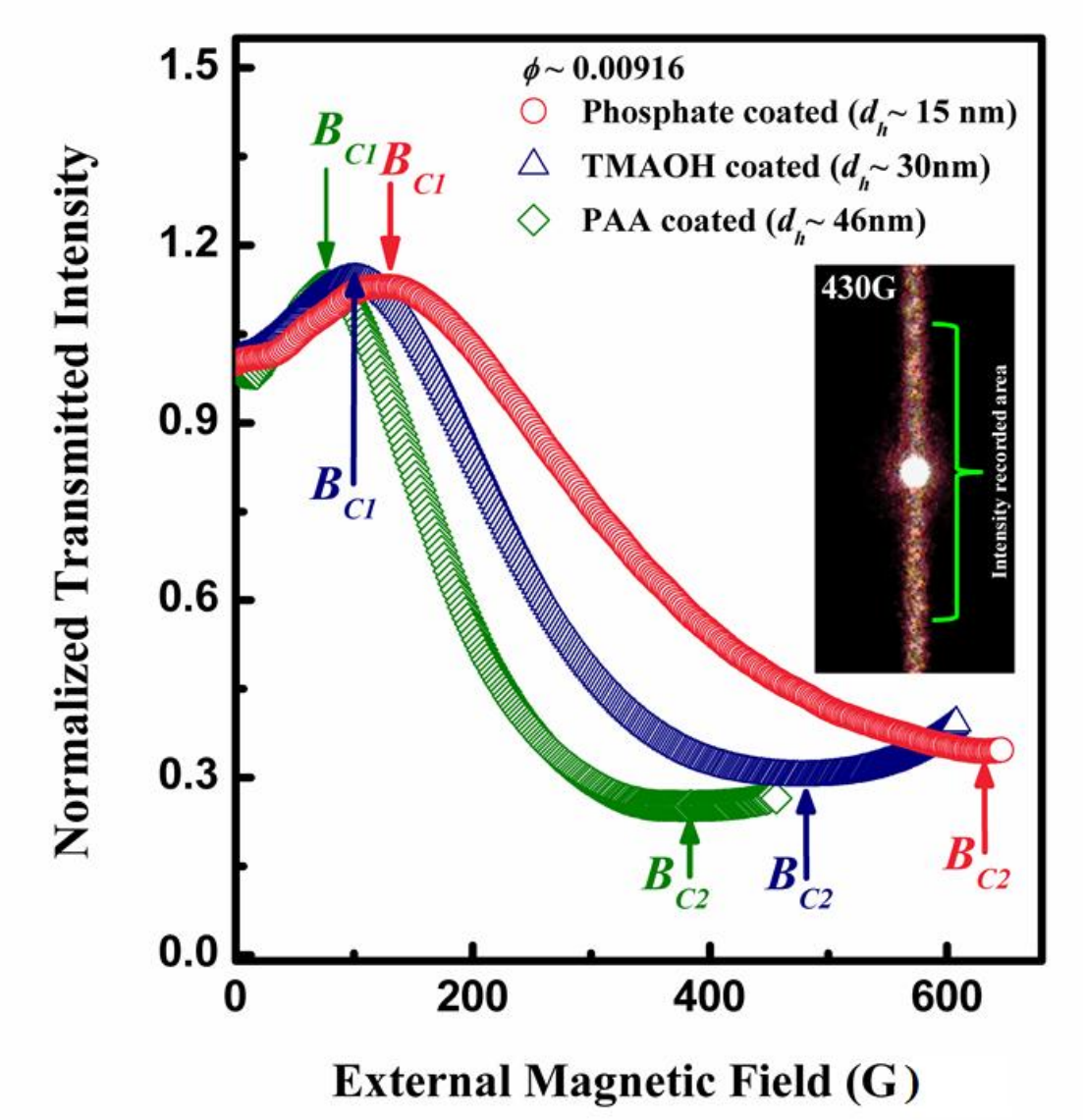

Fig. 7.2. Normalized transmitted light intensity as a function of external magnetic field from three different ferrofluids in the same dispersion (water) but with different particle hydrodynamic diameters (d_h = 46, 30, 15 nm) and surface coating agents (PAA, TMAOH, Phosphate). ϕ ~ 0.00916 and the field ramp rate ~2.5 G/s in all the three systems. Inset image shows the transmitted light pattern from a ferrofluid at 430G.

It has been earlier reported that the magnitudes of the critical magnetic fields (B_{C1} and B_{C2}) depend on ϕ and follows a power law dependence [271] due to a disorder–order transition of magnetic nanoparticles in dispersions [183, 272]. Here, we have shown that for three different ferrofluids, with same ϕ and varying d_h, the critical fields shift towards higher B with decreasing d_h of dispersed magnetic nanoparticles.

Figure 7.3 shows the variation of the critical magnetic fields as a function of d_h of the magnetic nanoparticles. B_{C1}, B_{C2} show power law dependence with d_h ($B_C \sim d_h^{-y}$). The values of the exponent (y) for B_{C1}, B_{C2} are 0.41, 0.44 respectively.

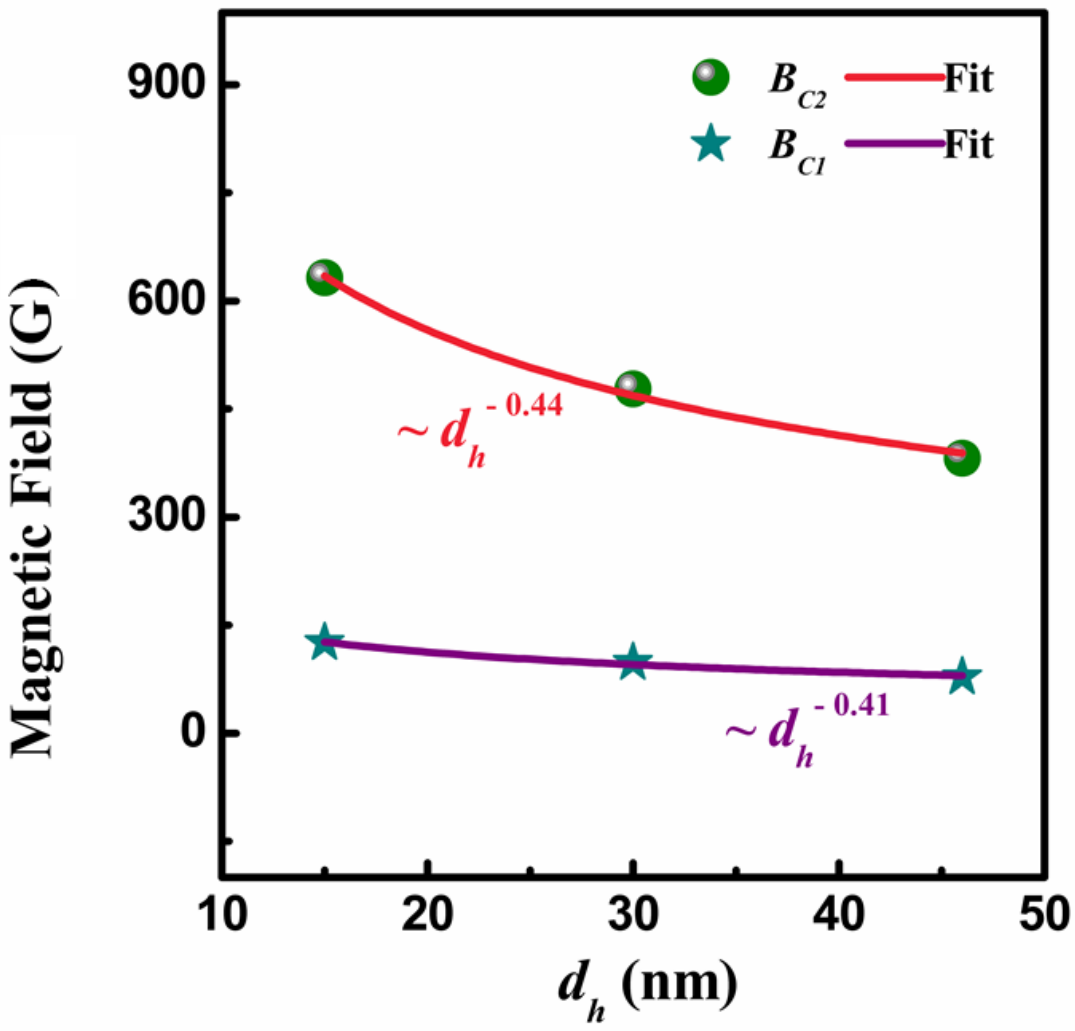

Fig. 7.3. Critical magnetic fields (B_{C1} and B_{C2})as a function of hydrodynamic diameter (d_h). B_{C1} and B_{C2} follow power law decay with d_h ($B_C \sim d_h^{-y}$) where the exponents are 0.41and 0.44, respectively.

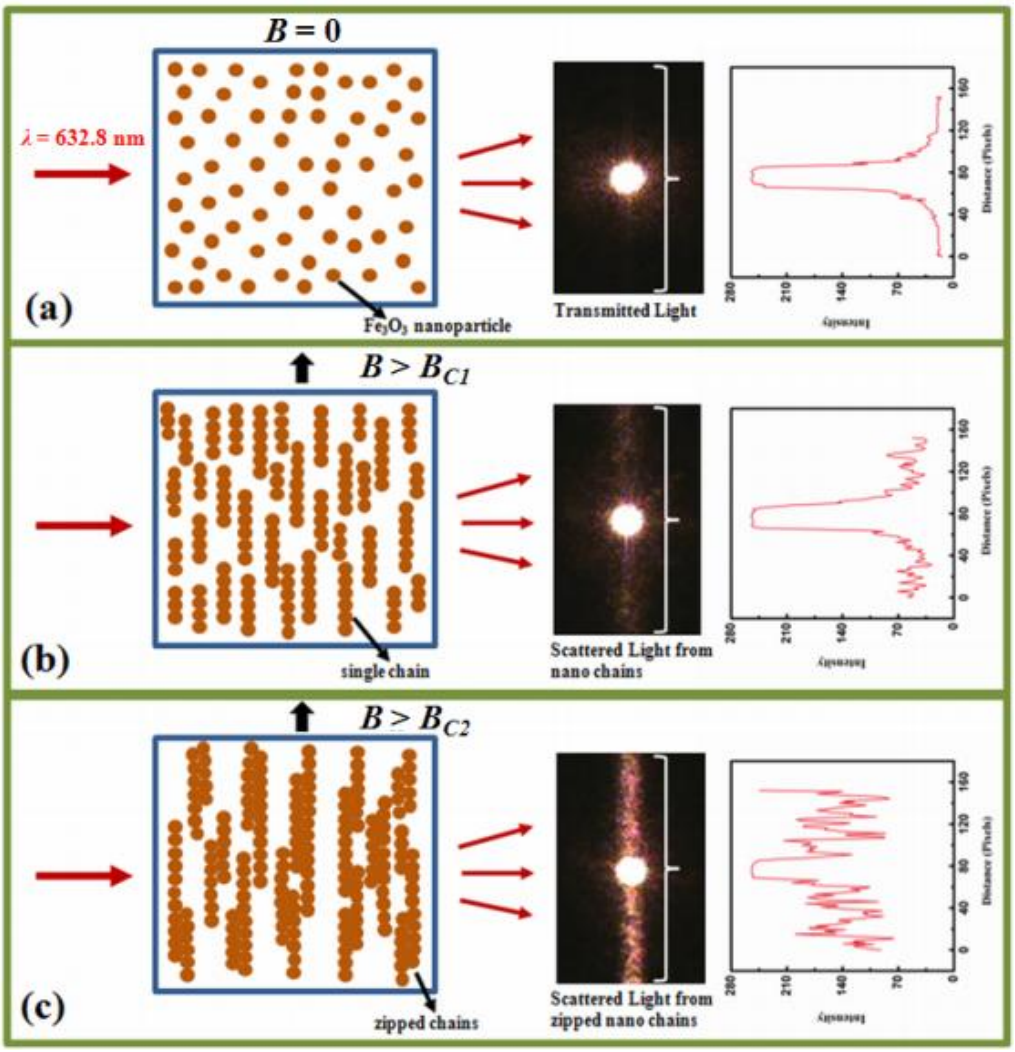

Fig.7.4. (a–c) The schematic of the aggregation process (left), the transmitted light pattern (centre) and the intensity profile of the scattered pattern across the length (right), at $B = 0$, $B > B_{C1}$, $B > B_{C2}$.

Near the first critical field, the magnetic nanoparticles form single chain like structure along the direction of B and the aspect ratio of these nanochains increases progressively with increasing B. Beyond the second critical field, structural rearrangement occurs due to lateral aggregation of nanochains where several chains are zipped to form bundles [172]. This aggregation process depends on B and exposure time [172, 235]. Figure 7.4 shows the schematic of the aggregation process, the transmitted light pattern and the intensity profile of the scattered pattern at $B = 0$, $B > B_{C1}$ and $B > B_{C2}$. In the absence of B, the magnetic nanoparticles are in random motion where the transmitted light shows a circular spot with the entire light intensity distributed within the spot. For $B > B_{C1}$, the magnetic nanoparticles form single chainlike structures along the direction of B, where some intensity of the transmitted light is distributed in the straight line like pattern. At $B > B_{C2}$, nanochains are zippered due to lateral attraction where the intensity distribution along the line is significantly larger compared to the earlier two cases.

7.3.2 Possible Reasons for Size Dependent Variations of Field Induced Extinction of Light

For a given ϕ, a nanofluid sample with smaller d_h requires a higher field strength to meet the condition $\Lambda_{coup} >> 1$. The observation of shifting of B_{C1} and B_{C2} towards higher B with decreasing d_h (Fig. 7.3) is in good agreement with the above condition. The field induced aggregation increases the particle aggregate size and is related to Stokes–Einstein's relation (Equation 2.7, Section 2.5). Therefore, with increasing d_h of magnetic nanoparticles, the diffusion coefficient decreases [67, 253, 377]. Thus, for particles with larger diameter, the onset of chain formation commences at a lower B, which is in good agreement with the shifting of the critical fields to a lower B with increasing d_h of the magnetic nanoparticles (Figs. 7.2 and 7.3).

The optical absorption studies in ferrofluids show that there is no absorption peak in the visible region in presence of a weak field [183]. Therefore, the extinction of transmitted light from a ferrofluid in the presence of B is due to the increase in light scattering from the induced chainlike structures oriented along the B direction [271]. The total light extinction efficiency factor (Q_{ext}) and transport mean free path (ℓ^*) are given in section 3.3.2 [285, 286].

For ferrofluids, the refractive index increases with external magnetic field [224, 227] , which affects the Mie scattering parameters. Further, an increase in scatterer size, due to increased dipolar attractions leads to an enhancement of ℓ^* [271]. At certain values of B (critical fields), the scatterer sizes are such that dipolar resonances occur, which significantly increases light scattering and thereby causing an extinction of light. The external field induced resonant behavior causes a buildup of standing waves inside the scattering medium and leads to a significant decrease in the transmitted light through ferrofluids [183, 225]. With increasing d_h of the magnetic nanoparticles, the onset of external field induced aggregation takes place at a lower field value.

7.3.3 Effect of Suspended Nanoparticle Size on Time Dependent Field Induced Light Transmission

Figure 7.5 shows the normalized transmitted light intensity as a function of time at the second critical fields 382, 478 and 632 G for the PAA, TMAOH and phosphate coated ferrofluids, respectively for ϕ =0.00916. The higher critical fields correspond to the zippering of magnetic field induced chains due to attractive energy between them when the chains are off registry [172]. It can be observed from Figure 7.5 that the normalized light intensity decreases with time and reaches a minimum value. The time corresponding to the minimum value of the normalized transmitted light intensity is designated as t_{min}. Beyond t_{min}, the normalized transmitted intensity is found to increase with time. It is speculated that after achieving

equilibrium zipped structures, more space is available between them, which causes the normalized transmitted light intensity to increase further. The effect of d_h on the t_{min} is also evident from Figure 7.5. For the PAA coated magnetic nanoparticles (d_h ~ 46 nm), the decay of normalized transmitted light intensity is the fastest with the lowest t_{min}. On the other hand, the rate of increase of normalized transmitted light intensity is slowest for the phosphate coated magnetic nanoparticles (d_h ~ 15nm). Overall, t_{min} shifts towards lower values with increase in d_h.

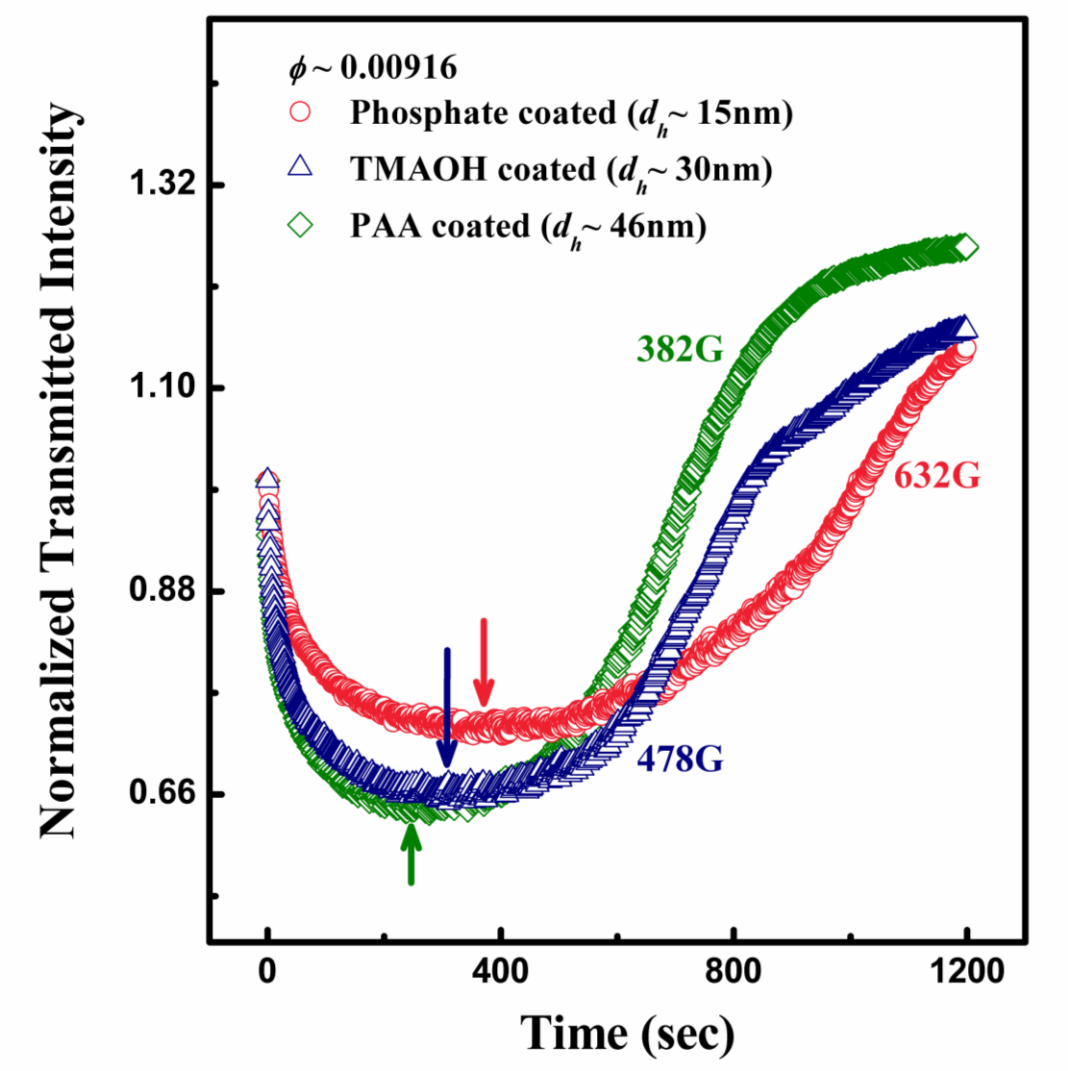

Fig. 7.5. Normalized transmitted light intensity as a function of time at critical magnetic fields 382, 478, 632 G for three different ferrofluids.

7.3.4 Effect of Suspended Nanoparticle Size on Field Induced Transmitted Lobe Intensity and Lobe Speckle Contrast

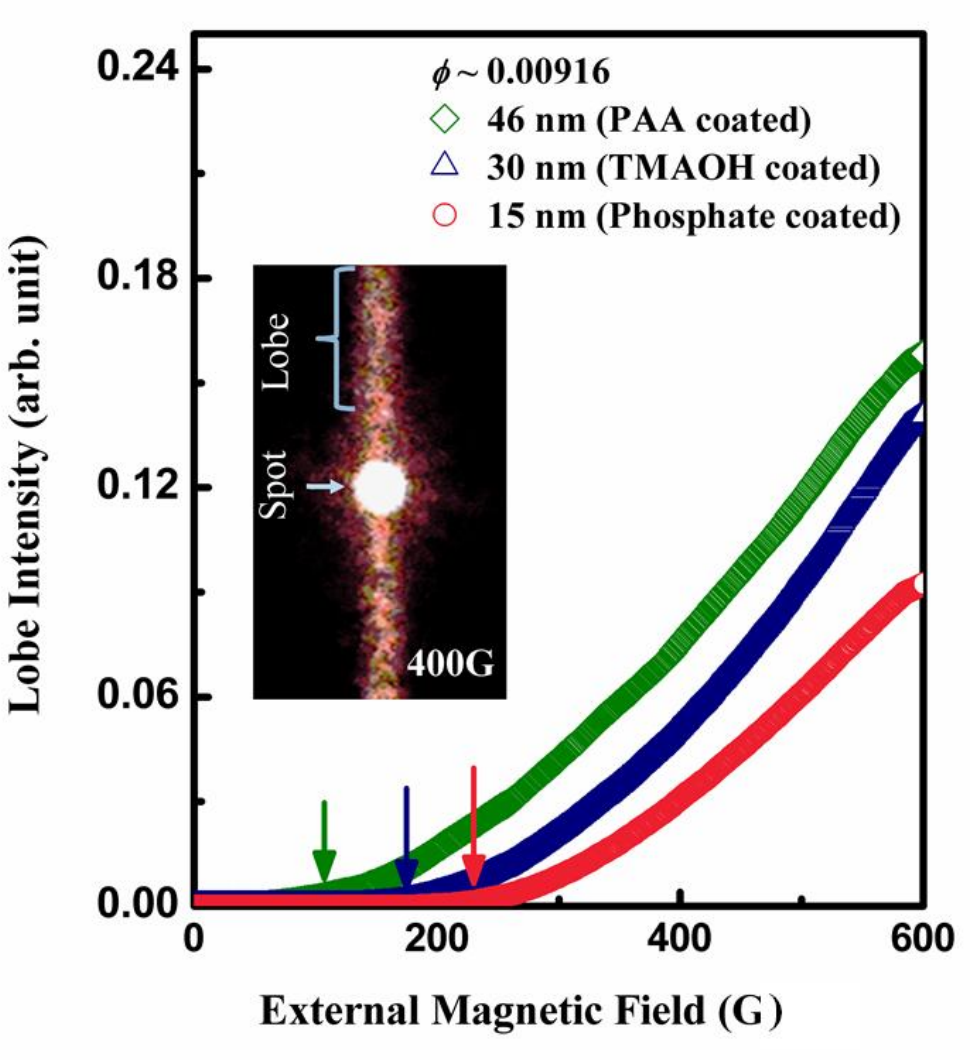

Fig. 7.6. Lobe intensity as a function of external magnetic field from three different ferrofluids. (Inset) The transmitted light is from a ferrofluid at 400 G. The arrows indicate the lobe critical fields.

The straight line lobe part in the transmitted light pattern is due to scattering of incident light from chain like structures oriented along the direction of *B*, which is perpendicular to the direction of the incident light in the present case. Figure 7.6 shows the variation of the intensity of a portion of the lobe part (indicated in the inset of Fig. 7.6 for phosphate coated ferrofluid at

400 G) as a function of B for the three ferrofluids with different d_h. It can be seen that for all the three samples, the intensity of the lobe part remained constant at a very low value up to a certain field, designated as lobe critical field (B_{LC}). Beyond B_{LC}, the intensity of the lobe part increases continuously with increasing B due to field induced chain like structure formation. The B_{LC} is the highest for the phosphate coated magnetic nanoparticles dispersed in water with the smallest d_h (i.e. 15 nm) whereas, the B_{LC} was the lowest for the PAA coated magnetic nanoparticles. Therefore, the critical lobe field shifts to higher values with decreasing d_h.

The combination of bright and dark intensity points and the irradiance level in-between these two extremities on the lobe part of the transmitted light intensity pattern constitutes speckles [244, 296]. If the randomness of the media dies out and approaches towards an ordered state, the probability that the scattered wavelets from the media will be in phase rather than dephased is higher. This leads to the enhanced probability of constructive interference of the scattered waves [296]. In the present case, the speckles on the lobe part of the transmitted light intensity pattern become prominent after the first critical field.

Figure 7.7 shows the variation of the speckle contrast on a lobe part as a function of B for all three ferrofluids. The measurement of the speckle contrast is done in the range of 100–600 G by using Equation 4.5 (Section 4.3.1.3).

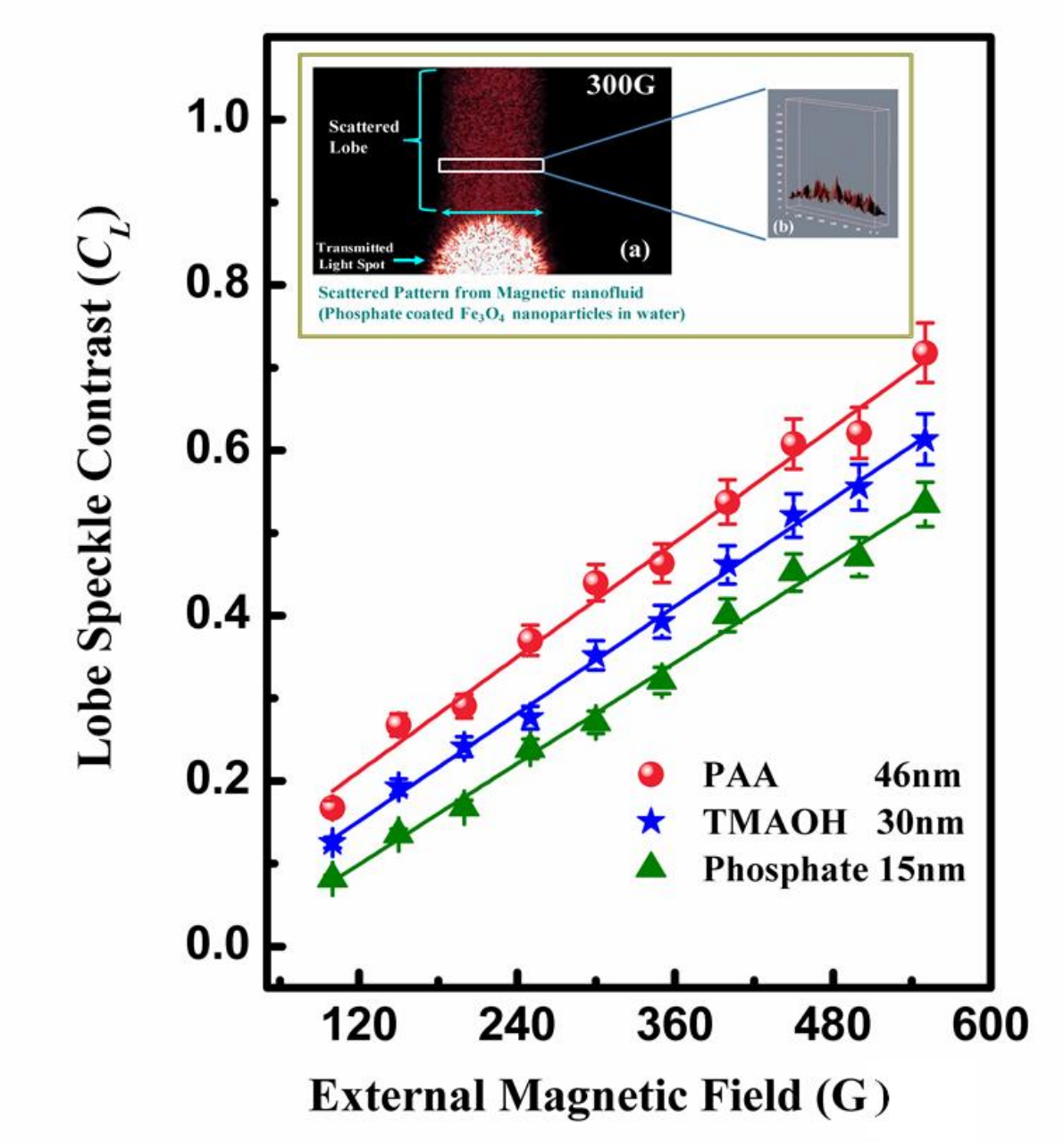

Fig. 7.7. Lobe speckle contrast (C_L) as a function of external magnetic field (B) in three different ferrofluids. Solid lines correspond to linear regression analysis of the experimental data. Inset image (a) the scattered pattern from ferrofluid (phosphate coated Fe_3O_4 nanoparticles in water) at B = 300 G and image (b) 3D surface plot for intensities of speckles on small portion of the scattered lobe part at B = 300 G.

The speckle contrast on the lobe part originates due to the scattering from the ordered internal structures (i.e. linear aggregates). Inset (a and b) of Figure 7.7 shows the scattered light pattern from the phosphate coated ferrofluid (at 300 G) and the 3D surface plot of speckle intensity distribution of a part of the lobe, respectively. For a static speckle pattern, the speckle contrast is close to unity (maximum value), which is called a 'fully developed' speckle pattern. In dynamic systems, the speckle contrast is less than unity due to the motion of scattering centers and the overall speckle pattern appears blurred. It is observed that the speckle contrast (C_L) in the lobe part increases linearly with increasing *B*. This shows that the random Brownian movement of aggregates decreases with increasing field strength. Similar trend is observed in all the three samples. For a given external magnetic field, C_L is higher for ferrofluid with larger d_h. It should be noted from Figure 7.7 that the speckle contrast value is significantly lower than unity at higher fields (B > 500 G), though the scatterers are almost stationary in the dispersion medium. This is probably due to the surface roughness of the field induced chain like structures. Also, the thermal fluctuations in the carrier liquid can restrict the speckle pattern from being 'fully developed' [296]. For a given field strength, the nanoparticles with the highest particle diameter will have the strongest coupling within the chains. Therefore, with increasing d_h, a reduced thermal fluctuation and a higher value of speckle contrast is expected, which is in good agreement with our experimental findings (Fig. 7.7).

7.4 Conclusions

The effect of hydrodynamic particle size on the magnetic field induced light transmission and transmitted speckle pattern in water based ferrofluids, containing poly-acrylic acid (PAA), tetra-methyl ammonium hydroxide (TMAOH) and phosphate functionalized Fe_3O_4 nanoparticles of size ranging from 15 to 46 nm, is studied in this chapter. In all the three ferrofluids, the transmitted light intensity shows two distinct critical magnetic fields,

corresponding to the onset of aggregation and the onset of zippering, respectively. Both the critical fields shift towards lower magnetic fields, as the hydrodynamic particle diameter increases. The critical fields also show power law dependence on the hydrodynamic diameter. The time dependent study shows that the transmitted intensity becomes a minimum prior to zippering transition but increases on zippering transitions due to opening up of the otherwise filled space between the chains. The first critical field decreases with increasing hydrodynamic diameter. Above the first critical field, the lobe part of the transmitted intensity and the lobe speckle contrast increases with increasing magnetic field. The speckle contrast is higher for nanoparticles with larger hydrodynamic diameter, due to reduced Brownian motion of the aggregates, owing to a stronger dipolar coupling.

Chapter VIII Probing the Effect of Temperature on Magnetic Field Induced Structural Transitions in Ferrofluids

8.1 Introduction

Particle aggregation changes the physical properties in colloidal systems [261, 378-380]. The fundamental understanding of the influence of aggregation parameters such as particle size, temperature, viscosity on aggregation process in colloidal systems is important from practical applications point of view [375, 381]. The field induced aggregation in magnetic nano-colloidal systems is mainly due to dipolar interaction between the dispersed magnetic nanoparticles [235, 274, 275]. Though numerous studies have considered the effect of dipolar interaction on field induced aggregation in magnetic nano-colloidal systems, the effect of temperature on field induced aggregation and related magneto-optical properties has not been systematically studied earlier. In this chapter, we have systematically studied the effect of temperature on the external field induced light transmission in kerosene based ferrofluids.

8.2 Experimental Details

The kerosene based ferrofluid samples used in this study is a disordered magnetic medium as explained in Chapter II (section 2.2). The detailed procedure of acquiring the transmission spectra through the samples as a function of B has been explained in Chapter II (section 2.4). Here, the direction of incident light was kept parallel to the direction of B and the ferrofluid was taken in a cuvette of path length, L = 10 mm and kept inside a Peltier based temperature controlled cuvette holder. The specimen temperature was varied using a programmable temperature controller. The ϕ was kept constant at 0.00155 throughout the experiments.

8.3 Results and Discussions

8.3.1 Wavelength Dependent Behavior of Magnetic Field Induced Light Transmission in Ferrofluids at Fixed Sample Temperature

Figure 8.1 shows light transmission through the ferrofluid as a function of λ at five different B = 0, 62, 130, 196 and 264 G. The specimen temperature is kept constant at 278 K. The light transmission increases with λ for all B. As the Fe_3O_4 nanoparticle size is much lower than λ ($a << \lambda$) the light scattering can be described using Rayleigh's theory, where the scattering efficiency is inversely proportional to the fourth power of the incident wavelength, i.e. $Q_{sca} \propto \frac{1}{\lambda^4}$ [286]. Hence, the observed decrease in the scattering intensity with increasing λ is in good agreement with Rayleigh's theory and this explains the increase in the transmission of incident light with increasing λ in the ferrofluid. It can be further observed from Figure 8.1 that the transmission of incident light is highest at B = 0 G and it decreases with increase in B.

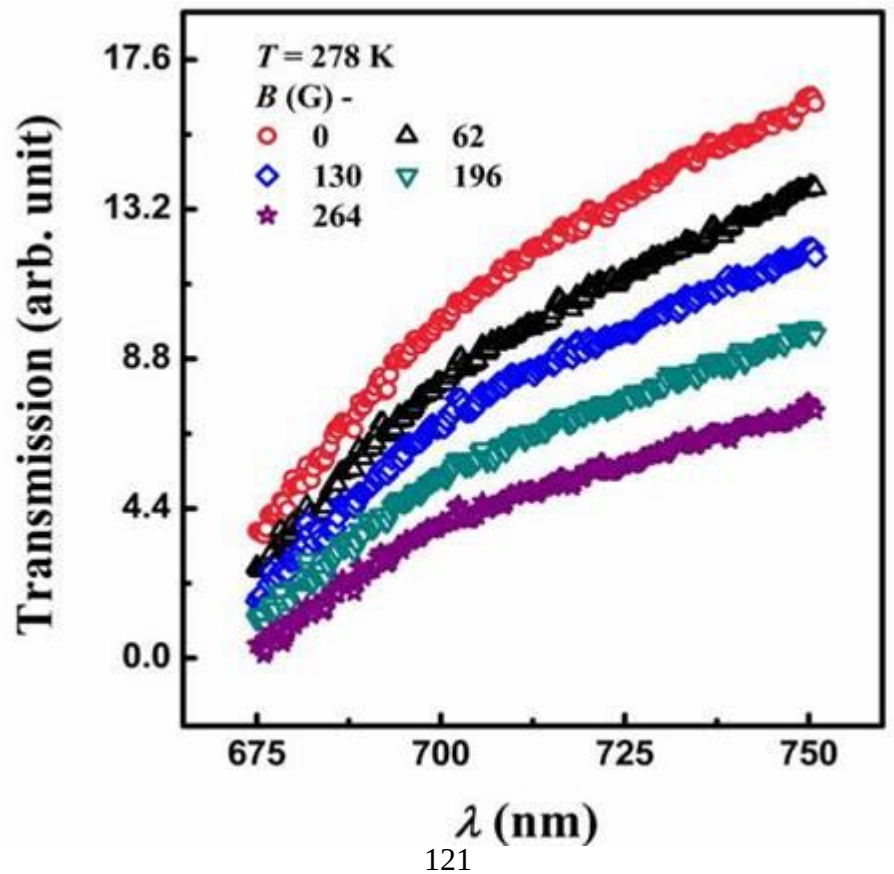

Fig. 8.1 Light transmission as a function of light wavelength (λ) at different external magnetic fields (B = 0, 62, 130, 196, 264 G) in a ferrofluid. Range of λ is 675-750 nm and specimen temperature (T) was kept constant at 278 K.

In the absence of B, the oleic acid coated Fe_3O_4 nanoparticles are randomly dispersed in the carrier liquid due to Brownian motion of particles. On application of B, the magnetic moments of the individual nanoparticles orient themselves along the direction of B and form linear chain like structures [59, 273]. When the magnetic coupling constant (Λ_{Coup}) between two nanoparticles is greater than one ($\Lambda_{Coup}>>1$), the dispersed magnetic nanoparticles undergo a disorder to order transition leading to the formation of linear chain like structures due to head-on aggregation of the dispersed nanoparticles along the direction of B [172, 284, 382]. The interaction of incident light with such linear chain like structures with their axis parallel to the direction of propagation of light gives rise to a ring like transmission spectrum [282]. The aggregation of nanoparticles increases with B due to increase in the dipolar interaction leading to a larger scatterer size [376]. On application of B, the magnetic nanoparticles form single chain like structures along the direction of B up to B_{C1} and beyond that zippering of chains takes place due to lateral aggregation resulting in bundles of nanochains [172]. The length of these chains increases with B and the aggregation process depends on the strength of the field and exposure time. When the scatterer size is comparable with the λ the scattering regime changes from Rayleigh to Mie region.

The transmission, absorption and distribution of the scattered light, during passage through a magnetic nanofluid depend on the nature of the dispersed scatterers [256, 285]. The total extinction efficiency (Q_{ext}) is the sum of scattering efficiency (Q_{sca}) and absorption efficiency (Q_{abs}) and can be expressed by the following equation [285].

$$Q_{ext} = Q_{sca} + Q_{abs} \tag{8.1}$$

The mathematical expressions of Q_{ext} and Q_{abs} have been provided in Chapter VII (Equation 7.1) and Chapter VI (Equation 6.4), respectively and

$$Q_{sca} = \frac{2}{x^2}\sum_{n=1}^{\infty}(2n+1)(|a_n|^2 + |b_n|^2) \tag{8.2}$$

where, a_n and b_n are the Mie scattering parameters which depend on the scatterer size parameter (x = ka, where a is the radius of the nanoparticle and $k = 2\pi/\lambda$).

The magnetic permeability (μ) increases with increasing B for ferromagnetic scatterers [289]. At certain values of the external magnetic field the scatterer sizes are such that Mie resonances occur leading to a buildup of standing waves inside the scattering medium resulting in subsequent delay in light propagation causing the light transmission to decrease with increasing magnetic field as shown in Figure 8.1 [225].

Figure 8.2 shows the theoretical plot of Q_{ext} at lower values of the ka for four different λ (= 675, 700, 725 and 750 nm). It can be seen from the figure that the peak value of the extinction efficiency decreases with increasing λ and hence, light transmission increases with λ for a constant B as shown in Figure 8.1. As discussed earlier, in the absence of field, the increase in light transmission with increasing λ can be described by the Rayleigh scattering theory, whereas, in presence of an external field the individual nanoparticles form linear chain like structures due to dipolar interaction leading to a larger scatterer size and the system can be described by Mie scattering theory where the extinction efficiency decreases with increasing λ resulting in an increase in field induced light transmission with λ.

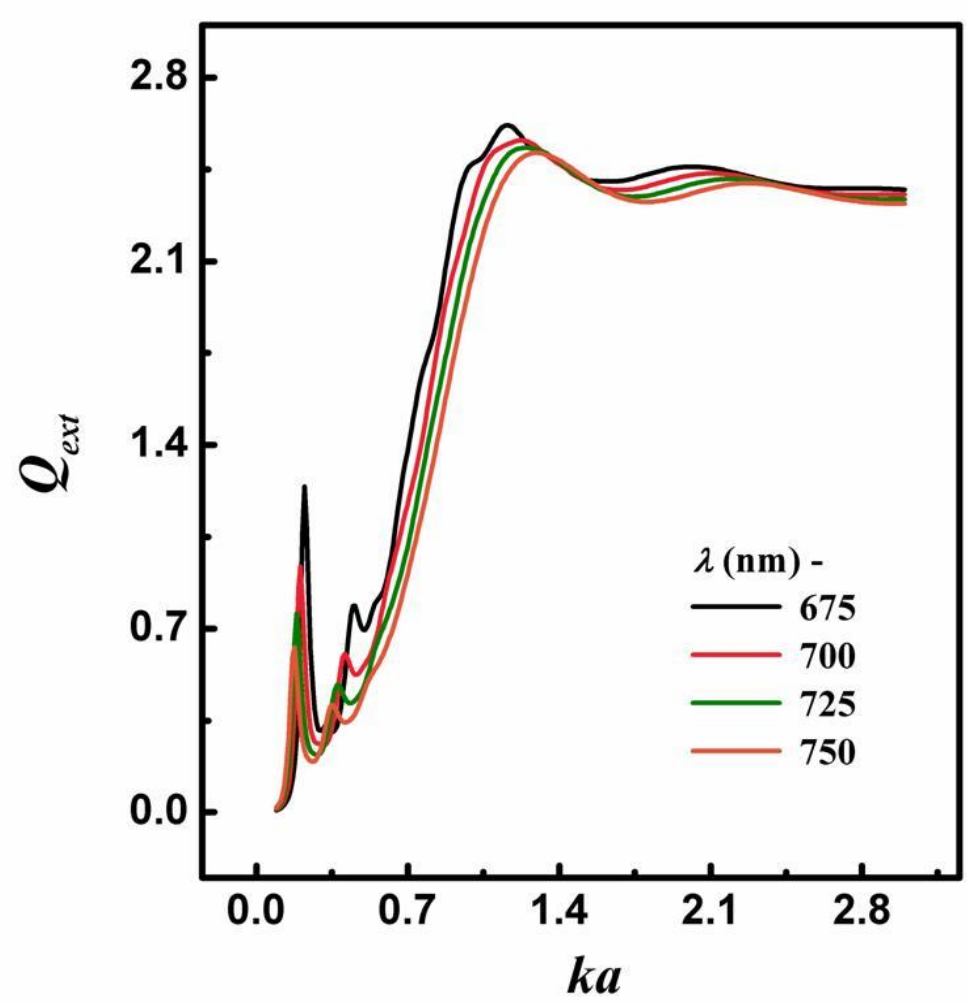

Fig. 8.2 Q_{ext} as a function of *ka* at different λ ~ 675, 700, 725, 750 nm. Variation of Q_{ext} is shown at lower values of *ka*.

8.3.2 Temperature Dependent Field Induced Light Transmission and Possible Reasons of Temperature Effect on Transmission

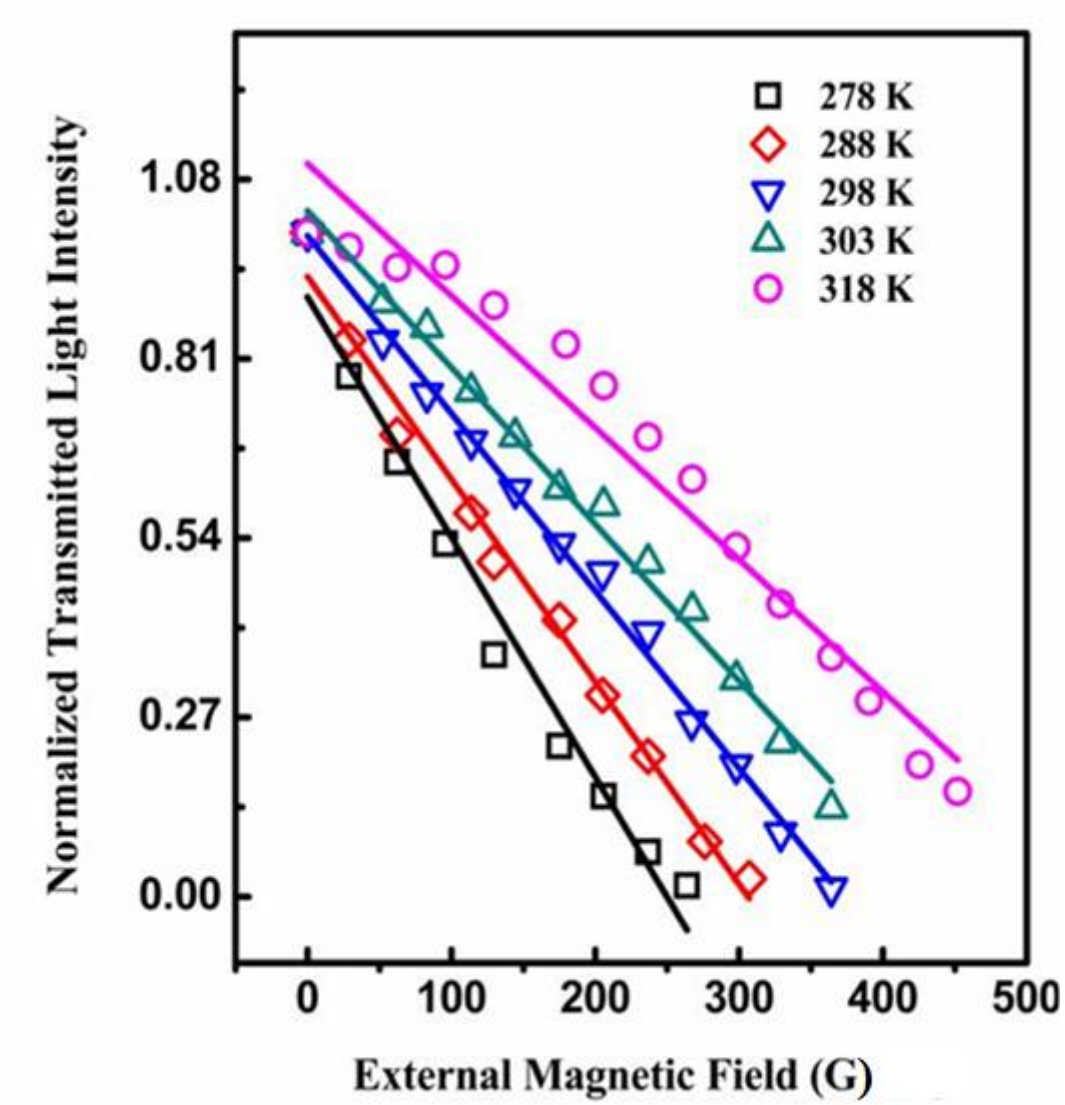

Fig. 8.3 Normalized transmitted light intensity as a function of external magnetic field (B) at different sample temperature (T = 278, 288, 298, 303, 318K) in ferrofluid. Light wavelength, λ = 700 nm. Solid lines correspond to the linear regression analyses of the experimental data. The adjusted R^2 for the linear regression analyses are 0.97, 0.99, 0.99, 0.99 and 0.96 for T = 278, 288, 298, 303 and 318K, respectively.

Figure 8.3 shows the variation of normalized transmitted light intensity as a function of *B* for ferrofluid at five different specimen temperatures viz. *T* = 278, 288, 298, 303 and 318 K. For all the cases the λ is kept constant at 700 nm. It can be seen from the figure that for all values of *T*, the normalized transmitted light intensity decreases with increasing *B* owing to the Mie resonance induced buildup of standing waves inside the scattering medium due to enhancement of *ka* with *B*. It can be further observed from Figure 8.3 that the field induced light extinction occurs at lower *B* for lower *T*. The solid lines in Figure 8.3 indicate the linear regression analyses on the experimental data points where the slopes provide the rate of field induced light extinction (R_{trans}). Figure 8.4 shows the variation of R_{trans} as a function of *T* and it can be seen that R_{trans} linearly decreases with increasing *T*. The normalized transmitted light intensity shows linear dependence with *B* for all five *T* and does not show critical field like behavior [376] or saturation in the transmitted intensity profile due to extremely low ϕ of the ferrofluid used in the present study.

The coupling constant, which determines the strength of the dipolar interaction with respect to the thermal energy of the specimen, is inversely proportional to *T* and hence, aggregation kinetics will vary with *T*. In the absence of *B*, the dispersed nanoparticles undergo random Brownian motion and the diffusion coefficient can be expressed by the Stokes-Einstein equation (Chapter II, Equation 2.7).

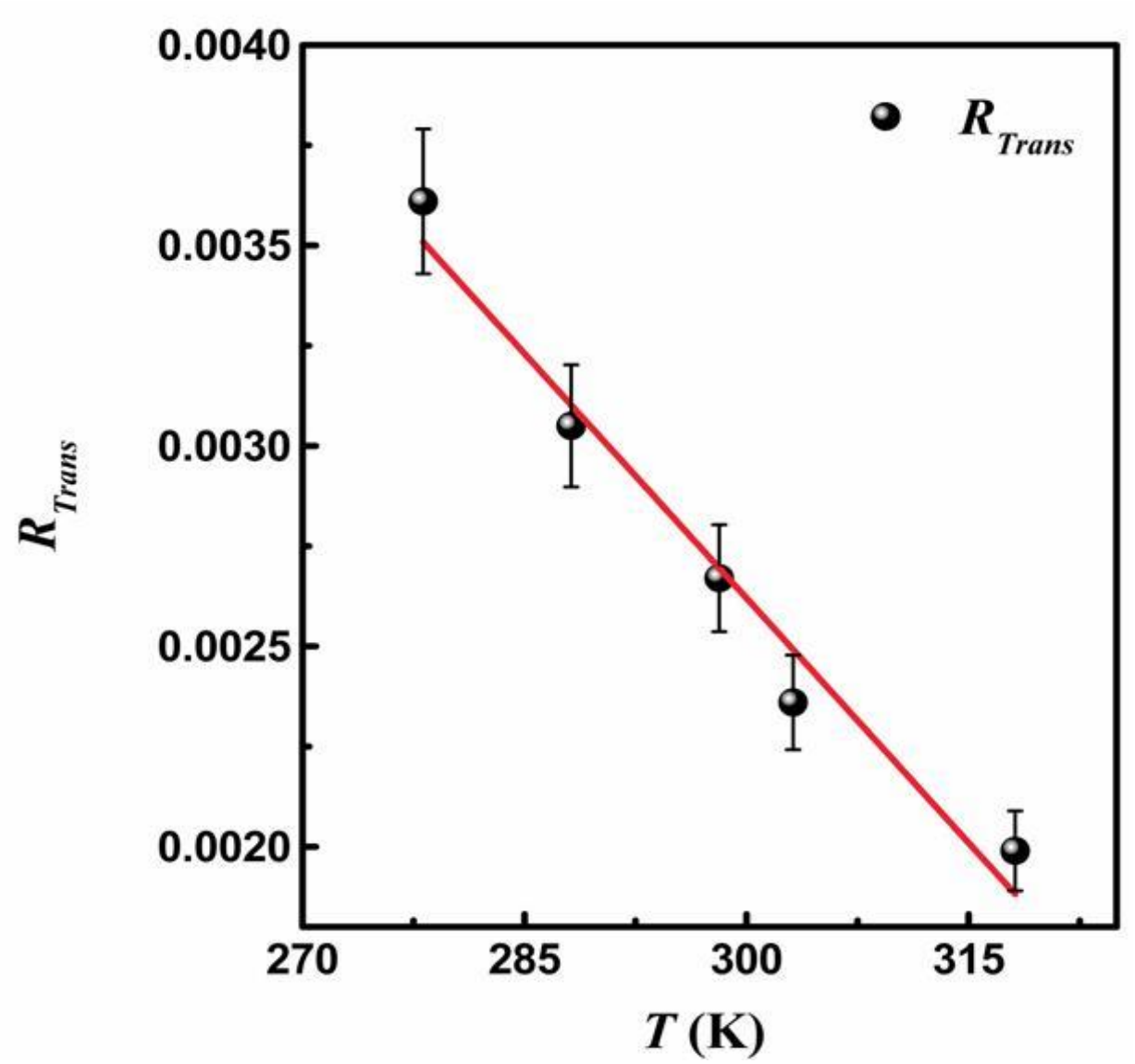

Fig. 8.4 Rate of extinction of normalized transmitted light intensity (R_{Trans}) as a function of sample temperature (T). Solid line corresponds to linear regression analysis of the experimental data and adjusted R^2 is 0.96.

From the Stokes-Einstein equation it is evident that the diffusivity linearly increases with T (as shown in the inset of Fig. 8.5). Moreover, the root mean square velocity (V_{RMS}) of the dispersed

nanoparticles undergoing random Brownian motion also increases with T (V_{RMS} is directly proportional to $T^{0.5}$) and can be expressed by the following equation [383].

$$V_{RMS} = \frac{1}{d_h}\sqrt{\frac{18k_BT}{\pi\rho d_h}} \tag{8.3}$$

Here, ρ is the density of the nanoparticles. It has been reported earlier that for kerosene based ferrofluid, the variation in absolute viscosity with T is not significant for the ferrofluid and the base fluid. Hence, with increase in T, the root mean square velocity and diffusivity of dispersed nanoparticles increases because of an enhancement of Brownian motion. On application of B, the dipolar attraction between the magnetic nanoparticles causes the particles to form linear chain like structures along the direction of B. The aggregation process is hindered by the enhanced Brownian motion for higher T leading to slower aggregation kinetics at higher T. Figure 8.5 shows the variation of coupling constant as a function of T (using Eq. 3.3,) for three different values of B (= 100, 150 and 200 G). It can be seen that for all values of B, the coupling constant decreases with increasing T indicating a slower aggregation kinetics at higher T.

With increasing T, the Brownian motion of the dispersed nanoparticles increases and hence, higher B is required to form linear chain like structures, causing the extinction of transmitted light intensity to shift to higher B values as shown in Figure 8.3. The rate of extinction of light transmission also decreases linearly with T (Figure 8.4) indicating an increase in the time scale of aggregation kinetics at higher T due to a linear increase of diffusion coefficient with T.

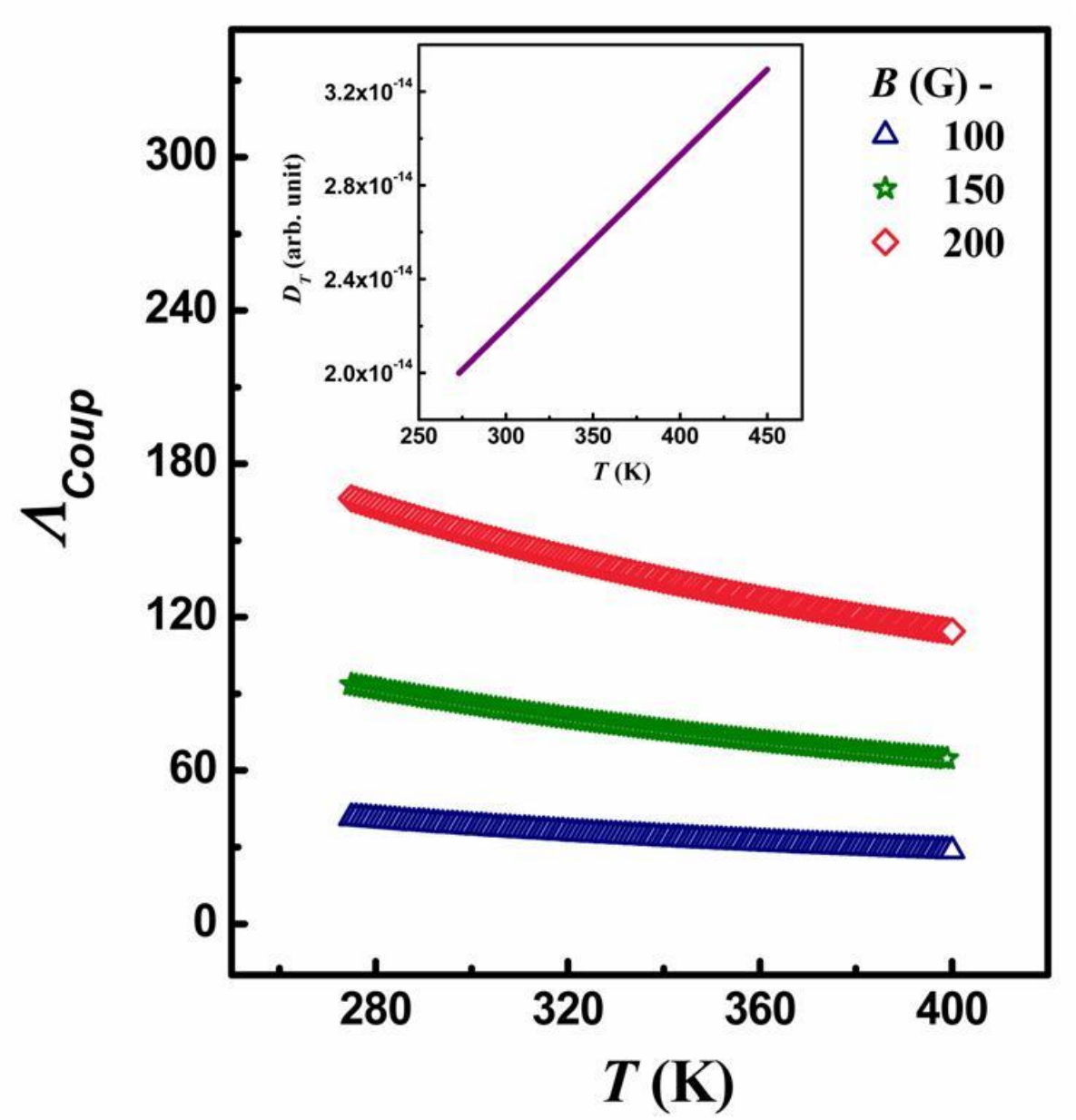

Fig. 8.5. Coupling constant (Λ_{Coup}) as a function of sample temperature (T) at three different external magnetic fields (B = 100, 150, 200 G). (Inset) Diffusion coefficient (D_T) as a function of T.

Such temperature dependent field induced extinction of normalized transmitted light intensity is possible only under the influence of B and not under thermo-optical effects as the rate of

change of refractive index as a function of T is extremely low in nano-colloidal systems without external fields. Thermo-optical effect occurs due to modulation of refractive index of a medium as a function of T. For nano-colloidal systems the rate of change of refractive index with respect to the T is very low ($\sim 10^{-4}$) [384]. Hence, the change of refractive index is negligible for nominal variation in T (278 – 318 K in the present study). On the other hand, in the presence of B, ferrofluids exhibit magneto-optical effects due to spatial anisotropy caused by external field induced structural reorganization which ultimately causes enhancement of size parameters and an extinction of transmitted light intensity at a certain value of B and T. With increase in T, the field induced extinction of transmitted light intensity occurs at a higher field giving rise to temperature dependent magneto-optical properties.

Figure 8.6 shows the variation of light transmission as a function of λ at four different T (= 278, 288, 303 and 318 K) and at B = 130 G. As discussed earlier, the light transmission increases with λ due to decrease in extinction efficiency with increasing λ. It can be seen from the figure that the light transmission is higher at higher T due to the higher contribution from the thermal energy, which hinders the aggregation process to form field induced linear chain like structures along the direction of B. Due to increase in diffusivity of the suspended nanoparticles, the size parameter decreases which results in an increase of light transmission at higher T as depicted in Figure 8.6. It can be further observed from Figure 8.6 that the field induced light transmission (at 750 nm) increases by 11 , 25 and 33% when the temperature is increased by 10, 25 and 40 K, respectively from 278 K. This shows that there exist possibilities of temperature sensitive tuning of field induced light transmission in ferrofluids which can be used for temperature sensitive optical sensors.

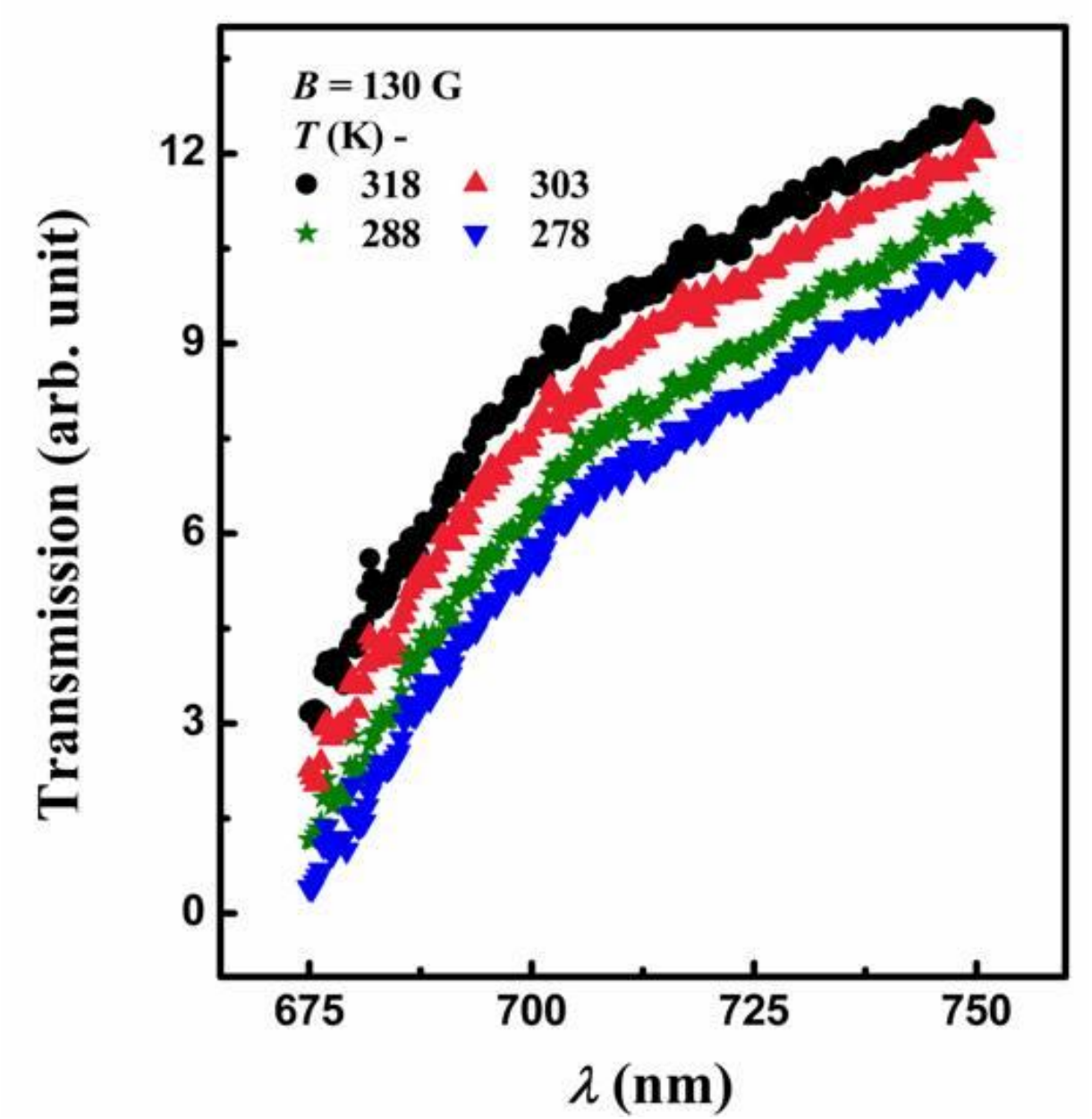

Fig. 8.6. Light transmission as a function of incident wavelength (λ) at different sample temperature (T = 278, 288, 303, and 318 K) for the ferrofluids. Here, external field, B = 130 G.

8.3 Conclusions

The effect of temperature on field induced light transmission in a kerosene based ferrofluid containing oleic acid coated Fe_3O_4 nanoparticles of average size 6.5 nm is studied. At a fixed specimen temperature the light transmission monotonically increased with wavelength in the presence of an external magnetic field due to reduced extinction efficiency at higher wavelength. It is further observed that the light transmission decreased with increasing external magnetic field due to enhancement of size parameter and the resulting buildup of standing waves in the scattering medium. The normalized transmitted light intensity decreased with increase in external magnetic field and the extinction occurred at lower value of external magnetic field for lower specimen temperature. Moreover, the rate of light extinction is found to decrease linearly with increasing temperature due to the linear increase in diffusivity of the dispersed magnetic nanoparticles. With increase in temperature the coupling constant decreases and hence, the field induced aggregation occurred at a slower rate leading to an increase in light transmission.

Chapter IX Conclusions and Future Perspective

The present chapter summarizes the results obtained from the studies on magnetic field dependent structural transitions in magnetic fluids using light scattering, absorption and speckle pattern analysis.

9.1 Conclusions

- The dramatic changes in the transmitted light intensity in magnetic fluids in presence of magnetic fields are explained using the dipolar Mie resonance phenomena in the scattering medium [376, 385].

- Magnetic field induced aggregation of nano sized particles in magnetic fluids changes the dimension and surface roughness of the aggregates which strongly influences the transmitted light speckle parameters such as contrast, polarization, speckle correlation coefficients etc [376, 385].

- Speckle pattern on the transmitted light spot from magnetic fluids in the presence of an external magnetic field shows a linear increase in speckle contrast with external magnetic field, which indicates a transformation from 'dynamic' to 'fully developed' speckle pattern due to the formation of chain-like structures by nano sized particles in dispersion [376].

- The surface roughnes of field induced aggregates is found to hamper the speckle pattern from being 'fully developed'. The speckle contrast is found to increase linearly with external magnetic field because of the evolution from highly dynamic to nearly static scatterers in the dispersion.

- The backscattered light intensity is found to diminish with external magnetic field due to a delay of light propagation due to the formation of standing waves in the scatterering medium [386].

- The backscattered speckle contrast is found to increase with external field due to evolution of scatterers from dynamic to a nearly static state. Also, it is observed that a small change in backscatter angle causes a large variation in field dependent backscattered light intensity [386].

- The study of magnetic field dependent near infrared photon absorption in nanoemulsion shows a volume fraction and field dependent variations in absorption because of the variation in the Mie absorption efficiency during the structural transitions [387].

- The imaginary part of the refractive index of nanoemulsion is found to vary with external magnetic field and sample volume fractions.

- After a critical magnetic field, the field induced absorption of near infrared photons decrease because of the increase in the aspect ratio of the chain like aggregates and inter-chain spacing.

- In water based ferrofluids, the transmitted light intensity starts decreasing above a certain magnetic field and becomes a minimum at another field. These two critical fields signify the onset of linear aggregation process and zippering transitions. Both these critical fields shift towards a lower magnetic field with the increasing of hydrodynamic diameter of particles, due to reduced Brownian movement and stronger magnetic dipolar interaction [388].

- The lobe part of the transmitted intensity and the lobe speckle contrast values increase with external magnetic field and the lobe intensity, speckle contrast values found to be highest for the nanoparticles with largest hydrodynamic diameter due to the reduced Brownian motion of field induced aggregates [388].
- The temperature dependent study shows that the rate of extinction of normalized transmitted light intensity linearly decreases with increasing specimen temperature, indicating a slower rate of field induced aggregation kinetics at higher specimen temperature due to enhanced Brownian motion [389].

9.2 Applications

Based on above findings, the potential applications of magnetic fluids are – making of tunable photonic devices, tunable optical grating, optical limiter, optical switches, optical fiber modulator, temperature & field dependent optical sensors, infra red optical sensors etc.

9.3 Future Perspective

- Probing the role of viscosity of carrier liquid on the aggregation kinetics and magneto-optical properties in magnetic fluids.
- Probing the nature of stabilizing moieties on the aggregation kinetics and magneto-optical properties in magnetic fluids.
- Probing the role of non-magnetic particles in magnetic fluids on magnetic field induced structural transitions and associated magneto-optical properties.
- Development of optical limiters, field sensors etc using magnetic fluids.

LIST OF REFERENCES

1. P. W. Anderson, *Basic Notions of Condensed Matter Physics* (The Benjamin/Cummings Publishing Company, Inc., California, 1984).
2. G. R. Strobl, *Condensed Matter Physics: Crystals, Liquids, Liquid Crystals and Polymers* (Springer-Verlag, Berlin, 2004).
3. M. P. Marder, *Condensed Matter Physics* (John Wiley & Sons, Inc., New Jersey, 2010).
4. C. Kittel, *Quantum Theory of Solids* (John Wiley & Sons,Inc., New York, 1967).
5. G. D. Mahan, *MANY-PARTICLE PHYSICS* (Plenum Press, New York, 1981).
6. P. M. Chaikin, and T. C. Lubensky, *Principles of Condensed Matter Physics* (Cambridge University Press, 1998).
7. M. Kleman, and O. D. Lavrentovich, *Soft Matter Physics: An Introduction* (Springer-Verlag, New York, 2003).
8. M. Doi, *Soft Matter Physics* (Oxford University Press, Oxford, 2013).
9. D. F. Evans, and H. Wennerstrom, *The Colloidal Domain: Where Physics, Chemistry, Biology, and Technology Meet* (Wiley, New York, 1999).
10. V. G. Sakai, C. A.-. Simionesco, and S.-H. Chen, *Dynamics of Soft Matter: Neutron Applications (Neutron Scattering Applications and Techniques)* (Springer, New York, 2012).
11. R. A. L. Jones, *Soft Condensed Matter* (Oxford University Press, Oxford, 2002).
12. P.-G. d. Gennes, and J. Badoz, *Fragile Objects: Soft Matter, Hard Science, and the Thrill of Discovery* (Copernicus Books, Springer-Verlag, 1996).
13. D. Demus, J. W. Goodby, G. W. Gray, H.-W. Spiess, and V. Vill, *Handbook of Liquid Crystals* (Wiley, New York, 1997).
14. G. L. Hunter, and E. R. Weeks, "The physics of the colloidal glass transition," Rep. Prog. Phys. **75**, 066501 (2012).
15. M. Orczykowska, and M. Dziubiński, "Viscoelastic Properties of Soft Materials on a Basis of Starch Mixtures," J. Food Sci. **79**, E849-E858 (2014).
16. F. Sciortino, and E. Zaccarelli, "Soft heaps and clumpy crystals," Nature **493**, 30-31 (2013).
17. D. M. Ebenstein, and L. A. Pruitt, "Nanoindentation of biological materials," Nano Today **1**, 26-33 (2006).
18. B. Weidenfeller, M. Anhalt, and S. Kirchberg, "Thermal diffusivity and mechanical properties of polymer matrix composites," J. Appl. Phys. **112**, 093513 (2012).
19. P. M. Sousa, V. Chu, and J. P. Conde, "Mechanical properties of polymer/carbon nanotube composite micro-electromechanical systems bridges," J. Appl. Phys. **113**, 134508 (2013).
20. G. M. Whitesides, and B. Grzybowski, "Self-Assembly at All Scales," Science **295**, 2418-2421 (2002).
21. I. Musevic, M. Skarabot, U. Tkalec, M. Ravnik, and S. Zumer, "Two-Dimensional Nematic Colloidal Crystals Self-Assembled by Topological Defects," Science **313**, 954-958 (2006).
22. Q. Chen, S. C. Bae, and S. Granick, "Directed self-assembly of a colloidal kagome lattice," Nature **469**, 381-384 (2011).
23. K. Busch, and S. John, "Photonic band gap formation in certain self-organizing systems," Phys. Rev. E **58**, 3896 (1998).
24. R. Kimmich, *Principles of Soft-Matter Dynamics: Basic Theories, Non-invasive Methods, Mesoscopic Aspects* (Springer, Dordrecht, 2012).

25. J. Lyklema, *Fundamentals of Interface and Colloid Science* (Academic, London, 1991).
26. P. G. d. Gennes, *Scaling Concepts in Polymer Physics* (Cornell University Press, Ithaca, 1979).
27. S. Nojd, P. S. Mohanty, P. Bagheri, A. Yethiraj, and P. Schurtenberger, "Electric field driven self-assembly of ionic microgels," Soft Matter **9**, 9199-9207 (2013).
28. E. M. White, J. Yatvin, J. B. G. III, J. A. Bilbrey, and J. Locklin, "Advances in Smart Materials: Stimuli-Responsive Hydrogel Thin Films," J. Polym. Sci., Part B: Polym. Phys. **51**, 1084-1099 (2013).
29. P. M. Mendes, "Stimuli-responsive surfaces for bio-applications," Chem. Soc. Rev. **37**, 2512-2529 (2008).
30. T. Ikeda, "Photomodulation of liquid crystal orientations for photonic applications," J. Mater. Chem. **13**, 2037-2057 (2003).
31. D. Liu, and D. J. Broer, "Liquid Crystal Polymer Networks: Preparation, Properties, and Applications of Films with Patterned Molecular Alignment," Langmuir **30**, 13499-13509 (2014).
32. M. Burnworth, L. Tang, J. R. Kumpfer, A. J. Duncan, F. L. Beyer, G. L. Fiore, S. J. Rowan, and C. Weder, "Optically healable supramolecular polymers," Nature **472**, 334-338 (2011).
33. J. H. Fendler, and P. Tundo, "Polymerized Surfactant Aggregates: Characterization and Utilization," Acc. Chem. Res. **17**, 3-8 (1984).
34. K. E. Evans, "Auxetic polymers: a new range of materials," **2001**, 9 (2001).
35. S. Babaee, J. Shim, J. C. Weaver, E. R. Chen, N. Patel, and K. Bertoldi, "3D Soft Metamaterials with Negative Poisson's Ratio," Adv. Mater. **25**, 5044-5049 (2013).
36. M. Bowick, A. Cacciuto, G. Thorleifsson, and A. Travesset, "Universal Negative Poisson Ratio of Self-Avoiding Fixed-Connectivity Membranes," Phys. Rev. Lett. **87**, 148103 (2001).
37. V. Koning, B. C. v. Zuiden, R. D. Kamien, and V. Vitelli, "Saddle-splay screening and chiral symmetry breaking in toroidal nematics," Soft Matter **10**, 4192-4198 (2014).
38. J. E. Martin, and K. J. Solis, "Symmetry-breaking magnetic fields create a vortex fluid that exhibits a negative viscosity, active wetting, and strong mixing," Soft Matter **10**, 3993-4002 (2014).
39. M. Kleman, and O. D. Lavrentovich, "Topological point defects in nematic liquid crystals," Philos. Mag. **86**, 4117–4137 (2006).
40. A. Yethiraj, and A. V. Bladderen, "A colloidal model system with an interaction tunable from hard sphere to soft and dipolar," Nature **421**, 513-517 (2003).
41. A. P. R. Eberle, N. J. Wagner, and R. Castaneda-Priego, "Dynamical Arrest Transition in Nanoparticle Dispersions with Short-Range Interactions," Phys. Rev. Lett. **106**, 105704 (2011).
42. S. Amemori, K. Kokado, and K. Sada, "Polymer Phase-Transition Behavior Driven by a Charge-Transfer Interaction," Angew. Chem. Int. Ed. **52**, 4174-4178 (2013).
43. P. N. Pusey, and W. V. Megen, "Observation of a Glass Transition in Suspensions of Spherical Colloidal Particles," Phys. Rev. Lett. **59**, 2083 (1987).
44. J. Mattsson, H. M. Wyss, A. Fernandez-Nieves, K. Miyazaki, Z. Hu, D. R. Reichman, and D. A. Weitz, "Soft colloids make strong glasses," Nature **462**, 83-86 (2009).
45. S. Gokhale, K. H. Nagamanasa, R. Ganapathy, and A. K. Sood, "Growing dynamical facilitation on approaching the random pinning colloidal glass transition," Nat. Commun. **5**, 4685 (2014).

46. J. Philip, G. G. Prakash, T. Jaykumar, P. Kalyanasundaram, and B. Raj, "Stretching and Collapse of Neutral Polymer Layers under Association with Ionic Surfactants," Phys. Rev. Lett. **89**, 268301 (2002).
47. V. J. Anderson, and H. N. W. Lekkerkerker, "Insights into phase transition kinetics from colloid science. Nature ." Nature **416**, 811–815 (2002).
48. A. Savelyev, and G. A. Papoian, "Molecular Renormalization Group Coarse-Graining of Polymer Chains: Application to Double-Stranded DNA," Biophys. J. **96**, 4044-4052 (2009).
49. C. N. Likos, "Effective Interactions in Soft Condensed Matter Physics," Phys. Rep. **348**, 267-439 (2001).
50. M. Nikkhou, M. Škarabot, S. Copar, M. Ravnik, S. Žumer, and I. Muševic, "Light-controlled topological charge in a nematic liquid crystal," Nat. Phys. **11**, 183-187 (2015).
51. C. Conti, G. Ruocco, and S. Trillo, "Optical Spatial Solitons in Soft Matter," Phys. Rev. Lett. **95**, 183902 (2005).
52. R. Signorell, and J. P. Reid, *Fundamentals and Applications in Aerosol Spectroscopy* (Taylor & Francis Group, Boca Raton, 2011).
53. D. Gromadzki, "Engineering soft nanostructured functional materials via orthogonal chemistry," Rev. Environ. Sci. Biotechnol. **9**, 301-306 (2010).
54. X. Liu, L. Chen, H. Liu, G. Yang, P. Zhang, D. Han, S. Wang, and L. Jiang, "Bio-inspired soft polystyrene nanotube substrate for rapid and highly efficient breast cancer-cell capture," NPG Asia Materials **5**, e63 (2013).
55. E. Ye, P. L. Chee, A. Prasad, X. Fang, C. Owh, V. J. J. Yeo, and X. J. Loh, "Supramolecular soft biomaterials for biomedical applications," Mater. Today **17**, 194-202 (2014).
56. E. I. Nep, P. O. Odumosu, N. C. Ngwuluka, P. O. Olorunfemi, and N. A. Ochekpe, "Pharmaceutical Properties and Applications of a Natural Polymer from Grewia mollis," J. Polym. **2013**, 938726 (2013).
57. M. Malmsten, "Soft drug delivery systems," Soft Matter **2**, 760-769 (2006).
58. E. Soussan, S. Cassel, M. Blanzat, and I. Rico-Lattes, "Drug Delivery by Soft Matter: Matrix and Vesicular Carriers," Angew. Chem. Int. Ed. **48**, 274-288 (2009).
59. R. E. Rosensweig, *Ferrohydrodynamics* (Dover Publications, Inc. New York, 1997).
60. S. Odenbach, *Colloidal Magnetic Fluids: Basics, Dvelopment and Application of Ferrofluids* (Springer-Verlag, Berlin Hiedelberg, 2009).
61. E. Blums, A. Cebers, and M. M. Maiorov, *Magnetic Fluids* (Walter de Gruyter, Berlin, 1997).
62. J. Bibette, F. Leal-Calderon, V. Schmitt, and P. Poulin, *Emulsion Science Basic Principles. An Overview* (Springer, New York, 2002).
63. J. Philip, and J. M. Laskar, "Optical Properties and Applications of Ferrofluids—A Review," J. Nanofluids **1**, 3-20 (2012).
64. J. Philip, O. Mondain-Monval, F. L. Calderon, and J. Bibette, "Colloidal force measurements in the presence of a polyelectrolyte," J. Phys. D: Appl. Phys. **30** 2798-2803 (1997).
65. S. Menear, A. Bradbury, and R. Chantrell, "A model of the properties of colloidal dispersions of weakly interacting fine ferromagnetic particles," J. Magn. Magn. Mater. **43**, 166-176 (1984).
66. K. Marton, L. Tomco, R. Cimbala, J. Király, I. M. Rajnák, M. Timko, P. Kopcanský, I. Kolcunová, J. Kurimský, and M. German-Sobek, "Magnetic fluid in ionizing electric field," J. Electrostate. **71**, 467-470 (2013).
67. S. L. Saville, R. C. Woodward, M. J. House, A. Tokarev, J. Hammers, B. Qi, J. Shaw, M. Saunders, R. R. Varsani, T. G. S. Pierre, and O. T. Mefford, "The effect of magnetically

induced linear aggregates on proton transverse relaxation rates of aqueous suspensions of polymer coated magnetic nanoparticles," Nanoscale **5** 2152-2163 (2013).
68. R. V. Mehta, "Ferromagnetic fluids," J. Sci. Ind. Res. **44**, 500-507 (1985).
69. F. Bitter, "Experiments on the Nature of Ferromagnetism," Phys. Rev. **41**, 507 (1932).
70. W. C. Elmore, "Ferromagnetic Colloid for Studying Magnetic Structures," Phys. Rev. **54**, 309 (1938).
71. Q. Li, *Intelligent Stimuli-Responsive Materials: From Well-Defined Nanostructures to Applications* (John Wiley & Sons, Inc. , New Jersey, 2013).
72. D. Roy, J. N. Cambre, and B. S. Sumerlin, "Future perspectives and recent advances in stimuli-responsive materials," Prog. Polym. Sci. **35**, 278-301 (2010).
73. M. W. Urban, *Handbook of Stimuli-Responsive Materials* (WILEY-VCH Verlag & Co. KGaA, Weinheim, Germany, 2011).
74. L.-B. Xing, B. Yang, X.-J. Wang, J.-J. Wang, B. Chen, Q. Wu, H.-X. Peng, L.-P. Zhang, C.-H. Tung, and L.-Z. Wu, "Reversible Sol-to-Gel Transformation of Uracil Gelators: Specific Colorimetric and Fluorimetric Sensor for Fluoride Ions," Langmuir **29**, 2843-2848 (2013).
75. P. Bawa, V. Pillay, Y. E. Choonara, and L. C. d. Toit, "Stimuli-responsive polymers and their applications in drug delivery," Biomed. Mater. **4**, 022001 (2009).
76. C. d. l. H. Alarcon, S. Pennadam, and C. Alexander, "Stimuli responsive polymers for biomedical applications," Chem. Soc. Rev. **34**, 276-285 (2005).
77. S.-M. Lee, and S. T. Nguyen, "Smart Nanoscale Drug Delivery Platforms from Stimuli-Responsive Polymers and Liposomes," Macromolecules **46**, 9169-9180 (2013).
78. J. Philip, P. D. Shima, and B. Raj, "Nanofluid with tunable thermal properties," Appl. Phys. Lett. **92**, 043108 (2008).
79. J. J. M. Janssen, and J. A. A. J. Perenboom, "Magneto-optical phenomena in magnetic fluids: the influence of orientation of anisotropic scatterers," J. Magn. Magn. Mater. **81**, 14-24 (1989).
80. G. Meriguet, E. Wandersman, E. Dubois, A. Cebers, J. d. A. Gomes, G. Demouchy, J. Depeyrot, A. Robert, and R. Perzynski, "Magnetic Fluids with Tunable Interparticle Interaction: Monitoring the under Field Local Structure," Magnetohydrodyn. **48**, 415–425 (2012).
81. K. I. Morozov, A. F. Pshenichinikoz, Y. L. Raikher, and M. I. Shliomis, "Magnetic Properties of Ferrocolloids: The Effect of Interparticle Interactions," J. Magn. Magn. Mat. **65**, 269-272 (1987).
82. P. C. Fannin, and S. W. Charles, "The study of a ferrofluid exhibiting both Brownian and Neel Relaxation," J. Phys D: Appl. Phys **22**, 187-191 (1989).
83. L. C. Figueiredo, P. P. Gravina, K. S. Neto, P. C. Morais, L. P. Silva, R. B. Azevedo, M. Wagener, and N. Buske, "Particle–particle interaction in magnetic fluids: A static magnetic birefringence investigation," J. Appl. Phys. **93**, 8453 (2003).
84. A. F. Bakuzis, A. R. Pereira, J. G. Santos, and P. C. Morais, "Superexchange coupling on oleylsarcosine-coated magnetite nanoparticles," J. Appl. Phys. **99**, 08C301 (2006).
85. B. Huke, and M. Lucke, "Magnetization of ferrofluids with dipolar interactions: A Born-Mayer expansion," Phys. Rev. E **62**, 6875 (2000).
86. A. O. Ivanov, and O. B. Kuznetsova, "Magnetic properties of dense ferrofluids: An influence of interparticle correlations," Phys. Rev. E **64**, 041405 (2001).
87. F. L. Calderon, T. Stora, O. M. Monval, P. Poulin, and J. Bibette, "Direct Measurement of Colloidal Forces," Phys. Rev. Lett. **72**, 2959 (1994).
88. P. Poulin, V. Cabuil, and D. A. Weitz, "Direct Measurement of Colloidal Forces in an Anisotropic Solvent," Phys. Rev. Lett. **79**, 4862 (1997).

89. X. Zhang, L. Liu, Y. Qi, Z. Liu, J. Shi, and W. Wen, "Frequency-controlled interaction between magnetic microspheres," Appl. Phys. Lett. **88**, 134107 (2006).
90. A. M. F. Neto, and M. M. F. Saba, "Determination of the minimum concentration of ferrofluid required to orient nematic liquid crystals," Phys. Rev. A **34**, 3483 (1986).
91. W. Luo, S. R. Nagel, T. F. Rosenbaum, and R. E. Rosensweig, "Dipole Interactions with Random Anisotropy in a Frozen Ferrofluid," Phys. Rev. Lett. **67**, 2721 (1991).
92. T. Johnsson, J. Mattsson, C. Djurberg, F. A. Khan, P. Nordblad, and P. Svedlindh, "Aging in a magnetic particle system," Phys. Rev. Lett. **75**, 4138 (1995).
93. J. J. O'Mahony, M. Platt, D. Kilinc, and G. Lee, "Synthesis of Superparamagnetic Particles with Tunable Morphologies: The Role of Nanoparticle−Nanoparticle Interactions," Langmuir **29**, 2546−2553 (2013).
94. T. Neuberger, B. Schopf, H. Hofmann, M. Hofmann, and B. v. Rechenberg, "Superparamagnetic nanoparticles for biomedical applications: Possibilities and limitations of a new drug delivery system," J. Magn. Magn. Mater. **293**, 483–496 (2005).
95. T. M. Nocera, J. Chen, C. B. Murray, and G. Agarwal, "Magnetic anisotropy considerations in magnetic force microscopy studies of single superparamagnetic nanoparticles," Nanotechnology **23**, 495704 (2012).
96. P. Kuswik, A. Ehresmann, M. Tekielak, B. Szymanski, I. Sveklo, P. Mazalski, D. Engel, J. Kisielewski, D. Lengemann, M. Urbaniak, C. Schmidt, A. Maziewski, and F. Stobiecki, "Colloidal domain lithography for regularly arranged artificial magnetic out-of-plane monodomains in Au/Co/Au layers," Nanotechnology **22**, 095302 (2011).
97. I. Hrianca, C. Caizer, and Z. Schlett, "Dynamic magnetic behavior of Fe_3O_4 colloidal nanoparticles," J. Appl. Phys. **92**, 2125 (2002).
98. J. L. Viota, J. D. G. Duran, F. Gonzalez-Caballero, and A. V. Delgado, "Magnetic properties of extremely bimodal magnetite suspensions," J. Magn. Magn. Mater. **314**, 80–86 (2007).
99. J. C. Bacri, A. Cebers, A. Bourdon, G. Demouchy, B. M. Heegaard, and R. Perzynski, "Forced Rayleigh Experiment in a Magnetic Fluid," Phys. Rev. Lett. **74**, 5032 (1995).
100. J. C. Bacri, A. Cebers, A. Bourdon, G. Demouchy, B. M. Heegaard, B. Kashevsky, and R. Perzynski, "Trasient grating in a ferrolfuid under magnetic field: Effect of magnetic interactions on the diffusion coefficient of translation," Phys. Rev. E **52**, 3936 (1995).
101. P. C. Fannin, and S. W. Charles, "Frequency of ferromagnetic resonance in ferrolfuids," Phys. Rev. B **52**, 16055 (1995).
102. P. C. Fannin, S. W. Charles, and T. Relihan, "On the broadband measurement of the permittivity and magnetic susceptibility of ferrofluids," J. Magn. Magn. Mater. **167**, 274-280 (1997).
103. P. C. Fannin, and C. N. Marin, "Determination of the Landau–Lifshitz damping parameter by means of complex susceptibility measurements," J. Magn. Magn. Mater. **299**, 425–429 (2006).
104. T. Jonsson, P. Svedlindh, and M. F. Hansen, "Static Scaling on an Interacting Magnetic Nanoparticle System," Phys. Rev. Lett. **81**, 3976 (1998).
105. P. C. Fannin, S. W. Charles, and A. T. Skjeltorp, "Apparent superdiamagnetism of diamagnetic spheres in ferrofluids," J. Magn. Magn. Mater. **201**, 113-115 (1999).
106. J. v. Lierop, and D. H. Ryan, "Superparamagnetic Spin Dynamics Studied Using Selective Excitation Double Mössbauer Spectroscopy," Phys. Rev. Lett. **85**, 3021 (2000).
107. M. Mohebi, N. Jamasbi, and J. Liu, "Simulation of the formation of nonequilibrium structures in magnetorheological fluids subject to an external magnetic field," Phys. Rev. E **54**, 5407 (1996).

108. E. Ghasemi, A. Mirhabibi, M. Edrissi, R. Aghababazadeh, and R. M. Brydson, "Study on the Magnetorheological Properties of Maghemite-Kerosene Ferrofluid," J. Nanosci. Nanotechnol. **9**, 4273–4278 (2009).
109. S. A. Lira, and J. A. Miranda, "Adhesion properties of chain-forming ferrofluids," Phys. Rev. E **79**, 046303 (2009).
110. O. Müller, D. Hahn, and M. Liu, "Non-Newtonian behaviour in ferrofluids and magnetization relaxation," J. Phys. Condens. Matter **18**, S2623-S2632 (2006).
111. P. Ilg, M. Kröger, and S. Hess, "Magnetoviscosity of semidilute ferrofluids and the role of dipolar interactions: Comparison of molecular simulations and dynamical mean-field theory," Phys. Rev. E **71**, 031205 (2005).
112. B. J. d. Gans, C. Blom, A. P. Philipse, and J. Mellema, "Linear viscoelasticity of an inverse ferrofluid," Phys. Rev. E **60**, 4518 (1999).
113. J. Nowak, F. Wiekhorst, L. Trahms, and S. Odenbach, "The influence of hydrodynamic diameter and core composition on the magnetoviscous effect of biocompatible ferrofluids," J. Phys. Condens. Matter **26**, 176004 (2014).
114. L. J. Felicia, and J. Philip, "Magnetorheological properties of a magnetic nanofluid with dispersed carbon nanotubes," Phys. Rev. E **89**, 022310 (2014).
115. M. I. Shliomis, and K. I. Morozov, "Negative viscosity of ferrofluid under alternating magnetic field," Phys. Fluids **6**, 2855-2861 (1994).
116. J. C. Bacri, R. Perzynski, M. I. Shliomis, and G. I. Burde, ""Negative-Viscosity" Effect in a Magnetic Fluid," Phys. Rev. Lett. **75**, 2128-2131 (1995).
117. G. Demouchy, A. Mezulis, A. Bee, D. Talbot, J. C. Bacri, and A. Bourdon, "Diffusion and thermodiffusion studies in ferrofluids with a new two-dimensional forced Rayleigh-scattering technique," J. Phys. D: Appl. Phys. **37**, 1417-1428 (2004).
118. A. Chaves, C. Rinaldi, S. Elborai, X. He, and M. Zahn, "Bulk Flow in Ferrofluids in a Uniform Rotating Magnetic Field," Phys. Rev. Lett. **96**, 194501 (2006).
119. R. Toussaint, E. G. Flekkøy, and G. Helgesen, "Memory of fluctuating Brownian dipolar chains," Phys. Rev. E **74**, 051405 (2006).
120. W. Luo, T. Du, and J. Huang, "Novel Convective Instabilities in a Magnetic Fluid," Phys. Rev. Lett. **82**, 4134-4137 (1999).
121. D. P. Jackson, R. E. Goldstein, and A. O. Cebers, "Hydrodynamics of fingering instabilities of dipolar fluids," Phys. Rev. E **50**, 298 (1994).
122. J. Singh, and R. Bajaj, "Convective instability in a ferrofluid layer with temperature-modulated rigid boundaries," Fluid Dyn. Res. **43**, 025502 (2011).
123. D. Laroze, J. Martinez-Mardones, and H. Pleiner, "Benard-Marangoni instability in a viscoelastic ferrofluid," Eur. Phys. J. Spec. Top. **219**, 71-80 (2013).
124. G. Pacitto, C. Flament, J.-C. Bacri, and M. Widom, "Rayleigh-Taylor instability with magnetic fluids: Experiment and theory," Phys. Rev. E **62**, 7941 (2000).
125. Z. Huang, A. D. Luca, T. J. Atherton, M. Bird, C. Rosenblatt, and P. Carles, "Rayleigh-Taylor Instability Experiments with Precise and Arbitrary Control of the Initial Interface Shape," Phys. Rev. Lett. **99**, 204502 (2007).
126. J. White, J. Oakley, M. Anderson, and R. Bonazza, "Experimental measurements of the nonlinear Rayleigh-Taylor instability using a magnetorheological fluid," Phys. Rev. E **81**, 026303 (2010).
127. A. G. Boudouvis, J. L. Puchalla, L. E. Scriven, and R. E. Rosensweig, "Normal field instability and patterns in pools of ferrofluid," J. Magn. Magn. Mater. **65**, 307-310 (1987).
128. E. I. Kats, "Rosensweig instability in ferrofluids," Low Temp. Phys. **37**, 812-814 (2011).
129. M. D. Cowley, and R. E. Rosensweig, "The interfacial stability of a ferromagnetic fluid," J. Fluid. Mech. **30**, 671-688 (1967).

130. A. Ryskin, and H. Pleiner, "Magnetic Field Driven Instability in Stratified Ferrofluids," Phys. Rev. E **75**, 056303 (2007).
131. S. A. Langer, R. E. Goldstein, and D. P. Jackson, "Dynamics of labyrinthine pattern formation in magnetic fluids," Phys. Rev. A **46**, 4894 (1992).
132. C.-Y. Chen, S.-Y. Wu, and J. A. Miranda, "Fingering patterns in the lifting flow of a confined miscible ferrofluid," Phys. Rev. E **75**, 036310 (2007).
133. F. Boyer, and E. Falcon, "Wave Turbulence on the Surface of a Ferrofluid in a Magnetic Field," Phys. Rev. Lett. **101**, 244502 (2008).
134. S. Dorbolo, and E. Falcon, "Wave turbulence on the surface of a ferrofluid in a horizontal magnetic field," Phys. Rev. E **83**, 046303 (2011).
135. R. Richter, and V. Barashenkov, "Two-Dimensional Solitons on the Surface of Magnetic Fluids," Phys. Rev. Lett. **94**, 184503 (2005).
136. N.-T. Nguyen, K. M. Ng, and X. Huang, "Manipulation of ferrofluid droplets using planar coils," Appl. Phys. Lett. **89**, 052509 (2006).
137. N.-T. Nguyen, G. Zhu, Y.-C. Chua, V.-N. Phan, and S.-H. Tan, "Magnetowetting and Sliding Motion of a Sessile Ferrofluid Droplet in the Presence of a Permanent Magnet," Langmuir **26**, 12553–12559 (2010).
138. G.-P. Zhu, N.-T. Nguyen, R. V. Ramanujan, and X.-Y. Huang, "Nonlinear Deformation of a Ferrofluid Droplet in a Uniform Magnetic Field," Langmuir **27**, 14834–14841 (2011).
139. J. Philip, P. D. Shima, and B. Raj, "Enhancement of thermal conductivity in magnetite based nanofluid due to chainlike structures," Appl. Phys. Lett. **91**, 203108 (2007).
140. A. Engel, H. W. Muller, P. Reimann, and A. Jung, "Ferrofluids as Thermal Ratchets," Phys. Rev. Lett. **91**, 060602 (2003).
141. F. Boyer, and E. Falcon, "Two-Dimensional Melting of a Crystal of Ferrofluid Spikes," Phys. Rev. Lett. **103**, 144501 (2009).
142. A. F. Bakuzis, M. F. D. Silva, P. C. Morais, and K. S. Neto, "Irreversibility of zero-field birefringence in ferrofluids upon temperature reversal," J. Appl. Phys. **87**, 2307 (2000).
143. P. Zu, C. C. Chan, W. S. Lew, Y. Jin, H. F. Liew, W. C. Wong, X. Dong, and C. Z. Foo, "Laser self-induced tunable birefringence of magnetic fluid," Appl. Phys. Lett. **102**, 181116 (2013).
144. S. Pu, X. Chen, W. Liao, L. Chen, Y. Chen, and Y. Xia, "Laser self-induced thermo-optical effects in a magnetic fluid," J. Appl. Phys. **96**, 5930 (2004).
145. K. Raj, B. Moskowitz, and R. Casciari, "Advances in ferrofluid technology," J. Magn. Magn. Mater. **149**, 174-180 (1995).
146. N. Saga, and T. Nakamura, "Elucidation of propulsive force of microrobot using magnetic fluid," J. Appl. Phys. **91**, 7003 (2002).
147. J. Hesselbach, and C. Abel-Keilhack, "Active hydrostatic bearing with magnetorheological fluid," J. Appl. Phys. **93**, 8441 (2003).
148. R. Ravaud, G. Lemarquand, and V. Lemarquand, "Magnetic pressure and shape of ferrofluid seals in cylindrical structures," J. Appl. Phys. **106**, 034911 (2009).
149. J. Philip, C. B. Rao, T. Jayakumar, and B. Raj, "A new optical technique for detection of defects in ferromagnetic materials and components," NDT & E Int. **33**, 289-295 (2000).
150. V. Mahendran, and J. Philip, "Nanofluid based optical sensor for rapid visual inspection of defects in ferromagnetic materials," Appl. Phys. Lett. **100**, 073104 (2012).
151. S. Pu, X. Chen, L. Chen, W. Liao, Y.Chen, and Y.Xia, "Tunable magnetic fluid grating by applying a magnetic field," Appl. Phys. Lett. **87**, 021901 (2005).
152. S. Pu, L. Yao, F. Guan, and M. Liu, "Threshold-tunable optical limiters based on nonlinear refraction in ferrosols," Opt. Commun. **282**, 908-913 (2009).

153. Y. Melikhov, S. J. Lee, D. C. Jiles, D. H. Schmidt, M. D. Porter, and R. Shinar, "Microelectromagnetic ferrofluid-based actuator," J. Appl. Phys. **93**, 8438 (2003).
154. J. J. Chieh, S. Y. Yang, H. E. Horng, C. Y. Hong, and H. C. Yang, "Magnetic-fluid optical-fiber modulators via magnetic modulation," Appl. Phys. Lett. **90**, 133505 (2007).
155. S. Pu, X. Chen, Z. Di, and Y. Xia, "Relaxation property of the magnetic-fluid-based fiber-optic evanescent field modulator," J. Appl. Phys. **101**, 053532 (2007).
156. F. Choueikani, F. Royer, D. Jamon, A. Siblini, J. J. Rousseau, S. Neveu, and J. Charara, "Magneto-optical waveguides made of cobalt ferrite nanoparticles embedded in silica/zirconia organic-inorganic matrix," Appl. Phys. Lett. **94,** , 051113 (2009).
157. T. Liu, X. Chen, Z. Di, J. Zhang, X. Li, and J. Chen, "Tunable magneto-optical wavelength filter of long-period fiber grating with magnetic fluids," Appl. Phys. Lett. **91**, 121116 (2007).
158. H. E. Horng, C. S. Chen, K. L. Fang, S. Y. Yang, J. J. Chieh, C. Y. Hong, and H. C. Yang, "Tunable optical switch using magnetic fluids," Appl. Phys. Lett. **85**, 5592 (2004).
159. S. Pu, and S. Dong, "Magnetic Field Sensing Based on Magnetic-Fluid-Clad Fiber-Optic Structure With Up-Tapered Joints," IEEE Photon. J. **6**, 5300206 (2014).
160. V. Mahendran, and J. Philip, "A methanol sensor based on stimulus-responsive magnetic nanoemulsions," Sensors and Actuators B **185**, 488-495 (2013).
161. L. Mao, and H. Koser, "Towards ferrofluidics for μ-TAS and lab on-a-chip applications," Nanotechnology **17**, S34-S47 (2006).
162. V. Mahendran, and J. Philip, "An optical technique for fast and ultrasensitive detection of ammonia using magnetic nanofluids," Appl. Phys. Lett. **102**, 063107 (2013).
163. P. D. Shima, and J. Philip, "Tuning of Thermal Conductivity and Rheology of Nanofluids Using an External Stimulus," J. Phys. Chem. C **115**, 20097-20104 (2011).
164. E. Tombacz, D. Bica, A. Hajdu, E. Illes, A. Majzik, and L. Vekas, "Surfactant double layer stabilized magnetic nanofluids for biomedical application," J. Phys. Condens. Matter **20**, 204103 (2008).
165. M. Strömberg, K. Gunnarsson, S. Valizadeh, P. Svedlindha, and M. Strømme, "Aging phenomena in ferrofluids suitable for magnetic biosensor applications," J. Appl. Phys. **101**, 023911 (2007).
166. N. Pekas, M. D. Porter, M. Tondra, A. Popple, and A. Jander, "Giant magnetoresistance monitoring of magnetic picodroplets in an integrated microfluidic system," Appl. Phys. Lett. **85**, 4783 (2004).
167. R. Kappiyoor, M. Liangruksa, R. Ganguly, and I. K. Puri, "The effects of magnetic nanoparticle properties on magnetic fluid hyperthermia," J. Appl. Phys. **108**, 094702 (2010).
168. D. F. Coral, P. M. Zelis, M. E. d. Sousa, D. Muraca, V. Lassalle, P. Nicolas, M. L. Ferreira, and M. B. F. v. Raap, "Quasi-static magnetic measurements to predict specific absorption rates in magnetic fluid hyperthermia experiments," J. Appl. Phys. **115**, 043907 (2014).
169. Y. Huang, J. H. Kim, S. I. Park, H. Shao, and C. O. Kim, "Preparation of nanometric $Cu_xFe_{1-x}OFe_2O_3$ for treatment of tumor," J. Appl. Phys. **93**, 8444 (2003).
170. P. P. Macaroff, A. R. Simioni, Z. G. M. Lacava, E. C. D. Lima, P. C. Morais, and A. C. Tedesco, "Studies of cell toxicity and binding of magnetic nanoparticles with blood stream macromolecules," J. Appl. Phys. **99**, 08S102 (2006).
171. J. B. Mathieu, and S. Martel, "Aggregation of magnetic microparticles in the context of targeted therapies actuated by a magnetic resonance imaging system," J. Appl. Phys. **106**, 044904 (2009).
172. J. M. Laskar, J. Philip, and B. Raj, "Experimental evidence for reversible zippering of chains in magnetic nanofluids under external magnetic fields," Phys. Rev. E **80**, 041401 (2009).

173. S. Altmeyer, "Time-Dependent Ferrofluid Dynamics in Symmetry Breaking Transverse," Open J. Fluid Dyn. **3**, 116-126 (2013).
174. A. Wiedenmann, U. Keiderling, M. Meissner, D. Wallacher, R. Gähler, R. P. May, S. Prévost, M. Klokkenburg, B. H. Erné, and J. Kohlbrecher, "Low-temperature dynamics of magnetic colloids studied by time-resolved small-angle neutron scattering," Phys. Rev. B **77**, 184417 (2008).
175. M. Klokkenburg, B. H. Erné, A. Wiedenmann, A. V. Petukhov, and A. P. Philipse, "Dipolar structures in magnetite ferrofluids studied with small-angle neutron scattering with and without applied magnetic field," Phys. Rev. E **75**, 051408 (2007).
176. A. Wiedenmann, A. Hoell, M. Kammel, and P. Boesecke, "Field-induced pseudocrystalline ordering in concentrated ferrofluids," Phys. Rev. E **68**, 031203 (2003).
177. A. V. Teixeira, I. Morfin, F. Ehrburger-Dolle, C. Rochas, E. Geissler, P. Licinio, and P. Panine, "Scattering from dilute ferrofluid suspensions in soft polymer gels," Phys. Rev. E **67**, 021504 (2003).
178. E. Dubois, V. Cabuil, F. Boue, and R. Perzynski, "Structural analogy between aqueous and oily magnetic fluids," J. Chem. Phys. **111**, 7147-7160 (1999).
179. A. Wiedenmann, U. Keiderling, K. Habicht, M. Russina, and R. Gahler, "Dynamics of Field-Induced Ordering in Magnetic Colloids Studied by New Time-Resolved Small-Angle Neutron-Scattering Techniques," Phys. Rev. Lett. **97** 057202 (2006).
180. M. F. d. Silva, and A. M. F. Neto, "Optical- and x-ray-scattering Studies of ionic ferrofluids of $MnFe_2O_4$, γ-Fe_2O_3, and $CoFe_2O_4$," Phys. Rev. E **48**, 4483 (1993).
181. T. Kruse, H.-G. Krauthauser, A. Spanoudaki, and R. Pelster, "Agglomeration and chain formation in ferrofluids: Two-dimensional x-ray scattering," Phys. Rev. B **67**, 094206 (2003).
182. B. J. Lemaire, P. Davidson, P. Panine, and J. P. Jolivet, "Magnetic-Field-Induced Nematic-Columnar Phase Transition in Aqueous Suspensions of Goethite (α-FeOOH) Nanorods," Phys. Rev. Lett. **93** 267801 (2004).
183. J. M. Laskar, J. Philip, and B. Raj, "Light scattering in a magnetically polarizable nanoparticle suspension," Phys. Rev. E **78**, 031404 (2008).
184. J. Li, Y. Lin, X. Liu, Q. Zhang, H. Miao, J. Fu, and L. Lin, "A magnetic field-dependent modulation effect tends to stabilize light transmission through binary ferrofluids," Opt. Commun. **285**, 3111–3115 (2012).
185. M. Saito, and Y. Hirose, "Anisotropic transmission properties of magnetic fluids in the midinfrared region," J. Opt. Soc. Am. B **28**, 1645-1649 (2011).
186. S. Chen, F. Fan, S. Chang, Y. Miao, M. Chen, J. Li, X. Wang, and L. Lin, "Tunable optical and magneto-optical properties of ferrofluid in the terahertz regime," Opt. Express **22**, 6313-6321 (2014).
187. D. Heinrich, A. R. Goñi, and C. Thomsen, "Dynamics of magnetic-field-induced clustering in ionic ferrofluids from Raman scattering," J. Chem. Phys. **126**, 124701 (2007).
188. J. E. Weber, A. R. Goni, and C. Thomsen, "Raman study of magnetic field effects on surfacted and ionic ferrofluids," J. Magn. Magn. Mater. **277**, 96-100 (2004).
189. S. Melle, M. A. Rubio, and G. G. Fuller, "Time Scaling Regimes in Aggregation of Magnetic Dipolar Particles: Scattering Dichroism Results," Phys. Rev. Lett. **87**, 115501 (2001).
190. M. Klokkenburg, B. H. Erne, J. D. Meeldijk, A. Wiedenmann, A. V. Petukhov, R. P. A. Dullens, and A. P. Philipse, "In Situ Imaging of Field-Induced Hexagonal Columns in Magnetite Ferrofluids," Phys. Rev. Lett. **97**, 185702 (2006).
191. J. Wu, M. Aslam, and V. P. Dravid, "Imaging of magnetic colloids under the influence of magnetic field by cryogenic transmission electron microscopy," Appl. Phys. Lett. **93** 082505 (2008).

192. W.-X. Fang, Z.-H. He, X.-Q. Xu, Z.-Q. Mao, and H. Shen, "Magnetic-field-induced chain-like assembly structures of Fe_3O_4 nanoparticles," Europhys. Lett. **77**, 68004 (2007).
193. Y. Sahoo, A. Goodarzi, M. T. Swihart, T. Y. Ohulchanskyy, N. Kaur, E. P. Furlani, and P. N. Prasad, "Aqueous Ferrofluid of Magnetite Nanoparticles: Fluorescence Labeling and Magnetophoretic Control," J. Phys. Chem. B **109**, 3879-3885 (2005).
194. M. F. Islam, K. H. Lin, D. Lacoste, T. C. Lubensky, and A. G. Yodh, "Field-induced structures in miscible ferrofluid suspensions with and without latex spheres," Phys. Rev. E **67**, 021402 (2003).
195. F. Martínez-Pedrero, A. El-Harrak, J. C. Fernández-Toledano, M. Tirado-Miranda, J. Baudry, A. Schmitt, J. Bibette, and J. Callejas-Fernández, "Kinetic study of coupled field-induced aggregation and sedimentation processes arising in magnetic fluids," Phys. Rev. E **78**, 011403 (2008).
196. A. Skumiel, T. Hornowski, and A. Jozefczak, "Investigation of magnetic fluids by ultrasonic and magnetic methods," Ultrasonics **38**, 864–867 (2000).
197. A. Jozefczak, "Ultrasonic study of the effect of time of the ferrofluid exposure to magnetic field on its structure," J. Magn. Magn. Mater. **272–276**, e1691–e1692 (2004).
198. A. Jozefczak, and A. Skumiel, "Field-induced aggregates in a bilayer ferrofluid characterized by ultrasound spectroscopy," J. Phys. Condens. Matter **18**, 1869–1876 (2006).
199. J. Masajada, M. Bacia, and S. Drobczyński, "Cluster formation in ferrofluids induced by holographic optical tweezers," Opt. Lett. **38**, 3910-3913 (2013).
200. T. Kruse, A. Spanoudaki, and R. Pelster, "Monte Carlo simulations of polydisperse ferrofluids: Cluster formation and field-dependent microstructure," Phys. Rev. B **68**, 054208 (2003).
201. M. J. Stevens, and G. S. Grest, "Coexistence in dipolar fluids in a field," Phys. Rev. Lett. **72**, 3686-3689 (1994).
202. P. J. Camp, and G. N. Patey, "Structure and scattering in colloidal ferrofluids," Phys. Rev. E **62**, 5403-5408 (2000).
203. J. Richardi, and M. P. Pileni, "Self-organization of magnetic nanoparticles: A Monte Carlo study," Phys. Rev. E **77**, 061510 (2008).
204. E. A. Polyakov, and P. N. Vorontsov-Velyaminov, "Reference hypernetted chain theory for ferrofluid bilayer: Distribution functions compared with Monte Carlo," J. Chem. Phys. **141**, 084109 (2014).
205. D. Q. Wei, and G. N. Patey, "Orientational order in simple dipolar liquids: Computer simulation of a ferroelectric nematic phase," Phys. Rev. Lett. **68**, 2043-2045 (1992).
206. P. Jund, S. G. Kim, D. Tomanek, and J. Hetherington, "Stability and Fragmentation of Complex Structures in Ferrofluids," Phys. Rev. Lett. **74**, 3049 (1995).
207. J. Jordanovic, S. Jäger, and S. H. L. Klapp, "Crossover from Normal to Anomalous Diffusion in Systems of Field-Aligned Dipolar Particles," Phys. Rev. Lett. **106**, 038301 (2011).
208. T. Ukai, and T. Maekawa, "Patterns formed by paramagnetic particles in a horizontal layer of a magnetorheological fluid subjected to a dc magnetic field," Phys. Rev. E **69**, 032501 (2004).
209. P. D. Duncan, and P. J. Camp, "Aggregation Kinetics and the Nature of Phase Separation in Two-Dimensional Dipolar Fluids," Phys. Rev. Lett. **97**, 107202 (2006).
210. E. A. Elfimova, A. O. Ivanov, and P. J. Camp, "Theory and simulation of anisotropic pair correlations in ferrofluids in magnetic fields," J. Chem. Phys. **136**, 194502 (2012).
211. C. Z. Fan, E. J. Liang, and J. P. Huang, "Optical properties in the soft photonic crystals based on ferrofluids," J. Phys. D: Appl. Phys. **44**, 325003 (2011).

212. J. Wu, Y. Miao, B. Song, W. Lin, H. Zhang, K. Zhang, B. Liu, and J. Yao, "Low temperature sensitive intensity-interrogated magnetic field sensor based on modal interference in thin-core fiber and magnetic fluid," Appl. Phys. Lett. **104**, 252402 (2014).
213. Y. Miao, J. Wu, W. Lin, K. Zhang, Y. Yuan, B. Song, H. Zhang, B. Liu, and J. Yao, "Magnetic field tunability of optical microfiber taper integrated with ferrofluid," Opt. Express **21**, 29914-29920 (2013).
214. C. Fan, J. Wang, S. Zhu, J. He, P. Ding, and E. Liang, "Optical properties in one-dimensional graded soft photonic crystals with ferrofluids," J. Opt. **15**, 055103 (2013).
215. Y. Gao, J. P. Huang, Y. M. Liu, L. Gao, K. W. Yu, and X. Zhang, "Optical Negative Refraction in Ferrofluids with Magnetocontrollability," Phys. Rev. Lett. **104**, 034501 (2010).
216. M. Fu, Y. Zhang, J. Wu, X. Dai, and Y. Xiang, "Large and negative Goos–Hanchen shift with magneto-controllability based on a ferrofluid," J. Opt. **15**, 035103 (2013).
217. L. Li, Q. Han, T. Liu, Y. Chen, and R. Zhang, "Reflective all-fiber current sensor based on magnetic fluids," Rev. Sci. Instrum. **85**, 083107 (2014).
218. M. Xu, and P. J. Ridler, "Linear dichroism and birefringence effects in magnetic fluids," J. Appl. Phys. **82**, 326 (1997).
219. K. S. Neto, A. F. Bakuzis, A. R. Pereira, and P. C. Morais, "Magnetic aging in magnetic fluids: a static magnetic birefringence investigation," J. Magn. Magn. Mater. **226-230** 1893-1895 (2001).
220. N. A. Yusuf, A. A. Rousan, and H. M. El-Ghanem, "The wavelength dependence of Faraday rotation in magnetic fluids " J. Appl. Phys. **64**, 2781 (1988).
221. N. A. Yusuf, "The Transient Behavior of Light Transmission and Faraday Rotation in Magnetic Fluids " Jpn. J. Appl. Phys. **27**, 2418 (1988).
222. J.-F. Lin, and M.-Z. Lee, "Concurrent measurement of linear birefringence and dichroism in ferrofluids using rotating-wave-plate Stokes polarimeter," Opt. Commun. **285** 1669-1674 (2012).
223. H. Bhatt, and R. Patel, "Optical Transport in Bidispersed Magnetic Colloids with Varying Refractive Index," J. Nanofluids **2**, 188-193 (2013).
224. S. Y. Yang, J. J. Chieh, H. E. Horng, C. Y. Hong, and H. C. Yang, "Origin and applications of magnetically tunable refractive index of magnetic fluid films," Appl. Phys. Lett. **84**, 5204 (2004).
225. F. A. Pinheiro, A. S. Martinez, and L. C. Sampaio, "Vanishing of Energy Transport Velocity and Diffusion Constant of Electromagnetic Waves in Disordered Magnetic Media," Phys. Rev. Lett. **85**, 5563 (2000).
226. F. A. Pinheiro, A. S. Martinez, and L. C. Sampaio, "New Effects in Light Scattering in Disordered Media and Coherent Backscattering Cone : Systems of Magnetic Particles," Phys. Rev. Lett. **84**, 1435 (2000).
227. H. Bhatt, R. Patel, and R. V. Mehta, "Energy transport velocity in bidispersed magnetic colloids," Phys. Rev. E **86**, 011401 (2012).
228. D. Lacoste, F. Donatini, S. Neveu, J. A. Serughetti, and B. A. V. Tiggelen, "Photonic Hall effect in ferrofluids: Theory and experiments," Phys. Rev. E **62**, 3934 (2000).
229. J. M. Laskar, B. Raj, and J. Philip, "Enhanced transmission with tunable Fano-like profile in magnetic nanofluids," Phys. Rev. E **84**, 051403 (2011).
230. M. Shalaby, M. Peccianti, Y. Ozturk, M. Clerici, I. Al-Naib, L. Razzari, T. Ozaki, A. Mazhorova, M. Skorobogatiy, and R. Morandotti, "Terahertz Faraday rotation in a magnetic liquid: High magneto-optical figure of merit and broadband operation in a ferrofluid," Appl. Phys. Lett. **100**, 241107 (2012).
231. C. Vales-Pinzón, J. J. Alvarado-Gil, R. Medina-Esquivel, and P. Martínez-Torres, "Polarized light transmission in ferrofluids loaded with carbon nanotubes in the presence of a uniform magnetic field," J. Magn. Magn. Mater. **369**, 114-121 (2014).

232. M. Adrian, and L. E. Helseth, "Magnetically tunable optical absorbance in a colloidal system," Phys. Rev. E **77**, 021403 (2008).
233. C. Rablau, P. Vaishnava, C. Sudakar, R. Tackett, G. Lawes, and R. Naik, "Magnetic-field-induced optical anisotropy in ferrofluids: A time-dependent light-scattering investigation," Phys. Rev. E **78**, 051502 (2008).
234. M. Vivacqua, D. Espinosa, and A. M. F. Neto, "Application of the Z-scan technique to determine the optical Kerr coefficient and two-photon absorption coefficient of magnetite nanoparticles
colloidal suspension," J. Appl. Phys. **111**, 113509 (2012).
235. J. M. Laskar, J. Philip, and B. Raj, "Experimental investigation of magnetic-field-induced aggregation kinetics in nonaqueous ferrofluids," Phys. Rev. E **82**, 021402 (2010).
236. A. F. Pshenichnikov, and V. Mekhonoshin, "Cluster structure and the first-order phase transition in dipolar systems," Eur. Phys. J. E **6**, 399-407 (2001).
237. J. Li, X. Liu, Y. Lin, X. Qiu, X. Ma, and Y. Huang, "Field–induced transmission of light in ionic ferrofluids of tunable viscosity," J. Phys. D: Appl. Phys. **37** 3357–3360 (2004).
238. J. Li, B. Zhao, Y. Lin, X. Qiu, and X. Ma, "Transmission of light in ionic ferrofluid," J. Appl. Phys. **92**, 1128 (2002).
239. L. Chen, J. Li, X. Qiu, Y. Lin, X. Liu, H. Miao, and J. Fu, "Magneto-optical effect in a system of colloidal particle having anisotropic dielectric property," Opt. Commun. **316**, 146-151 (2014).
240. M. T. A. Eloi, J. J. L. Santos, P. C. Morais, and A. F. Bakuzis, "Field-induced columnar transition of biocompatible magnetic colloids:An aging study by magnetotransmissivity," Phys. Rev. E **82**, 021407 (2010).
241. R. Patel, and A. Raval, "Magneto-optical techniques to determine Curie temperature of magnetic fluids," Appl. Phys. Lett. **90**, 254104 (2007).
242. A. P. R. Mary, C. S. S. Sandeep, T. N. Narayanan, R. Philip, P. Moloney, P. M. Ajayan, and M. R. Anantharaman, "Nonlinear and magneto-optical transmission studies on magnetic nanofluids of non-interacting metallic nickel nanoparticles," Nanotechnology **22**, 375702 (2011).
243. C. Z. Fan, G. Wang, and J. P. Huang, "Magnetocontrollable photonic crystals based on colloidal ferrofluids," J. Appl. Phys. **103**, 094107 (2008).
244. H. E. Ghandoor, H. M. Zidan, M. M. H. Khalil, and M. I. M. Ismail, "Application of laser speckle interferometry for the study of $Co_xFe_{(1-x)}Fe_2O_4$ magnetic fluids," Phys. Scr. **86**, 015403 (2012).
245. R. Massart, "Preparation of aqueous magnetic liquids in alkaline and acidic media," IEEE Trans. Magn. **17**, 1247-1248 (1981).
246. G. Gnanaprakash, J. Philip, T. Jayakumar, and B. Raj, "Effect of Digestion Time and Alkali Addition Rate on Physical Properties of Magnetite Nanoparticles," J. Phys. Chem. B **111**, 7978-7986 (2007).
247. J. Bibette, "Monodisperse ferrofluid emulsions," J. Magn. Magn. Mater. **122**, 37-41 (1993).
248. P. D. Shima, J. Philip, and B. Raj, "Synthesis of Aqueous and Nonaqueous Iron Oxide Nanofluids and Study of Temperature Dependence on Thermal Conductivity and Viscosity," J. Phys. Chem. C **114**, 18825–18833 (2010).
249. S. Ayyappan, G. Gnanaprakash, G. Panneerselvam, M. P. Antony, and J. Philip, "Effect of Surfactant Monolayer on Reduction of Fe_3O_4 Nanoparticles under Vacuum," J. Phys. Chem. C **112**, 18376–18383 (2008).
250. V. Mahendran, and J. Philip, "Influence of Ag+ Interaction on 1D Droplet Array Spacing and the Repulsive Forces between Stimuli-Responsive Nanoemulsion Droplets," Langmuir **30**, 10213–10220 (2014).

251. G. F. Knoll, *Radiation Detection and Measurement* (John Wiley and Sons, New York, 1979).
252. *Photomultiplier Tubes: Basics and Applications* (HAMAMATSU, 2007).
253. B. J. Berne, and R. Pecora, *Dynamic Light Scattering With Applications to Chemistry, Biology, and Physics* (Dover Publications, Inc., New York, 2000).
254. P. C. Hiemenz, and T. P. Lodge, *Polymer Chemistry* (Taylor & Francis Group, Boca Raton, 2007).
255. A. H. Bennett, H. Osterberg, H. Jupnik, and O. W. Richards, *Phase Microscopy: Principles and Applications* (Wiley, New York, 1951).
256. M. I. Mischenko, L. D. Travis, and A. A. Lacis, *Scattering, Absorption, and Emission of Light by Small Particles* (Cambride University Press, Cambridge, UK, 2002).
257. L. Novotony, and B. Hecht, *Principles of Nano-Optics* (Cambridge University Press, New York, 2006).
258. W. Schartl, *Light Scatering from Polymers Solutions and Nanoparticle Dispersions* (Springer, Berlin, 2007).
259. R. Lenke, R. Tweer, and G. Maret, "Coherent backscattering of turbid samples containing large Mie spheres," J. Opt. A: Pure Appl. Opt. **4**, 293-298 (2002).
260. F. Scheffold, and G. Maret, "Universal Conductance Fluctuations of Light," Phys. Rev. Lett. **81**, 5800 (1998).
261. Y. Piederriere, J. L. Meur, J. Cariou, J. F. Abgrall, and M. T. Blouch, "Particle aggregation monitoring by speckle size measurement; application to blood platelets aggregation," Opt. Express **12**, 4596-4601 (2004).
262. W. H. Slade, E. Boss, and C. Russo, "Effects of particle aggregation and disaggregation on their inherent optical properties," Opt. Express **19**, 7945-7959 (2011).
263. Y. Fainman, L. Lee, D. Psaltis, and C. Yang, *Optofluidics: Fundamentals, Devices, and Applications* (McGraw-Hill Companies, Inc., New York, 2010).
264. D. Psaltis, S. R. Quake, and C. Yang, "Developing optofluidic technology through the fusion of microfluidics and optics," Nature **442**, 381-386 (2006).
265. X. Fan, and I. M. White, "Optofluidic microsystems for chemical and biological analysis," Nature Photon. **5**, 591-597 (2011).
266. J. R. Henderson, and T. M. Crawford, "Repeatability of magnetic-field driven self-assembly of magnetic nanoparticles," J. Appl. Phys. **109**, 07D329 (2011).
267. C.-P. Lee, H.-C. Chang, and M.-F. Lai, "Magnetocapillary phenomenon affected by magnetic films," J. Appl. Phys. **109**, 07E310 (2011).
268. C.-Y. Chen, W.-L. Wu, and J. A. Miranda, "Magnetically induced spreading and pattern selection in thin ferrofluid drops," Phys. Rev. E **82**, 056321 (2010).
269. P. D. Shima, J. Philip, and B. Raj, "Magnetically controllable nanofluid with tunable thermal conductivity and viscosity," Appl. Phys. Lett. **95**, 133112 (2009).
270. H. Bhatt, R. Patel, and R. V. Mehta, "Magnetically induced Mie resonance in a magnetic sphere suspended in a ferrofluid," J. Opt. Soc. Am. A **27**, 873-877 (2010).
271. J. Philip, J. M. Laskar, and B. Raj, "Magnetic field induced extinction of light in a suspension of Fe_3O_4 nanoparticles," Appl. Phys. Lett. **92**, 221911 (2008).
272. M. Ivey, J. Liu, Y. Zhu, and S. Cutillas, "Magnetic-field-induced structural transitions in a ferrofluid emulsion," Phys. Rev. E **63**, 011403 (2000).
273. R. Haghgooie, and P. S. Doyle, "Transition from two-dimensional to three-dimensional behavior in the self-assembly of magnetorheological fluids confined in thin slits," Phys. Rev. E **75**, 061406 (2007).
274. V. Danilov, T. Prokopyeva, and S. Kantorovich, "Ground-state structures and structural transitions in a monolayer of magnetic dipolar particles in the presence of an external magnetic field," Phys. Rev. E **86**, 061408 (2012).

275. D. Heinrich, A. R. Goni, A. Smessaert, S. H. L. Klapp, L. M. C. Cerioni, T. M. Osan, D. J. Pusiol, and C. Thomsen, "Dynamics of the Field-Induced Formation of Hexagonal Zipped-Chain Superstructures in Magnetic Colloids," Phys. Rev. Lett. **106**, 208301 (2011).
276. F. Martinez-Pedredo, A. El-Harrak, J. C. Fernandez-Tolenado, M.Tirado-Miranda, J. Baudry, A. Schmitt, J. Bibette, and J. C. Fernandez, "Kinetic study of coupled field-induced aggregation and sedimentation processes arising in magnetic fluids," Phys. Rev. E **78**, 011403 (2008).
277. D. Lorenzo, D. Fragouli, G. Bertoni, C. Innocenti, G. C. Anyfantis, P. D. Cozzoli, R. Cingolani, and A. Athanassiou, "Formation and magnetic manipulation of periodically aligned microchains in thin plastic membranes," J. Appl. Phys. **112**, 083927 (2012).
278. E. Pyanzina, S. Kantorovich, J. J. Cerd, and C. Holm, "Structure factor of ferrofluds with chain aggregates:Theory and computer simulations," J. Magn. Magn. Mater. **323**, 1263-1268 (2011).
279. P. J. Camp, "Dynamics in a two-dimensional core-softened fluid," Phys. Rev. E **71**, 031507 (2005).
280. G. L. J. A. Rikken, and B. A. V. Tiggelen, "Observation of magnetically induced transverse diffusion of light " Nature **381**, 54-55 (1996).
281. B. A. V. Tiggelen, "Transverse Diffusion of Light in Faraday-Active Media," Phys. Rev. Lett. **75**, 422 (1995).
282. J. M. Laskar, S. Brojabasi, B. Raj, and J. Philip, "Comparison of light scattering from self assembled array of nanoparticle chains with cylinders " Opt. Commun. **285 (6)**, 1242 - 1247 (2012).
283. A. Wiedenmann, U. Keiderling, R. P. May, and C. Dewhurst, "Dynamics of field-induced ordering processes in ferrofluids studied by polarised small-angle neutron scattering," Physica B **385-386**, 453-456 (2006).
284. J. Li, Y. Lin, X. Liu, B. Wen, T. Zhang, Q. Zhang, and H. Miao, "The modulation of coupling in the relaxation behavior of light transmitted through binary ferrofluids," Opt. Commun. **283**, 1182–1187 (2010).
285. A. Ishimaru, *Wave Propagation and Scattering in Random Media* (Academic Press, New York, 1978).
286. C. F. Bohren, and D. R. Huffman, *Absorption and Scattering of Light by Small Particles* (Wiley, New York, 1983).
287. L. D. Landau, E.M.Lifshitz, and L.P.Pitaevskii, *Electrodynamics of Continuous Media* (Butterworth Heinmann, 1984).
288. M. Kerker, *The Scattering of Light and Other Electromagnetic Radiation* (Academic Press, New York and London, 1969).
289. M. Kerker, D. S. Wang, and C. L. Giles, "Electromagnetic scattering by magnetic spheres," J. Opt. Soc. Am. **73**, 765-767 (1983).
290. P. E. Wolf, and G. Maret, "Weak Localization and Coherent Backscattering of Photons in Disordered Media," Phys. Rev. Lett. **55**, 2696 (1985).
291. P. Sheng, *Scattering and Localization of Classical Waves in random Media* (World Scientific, 1990).
292. D. Lacoste, B. A. V. Tiggelen, G. L. J. A. Rikken, and A. Sparenberg, "Optics of a Faraday- active Mie Sphere," J. Opt. Soc. Am. A **15**, 1636-1642 (1998).
293. C.-C. Cheng, and M. G. Raymer, "Long-Range Saturation of Spatial Decoherence in Wave-Field Transport in Random Multiple-Scattering Media," Phys. Rev. Lett. **82**, 4807 (1999).
294. J. Wang, and A. Z. Genack, "Transport through modes in random media," Nature **471**, 345-349 (2011).
295. J. C. Dainty, *Laser Speckle and related phenomena* (Springer-Verlag, Berlin, 1975).

296. J. W. Goodman, *Speckle Phenomena in Optics: Theory and Applications* (Viva Books Private Limited, New Delhi, 2008).
297. R. Berlasso, F. P. Quintian, M. A. Rebollo, C. A. Raffo, and N. G. Gaggioli, "Study of speckle size of light scattered from cylindrical rough surfaces," Appl. Opt. **39**, 5811-5819 (2000).
298. Y. Piederrière, J. Cariou, Y. Guern, B. L. Jeune, G. L. Brun, and J. Lotrian, "Scattering through fluids: speckle size measurement and Monte Carlo simulations close to and into the multiple scattering," Opt. Express **12**, 176-188 (2004).
299. S. P. Morgan, and M. E. Ridgway, "Polarization properties of light backscattered from a two layer scattering medium," Opt. Express **7**, 395-402 (2000).
300. R. Bandyopadhyay, A. S. Gittings, S. S. Suh, P. K. Dixon, and D. J. Durian, "Speckle visibility spectroscopy: A tool to study time-varying dynamics," Rev. Sci. Instrum. **76**, 093110 (2005).
301. G. S. Spagnolo, and L. Cozzella, "Laser speckle decorrelation for fingerprint acquisition," J. Opt. **14**, 094006 (2012).
302. R. G. Berlasso, F. P. Quintian, M. A. Rebollo, N. G. Gaggioli, L. M. S. Brea, and E. B. Martinez, "Speckle size of light scattered from slightly rough cylindrical surfaces," Appl. Opt. **41**, 2020-2027 (2002).
303. A. Pino, J. Pladellorens, O. Cusola, and J. Caum, "Roughness measurement of paper using speckle," Opt. Eng. **50**, 093605 (2011).
304. A. Sadhwani, K. T. Schomacker, G. J. Tearney, and N. S. Nishioka, "Determination of Teflon thickness with laser speckle. I. Potential for burn depth diagnosis," Appl. Opt. **35**, 5727-5735 (1996).
305. Z. Hajjarian, and S. K. Nadkarni, "Evaluating the Viscoelastic Properties of Tissue from Laser Speckle Fluctuations," Sci. Rep. **2**, 316 (2012).
306. D. Brogioli, D. Salerno, F. Croccolo, R. Ziano, and F. Mantegazza, "Speckles generated by skewed, short-coherence light beams," New J. Phys. **13**, 123007 (2011).
307. H. D. L. Pires, J. Woudenberg, and M. P. V. Exter, "Statistical properties of two-photon speckles," Phys. Rev. A **85**, 033807 (2012).
308. P. Zakharov, F. Cardinaux, and F. Scheffold, "Multispeckle diffusing-wave spectroscopy with a single-mode detection scheme," Phys. Rev. E **73**, 011413 (2006).
309. P. Snabre, and J. Crassous, "Multispeckle diffusing wave spectroscopy of colloidal particles suspended in a random packing of glass spheres," Eur. Phys. J. E **29**, 149-155 (2009).
310. P. Rodriguez, S. Trivedi, F. Jin, C.-C. Wang, S. Stepanov, G. Elliott, J. F. Meyers, J. Lee, and J. Khurgin, "Pulsed-laser vibrometer using photoelectromotive-force sensors," Appl. Phys. Lett. **83**, 1893 (2003).
311. T. O. d. Santos, J. C. Launay, and J. Frejlich, "Photo-electromotive-force from volume speckle pattern vibration with large amplitude," J. Appl. Phys. **103**, 113104 (2008).
312. S. Feng, and P. A. Lee, "Mesoscopic Conductors and Correlations in Laser Speckle Patterns," Science **251**, 633-639 (1991).
313. I. Freund, M. Rosenbluh, and S. Feng, "Memory Effects in Propagation of Optical Waves through Disordered Media," Phys. Rev. Lett. **61**, 2328 (1988).
314. A. R. McGurn, and A. A. Maradudin, "Speckle correlations in the light scattered by a dielectric film with a rough surface:Guided wave effects," Phys. Rev. B **58**, 5022 (1998).
315. L. Florescu, and S. John, "Theory of photon statistics and optical coherence in a multiple-scattering random-laser medium," Phys. Rev. E **69**, 046603 (2004).
316. S. Pu, X. Chen, Y. Chen, Y. Xu, W. Liao, L. Chen, and Y. Xia, "Fiber-optic evanescent field modulator using a magnetic fluid as the cladding," J. Appl. Phys. **99**, 093516 (2006).

317. H.-C. Cheng, S. Xu, Y. Liu, S. Levi, and S.-T. Wu, "Adaptive mechanical-wetting lens actuated by ferrofluids," Opt. Commun. **284**, 2118–2121 (2011).
318. S. Radha, S. Mohan, and C. Pai, "Diffraction patterns in ferrofluids: Effect of magnetic field and gravity," Physica B **448**, 341-345 (2014).
319. T.-H. Tsai, P.-H. Chen, D.-S. Lee, and C.-T. Yang, "Investigation of electrical and magnetic properties of ferro-nanofluid on transformers," Nanoscale Res. Lett. **6**, 264 (2011).
320. M.-F. Chung, S. E. Chou, and C.-M. Fu, "Time-dependent dynamic behavior of light diffraction on ferrofluid," J. Appl. Phys. **111**, 07B333 (2012).
321. M. S. Singh, K. Rajan, and R. M. Vasu, "Estimation of elasticity map of soft biological tissue mimicking phantom using laser speckle contrast analysis," J. Appl. Phys. **109**, 104704 (2011).
322. A. Mazhar, D. J. Cuccia, T. B. Rice, S. A. Carp, A. J. Durkin, D. A. Boas, B. Choi, and B. J. Tromberg, "Laser speckle imaging in the spatial frequency domain," Biomed. Opt. Express **2**, 1553-1563 (2011).
323. A. P. Mosk, A. Lagendijk, G. Lerosey, and M. Fink, "Controlling waves in space and time for imaging and focusing in complex media," Nature Photon. **6**, 283 - 292 (2012).
324. G. D. Costa, and J. Ferrari, "Anisotropic speckle patterns in the light scattered by rough cylindrical surfaces," Appl. Opt. **36**, 5231-5237 (1997).
325. M. N. Akram, Z. Tong, G. O. Chen, and V. Kartashov, "Laser speckle reduction due to spatial and angular diversity introduced by fast scanning micromirror," Appl. Opt. **49**, 3297-3304 (2010).
326. S. V. Egge, K. Welde, U. Österberg, A. Aksnes, M. N. Akram, V. Kartashov, and Z. Tong, "Sinusoidal rotating grating for speckle reduction in laser projectors: feasibility study," Opt. Eng. **50**, 083202 (2011).
327. S. John, G. Pang, and Y. Yang, "Optical Coherence Propagation And Imaging In A Multiple Scattering Medium " J. Biomed. Opt. **1**, 180-191 (1996).
328. C. Yang, K. An, L. T. Perelman, R. R. Dasari, and M. S. Feld, "Spatial coherence of forward-scattered light in a turbid medium," J. Opt. Soc. Am. A **16**, 866-871 (1999).
329. J. R. Ott, N. A. Mortensen, and P. Lodahl, "Quantum Interference and Entanglement Induced by Multiple Scattering of Light," Phys. Rev. Lett. **105**, 090501 (2010).
330. M. Born, and E. Wolf, *Principles of Optics* (Peragmon, Oxford, 1980).
331. W. G. Egan, J. Grusauskas, and H. B. Hallock, "Optical Depolarization Properties of Surfaces Illuminated by Coherent Light," Appl. Opt. **7**, 1529-1534 (1968).
332. J. Li, G. Yao, and L. V. Wang, "Degree of polarization in laser speckles from turbid media:Implications in tissue optics," J. Biomed. Opt. **7**, 307-312 (2002).
333. Z. Tong, and X. Chen, "Speckle contrast for superposed speckle patterns created by rotating the orientation of laser polarization," J. Opt. Soc. Am. A **29**, 2074 - 2079 (2012).
334. Z. H. Yang, M. A. Haase, C. A. Leatherdale, and T. L. Smith, "Enhanced efficiency of CdMgZnSe down-converted light emitting diodes using light extraction features fabricated by laser-speckle lithography," J. Appl. Phys. **108**, 123106 (2010).
335. M. Draijer, E. Hondebrink, T. V. Leeuwen, and W. Steenbergen, "Review of laser speckle contrast techniques for visualizing tissue perfusion," Lasers Med. Sci. **24**, 639-651 (2009).
336. B. Redding, G. Allen, E. R. Dufresne, and H. Cao, "Low-loss high-speed speckle reduction using a colloidal dispersion," Appl. Opt. **52**, 1168-1172 (2013).
337. B. Ruffing, and J. Fleischer, "Spectral correlation of partially or fully developed speckle patterns generated by rough surfaces," J. Opt. Soc. Am. A **2**, 1637-1643 (1985).
338. K. Uno, J. Uozumi, and T. Asakura, "Correlation properties of speckles produced by diffractal-illuminated diffusers," Opt. Commun. **124**, 16-22 (1996).

339. B. Ruffing, "Application of speckle-correlation methods to surface-roughness measurement: a theoretical study," J. Opt. Soc. Am. A **3**, 1297-1304 (1986).
340. G. Volpe, G. Volpe, and S. Gigan, "Brownian Motion in a Speckle Light Field:Tunable Anomalous Diffusion and Selective Optical Manipulation," Sci. Rep. **4**, 1-6 (2014).
341. P. Sheng, ed. *Scattering and Localization of Classical Waves in Random Media* (World Scientific, 1990).
342. A. Lagendijk, B. V. Tiggelen, and D. S. Wiersma, "Fifty years of Anderson Localization," Phys. Today **62**, 24-29 (2009).
343. A. E. Miroshnichenko, S. Flach, and Y. S. Kivshar, "Fano resonances in nanoscale structures," Rev. Mod. Phys. **82**, 2257-2298 (2010).
344. S. Faez, A. Strybulevych, J. H. Page, A. Lagendijk, and B. A. V. Tiggelen, "Observation of Multifractality in Anderson Localization of Ultrasound," Phys. Rev. Lett. **103**, 155703 (2009).
345. M. P. V. Albada, and A. Lagendijk, "Observation of Weak Localization of Light in a Random Media," Phys. Rev. Lett. **55**, 2692 (1985).
346. G. Labeyrie, D. Delande, C. A. Muller, C. Miniatura, and R. Kaiser, "Coherent backscattering of light by cold atoms:Theory meets experiment," Europhys. Lett. **61**, 327-333 (2003).
347. J. P. McClymer, and H. M. Shehadeh, "Photon localization in a nematic liquid crystal," Phys. Rev. A **79**, 031802 (2009).
348. K. J. Vahala, "Optical microcavities," Nature **424**, 839-846 (2003).
349. Y. Piederrière, F. Boulvert, J. Cariou, B. L. Jeune, Y. Guern, and G. L. Brun, "Backscattered speckle size as a function of polarization: influence of particle-size and -concentration," Opt. Express **13**, 5030-5039 (2005).
350. C. P. Pang, C. T. Hsieh, and J. T. Lue, "A study of magneto-optical effect in dilute Fe_3O_4 ferrofluid by attenuated total reflection, ferromagnetic resonance and Faraday rotation," J. Phys. D: Appl. Phys. **36** 1764-1768 (2003).
351. A. F. Bakuzis, K. S. Neto, P. P. Gravina, L. C. Figueiredo, P. C. Moraisa, L. P. Silva, R. B. Azevedo, and O. Silva, "Magneto-optical properties of a highly transparent cadmium ferrite-based magnetic fluid," Appl. Phys. Lett. **84**, 2355 (2004).
352. F. C. MacKintosh, and S. John, "Coherent backsacttering of light in the presence of time-reversal-noninvariant and parity non-conserving media," Phys. Rev. B **37**, 1884 (1988).
353. R. Lenke, R. Lehner, and G. Maret, "Magnetic-field effects on coherent backscattering of light in case of Mie spheres," Europhys. Lett. **52** 620-626 (2000).
354. J. P. Embs, S. May, C. Wagner, A. V. Kityk, A. Leschhorn, and M. Lücke, "Measuring the transverse magnetization of rotating ferrofluids," Phys. Rev. E **73**, 036302 (2006).
355. E. Rosenkrantz, and S. Arnon, "Enhanced absorption of light by charged nanoparticles," Opt. Lett. **35**, 1178-1180 (2010).
356. F. J. G. d. Abajo, A. Asenjo-Garcia, and M. Kociak, "Multiphoton Absorption and Emission by Interaction of Swift Electrons with Evanescent Light Fields," Nano Lett. **10** 1859-1863 (2010).
357. P. Wangyang, Q. Wang, X. Wan, K. Hu, and K. Huang, "Optical absorption enhancement in silicon square nanohole and hybrid square nanowire-hole arrays for photovoltaic applications," Opt. Commun. **294**, 377–383 (2013).
358. N. C. Das, "Tunable infrared plasmonic absorption by metallic nanoparticles," J. Appl. Phys. **110**, 046101 (2011).

359. W. Jiang, A. Saxena, B. Song, B. B. Ward, T. J. Beveridge, and S. C. B. Myneni, "Elucidation of Functional Groups on Gram-Positive and Gram-Negative Bacterial Surfaces Using Infrared Spectroscopy," Langmuir **20**, 11433-11442 (2004).
360. X. Hao, J. Li, C. Ding, P. Song, and X. Yang, "Phase-dependent gain and absorption properties of mid- to far-infrared lights in three-coupled-quantum-wells," Opt. Commun. **282**, 4276–4282 (2009).
361. M. S. Anderson, "Enhanced infrared absorption with dielectric nanoparticles," Appl. Phys. Lett. **83**, 2964-2966 (2003).
362. L. M. Liz-Marzan, "Tailoring Surface Plasmons through the Morphology and Assembly of Metal Nanoparticles," Langmuir **22**, 32-41 (2006).
363. S. Dong, S. Pu, and J. Huang, "Magnetic field sensing based on magneto-volume variation of magnetic fluids investigated by air-gap Fabry-Perot fiber interferometers," Appl. Phys. Lett. **103**, 111907 (2013).
364. H. Ji, S. Pu, X. Wang, and G. Yu, "Influence of switchable magnetic field on the modulation property of nanostructured magnetic fluids," Opt. Commun. **285**, 4435–4440 (2012).
365. J. Philip, T. Jaykumar, P. Kalyanasundaram, and B. Raj, "A tunable optical filter," Meas. Sci. Technol. **14**, 1289-1294 (2003).
366. X. Fang, Y. Xuan, and Q. Li, "Measurement of the extinction coefficients of magnetic fluids," Nanoscale Res. Lett. **6**, 237 (2011).
367. X. Fang, Y. Xuan, and Q. Li, "Theoretical investigation of the extinction coefficient of magnetic fluid," J. Nanoparticle Res. **15**, 1652 (2013).
368. C.-Y. Hong, J.-J. Chieh, S.-Y. Yang, H.-C. Yang, and H.-E. Horng, "Simultaneous identification of the low-field-induced tiny variation of complex refractive index for anisotropic and opaque magnetic-fluid thin film by a stable heterodyne Mach-Zehnder interferometer," Appl. Opt. **48**, 5604-5611 (2009).
369. D. L. Koch, and S. B. Pope, "Coagulation-induced particle-concentration fluctuations in homogeneous,isotropic turbulence," Phys. Fluids **14**, 2447-2455 (2002).
370. F. Gu, S. F. Wang, M. K. Lu, G. J. Zhou, D. Xu, and D. R. Yuan, "Photoluminescence Properties of SnO2 Nanoparticles Synthesized by Sol-Gel Method," J. Phys. Chem. B **108**, 8119-8123 (2004).
371. C.-Y. Hong, S. Y. Yang, H. E. Horng, and H. C. Yang, "Control parameters for the tunable refractive index of magnetic fluid films," J. Appl. Phys. **94**, 3849-3852 (2003).
372. J. Promislow, A. P. Gast, and M. Fermigier, "Aggregation kinetics of paramagnetic colloidal particles," J. Chem. Phys. **102**, 5492 (1995).
373. F. M. Pedrero, M. T. Miranda, A. Schmitt, and J. C. Fernández, "Forming chainlike filaments of magnetic colloids: The role of the relative strength of isotropic and anisotropic particle interactions," J. Chem. Phys. **125**, 084706 (2006).
374. R. Regmi, C. Black, C. Sudakar, P. H. Keyes, R. Naik, G. Lawes, P. Vaishnava, C. Rablau, D. Kahn, M. Lavoie, V. K. Garg, and A. C. Oliveira, "Effects of fatty acid surfactants on the magnetic and magnetohydrodynamic properties of ferrofluids," J. Appl. Phys. **106**, 113902 (2009).
375. D. Espinosa, L. B. Carlsson, A. M. F. Neto, and S. Alves, "Influence of nanoparticle size on the nonlinear optical properties of magnetite ferrofluids," Phys. Rev. E **88**, 032302 (2013).
376. S. Brojabasi, and J. Philip, "Transmitted Light Intensity and the Speckle Pattern in a Poly-Acrylic Acid Stabilized Ferrofluid in the Presence of an External Magnetic Field," J. Nanofluids **2**, 237-248 (2013).
377. P. Licinio, and F. Frezard, "Diffusion Limited Field Induced Aggregation of Magnetic Liposomes," Braz. J. Phys. **31**, 356-359 (2001).

378. M. Elimelech, J. Gregory, X. Jia, and R. Williams, *Particle Depostion & Aggregation - Measurement, Modelling and Simulation* (Butterworth-Heinemann Ltd, Oxford, 1995).
379. J. Philip, P. D. Shima, and B. Raj, "Evidence for enhanced thermal conduction through percolating structures in nanofluids," Nanotechnology **19**, 305706 (2008).
380. M. A. G. Soler, L. G. Paterno, J. P. Sinnecker, J. G. Wen, E. H. C. P. Sinnecker, R. F. Neumann, M. Bahiana, M. A. Novak, and P. C. Morais, "Assembly of γ–Fe_2O_3/polyaniline nanofilms with tuned dipolar interaction," J. Nanopart. Res. **14**, 653 (2012).
381. P. E. Gharagozloo, and K. E. Goodson, "Temperature-dependent aggregation and diffusion in nanofluid," Int. J. Heat Mass Transfer **54**, 797-806 (2011).
382. R. V. Mehta, "Polarization dependent extinction coefficients of superparamagnetic colloids in transverse and longitudinal configurationsof magnetic field," Opt. Mater. **35**, 1436-1442 (2013).
383. R. Prasher, P. Bhattacharya, and P. E. Phelan, "Thermal Conductivity of Nanoscale Colloidal Solutions (Nanofluids)," Phys. Rev. Lett. **94**, 025901 (2005).
384. R. Karimzadeh, and N. Mansour, "The effect of concentration on the thermo-optical properties of colloidal silver nanoparticles," Opt. Laser Technol. **42**, 783-789 (2010).
385. S. Brojabasi, B. B. Lahiri, and J. Philip, "External magnetic field dependent light transmission and scattered speckle pattern in a magnetically polarizable oil-in-water nanoemulsion," Physica B **454**, 272-278 (2014).
386. S. Brojabasi, and J. Philip, "Magnetic field dependant backscattering of light in water based ferrofluid containing polymer covered Fe3O4 nanoparticles," J. Appl. Phys. **113**, 054902 (2013).
387. S. Brojabasi, V. Mahendran, B. B. Lahiri, and J. Philip, "Near infrared light absorption in magnetic nanoemulsion under external magnetic field," Opt. Commun. **323**, 54–60 (2014).
388. S. Brojabasi, T. Muthukumaran, J. M. Laskar, and J. Philip, "The effect of suspended Fe_3O_4 nanoparticle size on magneto-optical properties of ferrofluids," Opt. Commun. **336**, 278-285 (2015).